A Dynamic Rate Theory for the Response of Metals During Steady State and Pulsed Irradiation

Nasr M. Ghoniem

September 1977

UWFDM-154

Ph.D. thesis.

FUSION TECHNOLOGY INSTITUTE

UNIVERSITY OF WISCONSIN

MADISON WISCONSIN

A Dynamic Rate Theory for the Response of Metals During Steady State and Pulsed Irradiation

Nasr M. Ghoniem

Fusion Technology Institute
University of Wisconsin
1500 Engineering Drive
Madison, WI 53706

http://fti.neep.wisc.edu

September 1977

UWFDM-154

Ph.D. thesis.

A DYNAMIC RATE THEORY FOR THE RESPONSE OF METALS DURING STEADY STATE AND PULSED IRRADIATION

BY
NASR M. GHONIEM
UNIVERSITY OF WISCONSIN
SEPTEMBER 1977

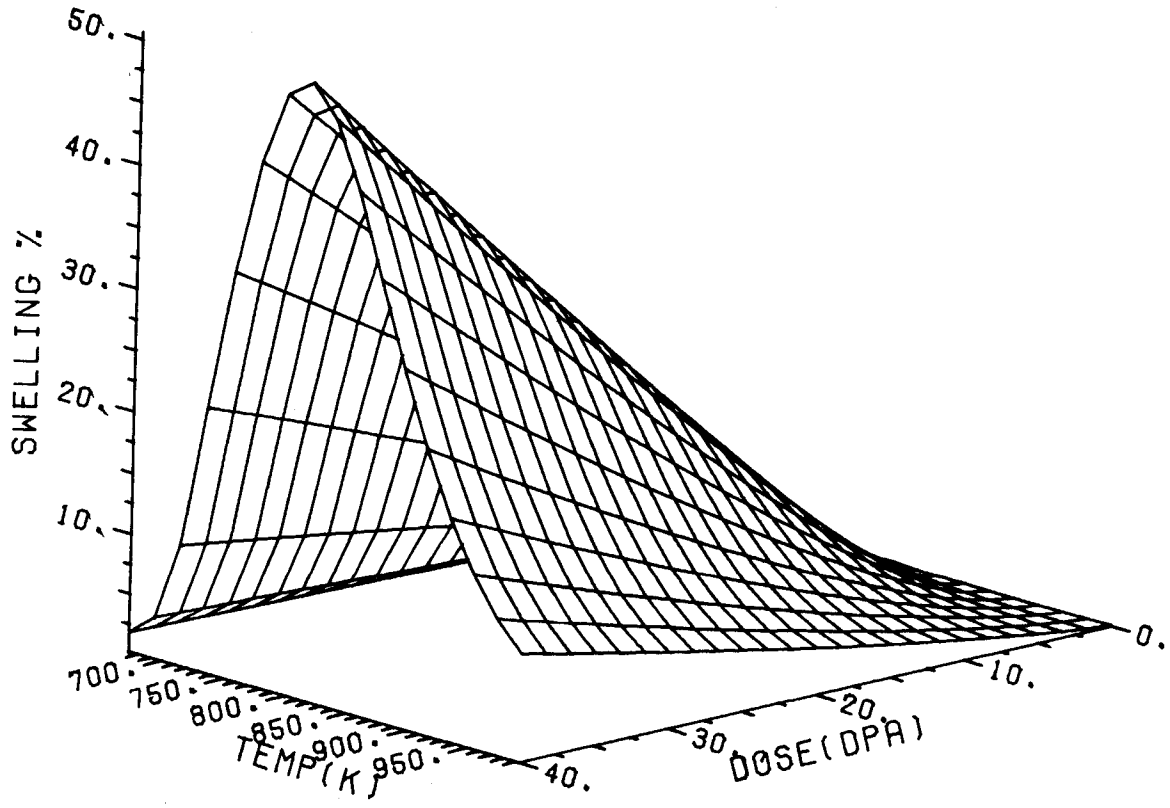

A DYNAMIC RATE THEORY FOR THE RESPONSE OF METALS DURING STEADY STATE AND PULSED IRRADIATION

BY

NASR MOSTAFA GHONIEM

A thesis submitted in partial fulfillment of the requirements for the degree of

DOCTOR OF PHILOSOPHY

(Nuclear Engineering)

at the

UNIVERSITY OF WISCONSIN-MADISON

1977

ABSTRACT

A DYNAMIC RATE THEORY FOR THE RESPONSE OF METALS DURING STEADY STATE AND PULSED IRRADIATION

NASR MOSTAFA GHONIEM

Under the supervision of Professor Gerald L. Kulcinski

This research is devoted to the development and applications of a Fully Dynamic Rate Theory (FDRT), for the growth of voids and loops. The FDRT is equally useful in the study and analysis of both steady-state and pulsed irradiation. It is shown that the development of such a theory is essential in the study of situations where the damage rate is time dependent. The study is generally concerned with four distinct areas: (a) The development and numerical solution of the FDRT, (b) Calibration of FDRT against experimental results, (c) Application of the theory to steady-state irradiation, (d) Application of the theory to pulsed irradiation.

A state variable approach to the formulation of the FDRT is used to describe the behavior of point defects, interstitial loops, vacancy loops and voids under different irradiation conditions. Based on the theory, and utilizing efficient numerical methods for stiff non-linear differential equations, a computer code, TRANSWELL, has been developed.

The program solves for the behavior of point defects and the microstructure of metals under a wide range of material and irradiation conditions. Another computer code, PL3D, has been constructed to handle and process the data generated by TRANSWELL, and display it in the form of 3-dimensional and contour plots.

Experimental data are selected from the open literature on three metals (316 SS, Al and Ni) irradiated with neutrons, heavy ions and electrons, and compared to the results of computations. The application of the theory to steady-state irradiations as well as void annealing under no irradiations, are shown to correlate closely to experimental findings.

The effect of dose rate and collision cascade collapse on the swelling phenomenon during steady-state irradiation is investigated. To understand dose rate and cascade collapse influence on swelling, the different microstructural and point defect process of 316 SS under irradiation are studied in this work as a function of irradiation dose and temperature.

The FDRT has been applied to a wide range of pulsed irradiation situations, where an inherently steady-state theory is generally not applicable. It is shown that for a fixed operating temperature, geometry and Inertial Confinement Thermonuclear Reactor plant output, the amount of swelling in the first wall can be reduced by using higher

yield pellets. This behavior is found to result from higher point defect mutual recombination rates during the irradiation pulse, and also because the annealing time between microexplosions of large yield pellets is longer.

Date: Sept 28, 1977 Signed: _____

Gerald L. Kulcinski
Professor of
Nuclear Engineering

ACKNOWLEDGEMENT

During the past 3 years of my graduate study at the University of Wisconsin, I have had the opportunity to work under the supervision of Professor G. L. Kulcinski. He has provided me with continuous help and encouragement through the different phases of my graduate residence at Wisconsin. His guidance, suggestions and inspiring discussions are greatly acknowledged.

I am indebted to Professor W. Wolfer and Professor P. Wilkes for the many comments and discussions throughout the work. Appreciation is also due to Dr. R. Bullough and Dr. B. Eyre of Harwell, for their constructive remarks and motivation during the summer of 1976.

My fellow Graduate Students and Research Associates in the radiation damage group have been of great help to me. So, I would like to thank the whole group, in particular, V. Smith, W. Yang, I. Saunderson, B. Weber, R. Lott, M. Sherman, J. Whitley, E. Opperman, K. McLaurin, T. Hunter, H. Avci and H. Attaya. Many thanks to the staff and faculty members of the Nuclear Engineering Department and both the Magnetic and Laser Fusion Design Teams of the University of Wisconsin for their interaction and great help.

I appreciate the persistent help of S. Schink in programming the Computer Code TRANSWELL and E. Anderson in constructing the Computer Code PL3D.

The endurance, care and relentless encouragement of my wife, Virginia, have been essential for the success of this achievement. I am deeply appreciative of her patience. Her continuous help in writing and editing have been important to produce this work.

The neat and diligent work of Lorraine Loken is greatly appreciated, for it has been very helpful in putting the thesis in its final form.

TABLE OF CONTENTS

TABLE OF CONTENTS (CONT'D)

TABLE OF CONTENTS (CONT'D)

LIST OF TABLES

LIST OF TABLES (CONT'D)

Page

Page

Page

Page

Page

Page

Page

Page

Page

CHAPTER I

INTRODUCTION

The generation of power from nuclear fusion or fission reactors produces large amounts of neutrons which unavoidably bombard the structural components. Unfortunately, these neutrons cause the metallic components to have much shorter useful lifetimes than normal, thus reducing the efficiency of the power plant and increasing the cost. Therefore, an understanding of the fundamental processes which produce such materials degradation is vital to the safe development of these long term solutions to the current energy crisis.

Radiation damage in metallic structures has been studied since the 1940's, and more recently (1966) the phenomena of void swelling has been added to the long list of mechanisms which reduce the lifetime of fast reactor cladding and fusion reactor blanket structures. Many experimental and theoretical studies have been conducted in the past 10 years on the growth of such voids, and a general understanding of the physics of this phenomenon has been developed for steady-state irradiation. It is now recognized that there is a complex relationship between irradiation parameters (energy and type of bombarding particle, flux, fluence, temperature, stress, etc.) and materials parameters (composition, dislocation microstructure, gaseous

content, crystal structure, etc.). However, one area which has not received a great deal of attention is the dynamic behavior under transient irradiation conditions. This area has remained relatively unexplored in spite of experimental [6-11] and theoretical[12-18] evidence which has shown that the time structure of the irradiation can have a considerable influence on the final state of void swelling in metals.

A dynamic analysis of the void swelling problem is long overdue for fission reactors and charged particle simulation studies. Recent progress in the inertial confinement area has made such a study absolutely imperative.

The object of this thesis is to provide a method by which the dynamic behavior of point defects in irradiated metals can be described.

More detail on the importance of a dynamic treatment of pulsed irradiation on the growth of voids is given in Chapter II, while some specific reactor concepts which may provide unique pulsed irradiation environments are described in Chapter III. The current concepts of void nucleation and growth are reviewed in Chapter IV, and the major contribution of this thesis to the Fully Dynamic Rate Theory (FDRT) of void growth is given in Chapter V. Chapter VI contains a brief description of the Computer Code, TRANSWELL, developed during the course of this work to handle the system of simultaneous equations developed in Chapter V. The general features of TRANSWELL are illustrated by a few examples in Chapter VII,

and compared to experimental measurements as a form of "calibration". The use of the FDRT for steady state is illustrated in Chapter VIII and the specific effects of dose rate and collision cascade collapse efficiency are examined. The response of void structures to pulsed irradiation is given in Chapter IX followed by the overall conclusions of this work.

Finally, the reader should be aware that much of this work has been published in more detail in the University of Wisconsin Fusion Design Memos (UWFDM's), listed in Table (1.1). The reason for prior publication before the completion of all the aspects of this study was to allow much more complete documentation of this very complicated area, and to allow a critical assessment of the FDRT before extensive (and costly) calculations were made on any given alloy. In any case, much of the work in Chapter VIII and almost all of the work in Chapter IX has not been published earlier.

TABLE (1.1)

SUMMARY OF AUTHOR'S PREVIOUS PUBLICATIONS OF WORK RELATED TO THIS THESIS

Ref.#	UWFDM#	Date	Title
99	138	Oct., 1975	Void Growth Kinetics Under an Irradiation Pulse.
	179[a]	Oct., 1976	Swelling of Metals Under Pulsed Irradiation.
53	180	Nov., 1976	Fully Dynamic Rate Theory (FDRT) Simulation of Radiation Induced Swelling of Metals.
81	181	Dec., 1976	TRANSWELL (VerI): A Computer Code for Metal Swelling and Creep Under Transient, Pulsed or Steady Irradiation Conditions.
116	199	Mar., 1977	Critical Assessment of Irradiation Pulse Annealing in Metals.
82	200	Mar., 1977	Calibration of the Fully Dynamic Rate Theory Using the Computer Code TRANSWELL.
126	203	Apr., 1977	The Importance of Materials and Irradiation Parameters on Void Growth in Metals; Part I: The Effect of Displacement Rate and Cascade Efficiency.
100	211	June, 1977	PL3D: A 3-Dimensional and Contour Plotting Computer Code.
127	(b)	July, 1977	Dose Rate and Cascade Collapse Effects on 316 SS Swelling.

(a) Published in the Proc. of the Int. Conf. on the Properties of Atomic Defects in Metals, Argonne, 1977.

(b) To be published in the ANS Transactions for the Winter Meeting, San Francisco, 1977.

CHAPTER II

IMPORTANCE OF A DYNAMIC TREATMENT OF IRRADIATION PRODUCED DEFECTS WITH RESPECT TO VOID GROWTH

II.A. Introduction

The object of this chapter is to outline in a qualitative manner the importance of the dynamic analysis of point defects in irradiated metals. It is well known (Chapter IV) that the nucleation and growth of voids is very sensitive to the vacancy and interstitial concentration in the matrix. These point defect concentrations in turn depend on the microstructure of the metal and the chronology of the irradiation cycle. During steady-state irradiation the microstructure changes on a relatively long time scale, e.g., minutes during charged particle simulation experiments to days during neutron irradiation. However, the lifetime of point defects in metals, at temperatures for void growth, is on the order of a second for vacancies and microseconds for interstitials (see Chapter VII for more detail). Therefore, if the duration of the damage production is shorter than the lifetime of either of the point defects, then the current approach of steady-state analysis will break down.

We will also see that annealing of defects between pulses of irradiation can also have a significant influence on the net result of the bombardment. This means that even if the duration of the damaging pulse is long enough to let the

vacancy and interstitial concentrations come to 'equilibrium' values, separation of such pulses by microseconds for interstitials or seconds for vacancies, means that point defect concentrations will decline to a value much lower than that present at the end of analysis. Therefore, the analysis of void growth must take into account these rapidly changing point defect concentrations if realistic results are to be expected.

We will next discuss some examples of where pulsed damage is important in nuclear systems and this will be followed by a brief description of a systematic approach to the analysis of pulsed irradiation.

II.B. Examples of Nuclear Systems Where Pulsed Irradiation is Important

II.B.1. Fast Breeder Reactors

The safe performance of Fast Breeder Reactors requires controlled operation of these reactors in the case of accidents. One of the types of accidents currently envisioned is a power excursion, where an abnormally high neutron flux environment is experienced in a short period of time. It is possible that neutron fluxes of 10^{16}-10^{17} n/cm^2/sec exist for milliseconds along with the generation of high temperatures. Obviously, equilibrium will not be achieved in these types of accidents and a dynamic treatment of defects is required to predict subsequent microstructural and property changes.

II.B.2. Ion Beam Scanning Experiments

Ion bombardment studies, using charged particle accelerators have been used to simulate, in a short period of time, radiation damage to reactor components. These experimental studies supplied invaluable information on the problem of metal swelling under irradiation. Simulation studies supplemented actual reactor experiments, since they are performed in a controlled atmosphere. They also furnished the necessary experimental results to develop and calibrate metal swelling theories.

Beam uniformity across the surface of the bombarded specimen is of prime concern in these experiments, and two methods have been used to obtain a uniform ion dose: scanning the ion beam across the specimen surface and holding a defocused beam in one position over the specimen. Dose rates of 0.32 dpa/sec in the rastered ion beam experiment and 8×10^{-2} dpa/sec in the defocused beam experiment, were used for studying Ni ion bombardment effects on Ni [11]. The two methods were found to produce very different microstructures. Again, a dynamic theory for defect analysis is required to understand the observed differences.

II.B.3. Pulsed Neutron Sources

Pulsed neutron sources for fusion reactor materials studies which use intense ion beams to irradiate tritiated targets, and intense relativistic beams to implode DT filled targets to thermonuclear burn are being developed at Sandia

Laboratories [19]. Recent experimental and theoretical results indicate that high current electron and ion beams are capable of producing, in nanoseconds, intense bursts of DD and DT neutrons from beam target interactions[20,21], as well as thermonuclear neutrons from imploded targets.

The duration times for neutron pulses are much shorter even than interstitial lifetime at high temperatures in metals and will require dynamical treatments to determine the ultimate fate of the material.

The Lawrence Livermore Laboratory is now contructing two intense sources of 14-MeV neutrons for materials research for the fusion energy program [22]. These sources will use the deuteron beam-rotating trituim target technology developed with RTNS-I (Rotating Target Neutron Source). A source strength of 4×10^{13} n/s will be produced with a maximum flux available for irradiation of small samples of $\sim 1.5 \times 10^{13}$ $n/cm^2 s$. Future upgrading to a source strength of 1×10^{14} n/s will be investigated.

The instantaneous damage rate in the rapidly rotating target means that high instantaneous dose rates will be followed by 'relatively' long periods of no defect generation. Accurate descriptions of the materials properties, such as tritium diffusivity will obviously require a dynamic analysis of this type of irradiation.

II.B.4. Pulsed Fusion Reactors

Neutron-degradiation problems will place an upper limit

on the life-time of the first-wall in all DT-burning fusion power plants, whether they are of the laser, the electron beam, the ion beam or of the magnetic-confinement type. Preliminary experiments indicate that the best first-wall materials may survive exposure to 14 MeV neutrons (the kind released by deuterium-tritium fusion) for 3-10 years at the most, provided that the neutron power flux is limited to about one megawatt per square meter. This implies that any one gigawatt-DT-burning fusion reactor may need as much as 1,000 square meters of first-wall area, either in one chamber or in several chambers.

Some CTR designs require pulsed operation with the interval between fusion burn cycles ranging from 1 to 10 seconds (theta pinches, electron beam, ion beam and laser reactors) to several hundred seconds (Tokamak reactors) and pulse widths ranging from nanoseconds (laser, electron beam and ion beam reactors) to tens of milliseconds (theta pinch reactors) to the neighborhood of several thousand seconds (Tokamak reactors). The fluctuations in temperature, stress and damage rate resulting from pulsed reactor operation are expected to significantly affect point defect concentrations which affect the microstructure and therefore the component life. Hence, theoretical and experimental studies are also needed to analyze and understand time-dependent materials responses.

II.C. A Systematic Approach to Pulsed Damage Analysis

In any of the previously considered pulsed systems,

analysis of radiation induced phenomena requires the study of a diversity of interrelated problems. Figure (2.1) shows a flow diagram of the theoretical and calculational procedures in the study of radiation damage in pulsed systems.

The primary pulsed system radiation source can be described by the spectra of neutrons, charged particles, or photons produced in each pulse. The neutron spectra will be determined by the fuel, the source density, and any recoil atoms produced by the source.

The charged particle spectra from a thermonuclear source will consist of the fusing nuclei, product nuclei and non-fusing species. The range will be limited to approximately the maximum kinetic energy given to a product nucleus in a fusion reaction.

The photon spectra will be determined by the confinement mechanism source temperature, and the species present in fusion systems. For most short duration systems, the energy range of interest for photons is up to about 100 KeV. However, higher energy photons will interact with the first-wall but they are principally due to the secondary radiation such as neutron capture. These high energy photons are also present in fusion reactors.

A final assessment of a certain material's response, like void swelling needs a considerable understanding of radiation damage physics and its effect on materials' properties. In a pulsed system, photonics and neutronics calculations for

THEORETICAL AND CALCULATIONAL PROCEDURES FOR RESEARCH ON RADIATION DAMAGE IN PULSED SYSTEMS

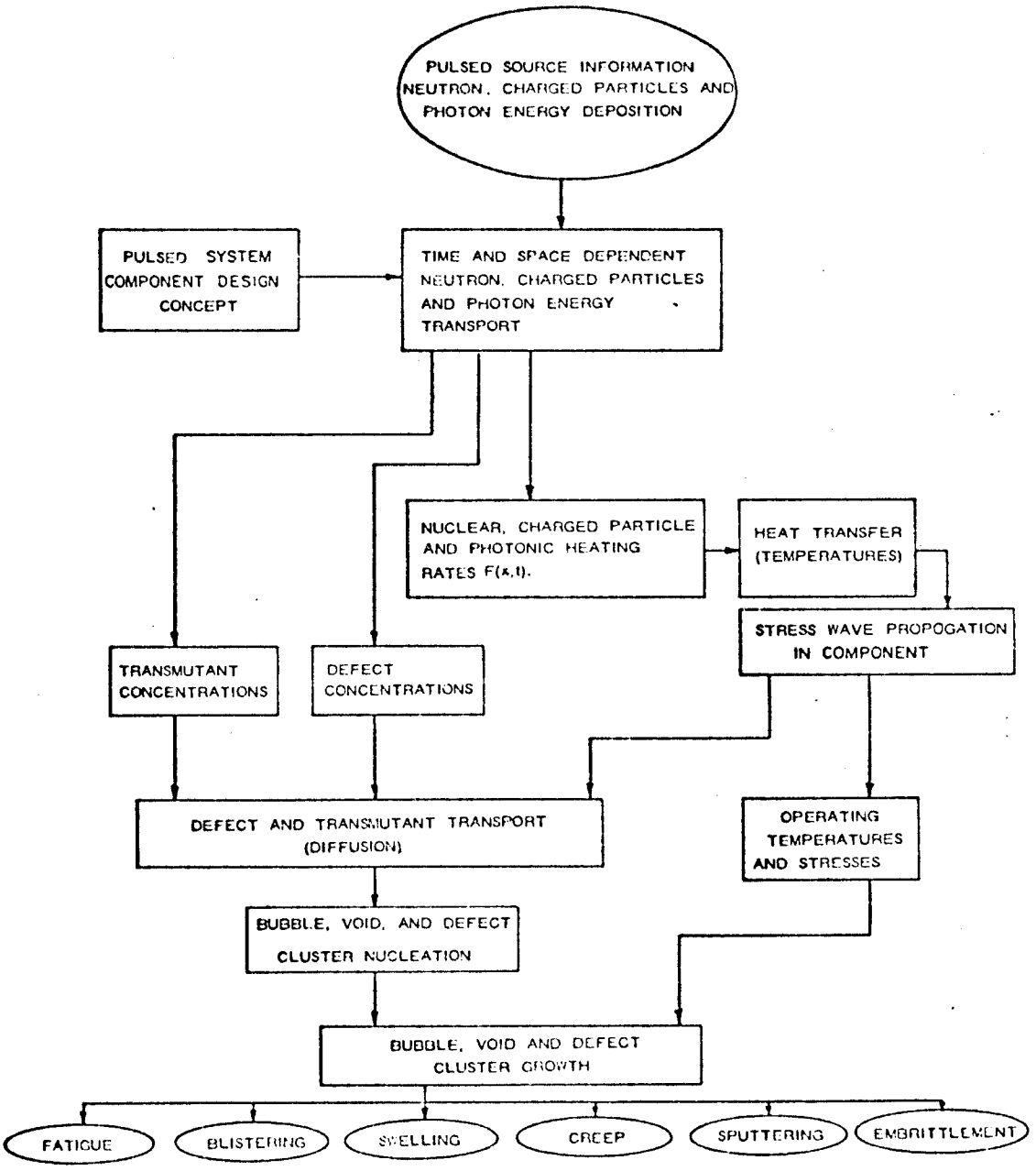

Figure (2.1)

a given design concept, are essential to determine spatial and time dependence of neutrons and photons.

Components of pulsed systems will encounter photon radiation which ranges from a few electron volts to a few million electron volts. The primary interaction of photons with materials in these energy ranges are:

(1) photo electric effect

(2) coherent scattering

(3) incoherent scattering

(4) pair production

Cross sections for each of these reactions have been tabulated in various forms [23-25] and are available for numerical calculations, from which heating rates and heat transport can be determined.

The primary interaction rates in first-walls to the current of neutrons from a pulsed fusion source will be determined by the corresponding neutron cross sections of the material. Each possible reaction will deposit some local energy and produce products such as neutrons, charged particles, or photons. A knowledge of the energy associated with each reaction, and the processes by which it is transported, allows the evaluation of local heating and the total number of atomic displacements.

Ions traversing first-wall materials may lose energy by the following interactions [26]:

(a) Excitation and ionization of the electrons in the atoms are the dominant mode of loss by moderate and low energy loss.

(b) Inelastic nuclear collisions become quite significant at high ion energies and contribute heavily to the total energy loss.

(c) Elastic interactions occur; in which the ion transfers kinetic energy to the struck atom.

(d) Photon emission due to particle deceleration in atomic fields is the least important of the ion energy-loss process. This interaction is commonly called Bremsstrahlung.

For the high energy region (approximately more than 1 MeV for He ions) the well known Bethe-Bloch [27] equation is applicable while for the low energy range (approximately less than 0.4 MeV for the ions) the Lindhard-Winther formulation is applicable [28]. Such energy loss calculations were used by Hunter and Kulcinski [29] to determine heating rates, temperatures and atomic displacements as a function of time and space for a reference inertial confinement reactor.

High energy radiation simultaneously produces vacancies and interstitials in crystalline materials and, therefore, both types of defects are supersaturated during irradiation. The nucleation of defect precipitates under this circumstance is fundamentally different from the usual nucleation problem because of the competing effects of interstitials and vacancies on the size distribution of precipitate embryos.

The precipitation of defect aggregates during elevated temperature irradiation is a rather complicated phenomenon because of the interaction of a number of competing processes.

Point defects, vacancies and interstitials, and defect clusters are produced by the radiation. Mobile defects diffuse, annihilate each other, aggregate into various types of clusters, and precipitate at sinks (such as dislocations and grain boundaries). Small defect clusters, especially the vacancy type, "evaporate" by emission of point defects. Because of the complexity, most treatments of the phenomenon have concentrated on certain aspects, e.g., the production of defects, the nucleation of defect clusters, and the growth of clusters, especially voids. When treating any one of the aspects, one usually makes some simplifying assumptions about the required input from other aspects; growth theories may assume a preexisting number-density of void nuclei, or nucleation theory assumes that quasi-steady-state defect concentrations are set up in which defect production is balanced by defect losses through recombination and annihilation at existing sinks. Nucleation theory applied to defect clusters has been used to calculate steady-state nucleation rates that are established in such an enviornment and, sometimes, to give estimates of the time required to reach steady-state [30-33].

Several treatments of the dynamic nature of microstructure nucleation emerged in the last few years [15-18]. A major conclusion of the studies is that the phenomenon of nucleation throttling of highly pulsed systems is particularly important because of the sensitivity of the damage process

to the nucleation step and the obvious fact that if defects do not nucleate, they cannot grow.

Diffusion, transport and clustering of point defects is a first step to final irradiation induced property changes. The dynamic growth of extended microstructures leads to swelling, creep, embrittlement, fatigue, blistering and sputtering. The temperature and stress environments for such changes are determined by detailed considerations of energy deposition rates, heat transfer and consequent stress wave propogation [29].

The present work concentrates on the dynamic nature of point defect diffusion and their impact on the growth of voids, vacancy loops and interstitial loops. This is necessary to satisfy the main objective of this study; this is to assess swelling of metals under steady-state and pulsed modes of operation.

The importance of pulsed damage on the analysis of irradiated materials has been shown to extend beyond fusion systems and include fission reactors, neutron sources and simulation experiments. A generalized treatment of this pulsed damage has been outlined and in the ensuing chapters we will investigate the details of such an analysis.

CHAPTER III

ANALYSIS METHODOLOGY OF PULSED FUSION SYSTEMS

In this chapter we will concentrate on one of the nuclear systems which has a wide range of potential pulsed damage problems, namely Fusion Reactors. The discussion will be centered around the various time domains during and between the damage pulses.

III.A. Specific Environments in Pulsed Fusion Reactors

III.A.1. Theta-Pinch Reactors (RTPR)

Important consequences of neutron radiation on the bulk properties of the insulator will result from (i) atomic displacements and (ii) the introduction of lattice impurities by neutron induced transmutations. These phenomena can result in dimensional changes, the formation of electrically active point-defects, and departure from stoichiometry [34].

The major task of the first-wall insulator is to prevent electrical breakdown between the plasma and blanket segments during the implosion heating stage.

Swelling leads to changes in the linear dimensions of the wall, and differential swelling rates between the insulator and the metal backing in the first-wall could produce stresses in the wall that would limit its lifetime. Therefore, it will be necessary to produce a first-wall composite that is matched in swelling characteristics.

Recent work suggests that cyclic stressing may also

influence void formation [35]. Cyclic stresses may set dislocation lines in vibratory motion, and moderate stress levels appear to be sufficient to upset the void formation mechanism at homologous temperatures of 0.3-0.4. The slight preference for interstitial absorption and corresponding vacancy super-saturation is lowered which has the effect of reducing the rate of void formation and growth. If this mechanism is important at frequencies which characterize the operation of the RTPR, first-wall swelling problems may be correspondingly reduced.

III.A.2. Relativistic Electron Beams Reactors (REB)

The use of relativistic electron beams (REB) fusion is similar in many respects to the better known laser fusion method. Both approaches require the irradiation of small spherical pellets containing deuterium and tritium and both require high energy beams which last for a few billionths of a second or less. In both approaches the beams compress the thermonuclear fuel to ultra-high densities, and techniques for charging and firing the energy storage system at a rate of approximately 10 sec^{-1} must be developed.

There are many similarities between REB-induced fusion systems and laser reactor systems. However, certain features are unique to the E-beam case. A high vacuum (10^{-4} torr) is required in the hollow cathode to prevent insulator flashover in the presence of the megavolt potentials utilized. This may require evacuation of the entire reactor vessel. At least two

problems arise. First, the vessel must be evacuated between pulses. Since high repetition rates are required for economic feasibility, a large vacuum system is probably required. Secondly, the utilization of a high vacuum complicates the problem of protecting the reactor first-wall. Debris and radiation from the pellet microexplosion impact the wall causing ablation and impulsive loading.

An important factor in overall system evaluation is the pulse rate to produce a given amount of electrical power. For the reference 100 MW reactor [36], the required pulse rate is minimized for economic reasons since component lifetime, number of fuel pellets used and charging requirements are all affected.

III.A.3. Laser-Controlled Thermonuclear-Reactor (LCTR)

Current LCTR studies are considering several cavity and blanket designs. These designs can be categorized according to the physical processes by which energy deposition from pellet microexplosion is accommodated by the first-wall of the reactor cavity. Energy deposition from incident X-rays, α particles, and pellet debris occurs in a very thin layer at the surface of the reactor structure. Thus, the inner surfaces of cavity walls to depths of a few μm must be designed to withstand energy deposition on the order of 20 MJ per microexplosion for each 100 MJ pellet. Blanket-coolant regions must accept total volume energy depositions of $\sim$80 MJ per microexplosion in addition to heat that must be conducted

through the cavity wall.

The threat presented to the first-wall by X-rays is more straightforward. Since many of the X-ray photons have energies greater than 5,000 volts, they penetrate deep into the wall and deposit their energy quite harmlessly with respect to displacements, and cause only moderate temperature increase. Although X-rays with energies of less than 1,000 volts carry off less than .1 percent of the energy of the microexplosion, they deposit their energy within a micrometer of the wall's surface, very rapidly heating a thin skin of the first-wall to a high temperature. The large thermal gradients and mechanical stresses so produced could cause the front surface of the first-wall to flake away very slightly with each micro-explosion. A possible solution is to build the first-wall of materials such as lithium, beryllium and carbon, which are relatively transparent to soft X-rays. The soft X-rays would therefore penetrate a considerable distance into such a surface layer, thereby heating a larger amount of mass to a lower temperature and reducing the peak stresses to acceptable levels.

The threats presented to the integrity of the first-wall by charged particles streaming from the microexplosion are complex and substantial. One threat is analogous to that presented by soft X-rays: the less energetic ions (thermal deutrons and tritons), also absorbed in a thin layer, are capable of producing sharp thermomechanical stresses in a

thin skin of the first wall. The more energetic ions are sufficiently penetrating and few in number, so that they should produce relatively little damage.

The second major threat presented by charged particles resembles the gas-bubble problem associated with neutrons: the energetic nuclei that bury themselves in the first few micrometers of the surface quickly acquire electrons and become gas atoms that agglomerate into growing bubbles with high internal pressures. These bubbles are also capable of rupturing the surface of any solid wall in a much shorter time than the desired service life of a fusion power plant [37].

Evaporation and ablation of lithium from the cavity surface is characteristic of phenomena which occur in both the wetted-wall and the BLASCON [38] concepts. The reactor cavity for the wetted-wall concept [39] is formed by a porous niobium wall through which coolant lithium flows to form a protective coating on the inside surface. The protective layer of lithium absorbs energy of the α particles and pellet debris and part of the X-ray energy, is vaporized and ablates into the reactor cavity and is subsequently exhausted through a supersonic blowdown nozzle. The ablative layer is restored between pulses by radial inflow of lithium from the blanket region.

In the BLASCON concept [38], a cavity is formed by a vortex in a rotating pool of lithium in which pellet microexplosions take place. Rotational velocity is imparted to the circulating lithium by tangential injection at the periphery of the reactor pressure vessel. Bubbles can be entrained in the rotating lithium to attenuate the shock waves created by pellet microexplosions. Energy deposition by X-rays and charged particles results in evaporation of lithium from the interior surface of the vortex.

Protection of cavity walls from α particles and charged particles in the pellet debris by means of a magnetic field is also a potential conceptual alternative [40].

Another design was proposed by Hovigh, et al. [41] which utilized a small yield pellet (7MJ) and lower power laser (0.1 MJ). This approach was used to suppress the ablation of a wetted-wall by improved pellet design, increased first-wall area (through pyramidical first-wall topography and increased wall radius), and by reducing the blast energy.

A recent study by Maniscalco [42] describes a low yield laser fusion reactor which employs a fissile (hybrid) blanket to get energy and fuel multiplication. This concept employs a graphite liner over a stainless steel first-wall. The total pellet yield is 10.5 MJ with a laser input to the pellet of 500 KJ. In another more recent design [43] they describe a lithium waterfall concept in which a lithium waterfall flows continuously between the pellet and first-wall.

This design eliminates the ablation and shock problems to the first wall while maintaining a high breeding ratio.

A gas-filled chamber concept was recently studied by the Wisconsin group [44]. In this design a low pressure inert gas was maintained in the chamber during microexplosions while a high speed vacuum system cleans the chamber in-between pulses. A major advantage of this design is the absorption of the blast energy in the gas which reduces first-wall problems.

III.B. Some General Time Domain Considerations for Damage in Pulsed Fusion Reactors

Most CTR designs would be considered of the pulsed type. Figure (3.1) is an illustration of the time scales connected with fusion reactors and they reflect the pulsed nature of most of the proposed designs. Such pulsed systems are designed under the following circumstances [45]:

(1) They are used in order to obtain extreme conditions, most notably high pressures which can only be obtained in transient circumstances and not under steady-state conditions. There are many examples of these, ranging from the generation of very high pulsed magnetic fields to the high energy fluxes that can be obtained in focused pulsed laser beams and pulsed electron beams.

Table (3.1) shows the typical Energy-Release Mechanisms from a 99-MJ DT Pellet microexplosion [46], and Table (3.2) displays a timescale of events for LCTR pellet fusion

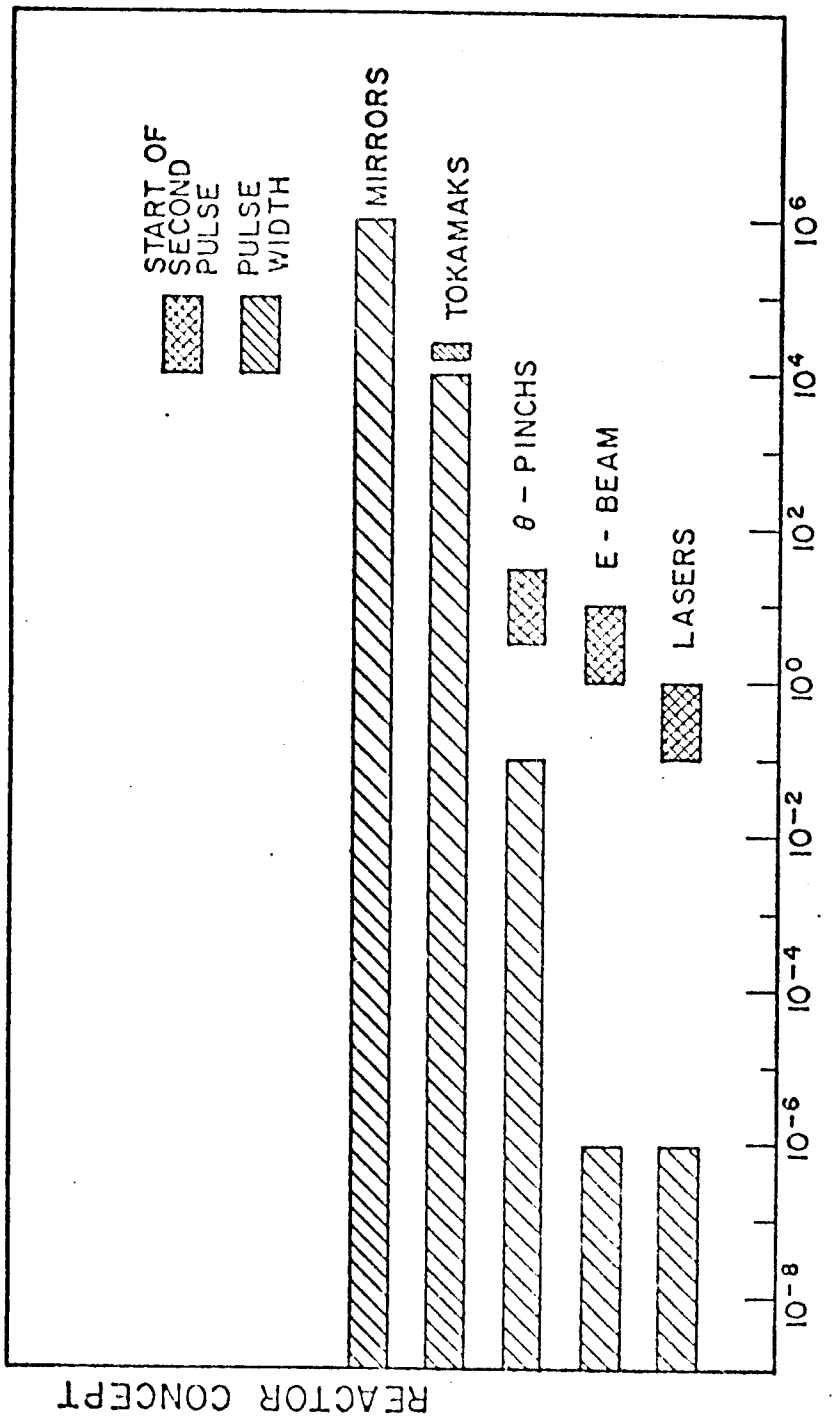

Fig. (3.1) Illustration of the Time Scales for Fusion Reactors.

TABLE (3.1)

TYPICAL ENERGY-RELEASE MECHANISMS FROM

A 99-MJ DT PELLET MICROEXPLOSION [46]

Mechanism	Fraction of Total Energy Release	Particles per Pulse	Average Energy per Particle	
X-rays	0.01		∿4 keV peak	
Alpha particles that escape plasma	0.07	2.2×10^{18}	2 MeV	
Plasma kinetic energy	0.15			
alpha particles		1.3×10^{19}	0.6 MeV	
deuterons		1.2×10^{20}	0.3 MeV	total average
tritons		1.2×10^{20}	0.4 MeV	0.37 MeV
Neutrons	0.77	3.3×10^{19}	14.1 MeV	

TABLE (3.2)

TIMESCALE OF EVENTS FOR LCTR PELLET FUSION PULSE [46]

Time	Primary Events	Secondary Events
-20 to -5 msec	pellet enters cavity	
-150 nsec	laser pulse fired	
-10 nsec	laser pulse arrives at pellet surface	
0	thermonuclear burn begins	
+10 psec	thermonuclear burn complete	
+6 nsec	x-rays strike first wall	ablative material begins expansion from first wall
+30 nsec	x-rays strike last optical surface	
+20-100 nsec	neutrons deposited in reactor vessel	shock wave induced in lithium
+50 nsec	neutrons strike last optical surface	ablative material and pellet debris interact
0.3 to 1.2 μsec	pellet debris strikes first wall	cavity atmosphere equilibrated
+1 msec	cavity blowdown begins	
0.01 to 10 sec	restoration of original cavity conditions complete	wetted-wall blowdown complete, lithium vortex restored, turbulence in rarified dry-wall cavity dissipated

pulse [46].

The thermonuclear burn completes in 10 picoseconds and the neutrons are deposited in the reactor vessel in the range of 20-100 nanoseconds. Pellet debris create large displacement rates in the order of 100 dpa/s when they bombard the first-wall [47].

(2) Engineering and technological advantages emerge from pulsed systems. The use of pulsing is thought to provide a period for scavenging the system of exhaust products and impurities. Also during this period, suitable material and operation conditions could be established to alleviate the swelling resulting from each pulse, as will be discussed in Chapter IX.

III.C. Concluding Remarks

It has been shown that a wide range of pulsed damage conditions exist in fusion reactors. The instantaneous dose rates can vary from 10^{-4} dpa/s in theta pinches to 100 dpa/s in inertial confinement devices. The development of a dynamic treatment for defect analysis is absolutely imperative for these systems because the more traditional steady-state approach will not be applicable.

CHAPTER IV

PREVIOUS THEORETICAL WORK IN VOID NUCLEATION AND GROWTH

There has been a great deal of effort in the area of void nucleation and growth in the past 10 years.[1-5] It is not the object of this chapter to review all of the work to date but rather to concentrate on that which is pertinent to the overall goal of this thesis, namely, the effect of a dynamic microstructure on the growth of voids. It is convenient to separate the past work into nucleation theories of which relatively less is known, and growth theories which appear to be in much better shape.

IV.A. Void and Loop Nucleation

IV.A.1. Steady State Nucleation Theories

The formation and growth of "second phase" particles, e.g., precipitates, voids, and interstitial loops in a "parent phase", can be expressed in a general manner by reaction-rate equations that give the rate of change in the population of any type of particle.

$$\frac{dC_j}{dt} = \sum_k k_{k\to j} C_k - \sum_k k_{j\to k}\, C_j + K_j - L_j \qquad j=1,2,\ldots,N \qquad (4.1)$$

If we consider as an example, the population of voids consisting of exactly m_j vacancies and n_j gas atoms, then C_j is the concentration of voids of type j. The rate constant,

$k_{k\to j}$, is the probability that a void of type k is converted into a type j void during a unit time interval. The first sum in Eq. (4-1) is the rate at which voids of type j are produced by reactions originating at all types of particles that can react to form type j, and the second sum is the rate at which voids of type j react to form other types. The third term, K_j, is the rate at which voids of type j are created directly, e.g., clusters of vacancies formed in a cascade, and L_j is the loss of voids of type j due to other mechanisms than those included in the second term, e.g., resolutioning in a cascade.

The set of differential equations, Eq. (4-1), for all j's of interest could describe completely the nucleation and growth of, for example, the void or dislocation structure that develops during irradiation.

The rate constants, $k_{k\to j}$, are derived from appropriate models. To get these rate constants the validity of the principle of detailed balance is assumed. This means that at equilibrium, each individual forward reaction is balanced by the corresponding back reaction. This principle excludes net "circular" flows at equilibrium, e.g., emission of divacancies should not be balanced by absorption of monovacancies that have formed by decomposition of divacancies.

The reaction rates derived in this manner are independent of the radiation induced excess defect concentrations and contain only properties of the reaction partners.

The rate constants for other reactions involving, for example, divacancies, diinterstitials, and gas atoms can also be derived in a similar fashion. With the knowledge of the rate constants and an appropriate assumption about the boundary conditions, e.g., initially only single vacancies and interstitials present and a constant production rate of defects, Eq. (4-1) could be integrated, which would yield a complete description of the evolution of the microstructure during irradiation. Such a unified treatment has not been attempted to date.

In conventional nucleation theory, expressions for the steady-state nucleation rates are derived for given sets of supersaturation, temperature, and other external variables. The assumption of a steady-state simplifies the general rate equations, Eq. (4-1), enormously because the concentrations C_j and the rate constants that contain the concentrations of the mobile species become time independent.

The two independent developments of void nucleation theory by Russell [15,33,48], and by Katz and Weidersich [30,49] differ in that the former may be applied to transient processes, whereas the latter is inherently a steady-state formulation. This distinction was not crucial in the simulation of cladding in the breeder, which is essentially a steady-state device (with the exception of occasional flux excursions).

A final note of caution must be added; Russell

emphasized that a metal under irradiation is a system driven into a highly irreversible state so that equilibrium thermodynamics are generally inapplicable [50].

IV.A.2. Time Dependent Nucleation Theories

At the start of an irradiation, the vacancies and interstitials will be at thermal equilibrium, and their concentrations will build to steady-state values as the irradiation progresses. If the microstructure does not change significantly during the build-up, the time required for the approach to steady-state may be expressed as a relaxation time [51]. In a study by Sprague, Russell and Choi [18], the initial time dependence of the point defect concentrations was calculated while allowing for the clustering of vacancies into void embryos and interstitials into dislocation loops. The interstitial clustering was calculated with the model used by Hayns [52]. The vacancy clustering was described by homogeneous void nucleation equations [30,31].

In the Choi, et al. analysis, two approximations were made which greatly relieved the computational difficulty, but which did not invalidate the analysis.

1. The duty cycle, temperature and point defect concentrations were taken as step functions of time.
2. The void size classes are grouped for evaluation prior to calculation of the void density.

The previous analysis lead to the following conclusions:

a. First-wall swelling has been simulated by a

numerical integration of the equations for void nucleation.

b. Steady-state nucleation conditions were not obtained in most cases, which necessitated the use of the transient formulation of nucleation theory.

3. Very little void dissolution occurred during the cooling cycle.

4. The effect of inert gas or surface-active impurities was to decrease the critical nucleus size and to sharply increase the void nucleation rate.

5. Inert gas may further increase the swelling rate by preventing complete dissolution of voids during the cooling cycle.

Sprague, et al.,[18] numerically evaluated a time-dependent void nucleation theory under ion bombardment conditions. They used a technique to account for the large changes in the microstructure of a metal, in high damage rate experiments, before the nucleation rate can approach steady-state.

Another procedure was investigated by Odette and Myers[17], who essentially solved equations describing multistate kinetic phenomena. An important simplification was made in this preliminary analysis of the pulsed irradiation problem: a square wave irradiation pulse of duration t_p and pulse interval t_d (source-off time) with interstitial and vacancy concentrations assumed to vary in phase with the irradiation

pulse.

A major conclusion of the previous treatments is that the phenomenon of nucleation throttling of pulsed systems is particularly important because of the sensitivity of the damage process to the nucleation step and the obvious fact that if defects do not nucleate, they cannot grow.

IV.B. Void and Loop Growth

IV.B.1. Steady-State Theoretical Models of Void Growth

Voids grow ultimately because edge dislocations have a stronger attraction for interstitials than for vacancies. Although vacancies are certainly attracted to dislocations, the larger distortion field associated with an interstitial results in a stronger attraction (particularly to the dilated region) and thus a preferential drift. The dislocations thus act as sinks for vacancies and interstitials but are more effective for interstitials; the relative strength of this bias for interstitials can be estimated from our basic knowledge of point defect-dislocation interactions and yields a value of a few percent [53,54]. Suitable dislocations are always present during the irradiation, some because they were present before the irradiation and others as a result of interstitial and vacancy clustering during the irradiation. The irradiation produces vacancies and interstitials at an identical rate and since the interstitials are much more mobile than the vacancies they will very soon begin to form interstitial dislocation loops — which are usually pure

edge in character. The growth of these loops will then be facilitated by the preferential drift to them of subsequently produced interstitials. This slight preferential loss of interstitials to the dislocations means that the net point defect flux into any other neutral sink, such as the small gas bubble (void embryo), will be vacancy in character and thus such void nuclei will grow. Void growth thus requires at least one other sink type in addition to the void nuclei and that additional sink must have a perferential bias for interstitials. The steady-state concentrations of vacancies and interstitials are achieved as a result of loss of such defects at sinks and by mutual recombination.

In addition to forming voids some vacancies will undoubtedly form small vacancy loops. Such loops will also preferentially attract interstitials and therefore their growth should be inhibited. However, the kinetics of void growth may be influenced by the transient presence of such vacancy loops if they form athermally within the central regions (instantaneously vacancy rich) of the displacement cascades.

In the last few years several theories of the void growth process have been developed with the principle object of both correlating with and hence explaining the available swelling data from reactors, accelerators and the high voltage electron microscopes. It was hoped that such theories, when based on sound physical principles and correlated with

data, could then be used to confidently predict the swelling behavior of (different) materials subjected to neutron doses greater than those the present testing facilities can usefully achieve.

All the theories of void growth are based on the fundamental hypothesis (which is supported by a wide range of metallurgical experience) that the interstitials are preferentially attracted to the existing dislocations compared with the vacancies. This drift flow of interstitials is almost invariably represented by giving the dislocation sinks a slight (local) preference for interstitials compared with vacancies. The theories may be divided into two classes.

IV.B.1.a. The Cellular Model

In this model the body containing ρ_c voids per unit volume is divided into spherical cells, each initially of radius R_o where

$$R_o = 0.68\ \rho_c^{-1/3} \tag{4.2}$$

and each with a spherical void, of radius $r_c(0)$ at its center. This approach has been developed in a series of papers by Bullough and Perrin (1971, 1972) [55,56] and by Forman (1971) [57]. The other sinks in the body, be they biased — the dislocations, or neutral — precipitates, are continuously distributed throughout the body. The subsequent swelling may then be studied by following the growth of one such void when diffusion processes are permitted in the cellular region around it.

The disadvantage with this model is that the governing diffusion equations for the steady-state interstitial and vacancy concentrations are second order non-linear simultaneous equations: the non-linearity arises from the recombination terms which are proportional to the product interstitial and vacancy concentrations and also couple the equations. However, Bullough and Perrin have developed a numerical technique for the solution of such equations and have presented a wide range of growth kinetics that illustrate the general dependence of the swelling kinetics on the types of sinks present and the other physical variables. However, useful though the cellular model is, its dependence on a purely numerical approach for its solution (at least when recombination is included) is a serious disadvantage and tends to obscure the precise dependence of the swelling kinetics on the relevent physical variables.

A more convenient theory is the rate theory approach which will now be discussed.

IV.B.1.b. The Rate Theory Model

Vacancies and interstitials produced by irradiation can suffer a number of different fates which may in turn influence the destiny of future generated point defects; these may be itemized as follows:

IV.B.1.b.i. Recombination in the Bulk

Recombination occurs when isolated vacancies and interstitials encounter one another during free migration. We

exclude any athermal recombination of interstitials and vacancies within displacement cascades or correlated recombination of the original Frenkel pairs; both these effects are presumed to be included in a net production rate of point defects, P displacements per atom per second (dpa/sec), available for long range migration processes. It is worth commenting here that current binary collision models [58] of displacement cascades do not adequately treat the low energy focused collision sequences and thus they underestimate [59] the initial separation of the interstitials from the inner vacancy-rich region. Such large separations are necessary to explain current observations [60] on the efficiency of cascade collapse and the formation of vacancy loops.

If q_{iR} and q_{vR} are respectively the fractional losses of interstitials and vacancies by such bulk recombination then

$$\frac{dq_{iR}}{dt} = \frac{dq_{vR}}{dt} = \alpha\, C_i C_v \qquad (4.3)$$

where α is the recombination coefficient and C_i and C_v are the steady-state fractional interstitial and vacancy concentrations respectively.

IV.B.1.b.ii. Cascade Collapse to Form Vacancy Loops

There is now extensive evidence [61-63] that vacancy loops form in many irradiated materials by the rapid collapse of the vacancy rich core of the displacement cascades at temperatures well into the void swelling regime. This

removal of vacancies from potential bulk recombination or migration to sinks has an important effect on the rate of void swelling and is the dominant reason for the observed recoil sensitivity between electron and neutron or ion irradiation data. Recent molecular dynamics studies [64] of vacancy mobility in crystals containing several percent vacancy concentrations indicate a large drop in the vacancy migration energy. This is consistent with the formation of such loops at temperatures well below the bulk vacancy migration temperature.

Since these vacancy loops are continuously generated within the overall evolving damage structure, we must include the transient variation of the instantaneous vacancy loop volume concentration N_{VL} in the damage model. The loops are essentially unstable, their lifetime being determined by the net flux of interstitials to them (they are biased dislocation sinks, see below) and their rate of vacancy emission; both these processes tend to reduce the lifetime of the loop — in complete contrast to loops of interstitial character. The variation of the lifetime of vacancy loops has been estimated, for M316 steel, by Bullough, Eyre and Krishan [65].

IV.B.1.b.iii. Migration to Existing Sinks

We may identify four distinct types of sinks that make up the evolving microstructure:

1. Field free non-saturable sinks such as the growing voids and grain boundaries.
2. Sinks with non-zero fields that are non-saturable such as dislocations (interstitial or vacancy loops or the dislocation network) that can climb freely.
3. Saturable sinks with fields such as solute pinned dislocations.
4. Saturable sinks with no fields such as various types of trapping sites.

The trapping sites can occur at single solute atoms or on coherent precipitates and either interstitials or vacancies can be trapped with finite binding energies. The important property of such a sink is that it must have a bounded steady-state occupation probability for either interstitials or vacancies, otherwise it will simply nucleate the appropriate point defect aggregate and then transform into one of the other growing sinks; traps are thus sites for enhanced recombination.

Voids and grain boundaries are treated here as neutral sinks for point defects. Due to the bias of dislocations to interstitials, there is a net flux of vacancies arriving at voids and grain boundaries. Consequently, metals swell under irradiation by the void growth mechanism. Thermal emission of vacancies from grain boundaries and its sensitivity to the presence of the stress is the origin of Herring-Nabarro creep [66,67] in the unirradiated material.

In addition to the loss to the vacancy loops already discussed, there is a fractional interstitial loss of point defects to the interstitial loops. A dislocation network develops with irradiation as a result of the growth and mutual interference of interstitial loops. They add to the dislocations already present due to prior deformation. In general, the density of such network dislocations cannot continue to increase continually with dose, as does the dislocation density arising from the growing loops. Prior to their mutual impingement, some effective recovery process involving the continuous mutual annihilation of interacting dislocation segments of opposite character eventually must stabilize the dislocation density.

Sessile dislocations are those network dislocations that for some reason, such as contamination by solute impurities, are unable to climb by absorbing the excess flux of interstitials migrating to them. In impure materials, deformations or "grown in" dislocations are likely to be contaminated and indeed the sessile behavior of these dislocations under irradiation has been observed [68]. We expect such dislocations to collect a finite number of interstitials around them, probably in the form of a dilute atmosphere; the interstitials being bound to the dislocation by a characteristic binding energy and hence possessing also a finite probability of thermal release. Vacancies on the other hand, have only a weak interaction with the dislocations and

thus will ignore the sink unless it is suitably occupied by interstitials, in which case a recombination event can occur. Further interstitials can only enter the binding region if it is suitably unoccupied with interstitials. Such dislocations thereby constitute regions of the crystal where enhanced recombination can occur and in this manner can influence the overall supply of vacancies to the voids, i.e., the swelling rate. Furthermore, since they must be saturable sinks they must maintain a finite steady-state occupation probability. We can also envisage similar "spherical" traps for interstitials which could be of atomic dimension (substitutional impurities) or larger precipitates. Again the occupation probability of such traps must be stationary otherwise they would simply act as interstitial aggregate nuclei. The theoretical and experimental impact of such traps on the swelling of impure metals and alloys is still in progress at both Harwell [69] and Wisconsin [70] as well as many other laboratories.

IV.B.1.c. Rate Equations

The steady-state concentrations of the intrinsic point defects C_i and C_v are defined, in terms of the various sink strengths and emission or release rates, by the two conservation equations [71,72]

$$P_i^e + P_i - k_i^2 D_i C_i - \alpha C_i C_v = 0 \qquad (4.4)$$

$$P_v^e + P_v - k_v^2 D_v C_v - \alpha C_i C_v = 0 \qquad (4.5)$$

where $P_i = P$ and $P_v = (1-\varepsilon)P$ with P the standard displacement damage production rate (dpa/sec). The quantities P_i^e and P_v^e are the interstitial and vacancy thermal emission rates (dpa/s) respectively. The quantities k_i^2 and k_v^2 are the total sink strengths for all the interstitial and vacancy losses. The conservation equations (4.4) and (4.5) are, of course, consistent with the necessary equality between the rate of loss of vacancies at the voids, grain boundaries (the neutral sinks) and in vacancy loops with the rate of loss of interstitials at the other dislocation sinks.

The swelling rate thus follows from computing the volumetric rate of flow of vacancies entering existing void nuclei. It only remains, therefore, to obtain suitable expressions for the various sink strengths and emission or release rates.

IV.B.1.d. Sink Strengths

An embedding procedure for voids as field free sinks has been discussed by Brailsford, Bullough and Hayns [73]. The procedure, which follows Maxwell's analysis [74] of the electrical resistivity of a composite consisting of spherical inhomogeneities, is to surround the spherical cavity by a sink free region outside of which is the "lossy" medium characterized by (k_i^2) and (k_v^2) containing all the effective sinks. The sink strength of the void is obtained by ensuring that the flux of interstitials or vacancies into this central cavity, for suitable boundary conditions at the void-sink free matrix interface, is precisely equal to the assumed

corresponding flux into the equivalent sink in the medium — a long distance from the void. The appropriate spatially varying diffusion equations are solved in the two regions with continuity of defect concentration at the sink free-lossy medium interface.

Similar embedding techniques have been adopted for grain boundaries as field free sinks [59].

Freely climbing dislocations include interstitial loops and vacancy loops with their edge dislocation perimeters and the network dislocations that have either evolved from the interstitial loop population during the irradiation or have been produced by prior deformation (cold work).

Dislocations have a spatially varying interaction with point defects which arises primarily from direct interaction between the stress field of the dislocation and the relaxation strain field of the point defect [75-77]. This interaction imposes a drift component on the point defect fluxes which, because the interstitial creates a much larger distortion of the host than does the vacancy (typically the relaxation volume strain for the interstitial is more than twice that of the vacancy [78]), is larger for interstitials than vacancies.

The central problem is to deduce the sink strength of such dislocations for incorporation in the equivalent spatially homogeneous effective medium appropriate to rate theory and that rigorously incorporates both the spatially

varying drift field effects and diffusion. To date, this has not yet been obtained rigorously [59], although some recent progress in this regard has been made by Brailsford and Bullough [79]. Their overall conclusion is that the original simple sink strength proposed by Brailsford, Bullough and Hayns to take some account of other sinks present is probably the most useful interior sink strength to use.

Appropriate field equations for the spatially varying $C_i(r)$ and $C_v(r)$ were solved by Bullough [59] around a spherical trap embedded in an effective medium containing all other sinks. Suitable boundary conditions, including trap occupation probabilities, were imposed for the saturable trap to obtain the sink strengths for vacancies and interstitials.

It is clear that the loss rates at fixed sinks are only of importance when intrinsic recombination is small, so that the procedure adopted is a valid first approximation. Nevertheless, corrections to these loss rates resulting from recombination remains a matter of concern. Such corrections will, in lowest order, be bi-linear in the C_i and C_v and effectively interfere with the basic recombination term and possibly simultaneously modify the sink strengths which are linear in C_i or C_v. The analytical treatment of such losses to fixed sinks is obviously far more difficult when the basic equations are non-linear. This aspect is under investigation by the Harwell group.

IV.B.2. Time Dependent Theoretical Models for Void Growth

Transient analysis of irradiated metals necessitates development of the rate theory to include dynamic variations in microstructure and point defect behavior. A qualitative description of the physical processes in the transient and pulsed irradiation model is given below. At the beginning of irradiation, the concentrations of both types of defects increase rapidly. However, the concentration of the very mobile interstitials tends to level off quickly with time as it approaches equilibrium with the existing dislocation network. The relatively slow moving vacancies require much more time to equilibrate with the dislocations; hence, their concentration continues to increase. As the vacancy concentration rises, an increasing fraction of interstitials are removed by annihilation with vacancies, and the interstitial concentration decreases. Consequently, the interstitial concentration should tend to pass through a maximum at a time when the interstitials are in near equilibrium with the dislocations and the vacancy concentration is far from its equilibrium value. If the pulse is long enough, of course, the vacancy and interstitial concentrations reach the values they would have during a continuous irradiation having the same defect production rate. At the end of the pulse, the vacancy and interstitial concentrations decrease rapidly, each tending toward its thermal equilibrium value at rates

determined by their mobility and the dislocation density. Hence, clusters may form and grow both during and/or between pulses depending on the factors controlling the vacancy and interstitial concentration levels.

Ideally one would like to obtain a detailed description of the time variation in the spatial distribution of the interacting point defects as they diffuse near each sink type. However, solving the appropriate set of continuity equations for each sink type is impractical, not to mention the difficulty of specifying self-consistent, interrelated boundary conditions.

Schiffgens, Graves, and Doran (1975) made some preliminary assessments of void growth under pulsed irradiation [12,13]. An approximate analytical solution of point defect coupled rate equations was used to study the effects of interrupted irradiation on the growth of voids. A similar approach that included mutual recombination of point defects was followed by Sprague and Smidt [11] to analyze the effects of beam scanning on Nickel ion damage in Nickel. However, the following aspects were not properly included in either analytical model:

1. Mutual recombination of point defects.
2. The dynamic variations in the various components of the microstructure.
3. Recoil spectra and collision cascade collapse effects.

4. Microstructure details.
5. Effects of diffusing gas atoms.
6. Stress effects.
7. Effects of alloying on point defect and void growth kinetics.

A fully Dynamic Rate Theory (FDRT), as developed in the next chapter, can be equally applied to steady-state or pulsed irradiation. The previously mentioned aspects and their implications are considered in detail in the theoretical analysis.

CHAPTER V

A FULLY DYNAMIC RATE THEORY (FDRT) APPROACH TO TIME DEPENDENT IRRADIATION

V.A. General Approach

It has been found that one can greatly simplify the mathematical complexities of a dynamic system by describing the kinetic behavior of that system with vector notation. This leads to a state variable approach which is briefly described below and is developed in more detail in the latter part of this chapter.

The state variables of a dynamic system are the smallest set of variables which determine the state of the dynamic system [80]. If at least n variables $Y_1(t)$, $Y_2(t)$,..., $Y_n(t)$ are needed to completely describe the behavior of a dynamic system, then such n variables $Y_1(t)$, $Y_2(t)$,...,$Y_n(t)$ are a set of state variables. These n variables could be described to be the components of a state vector $\overline{Y}(t)$. The set of state variables $Y_i(t)$, (i=1,2,...,n) are interdependent and, in principle, their change with time could be described. The state of a metal under irradiation can then be described by a vector $\overline{Y}$ whose components are defined as follows:

Y(1) = average void radius in cm. (5.D.1)*

Y(2) = average non-aligned interstitial loop radius in cm. (5.D.2)

*Equations with the prefix "D" refer to definitions.

Y(3) = concentration of non-aligned vacancy loops per cm^3. (5.D.3)

Y(4) = concentration of single vacancies tied up in non-aligned vacancy loops in at./at. (5.D.4)

Y(5) = total single vacancy concentration in at./at. (5.D.5)

Y(6) = total single interstitial concentration in at./at. (5.D.6)

Y(7) = average aligned interstitial loop radius in cm. (5.D.7)

Y(8) = concentration of aligned vacancy loops per cm^3. (5.D.8)

Y(9) = concentration of single vacancies tied up in aligned vacancy loops in at./at. (5.D.9)

Y(10) = network creep strain in cm/cm. (5.D.10)

We define aligned and nonaligned dislocations in this work according to the convention set-up in Figure (5.1). For example, a loop is aligned if the force is perpendicular to the plane of the loop and nonaligned if the plane of the loop and the direction of the force are parallel.

V.B. Analysis of the State Variables

Following the notations of previous work by Brailsford and Bullough [65], and Ghoniem and Kulcinski [53,81,82] more detailed expressions for the components of the Y vectors are now derived. First the dislocation densities must be determined and then vacancy emission rates, defect time constants, defect removal rates, vacancy loop behavior, and

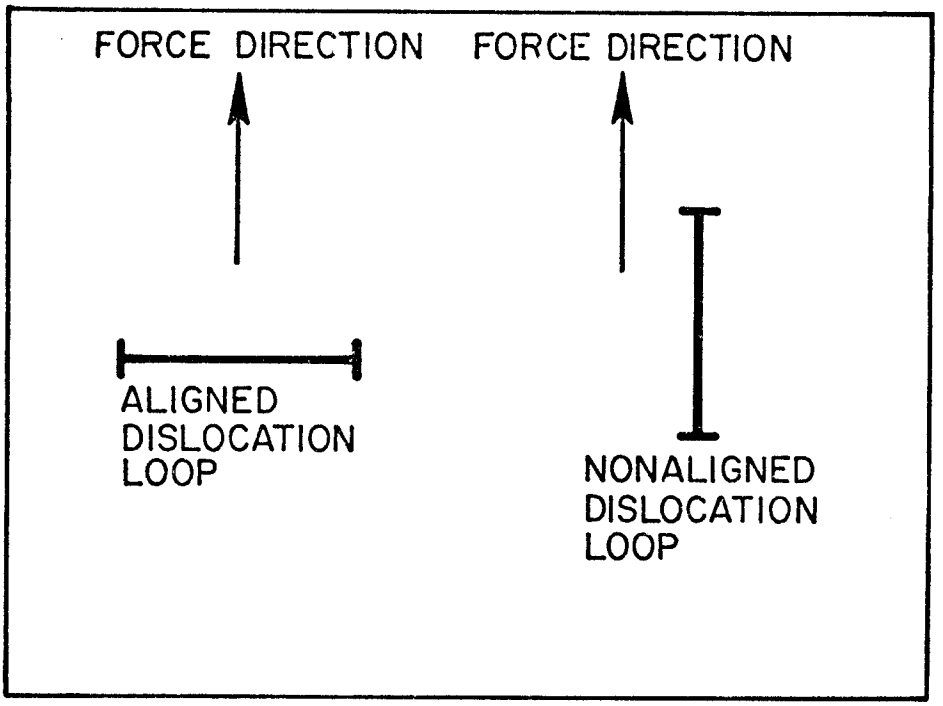

Fig.(5.1) DEFINITION OF ALIGNED AND NONALIGNED DISLOCATION LOOPS

finally swelling as well as irradiation creep rates can be calculated.

V.B.1. Dislocation Densities

Dislocations in the bulk of a metal can be produced by at least three different mechanisms:

(1) Cold work or deformation of the metal which results in initial dislocation network, ρ_d^e.

(2) Interstitial loops nucleated during the early stages of irradiation, a fraction of which are preferentially aligned with the applied stress. Their subsequent growth and coallescence form a dislocation network.

(3) Vacancy loops are assumed to athermally form in the vacancy rich region of the collision cascade [65] with the same initial radius, $r_{v\ell}(0)$. Their existence, which is also affected by the applied stress, is transient in nature because they have a bias to interstitials and they thermally emit vacancies at the same time.

If P is the Frenkel pair production rate (dpa/sec), then εP is the fractional rate at which vacancies are removed from solution to form vacancy loops. From conservation of vacancy volume within the loops, the fraction of vacancies tied up in vacancy loops is equal to the volume of a single vacancy loop multiplied by their number density, thus:

$$Y(4) = \pi b (r_{v\ell}^{n})^{2} \; Y(3) \tag{5.1}$$

for non-aligned vacancy loops, and

$$Y(9) = \pi b (r_{v\ell}^{a})^{2} \; Y(8) \tag{5.2}$$

for aligned vacancy loops.

For intersitial loops, the dislocation densities are expressed as:

$$\rho_{d}^{i\ell n} = 2\pi Y(2) N_{i\ell n} \tag{5.3}$$

$$\rho_{d}^{i\ell a} = 2\pi Y(7) N_{i\ell n} \tag{5.4}$$

while for vacancy loops:

$$\rho_d^{v\ell n} = 2\pi r_{v\ell}^{n}\ Y(3) \tag{5.5}$$

$$\rho_d^{v\ell a} = 2\pi r_{v\ell}^{a}\ Y(8) \tag{5.6}$$

where the following is defined:

- $\rho_d^{i\ell n}$ is the non-aligned dislocation loop line density; cm^{-2}. (5.D.11)
- $N_{i\ell n}$ is the non-aligned dislocation loop concentration; cm^{-3} (5.D.12)
- $\rho_d^{i\ell a}$ is the aligned dislocation loop line density; cm^{-2}. (5.D.13)
- $N_{i\ell a}$ is the aligned dislocation loop concentration; cm^{-3}. (5.D.14)
- $\rho_d^{v\ell n}$ is the non-aligned vacancy loop line density; cm^{-2}. (5.D.15)
- $\rho_d^{v\ell a}$ is the aligned vacancy loop line density; cm^{-2}. (5.D.16)
- ρ_d^{e} is the deformation produced edge dislocation line density; cm^{-2}. (5.D.17)
- ρ_d is the total dislocation line density produced by both deformation and radiation; cm^{-2}. (5.D.18)

From equations (5.1) and (5.2), equations (5.5) and (5.6) can be expressed as:

$$\rho_d^{v\ell n} = 2\sqrt{\pi Y(3)Y(4)/b} \tag{5.7}$$

$$\rho_d^{v\ell a} = 2\sqrt{\pi Y(8)Y(9)/b} \tag{5.8}$$

The total dislocation density in the metal is the algebraic sum of all previous components;

$$\rho_d = \rho_d^e + \rho_d^{i\ell n} + \rho_d^{i\ell a} + \rho_d^{v\ell n} + \rho_d^{v\ell a} \qquad (5.9)$$

V.B.2. Vacancy Emission from Sinks

V.B.2.a. Vacancy Emission from Voids

At high temperatures, the probability of emitting a vacancy from a void becomes appreciable. A larger void surface tension enhances vacancy emission while the presence of gas atoms inside reduces the probability for vacancies "boiling off" the surface of voids. A mathematical description of this process is given as:

$$P_C^e = 4\pi Y(1) N_C D_v C_v^e \exp\left\{ \left(\frac{2\gamma}{Y(1)} - P_g(Y(1), N_g) b^3/kT \right\} \right. \qquad (5.10)$$

where

- P_C^e is the vacancy emission rate from the surface of all voids, s^{-1} (5.D.19)
- N_C is the temperature dependent void concentration, cm^{-3} (5.D.20)
- D_v is the temperature dependent vacancy diffusion coefficient, $cm^2\ s^{-1}$ (5.D.21)
- C_v^e is the equilibrium vacancy concentration, at./at. (5.D.22)
- γ is the surface energy of the void surface, eV/cm^2 (5.D.23)
- P_g is the gas pressure inside the void, eV/cm^3 (5.D.24)
- N_g is the number of gas atoms in a void. (5.D.25)

Equation (5.10) is easily derived by considering the vacancy concentration at the voids, C_v as given by;

$$C_v/C_v^e = \exp\{(\frac{\partial F}{\partial n})/kT\} \tag{5.11}$$

where $\frac{\partial F}{\partial n}$ is the change in energy of the configuration per vacancy emitted, and C_v^e the equilibirum concentration of vacancies. For a spherical hole in an infinite isotropic solid, that involves the surface energy of the void, the elastic strain energy in the surrounding metal, the applied hydrostatic stress, and the pressure caused by trapped gas atoms inside.

Generalizing the analyses given in (83, 84, and 55); one can write the following expressions:

$$\frac{\partial F}{\partial n} = F_m \Omega \tag{5.12}$$

where Ω is the atomic volume. Here F_m is the mechanical force per unit surface area acting on a vacancy at the void surface.

$$F_m = P + \frac{2\gamma}{r_C} + \frac{\gamma^2}{2\mu r_C^2} - P_g \tag{5.13}$$

Here P is the hydrostatic pressure, γ, the surface energy, r_C the void radius, μ the shear modulus, and P_g the gas pressure.

The gas pressure is always expressed in terms of the number of gas atoms and void radius. If the perfect gas law

is used, one gets:

$$P_g = \frac{3NkT}{4\pi r_c^3} \tag{5.14}$$

While if Van der Waals law is assumed to hold, one gets:

$$P_g = \frac{NkT}{(4/3\pi r_c^3 - aN)} - \frac{bN^2}{16/9\pi^2 r_c^6} \tag{5.15}$$

where a and b are constants [85].

Normally, the elastic energy is negligibly small [92], so in the general case we have:

$$F_m = P + \frac{2\gamma}{r_c} - P_g \tag{5.16}$$

This formulation is useful in studying the general situation where gas atoms are trapped in voids and where stress waves accompany the damage production.

Although the principal concern in modeling void behavior has been void growth during irradiation, some consideration must be given to the response of voids during post irradiation annealing [86,87]. Annealing in the absence of irradiation is of interest for the practical reason that CTR first-wall materials will be subject to periods of irradiation and post irradiation annealing. (See Chapters II and III). Furthermore void annealing experiments present a unique opportunity to study void kinetic behavior in the absence of self interstitials and in the presence of a low vacancy supersaturation.

V.B.2.b. Vacancy Emission from Deformation Produced Dislocations

For simplicity of calculations, all deformation produced dislocations are assumed to be of the edge type. Edge dislocations that are aligned with stress have enhanced vacancy emission as analyzed below.

$$P_d^{ea} = Z_v^a D_v C_v^e \exp(\sigma\Omega/kT)\rho_d^{ea} \tag{5.17}$$

$$P_d^{en} = Z_v^n D_v C_v^e \rho_d^{en} \tag{5.18}$$

$$P_d^e = P_d^{ea} + P_d^{en} \tag{5.19}$$

where

- P_d^{ea} is the rate of vacancy emission from all aligned edge dislocations, s^{-1} (5.D.26)
- P_d^{en} is the rate of vacancy emission from all non-aligned edge dislocations, s^{-1} (5.D.27)
- P_d^e is the total rate of vacancy emission from edge dislocations (5.D.28)
- σ is the uniaxial externally applied stress, eV/cm^3 (5.D.29)
- Ω is the atomic volume, cm^3 (5.D.30)
- k is Bolzmann's constant, $eV°K^{-1}$ (5.D.31)
- ρ_d^{ea} is the aligned edge dislocation density, cm^{-2} (5.D.32)

- ρ_d^{en} is the nonaligned edge dislocation density, cm^{-2} (5.D.33)
- Z_v^a is the vacancy-aligned dislocation bias factor (5.D.34)
- Z_v^n is the vacancy non-aligned dislocation bias factor (5.D.35)
- T is the temperature, °K (5.D.36)

V.B.2.c. Vacancy Emission from Interstitial Loops

Due to the inherent geometrical curvature of an interstitial loop, the vacancy concentration at the edge of the loop differs from the bulk thermal vacancy concentration. The actual vacancy concentration is controlled by the stacking fault energy and the line tension of the loop. Various emission rates are written as:

$$P_d^{i\ell a} = D_v C_v(Y(7)) Z_v^a \exp(\sigma\Omega/kT) \rho_d^{i\ell a} \quad (5.20)$$

$$P_d^{i\ell n} = D_v C_v(Y(2)) Z_v^n \rho_d^{i\ell n} \quad (5.21)$$

$$P_d^{i} = P_d^{i\ell a} + P_d^{i\ell n} \quad (5.22)$$

The equilibrium vacancy concentration at the edge of an interstitial dislocation loop of radius Y(7) is:

$$C_v(Y(7)) = C_v^e \exp-\left(\frac{\{\gamma_{sf}+F_{el}(Y(7))\}b^2}{kT}\right) \quad (5.23)$$

$$F_{el}(Y(7)) = \frac{\mu b^2}{(1-\nu)4\pi(Y(7)+b)} \ell n \left(\frac{Y(7)+b}{b}\right) \quad (5.24)$$

where

- $\cdot P_d^{i\ell a}$ is the rate of vacancy emission from aligned interstitial loops, s^{-1} (5.D.37)
- $\cdot P_d^{i\ell n}$ is the rate of vacancy emission from nonaligned interstitial loops, s^{-1} (5.D.38)
- $\cdot P_d^{i\ell}$ is the total rate of vacancy emission from all interstitial loops, s^{-1} (5.D.39)
- $\cdot \gamma_{sf}$ is the stacking fault-energy, eV cm^{-2} (5.D.40)
- $\cdot F_{e\ell}(Y(7))$ is the elastic energy of a dislocation loop of radius Y(7), eV cm^{-2} (5.D.41)
- $\cdot b$ is the Burger's vector, cm (5.D.42)
- $\cdot \mu$ is the shear modulus, ev cm^{-3} (5.D.43)
- $\cdot \nu$ is the Poisson's ratio (5.D.44)

V.B.2.d. Vacancy Emission from Vacancy Loops

The probability of vacancy emission from a faulted vacancy dislocation loop that is parallel to the applied stress is expressed as:

$$C_v^e \exp\left\{\frac{[\gamma_{sf}+F_{e\ell}(r_{v\ell})]b^2}{KT}\right\} \tag{5.25}$$

while for aligned vacancy loops it is written as:

$$C_v^e \exp(\sigma\Omega/KT)\exp\left\{\frac{[\gamma_{sf}+F_{e\ell}(r_{v\ell})]b^2}{KT}\right\} \tag{5.26}$$

From the last expressions, it is clear that these structures are thermally unstable and they dissolve quickly at high temperatures. The various emission rates are given by:

$$P_d^{v\ell a} = D_v C_v(r_{v\ell}^a) Z_v^a \exp(\sigma\Omega/kT) \rho_d^{v\ell a} \quad (5.27)$$

$$P_d^{v\ell n} = D_v C_v(r_{v\ell}^n) Z_v^n \rho_d^{v\ell n} \quad (5.28)$$

$$P_d^{v\ell} = P_d^{v\ell a} + P_d^{v\ell n} \quad (5.29)$$

$$r_{v\ell}^n = \sqrt{Y(4)/\pi b Y(3)} \quad (5.30)$$

$$r_{v\ell}^a = \sqrt{Y(9)/\pi b Y(8)} \quad (5.31)$$

$$C_v(r_{v\ell}) = C_v^e \exp\left\{\frac{\{\gamma_{sf}+F_{e\ell}(r_{v\ell})\}b^2}{kT}\right\} \quad (5.32)$$

and $F_{el}(r_{v\ell})$ is as defined in (5.24) before

where

- $P_d^{v\ell a}$ is the rate of vacancy emission from aligned vacancy loops, s^{-1} (5.D.45)
- $P_d^{v\ell n}$ is the rate of vacancy emission from nonaligned vacancy loops, s^{-1} (5.D.46)
- $P_d^{v\ell}$ is the total rate of vacancy emission from all vacancy loops, s^{-1} (5.D.47)
- $r_{v\ell}^a$ is the aligned vacancy loop radius, cm (5.D.48)
- $r_{v\ell}^n$ is the nonaligned vacancy loop radius, cm (5.D.49)
- $\rho_d^{v\ell a}$ is the aligned vacancy loop line dislocations density, cm^{-2} (5.D.50)
- $\rho_d^{v\ell n}$ is the nonaligned vacancy loop line dislocation density, cm^{-2} (5.D.51)

V.B.2.e. Total Rate of Vacancy Emission

The total rate of vacancy emission (P^e), in at./at/sec., is the algebraic sum of the previously derived rates.

$$P^e = P_V^e + P_d^e + P_{v\ell}^e + P_{i\ell}^e \tag{5.33}$$

V.B.3. Single Point Defect Time Constants

In a mathematical formulation that incorporates the kinetic behavior of different irradiation produced species, there exists a wide variety of time constants related to those different components. A time constant, λ, as defined here is the inverse of the time required to go through one e-folding change in a particular property, i.e., the ℓn (parameter) = $-\lambda t$. Single point defects have larger time constants than dimers, trimers and the rest of the microstructure. The diffusion coefficient of single interstitials is orders of magnitude larger than the diffusion coefficient of single vacancies. Once they are created by irradiation, interstitials tend to diffuse quickly to different sinks and to annihilate vacancies. Since the time constants of single point defects depend on the microstructure present at a particular instant, they are explicit functions of the metal's microstructure, and therefore, implicit functions of time. Their microstructural dependence can be simply expressed as:

$$\lambda_i = \lambda_i^d + \lambda_i^C \tag{5.34}$$

$$\lambda_v = \lambda_v^d + \lambda_v^C \tag{5.35}$$

$$\lambda_i^d = \rho_d D_i Z_i \tag{5.36}$$

$$\lambda_i^C = 4\pi N_C Y(1) D_i \tag{5.37}$$

$$\lambda_v^d = \rho_d D_v Z_v \tag{5.38}$$

$$\lambda_v^C = 4\pi N_C Y(1) D_v \tag{5.39}$$

where

- λ_i is the total single interstitial time constant, s^{-1} (5.D.52)
- λ_v is the total single vacancy time constant, s^{-1} (5.D.53)
- λ_i^d is the single interstitial time constant due to all dislocations, s^{-1} (5.D.54)
- λ_i^C is the single interstitial time constant due to all voids, s^{-1} (5.D.55)
- λ_v^d is the single vacancy time constant due to all dislocations, s^{-1} (5.D.56)
- λ_v^C is the single vacancy time constant due to all voids, s^{-1} (5.D.57)

V.B.4. Removal Rates

The importance of each type of sink on the dynamic behavior of point defects is reflected in the specific removal rate of the defect to that sink. Individual sink removal rates can be expressed as their relevant time constant, λ, multiplied by the temporal concentration of point defects. As indicated before, mutual recombination of point defects is a second order reaction that depends on the product of both concentrations. Collective point defect removal rates are expressed as:

$$P_{si} = \lambda_i Y(6) \tag{5.40}$$

$$P_{sv} = \lambda_v Y(5) \tag{5.41}$$

$$P_r = \alpha Y(5) Y(6) \tag{5.42}$$

$$\alpha = g(\nu_i \exp(-E_i^m/kT) + \nu_v \exp(-E_v^m/kT)) \tag{5.43}$$

where

- P_{si} is the total sink removal rate for interstitials, s^{-1} (5.D.58)
- P_{sv} is the total sink removal rate for vacancies, s^{-1} (5.D.59)
- P_r is the total recombination rate of vacancies and interstitials, s^{-1} (5.D.60)
- α is the recombination coefficient, s^{-1} (5.D.61)
- g is the number of unstable sites around a vacancy (5.D.62)
- $\nu_i \exp(-E_i^m/kT)$ is the interstitial jump frequency, s^{-1} (5.D.63)
- $\nu_v \exp(-E_v^m/kT)$ is the vacancy jump frequency, s^{-1} (5.D.64)

V.B.5. Vacancy Loop Behavior

If b is the magnitude of the Burger's vector, the atomic volume is b^3 and $n_{v\ell}$ is the fractional concentration* of vacancy loops created per second, then:

The number of vacancies in a vacancy loop =

*Here fractional concentration refers to number of loops per atomic lattice site.

$$\pi r_{v\ell}^{2} b/b^{3} \tag{5.44}$$

and

$$n_{v\ell} = \frac{\varepsilon P b^{2}}{\pi r_{v\ell}^{2}(0)} \tag{5.45}$$

When a vacancy loop has formed, it will immediately act as an interstitial sink because of the dislocation character of its perimeter. It will then instantly be attacked by interstitials and consequently shrink. At high temperatures the loops will also shrink by thermal emission and this process will be greatly assisted by the large line tension of such small loops and by the stacking fault energy if the loops remain faulted. Thus, each loop will have a finite lifetime τ and the number of vacancy loops per unit volume, $N_{v\ell}$, present at any time t is given by the simple rate equation

$$\frac{dN_{v\ell}(t)}{dt} = \frac{n_{v\ell}}{b^{3}} - \frac{N_{v\ell}(t)}{\tau} \tag{5.46}$$

where the first term on the righthand side is the loop generation rate and the second term represents the loss term due to shrinkage.

The lifetime, τ, of an individual loop is a function of time in the sense that it depends on the state of the overall sink distribution prevailing at its instant of creation. From a Taylor series expansion of $r_{v\ell}(t)$ we have

$$\tau = \tau(t) \simeq - \frac{r_{v\ell}(o)}{(dr_{v\ell}/dt)_{[r_{v\ell}(o)]}} \tag{5.47}$$

In the presence of uniaxial stress in the metal, the collapse mechanism of vacancy loops is assumed to be influenced by the stress [65]. Therefore, the following processes can be easily expressed:

$$\kappa_1^n = \frac{2}{3}(1-f)\frac{\varepsilon P}{\pi r_{v\ell}^2(o)b} \tag{5.48}$$

$$\kappa_1^a = \frac{1}{3}(1+2f)\frac{\varepsilon P}{\pi r_{v\ell}^2(o)b} \tag{5.49}$$

$$\kappa_2^n = \frac{2}{3}(1-f)\,\varepsilon P \tag{5.50}$$

$$\kappa_2^a = \frac{1}{3}(1+2f)\varepsilon P \tag{5.51}$$

$$\Lambda_1^n = Y(3)(Z_i^n D_i Y(6) - Z_v^n D_v Y(5) + D_v C_v^e Z_v^n \times \exp\{(\gamma_{sf}+F_{el}(r_{v\ell}(o)))b^2 kT\}/(r_{v\ell}(o)b) \tag{5.52}$$

$$\Lambda_1^a = Y(3)(Z_i^a D_i Y(6) - Z_v^a D_v Y(5) + D_v C_v^e Z_v^a \times \exp\{(\gamma_{sf}+F_{el}(r_{v\ell}(o)))b^2/kT\}\exp(\sigma\Omega/kT)/(r_{v\ell}(o)b) \tag{5.53}$$

$$\Lambda_2^n = (Z_i^n D_i Y(6) - Z_v^n D_v Y(5) + Z_v^n D_v C_v^e \times \exp\{(\gamma_{sf}+F_{el}(r_{v\ell}^n))b^2/kT\}) \times \sqrt{4\pi Y(4)Y(3)/b} \tag{5.54}$$

$$\Lambda_2^a = (Z_i^a D_i Y(6) - Z_v^a D_v Y(5) + Z_v^a D_v C_v^e \exp\{(\gamma_{sf}+F_{el}(r_{v\ell}^n))b^2/kT\} \times \exp(\sigma\Omega/kT))\sqrt{4\pi Y(9)Y(8)/b} \tag{5.55}$$

where

- κ_1^n is the production rate of nonaligned vacancy loops, $cm^{-3}\ s^{-1}$ (5.D.65)
- κ_1^a is the production rate of aligned vacancy loops, $cm^{-3}\ s^{-1}$ (5.D.66)

- κ_2^n is the production rate of vacancy fraction tied up in non aligned vacancy loops, s^{-1} (5.D.67)
- κ_2^a is the production rate of vacancy fraction tied up in aligned vacancy loops, s^{-1} (5.D.68)
- Λ_1^n is the decay rate of nonaligned vacancy loops, $s^{-1}\ cm^{-3}$ (5.D.69)
- Λ_1^a is the decay rate of aligned vacancy loops, $s^{-1}\ cm^{-3}$ (5.D.70)
- Λ_2^n is the decay rate of vacancy fraction tied up in nonaligned vacancy loops, $s^{-1}\ cm^{-3}$ (5.D.71)
- Λ_2^a is the decay rate of vacancy fraction tied up in aligned vacancy loops, $s^{-1}\ cm^{-3}$ (5.D.72)
- ε is the fraction of vacancies formed in vacancy loops (5.D.73)
- P is the production rate of point defects (5.D.74)
- $r_{v\ell}(o)$ is the initial radius of a vacancy loop formed in a cascade, cm (5.D.75)
- f is the fraction of total interstitial loop population that are aligned perpendicular to applied stress (5.D.76)

$$f = \frac{\exp(\sigma\Omega n/kT)-1}{\exp(\sigma\Omega n/kT)+2} \qquad (5.56)$$

- $n \simeq 10$ is the number of interstitials defining a planar nucleus. (5.D.78)

V.B.6. Swelling

The instantaneous percent swelling can now be easily

calculated as the number of voids per unit volume multiplied by the average volume of each, thus;

$$S\% = \frac{\Delta V}{V_o}\% = \frac{4}{3}\pi Y^3(1)N_C. \tag{5.57}$$

V.C. Final State Space Representation of Rate Equations for FDRT

In state space, at a particular time, there is one and only one point that defines completely the state of the metal under irradiation. The dimensions of this space depend on the system of equations chosen to simulate the metal's response to irradiation. In our general treatment of section V.B., the following time derivatives of 10 different components are obtained:

$$\dot{Y}(1) = \frac{1}{Y(1)}[(D_v Y(5) - D_i Y(6) - D_v C_v^e \exp\{(\frac{2\gamma}{Y(1)} P_g(Y(1), N_g)) \frac{\Omega}{kT}\} \tag{5.58}$$

$$\dot{Y}(2) = \frac{1}{b}[D_v Z_v^n Y(6) - D_v Z_v^n Y(5) + D_v Z_v^n C_v(Y(2))] \tag{5.59}$$

$$\dot{Y}(3) = \kappa_1^n - \Lambda_1^n \tag{5.60}$$

$$\dot{Y}(4) = \kappa_2^n - \Lambda_2^n \tag{5.61}$$

$$\dot{Y}(5) = (1-\varepsilon)P + P^e - P_{sv} - P_r \tag{5.62}$$

$$\dot{Y}(6) = P - P_{si} - P_r \tag{5.63}$$

$$\dot{Y}(7) = \frac{1}{b}[D_i Z_i^a Y(6) - D_v Z_v^a Y(5) + D_v Z_v^a C_v(Y(7)) \exp(\sigma\Omega/kT)] \tag{5.64}$$

$$\dot{Y}(8) = \kappa_1^a - \Lambda_1^a \tag{5.65}$$

$$\dot{Y}(9) = \kappa_2^a - \Lambda_2^a \tag{5.66}$$

$$\dot{Y}(10) = \rho_d^{ea}\{((Z_i^a - Z_i^n)D_i Y(6) + (Z_v^n - Z_v^a)D_v Y(5)) + Z_v^a D_v C_v^e \exp(\sigma\Omega/kT) - Z_v^n D_v C_v^e\} \quad (5.67)$$

It is this set of equations which form the basis for the FDRT. The methods used to solve these equations will be discussed in Chapter 6.

V.D. Irradiation Creep Strain

In contrast to the complexity of the factors that can influence void growth, the magnitude of irradiation-creep can be relatively confidently predicted and is not as acutely sensitive as is swelling to the metallurgical and physical variables [88]. The basis for this confidence is the stress-induced preferred absorption (SIPA) mechanism for irradiation-creep which was originally proposed by Heald and Speight [89] and Wolfer [90-92] and recently carefully examined by Bullough and Willis [93]. The mechanism requires that, when a body is subjected to a uniaxial tension, the stress-induced interaction energy between edge dislocations oriented with their extra planes orthogonal to the stress axis (aligned dislocations) and interstitials exceed the interaction energy between nonaligned edge dislocations and interstitials and vice-versa for the vacancies. In the absence of vacancy thermal emission (for temperatures below the peak swelling temperature), the total irradiation-creep rate $d\varepsilon_T/dt$ has the form

$$\frac{d\varepsilon_T}{dt} = \frac{d\varepsilon_{i\ell}}{dt} + \frac{d\varepsilon_N}{dt} + \frac{d\varepsilon_{v\ell}}{dt} \quad (5.68)$$

Here $\frac{d\varepsilon_N}{dt}$ is equivalent to $\dot{Y}(10)$ and the other two components can be integrated and are expressed as follows:

$$\varepsilon_{i\ell} = \pi b N_{i\ell}\{(1+2f)[Y(7)]^2 - (1-f)[Y(2)]^2\}/3 \qquad (5.69)$$

$$\varepsilon_{v1} = -(Y(4)-Y(9)/2) \qquad (5.70)$$

where

$\cdot\varepsilon_{i\ell}$ is the irradiation induced creep due to interstitial loops, cm/cm (5.D.78)

$\cdot\varepsilon_{v\ell}$ is the irradiation induced creep due to vacancy loops, cm/cm (5.D.79)

In this chapter we have discussed the physics of point defect and microstructure dynamics and the formulation of a unique time dependent rate theory. The present formulation of the theory makes it equally applicable to steady-state, transient and pulsed irradiation situations. The theory connects the behavior of all major microstructural components and of point objects in a unified dynamic treatment. The effects of other microstructural components such as precipitates and grain boundaries could be easily incorporated into the theory in the future.

CHAPTER VI

NUMERICAL AND COMPUTATIONAL ASPECTS OF THE FULLY DYNAMIC RATE THEORY

VI.A. Introduction

The object of this chapter is to outline the methods by which equations (5.58) to (6.67) can be solved. A more detailed description of the TRANSWELL Code developed for this purpose is given in reference (81) and only the highlights of that report will be given here.

Time dependent computations in the rapidly developing radiation damage field are fairly recent and early results have been discussed in previous documents [12-18]. Given the present fluidity of conceptual reactor designs it was felt that the existence of a flexible code that can easily accommodate new additions and changes must be developed to incorporate future developments.

The TRANSWELL code solves the kinetic rate equations for single vacancies and single interstitials in a homogeneous medium with spacially averaged concentrations. Coupled rate equations are solved for an average void radius, average aligned and non-aligned interstitial loop radii, the concentration of aligned and non-aligned vacancy loops, the concentration of vacancies tied up in aligned and non-aligned vacancy loops, and finally strain and strain rate equations,

(i.e., equation (5.58) to (5.67)). The code is built on the theoretical ideas in the rate formulation developed by Harkness and Li [94,95]; Wiedersich [96]; Brailsford and Bullough [71,72]; Bullough Eyre and Krishan [65]; and Ghoniem and Kulcinski [53,81]. It is written with the objective of standardizing transport kinetic calculations of point defects and their effect on the response of metals under different irradiation conditions.

TRANSWELL(VEROI) is designed to help the experimentalist as well as the theoritician to parametrically study the effect of input material properties on the final experimental observations. The code has not been developed to its ultimate potential at this point in time but its structure facilitates the modification of the inherent physics in the future.

VI.B. Method of Solution

Many physical systems give rise to ordinary differential equations in which the magnitudes of the eigenvalues vary greatly. Such situations arise in the study of point defects in metals using the rate theory as described in references [13,81].

For example, the production of highly mobile interstitials and relatively immobile vacancies at moderate temperatures presents a situation where the interstitials migrate quickly to their 'final' configuration while the vacancies have not begun to move. Later when the vacancies are annealing the interstitials are relatively fixed. It is common to

refer to the equations describing the behavior of such systems as stiff.

The TRANSWELL code contains a FØRTRAN subroutine collection called the GEAR package [97]. It is based on a program by C. W. Gear [98], for the solution of the initial value problem for systems of ordinary differential equations (ØDE's). Such a system has the form

$$\dot{y} = f(y,t)$$

or more specifically,

$$\frac{dy_i(t)}{dt} = f_1(y_1(t),\ldots,y_N(t),t) \qquad (6.1)$$

where $y,\dot{y}$ and f are vectors of length $N \geq 1$. Given an initial value of the vector

$$y(t_0) = y_0, \qquad (6.2)$$

and a subroutine for the calculation of f, the GEAR package computes a numerical solution to Eq. (6.1) at values of the independent variable t is some interval $[t_0,T]$, as desired by the user. (The endpoint T may not be known in advance).

The basic methods used for the solution are of implicit linear multistep type. There are two classes of such methods available to the user. The first is the implicit Adams methods (up to order 12), and the second is the backward differentiation formular (BDF) methods (up to order 5), also called Gear's stiff methods. In either case the implicitness of the

basic formula then requires an algebraic system of equations be solved at each step. A variety of corrector-iteration methods is available for this, such as described in reference (97).

A prime feature of GEAR (or of the methods of C. W. Gear on which it is based) is its ability to solve stiff ODE problems. Roughly speaking, an ODE system is called stiff if it involves both very rapidly changing terms and very slowly changing terms, all of a decaying nature. More precisely, we consider the eigenvalues λ_i of the N x N Jacobian matrix.

$$J = \frac{\partial f}{\partial y} = \left(\frac{\partial f_i}{\partial y_j}\right)_{i,j=1}^{N} \tag{6.3}$$

and suppose that the λ_i all have negative real parts. The "time constants" of the problem are then $\tau_i = 1/|\mathrm{Re}(\lambda_i)|$ and the decaying nature (locally) of the solution is given by the exponentials e^{-t/τ_i}. If the N time constants τ_i are widely spread, and those terms with the smaller τ_i have already decayed to an insignificant level while those with large value of τ_i are still active, then the system is stiff. (Actually, some of the $\mathrm{Re}(\lambda_i)$ may still be non-negative, meaning that some solution components are non-decaying, and the system would still be called stiff if the negative $\mathrm{Re}(\lambda_i)$ values have a relatively large magnitude). The property of stiffness is local in time; a problem may be stiff in some regions of t and not in others. It is also relative, the ratio max τ_i/ min τ_i being a measure of the stiffness.

The difficulty with stiff problems is that most conventional methods for solving ODE's require incremental values of t commensurate with min τ_i, while the size $|T-t_0|$ of the problem range is commensurate with max τ_i. As a result, the problem cannot be run to completion in a reasonable number of steps. With Gear's methods, however, the increment h is restricted to small values, by the requirements of accuracy, only where the solution is relatively active. By definition, the problem is not stiff in such regions, and accuracy is achieved at minimum cost by allowing both h and the order of the method to vary with time. Then in regions of stiffness, where the solution is inactive, Gear's methods have the property of "stiff stability", which assures that h is no longer restricted by the small time constants, unless or until the corresponding rapidly decaying terms become active again. This property necessitates, among other things, that the methods be implicit, and therefore that a system of (generally) non-linear algebraic equations be solved at each step. Moreover, stiffness dictates that a fairly powerful iteration method be used to solve this system, and the Gear package contains variants of Newton's method (called chord methods) for this purpose. Both the stiff and non-stiff methods are implemented in a manner which allows the step size and the order to vary in a dynamic way throughout the problem. This variability is now widely recognized as highly desirable for

efficiency in using linear multistep methods.

The GEAR package is a collection of seven subroutines, one of which is the single-step core integrator routine, STIFF. Subroutine STIFF is a heavily revised version of a routine written and published by GEAR [98].

The methods used in the GEAR package are documented in considerable detail elsewhere [97]. Hence, only a brief summary of them will be given here.

The basic methods are linear multipoint methods of the form

$$y_n = \sum_{j=1}^{K_1} \alpha_j y_{n-j} + h \sum_{j=0}^{K_2} \beta_j \dot{y}_{n-j}, \qquad (6.4)$$

where y_k is an approximation to $y(t_k)$, $\dot{y}_k = f(y_k, t_k)$ is an approximation to $\dot{y}(t_k)$, and h is a constant step size: $h = t_{k+1} - t_k$. In the case of the Adams method of order q, we have $k_1 = 1$ and $k_2 = q-1$. In the case of the backward differentiation formula (BDF) of order q, we have $k_1 = q$ and $k_2 = 0$. the BDF's are so called because, on dividing through by $h\beta_0$, they can be regarded as approximation formulas for $\dot{y}_n$ in terms of $y_n, y_{n-1}, \ldots, y_{n-q}$. In either case, the α_j and β_j are constants associated with the method, and $\beta_0 > 0$. The latter means that Eq. (6.4) is an implicit equation for y_n and is in general a non-linear algebraic system that must be solved on every step. The fact that the order of a given method is q means that if Eq. (6.4) is solved for y_n with all past values being exact, then y_n will differ from the correct solution of

the ODE by a local truncation error that is order of (h^{q+1}) for small h.

If Eq. (6.4) is written in the form

$$g(y_n) \equiv y_n - h\beta_0 f(y_n, t_n) - \sum_{1}^{K_1} \alpha_y y_{n-j} - h \sum_{1}^{K_2} \beta_j \dot{y}_{n-j} = 0, \quad (6.5)$$

then the non-linear system of $g(y_n) = 0$ can be solved, for example, by Newton's method.

In all of the iteration methods, a first approximation $y_n(0)$ is required. This is computed from the existing information corresponding to saved past values of y_k and $\dot{y}_k$. This prediction is such that $y_n(0)$, as well as the final value y_n, is accurate to q^{th} order.

Following a step of size h at order q, the GEAR package, at intervals of q+2 steps, attempts to choose a larger step size by estimating the local truncation erros at orders q-1, q, and q+1. The largest value of h' of the three step sizes obtained is then chosen, and the order reset accordingly. Also, the Nordsieck array must be rescaled by power of h'/h. The data used to take the subsequent steps of size h' is in effect obtained by interpolating with the data at a spacing of h.

VI.C. Jacobian Matrix of the System

We consider a system of n first order (in general non-linear) ordinary differential equations. Many higher order equations can be changed to such a system by simple

substitution of new letters for derivatives, and the form $\dot{Y} = f(Y,t)$ yields considerable insight into the qualitative behavior of the system through phase space analysis. P(i,j) has the interpretation of the local time constant of the element i due to the presence of element j. The non zero elements of the Jacobian matrix will be listed here for the full system of equations.

$$\frac{\partial F_{el}}{dx} = \frac{\mu b^2}{4(1-\nu)(x+b)^2}\left(1-\ell n\ \left(\frac{b+x}{b}\right)\right) \tag{6.6}$$

$$\phi_i = Z_i D_i Y(6) \tag{6.7}$$

$$\phi_v = Z_v D_v Y(5) \tag{6.8}$$

$$\phi_v^e = Z_v D_v C_v^e \tag{6.9}$$

$$\beta = 1/(kT) \tag{6.10}$$

$$\frac{\partial r_{vl}^n}{\partial Y(3)} = -\frac{Y(4)}{(2\pi r_{vl}^n b[Y(3)]^2)} \tag{6.11}$$

$$\frac{\partial r_{vl}^n}{\partial Y(4)} = \frac{1}{(2\pi r_{vl}^n bY(3))} \tag{6.12}$$

$$\frac{\partial r_{vl}^a}{\partial Y(8)} = -\frac{Y(9)}{(2\pi r_{vl}^n b[Y(8)]^2)} \tag{6.13}$$

$$\frac{\partial r_{vl}^a}{\partial Y(9)} = \frac{1}{(2\pi r_{vl}^a bY(8))} \tag{6.14}$$

where

- ϕ_i is the biased interstitial flux. (6.D.1)
- ϕ_v is the biased vacancy flux. (6.D.2)

$\cdot\phi_v^e$ is the thermal equilibrium biased vacancy flux.

(6.D.3)

We now will proceed to calculate the elements of this Jacobian matrix as outlined in Figure (6.1). Obviously there is not a cross dependence on all of the elements of this matrix and it will be seen that the major functional dependencies lie between the defect concentrations (C_v,C_I) and the rest of the variables. We now will list the various non zero elements.

First Row

$$P(1,1) = 2\gamma\beta \frac{\Omega}{[Y(1)]^3} \phi_v^e \{(\frac{2\gamma}{Y(1)} - P_g) \frac{\Omega}{kT}\} - (D_v Y(5) - D_i Y(6)$$

$$- \phi_v^e \exp \{(\frac{2\gamma}{Y(1)} - P_g) \frac{\Omega}{kT}) / [Y(1)]^2 \qquad (6.15)$$

$$P(1,5) = D_v/Y(1) \qquad (6.16)$$

$$P(1,6) = -D_i/Y(1) \qquad (6.17)$$

Second Row

$$P(2,2) = \phi_v^e \exp\left\{ \frac{-(\gamma_{sf}+F_{el}(Y(2))b^2}{kT} \right\} b\beta \frac{\partial F_{el}}{\partial Y(2)} \qquad (6.18)$$

$$P(2,5) = -Z_v D_v/b \qquad (6.19)$$

$$P(2,6) = Z_i D_i/b \qquad (6.20)$$

Third Row

$$P(3,3) = - (\phi_i - \phi_v + \phi_v^e \exp\left\{ \frac{\gamma_{sf}+F_{el}(r_{vl}(o))b^2}{kT} \right\}) / br_{vl}(o) \qquad (6.21)$$

$$P(3,5) - Y(3) Z_v D_v / br_{vl}(o) \qquad (6.22)$$

$$P(3,6) = -Y(3) Z_v D_v / br_{vl}(o) \qquad (6.23)$$

		R_c	$r^n_{i\ell}$	$N^n_{v\ell}$	$q^n_{v\ell}$	C_v	C_I	$r^a_{i\ell}$	$N^a_{v\ell}$	$q^a_{v\ell}$	ϵ_N
		1	2	3	4	5	6	7	8	9	10
R_c	1	P(1,1)	0	0	0	P(1,5)	P(1,6)	0	0	0	0
$r^n_{i\ell}$	2	0	P(2,2)	0	0	P(2,5)	P(2,6)	0	0	0	0
N^n_v	3	0	0	P(3,3)	0	P(3,5)	P(3,6)	0	0	0	0
$q^n_{v\ell}$	4	0	0	P(4,3)	P(4,4)	P(4,5)	P(4,6)	0	0	0	0
C_v	5	P(5,1)	P(5,2)	P(5,3)	P(5,4)	P(5,5)	P(5,6)	P(5,7)	P(5,8)	P(5,9)	0
C_I	6	P(6,1)	P(6,2)	P(6,3)	P(6,4)	P(6,5)	P(6,6)	P(6,7)	P(6,8)	P(6,9)	0
$r^a_{i\ell}$	7	0	0	0	0	P(7,5)	P(7,6)	P(7,7)	0	0	0
$N^a_{v\ell}$	8	0	0	0	0	P(8,5)	P(8,6)	0	P(8,8)	0	0
$q^a_{v\ell}$	9	0	0	0	0	P(9,5)	P(9,6)	0	P(9,8)	P(9,9)	0
ϵ_N	10	0	0	0	0	P(10,5)	P(10,6)	0	0	0	0

Fig. (6.1) Jacobian Matrix for the (FDRT).

Fourth Row

Define $T_2^n = \sqrt{4\pi Y(4)Y(3)/b}$ (6.24)

$$T_3^n = \phi_i - \phi_v + \phi_v^e \exp\left\{\frac{(\gamma_{sf}+F_{el}(r_{vl}^n))b^2}{kT}\right\} \quad (6.25)$$

Then

$$P(4,3) = 2\pi Y(4)T_3^n/T_2^n b - T_2^n b^2\beta \frac{\partial F_{el}}{\partial r_{vl}^n} \cdot \frac{\partial r_{vl}^n}{\partial Y(3)} \times \phi_v^e \exp \left\{\frac{(\gamma_{sf}+F_{el}(r_{vl}^n))b^2}{kT}\right\} \quad (6.26)$$

$$P(4,4) = -2\pi Y(e)T_3^n/T_2^n b - T_2^n b^2\beta \frac{\partial F_{el}}{\partial r_{vl}^n} \cdot \frac{\partial r_{vl}^n}{\partial Y(4)} \times \phi_v^e \exp \left\{\frac{(\gamma_{sf}+F_{el}(r_{vl}^n))b^2}{kT}\right\} \quad (6.27)$$

$$P(4,5) = T_2^n Z_v D_v \quad (6.28)$$

$$P(4,6) = -T_2^n Z_i D_i \quad (6.29)$$

Fifth Row

$$P(5,1) = 4\pi N_C D_v \{C_v^e \exp[(\frac{2\gamma}{Y(1)} - P_g)\frac{\Omega}{kT}](1-2\frac{\gamma\Omega\beta}{Y(1)}) - Y(5)\} \quad (6.30)$$

$$P(5,2) = 2\pi Z_v N_{i\ell}^n \{D_v C_v^e \exp[\frac{(\gamma_{sf}+F_{el}(Y(2)))b^2}{kT}] \times (1-Y(2)b^2\beta \frac{\partial F_{el}}{\partial Y(2)}) - Y(5)\} \quad (6.31)$$

$$P(5,3) = 2\pi Z_v D_v \{C_v^e \exp[\frac{(\gamma_{sf}+F_{el}(r_{vl}^n))b^2}{kT}] \times (\frac{\partial r_{vl}^n}{\partial Y(3)} \cdot Y(3) + r_{vl}^n + r_{vl}^n Y(3)b^2\beta \frac{\partial F_{el}}{\partial r_{vl}^n} \cdot \frac{\partial r_{vl}^n}{\partial Y(3)}) - Y(5)(r_{vl}^n + Y(3) \frac{\partial r_{vl}^n}{\partial Y(3)})\} \quad (6.32)$$

$$P(5,4) = 2\pi Z_v D_v \{C_v \exp[\frac{(\gamma_{sf}+F_{el}(r^n_{vl}))b^2}{kT}] \times (\frac{\partial r^n_{vl}}{\partial Y(4)} + r^n_{vl} b^2\beta \frac{\partial F_{el}}{\partial r^n_{vl}} \cdot \frac{\partial r^n_{vl}}{\partial Y(4)}) - Y(5) \frac{\partial r^n_{vl}}{\partial Y(4)}\} Y(3) \quad (6.33)$$

$$P(5,5) = -D_v(4\pi Y(1)N_C + Z_v\rho^{en}_d + Z^a_v\rho^{ea}_d + 2\pi Y(2)N^n_{i\ell} + 2\pi Y(7)N^a_{i\ell} + 2\pi r^n_{vl} + Y(3) + 2\pi r^a_{vl} Y(8)) - \alpha Y(6) \quad (6.34)$$

$$P(5,6) = -\alpha Y(5) \quad (6.35)$$

$$P(5,7) = 2\pi Z^a_v N^a_{i\ell} D_v \{C^e_v \exp(\frac{\sigma\Omega}{kT}) \exp[\frac{-(\gamma_{sf}+F_{el}(Y(7)))b^2}{kT}] \times (1-Y(7)b^2\beta \frac{\partial F_{el}}{\partial Y(7)}) - Y(5)\} \quad (6.36)$$

$$P(5,8) = 2\pi Z^a_v D_v \{C^e_v \exp(\frac{\sigma\Omega}{kT}) \exp[\frac{(\gamma_{sf}+F_{el}(r^a_{vl}))b^2}{kT}] \times (\frac{\partial r^a_{vl}}{\partial Y(8)} Y(8) + r^a_{vl} + r^a_{vl} Y(8) b^2\beta \frac{\partial F_{el}}{\partial r^a_{vl}} \cdot \frac{\partial r^a_{vl}}{\partial Y(8)} - Y(5)(r^a_{vl} + Y(8) \frac{\partial r^a_{vl}}{\partial Y(8)})\} \quad (6.37)$$

$$P(5,9) = 2\pi Z^a_v D_v \{C^e_v \exp(\frac{\sigma\Omega}{kT}) \exp[\frac{(\gamma_{sf}+F_{el}(r^a_{vl}))b^2}{kT}] \times (\frac{\partial r^a_{vl}}{\partial Y(9)} + r^a_{vl} b^2\beta \frac{\partial F_{el}}{\partial r^a_{vl}} \cdot \frac{\partial r^a_{vl}}{\partial Y(9)} - Y(5) \frac{\partial r^n_{vl}}{\partial Y(9)}\} Y(8) \quad (6.38)$$

Sixth Row

$$P(6,1) = -4\pi N_C D_i Y(6) \quad (6.39)$$

$$P(6,2) = -2\pi Z^n_i N^n_{i\ell} D_i Y(6) \quad (6.40)$$

$$P(6,3) = -2\pi Z^n_i D_i Y(6) [r^n_{vl} + Y(3) \frac{\partial r^n_{vl}}{\partial Y(3)}] \quad (6.41)$$

$$P(6,4) = -2\pi Z^n_i D_i Y(6) Y(3) \frac{\partial r^n_{vl}}{\partial Y(4)} \quad (6.42)$$

$$P(6,5) = -\alpha Y(6) \tag{6.43}$$

$$P(6,6) = -D_i(4\pi Y(1)N_C + Z_i^n \rho_d^{en} \rho_d^{ea} + 2\pi Z_i^n Y(2) N_{i\ell}^n + 2\pi Z_i^a Y(7) N_{i\ell}^a + 2\pi Z_i^n r_{vl}^n Y(3) + 2\pi Z_i^a r_{vl}^a Y(8)) - \alpha Y(5) \tag{6.44}$$

$$P(6,7) = -2 Z_i^a N_{i\ell}^a D_i Y(6) \tag{6.45}$$

$$P(6,8) = -2\pi Z_i^a D_i Y(6) \left[r_{vl}^a + Y(8) \frac{\partial r_{vl}^a}{\partial Y(8)}\right] \tag{6.46}$$

$$P(6,9) = -2\pi Z_i^a D_i Y(6) Y(8) \frac{\partial r_{vl}^a}{\partial Y(9)} \tag{6.47}$$

Seventh Row

$$P(7,5) = - Z_v^a D_v / b \tag{6.48}$$

$$P(7,6) = Z_i^a D_i / b \tag{6.49}$$

$$P(7,7) = \phi_v^e \exp\left(\frac{\sigma\Omega}{kT}\right) \exp\left\{\frac{-(\gamma_{sf} + F_{el}(Y(7)))b^2}{kT}\right\} b\beta \frac{\partial F_{el}}{\partial Y(7)} \tag{6.50}$$

Eigth Row

$$P(8,5) = Y(8) Z_v^a D_v / b r_{vl}(o) \tag{6.51}$$

$$P(8,6) = -Y(8) Z_i^a D_i / b r_{vl}(o) \tag{6.52}$$

$$P(8,8) = -(Z_i^a D_i Y(6) - Z_v^a D_v Y(5) + Z_v^a D_v C_v^e \exp\left(\frac{\sigma\Omega}{kT}\right) \times \exp\left\{\frac{[\gamma_{sf} + F_{el}(r_{vl}(o))]b^2}{kT}\right\}) / b r_{vl}(o) \tag{6.53}$$

Ninth Row

Define $T_2^a = \sqrt{4\pi Y(8) Y(9)}/b$ (6.54)

$$T_3^a = Z_i^a D_i Y(6) - Z_v^a D_v Y(5) + Z_v^a D_v C_v^e \exp\left(\frac{\sigma\Omega}{kT}\right) \times \frac{[\gamma_{sf} + F_{el}(r_{vl}^a)]b^2}{kT} \tag{6.55}$$

$$P(9,5) = T_2^a Z_v^a D_v \tag{6.56}$$

$$P(9,6) = - T_2^a Z_i^a D_i \tag{6.57}$$

$$P(9,8) = -2\pi Y(8) T_3^a / T_2^a b - T_2^a b\beta \frac{\partial F_{el}}{\partial r_{vl}^a} \cdot \frac{\partial r_{vl}^a}{\partial Y(8)} \times Z_v^a D_v C_v^e \exp\left(\frac{\sigma\Omega}{kT}\right) \exp\left\{\frac{[\gamma_{sf} + F_{el}(r_{vl}^a)]b^2}{kT}\right\} \tag{6.58}$$

$$P(9,9) = -2\pi Y(8) T_3^a / T_2 b - T_2^a b^2 \beta \frac{\partial F_{el}}{\partial r_{vl}^a} \cdot \frac{\partial r_{vl}^a}{\partial Y(9)} \times Z_v^a D_v C_v^e \exp\left(\frac{\sigma\Omega}{kT}\right) \exp\left\{\frac{[\gamma_{sf} + F_{el}(r_{vl}^a)]b^2}{kT}\right\} \tag{6.59}$$

Tenth Row

$$P(10,5) = \rho_d^{ea} (Z_v^n - Z_v^a) D_v \tag{6.60}$$

$$P(10,6) = \rho_d^{ea} (Z_i^a - Z_i^n) D_i \tag{6.61}$$

VI.D. TRANSWELL Computer Code

VI.D.1. Introduction

TRANSWELL I is structured with the following considerations:

(1) Minimizing the number of rate equations used in a specific condition. This is mainly to alleviate using more equations than necessary. It was noticed in early versions that using redundant equations increases computation time dramatically.

(2) Computing the minimum number of variables. Thus time invariant quantities are computed once at the beginning. Time dependent equations contain "almost" the minimum number of time invariant arithmetic operations.

(3) Ease of accessibility to most of the variables through the use of common areas as will be described.

(4) Since basic applications of this code are expected to be in the area of time dependent analysis, special attention was given to methods of reducing computational time.

(5) Minimum programming ambiguity with forward branching and abundance of comment cards to guide the interested researcher for future changes.

(6) Logical separation of different irradiation conditions. This slightly increases the storage requirements of the object code, but it will be extremely valuable when one wants to add more physics to the code.

VI.D.2. TRANSWELL Code Subroutines

TRANSWELL subroutines are written with the idea of affixing calculational as well as logical functions to each subroutine. 'Arguments' are avoided from most subroutines with only a few exceptions. All information is handled and passed between subroutines through the CØMMØN blocks. This section is concerned with describing all subroutines and functions in a general sense. Comments on the logic and method of calculation are amply dispersed in all of the subroutines. This provides detailed information on each of the separate subroutines. Figure (6.2) shows the general structure of TRANSWELL and we include below a brief description of each subroutine.

FLØW DIAGRAM ØF TRANSWELL (VEROI)

N. GHØNIEM - JAN. 1977

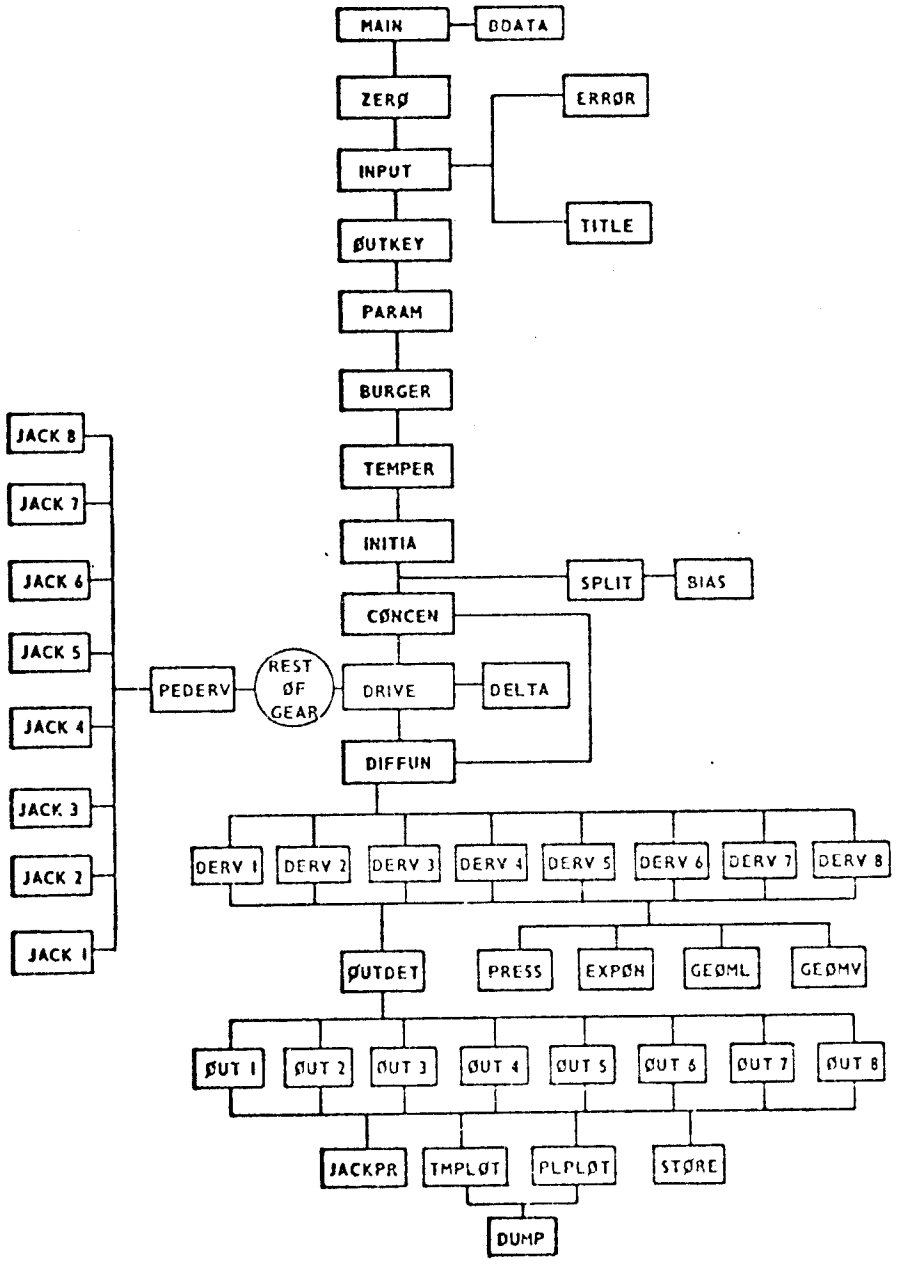

Fig. (6.2)

MAIN

The main program masters and manipulates the logic of any specific problem. It calls 10 subroutines for setting up the input and initial conditions, performing time independent calculations; and calling the core integrator subroutines.

ZERØ

This subroutine sets all of the CØMMØN blocks to zero. It uses double precision zeroes (0.DO) for all the variables. Having done this, it sets up some default values of input parameters .

INPUT

This is the main input subroutine. It is called only once after ZERØ and reads in numeric and alphanumeric input. Thus it supercedes default values set up by ZERØ. Description of input variables and their default values is given in reference (81).

ERROR (NAME, ERRFLG)

It prints misspelled input characters, and/or indicates if the input is in incorrect order.

TITLE

It reads numeric data using NAMELIST, then it reads alphanumeric input for each graph.

It is called only once when plotting option is specified.

ØUTKEY

This subroutine is designed merely to give full explanations (ENTRY TABLE) of output quantities. If one is familiar

with the output notation, he can omit it from the output stream by introducing a suitable data card as explained in reference (81).

PARAM

This subroutine picks up metal parameters under consideration. Best available data are stored at the compilation time in element BDATA. Metals and their ID numbers available now are:

Metal	ID
Nickel	1
Stainless steel	2
Aluminum	3
Niobium	4
Vanadium	5

The following quantities are defined for a metal from a 5 x 15 matrix.

Parameter	Matrix Element	Unit	Meaning
E_v^f	A(1,ID)	eV	vacancy formation energy
E_i^f	A(2,ID)	eV	interstitial formation energy
E_v^m	A(3,ID)	eV	vacancy migration energy
E_i^m	A(4,ID)	eV	interstitial migration energy
D_v^o	A(5,ID)	$cm^2 sec^{-1}$	vacancy diff. coef. preexpon.
D_i^o	A(6,ID)	$cm^2 sec^{-1}$	interstitial diff. coef. preexpon.
b	A(7,ID)	cm	Burger's vector
γ	A(8,ID)	eV cm^{-2}	surface energy
Z_v	A(9,ID)	dimensionless	vacancy bias factor
Z_i	A(10,ID)	dimensionless	interstitial bias factor
Ω	A(11,ID)	cm^3	atomic volume
γ_{sf}	A(12,ID)	eV cm^{-2}	stacking fault energy
μ	A(13,ID)	ergs cm^{-3}	shear modulus
ν_o	A(14,ID)	dimensionless	Poisson's ratio
e_i	A(15,ID)	dimensionless	Ratio of interstitial relaxation volume to atomic volume

Default values for the different parameters are listed in Table (6.1).

TABLE (6.1)

Metal Parameters Used in TRANSWELL

	Parameter	METAL Ni	S.S.	Al	Nb	Va
		1	2	3	4	5
1	E_v^f	1.39DO	1.6DO	0.7DO		
2	E_i^f	4.08DO	4.0DO	3.2DO		
3	E_v^m	1.38DO	1.3DO	0.57DO		
4	E_i^m	.15DO	.2DO	0.1DO		
5	D_v^o	.06DO	.58DO	0.045DO		
6	D_i^o	.12DO	1.D-3	0.08DO		
7	b	2.5D-8	2.0D-8	2.D-8		
8	γ	6.2415D14	1.25D15	6.2415D14		
9	Z_v	1.00DO	1.00DO	1.00DO		
10	Z_i	1.01DO	1.08DO	1.01DO		
11	Ω	1.5625D-23	0.8D-23	0.8D-23		
12	γ_{sf}	2.496D14	9.4D12	1.248D14		
13	μ	9.47D11	2.836D11	2.65D11	4.73D11	3.96D11
14	ν_o	0.276DO	0.291DO	0.347DO	9.35DO	0.392DO
15	e_i	1.40DO	1.40DO	1.40DO	1.40DO	1.40DO

BDATA

This is the BLØCK DATA of the program. Information is stored at the compilation time in CØMMØN Blocks CØNST and METDAT.

BURGER

This subroutine is called only once and it calculates all time independent quantities and stores them in CØMMØN Block /BURG/.

TEMPER

This subroutine is called only once and it calculates and prints out the temperature dependent information.

INITIA

This subroutine is called only once before starting the time dependent calculations. It sets up the initial value of the vector components Y(NEQ) and stores them in CØMMØN Block. INITL. It also selects the number of equations (NEQ), and the initial time step used in the core integrator (GEAR).

SPLIT

This is called only when input variable TYPE (5) = 'STRE'. It calculates the fraction f of the total interstitial loop population that is aligned perpendicular to the applied stress as given by Equation (5.56) and as defined in (5.D.75). It also calculates the concentration of aligned and non-aligned interstitial loops per cm^3.

BIAS

This subroutine calculates the aligned and non-aligned

dislocation loop-vacancy bias factor and the aligned and non-aligned dislocation loop-interstitial bias factor.

CØNCEN

This subroutine calculates the steady-state vacancy and interstitial concentrations (CV and CI) and their fluxes (DV*CV and DI*CI). It solves simultaneously Equations (5.62) and (5.63) for the special case: $\dot{Y}(5) = \dot{Y}(6) = 0.DO$.

GEAR Package

A full description of the theory and practice of this package is given in reference (97). However, we will repeat only the means of communication with the package. Figure (6.3) shows the interrelationship between the GEAR package and TRANSWELL.

To use the GEAR package, the user must provide: (a) a routine which defines the problem and which is called by the package (primarily Subroutine DIFFUN defining f(y,t)), and (b) a calling program which makes calls to Subroutine DRIVE. The routines called by the package are discussed below under External Names. The calling program must set the initial values, method parameters, and output values of t, and make calls to DRIVE. DRIVE in turn calls other routines for the solution of the problem. Since the integration process uses step sizes determined internally and dynamically, it will not generally hit the output values of t exactly. Normally, it will go slightly beyond each output point, and values of y at the output point are computed by interpolation.

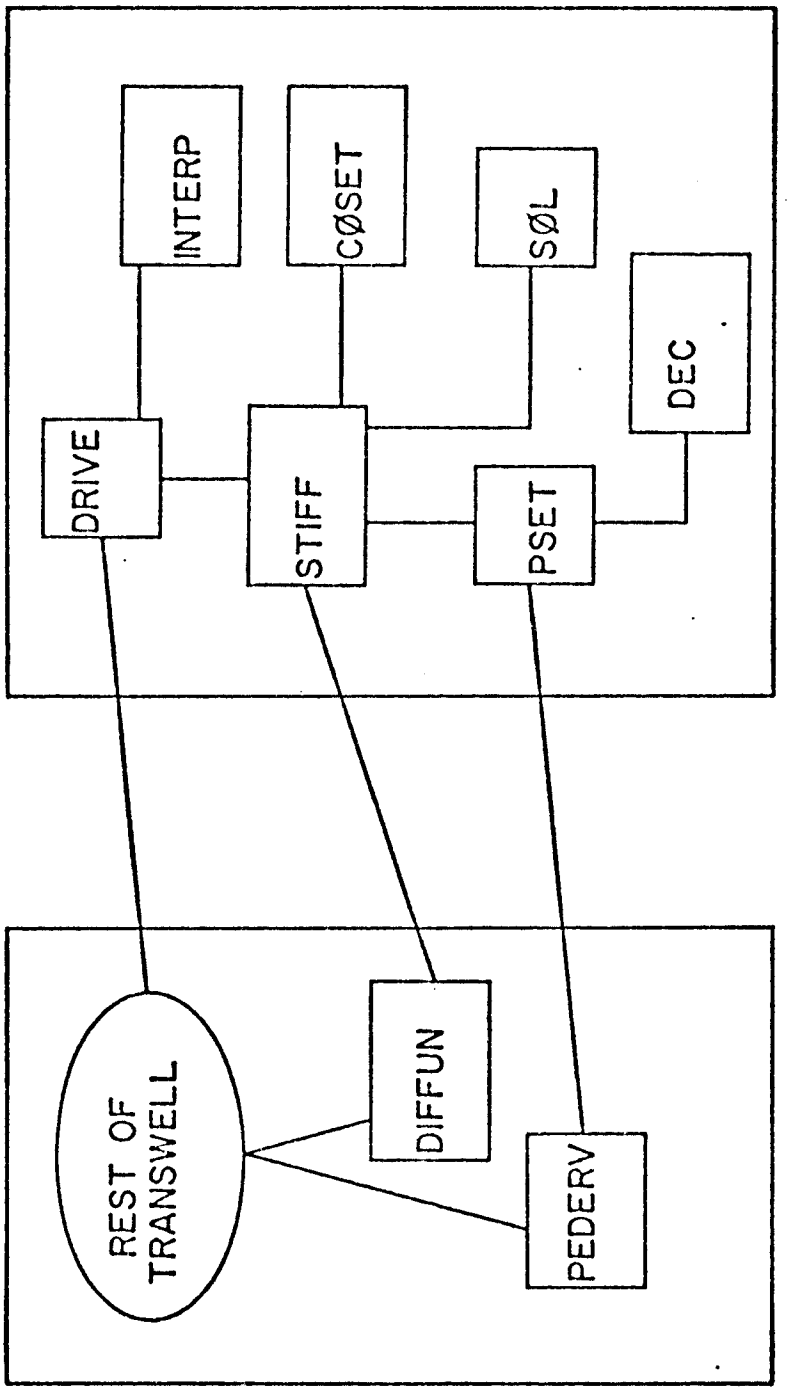

Fig. (6.3) Structure of the GEAR Package and Communication with TRANSWELL.

Communication with DRIVE

The calling sequence to Subroutine DRIVE is as follows:

Call DRIVE (N, TO, HO, YO, TØUT, EPS, MF, INDEX).

The arguments to DRIVE are defined in references (97) and (81).

External Names

Besides Subroutine DRIVE, the following six routines are supplied as part of the GEAR package. Their calling sequences and functions are described below, although this information is not essential for use of the package.

•Subroutine INTERP (TØUT, Y, NO, YO) is called by DRIVE. It computes interpolated values for y at t = TØUT, using the data in the Y array.

•Subroutine STIFF (Y,NO) is called by DRIVE. It performs a single step of the integration, and does the control of local error (which entails selection of step size and order for that step).

•Subroutine CØSET (METH, NQ, EL, TQ, MAXDER) is called by STIFF, and sets coefficients that are used there, both for the basic integration step and for error control.

•Subroutine PSET (Y, NO, CØN, MITER, IER) is called by STIFF if MITER is 1 or 2. It sets up the matrix $P = I - h\beta_0 J$, where I is the identity matrix, β_0 is a scalar related method, and J is the Jacobian matrix. It then processes P for subsequent solution of linear algebraic systems with P as coefficient matrix, as part of the chord iteration methods.

•Subroutine DEC (N, NDIM, A, IP, IER) is called by PSET and used for matrix triangularization by Gaussian elimination for later solution of a system of linear equations.

•Subroutine SØL (N, NDIM, A, B, IP) is called by STIFF if MITER is 1 or 2, and solves linear algebraic systems for which the matrix was processed by DEC.

PEDERV (N, X, Y, PD, NO)

This subroutine directs the path of calculation to one of the eight subroutines JACK1 through JACK8. It also receives the Jacobian matrix P(10,10) in CØMMØN area /JACK/ and puts it in the matrix PD(NEQ,NEQ).

It is called by PSET if MITER = 1. It is to supply the partial derivates of f(y,x) with respect to y, evaluated at x = y. It must form a two-dimensional array PD, stored as NOxNO array, according to

$$PD(i,j) = \frac{\partial f_i}{\partial y_j} \quad , \quad 1 \leq i, \; j \leq N. \tag{6.62}$$

N here is the number of equations used = NEQ.

JACK1, JACK2, JACK3, JACK4, JACK5, JACK6, JACK7, JACK8

This group of subroutines computes elements of the Jacobian matrix P(10,10) for the following cases respectively:

(1) Ion or neutron irradiation* in a transient or pulsed mode of operation with a uniaxial stress applied.

(2) Ion or neutron irradiation at a steady rate or annealing of voids after a long irradiation at the same or different

*The grouping here is associated with the ability to produce vacancy clusters in displacement cascades.

temperature, with uniaxial stress applied.

(3) Ion or neutron irradiation in a transient or pulsed mode of operation with no stress applied.

(4) Electron irradiation in a transient or pulsed mode of operation with a uniaxial stress applied.

(5) Electron irradiation at a steady rate, or annealing of voids after a long irradiation time at the same or different temperature, with uniaxial stress applied.

(6) Electron irradiation in a transient or pulsed mode of operation with no stress applied.

(7) Ion or neutron irradiation at a steady rate, or annealing of voids after a long irradiation time at the same or different temperature, with no stress applied.

(8) Electron irradiation at a steady rate, or annealing of voids after a long irradiation time at the same or different temperature with no stress applied.

The cases described above are classified according to the number of equations in each case. Case (1) is the most general and all other cases are subsets of this first case. Instead of lumping all the previous studies in one huge core subroutine, we chose to construct eight different subroutines. The main reason is to alleviate computational bottle necks and to give the code greater flexibility and to save computer time. For example, if one decided to study the growth behavior of a void size or dislocation loop size distribution, he might add other core subroutines for this study.

DIFFUN (N, X, Y, YDØT)

This subroutine is called by STIFF, and also by PSET if MITER = 2. It is to compute the vector YDØT = $\dot{y}$ = f(y,t) of length N for given values x = t and the vector Y = y of length N. It is required regardless of the value of MF chosen. It actually directs the path of computation to one of the DERV subroutines.

DERV1, DERV2, DERV3, DERV4, DERV5, DERV6, DERV7, DERV8

This subroutine computes the vector YDØT = $\dot{y}$ = f(y,x) of length (10) for given values x = t and the vector Y = y of length (10). The derivatives are those of cases 1 through 8 described above.

DELTA

This subroutine calculates for a delta function response of a metal under irradiation. Theory for this subroutine is in reference (99). It computes the vacancy and interstitial concentrations as well as average void and interstitial loop radii as a function of time.

EXPØN

This is one of the external functions in the program. It calculates double precision exponentials and guards against overflow and underflow.

GEØMV (RV)

This external function calculates the exponential part in Equation (5.10). It is defined as

$$GE\emptyset MV(RV) = \frac{c_v(r_v)}{c_v^e} \qquad (6.63)$$

where $c_v(r_v)$ is the vacancy concentration at the surface of a void of radius r_v, and c_v^e is the thermal equilibrium vacancy concentration.

GEØML (RL)

This internal function calculates the exponential part in Equation (5.26). It is defined as:

$$GE\emptyset ML\ (RL) = \frac{c_v(r_\ell)}{c_v^e} \qquad (6.64)$$

where $c_v(r_\ell)$ is the vacancy concentration at the surface of an interstitial loop of radius r_ℓ, and c_v^e is the thermal equilibrium vacancy concentration.

The corresponding geometry function for vacancy loops is obtained as the inverse of GEØML.

PRESS (RV)

This internal function calculates the internal pressure in a void of radius (RV) and containing (GAS) number of gas atoms.

ØUTDET

This subroutine merely choses a suitable output path according to the irradiation particle, mode of irradiation and stress state.

ØUTP1, ØUTP2, ØUTP3, ØUTP4, ØUTP5, ØUTP6, ØXTP7, ØUTP8

This group of subroutines is designed for output quantities for the previously described 8 cases. It gives

detailed output, brief output, plotted output or a combination of detailed and plotted output.

TMPLØT

This subroutine gives an approximate plot on the printer or the terminal using the GRAPH2 routine.

PLPLØT

This subroutine plots graphs using the plotter and the GRAPH and GRAPHM routines.

STØRE

This subroutine stores the values for each variable to be plotted and also the time values.

DUMP

This subroutine dumps out the values of all parameters stored in CØMMØN areas. It is very useful as a debugging aid throughout the code since it could be easily called at any point in the code. However, for normal computations, it prints out the contents of all CØMMØN blocks at the end of the run.

This subroutine also writes the contents of pertinent CØMMØN blocks on unit 2 using FØRTRAN unformatted write statements. Thus, once the CØMMØN blocks have been saved, the calculation can be restarted by reading them back into core and starting again as if the calculation never stopped.

VI.D.3. TRANSWELL Computer Code Variables

All TRANSWELL real variables are implicit double precision giving 14 decimal places of accuracy on an IBM or

UNIVAC computer. For a CDC computer the statement "IMPLICIT DØUBLE PRECISION (A-H,O-Z)" has to be deleted from the beginning of all subroutines.

Variable names were chosen to indicate the actual names used in current literature on rate theory applied to point defects. This facilitates understanding of the different subroutines for further development.

The variables are grouped such that a subroutine will find most of the variables that it needs in few CØMMØN blocks. The variables (by CØMMØN Blocks) along with their meaning and units are listed in reference (81).

VI.D.4. Implementing the TRANSWELL Code

A great deal of effort has been directed towards optimization of both CPU time and core storage requirements. The necessity for pulsed and transient irradiation analysis with a great number of time steps imposes strict efficiency requirements on any code for such studies.

Approximately 62000 decimal words on a UNIVAC 1110 computer are needed for total program storage, using an overlay structure. Certain irradiation cases are very inexpensive to study using TRANSWELL. A typical case of electron irradiation, steady production of point defects and no stress applied requires an average of 0.23 seconds of CPU time per simulated dpa over a wide range of temperatures.

TRANSWELL reads two NAMELIST inputs for I/Ø unit and writes BCD output to logical unit six. If it is requested,

subroutine DUMP writes, in unformatted FØRTRAN statements, to logical I/Ø number 2. This is read into CØMMØN blocks by subroutine BINARY using FØRTRAN unformatted read statements.

There should be no language compatibility problems, but the implicit double precision statements should be removed from all subroutines when using a CDC 6600 or 7600. The code was initiated on the Engineering Computing Laboratory (ECL) of the University of Wisconsin, and then developed on a UNIVAC 1110 using the FØRTRAN V compiler. Gear Package includes approximately 1200 card images while TRANSWELL (including GEAR) contains approximately 6700 card images.

VI.E. PL3D Three Dimensional Plotting Code

VI.E.1. Code Structure

The PL3D Computer program ($_{100}$) is constructed mainly as a post processor for the TRANSWELL Computer Code [81]. It is a plotting routine that utilizes the MACC† plotting packages, especially SURGEN and CONTR to display information from TRANSWELL in 3 dimensions and as contour plots. Interactive selection of plots with the choice of titles, angles, variables and scaling vectors are features of PL3D. The program can be equally used, with a slight modification, to furnish the same facilities to any computer code that generates data in a binary form, as will be described.

The data channel from TRANSWELL to PL3D is a FØRTRAN

---

†Madison Academic Computing Center

binary file called unit 4. The PL3D program allows the user to select from up to 15Z-variables and many different combinations of X and Y values for each selection. After the user has finished with one Z-variable he may then go on to another. For each selection of X, Y and Z variables an appropriate set of labels may be entered interactively. After the surface and labels have been chosen the user may select the angles that determine a veiw of the surface, this view is then displayed on the graphics terminal for the user to include or exclude from his plotting set.

Generally the output format from TRANSWELL (or equivalent) is as follows

1. A block of X and Y axes variables.
2. A 15 x 100 array of Z values.

Then, for each surface PL3D reads the entire data file, picking out the desired numbers. This method of data handling slightly sacrifices efficiency but it enables PL3D to be adapted easily on other computer systems.

Obviously, the full plotting potential of each TRANSWELL run will not be realized at one terminal setting. To avoid the loss of these unrealized potential plots without incurring tremendous file charges, the data files are stored on a tape, via the TAPE UTILITIES ROUTINES for later use.

A general flow diagram of the interrelationships between PL3D, TRANSWELL Computer Code, Mass Storage system and Operating system is shown in Figure (6.4).

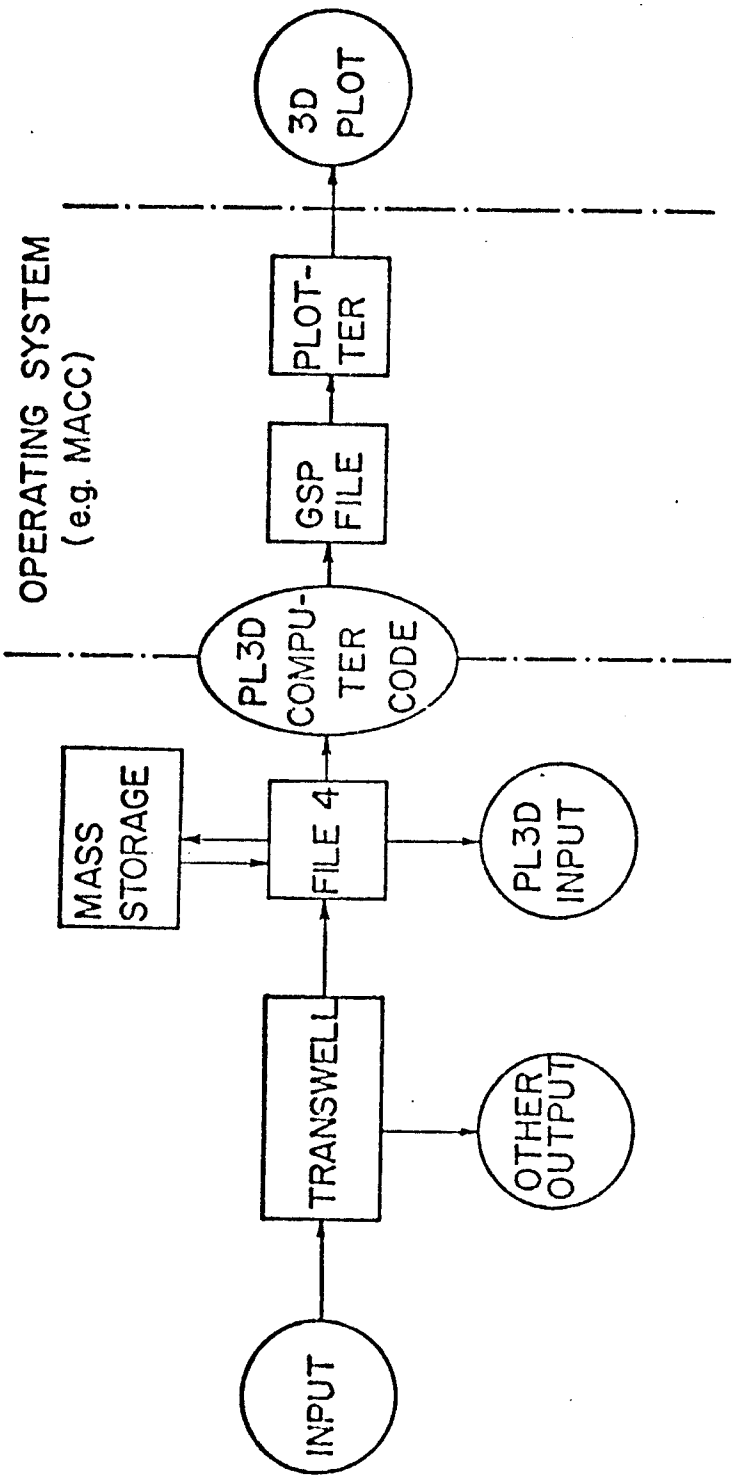

Fig. (6.4) Schematic of PL3D Computer Program Operation.

VI.E.2. PL3D Plotting Variables

The subroutine and the code variables are described in detail in Reference (100). Here we will only refer to the output variables that are accessible in a 3-dimensional or contour plotting forms. Any one of the following parameters can be plotted in the z-direction as a function of two independent variables in the x and y directions.

1. Average void radius, cm.
2. Average non-aligned interstitial loop radius, cm.
3. Number density of non-aligned vacancy loops, cm^{-3}.
4. Fraction of vacancies in non-aligned vacancy loops, at/at.
5. Vacancy concentration, at/at (space averaged).
6. Interstitial concentration, at/at (space averaged).
7. Average aligned interstitial loop radius, cm.
8. Number density of aligned vacancy loops, cm^{-3}.
9. Fraction of vacancies in aligned vacancy loops, at/at.
10. Network creep strain, cm/cm.
11. Rate of change of average void radius, cm/sec.
12. Rate of change of average non-aligned interstitial loop radius, cm/sec.
13. Rate of change of the number density of non-aligned vacancy loops, $cm^{-3}\ sec^{-1}$.
14. Rate of change of fraction of vacancies in non-aligned vacancy loops, at/at/sec.
15. Rate of change of vacancy concentration, at/at/sec.

16. Rate of change of interstitial concentration, at/at/sec.
17. Rate of change of average aligned interstitial loop radius, cm/sec.
18. Rate of change of number density of aligned vacancy loops, cm^{-3} sec^{-1}.
19. Rate of change of fraction of vacancies in aligned vacancy loops, at/at/sec.
20. Network creep strain rate, cm/cm/sec.
21. Total interstitial time constant, sec^{-1}.
22. Total vacancy time constant, sec^{-1}.
23. Total vacancy thermal emission rate from the surfaces of voids and dislocations, at/at/sec.
24. Vacancy flux ($D_v C_v$), cm^2/sec.
25. Interstitial flux ($D_i C_i$), cm^2sec.
26. Line dislocation density of non-aligned dislocation loops, cm/cm^3.
27. Line dislocation density of aligned dislocation loops, cm/cm^3.
28. Line dislocation density of non-aligned vacancy loops, cm/cm^3.
29. Line dislocation density of aligned vacancy loops, cm/cm^3.
30. Total line dislocation density, cm/cm^3.
31. Vacancy thermal emission rate from the surfaces of voids, at/at/sec.
32. Vacancy thermal emission rate from the surfaces of aligned edge dislocations, at/at/sec.

33. Vacancy thermal emission rate from the surfaces of non-aligned edge dislocations, at/at/sec.
34. Vacancy thermal emission rate from the surfaces of all edge dislocations (sum of 32 and 33), at/at/sec.
35. Vacancy thermal emission rate from the surfaces of aligned interstitial loops, at/at/sec.
36. Vacancy of thermal emission rate from the surfaces of non-aligned interstitial loops, at/at/sec.
37. Vacancy thermal emission rate from the surfaces of interstitial loops (sum of 35 and 36), at/at/sec.
38. Vacancy thermal emission rate from the surfaces of aligned vacancy loops, at/at/sec.
39. Vacancy thermal emission rate from the surfaces of non-aligned vacancy loops, at/at/sec.
40. Vacancy thermal emission rate from the surfaces of all vacancy loops, (sum of 38 and 39), at/at/sec.
41. Vacancy time constant due to the presence of voids only, sec^{-1}.
42. Interstitial time constant due to the presence of voids only, sec^{-1}.
43. Vacancy time constant due to the presence of dislocations only, sec^{-1}.
44. Interstitial time constant due to the presence of dislocations only, sec^{-1}.
45. Interstitial total sink removal rate, at/at/sec.

46. Vacancy total sink removal rate, at/at/sec.
47. Point defect recombination rate, at/at/sec.
48. Percent swelling.
49. Change of average void radius, $R_c - R_o$ (for pulsed irradiation), cm.
50. Change of average interstitial loop radius, $R_{i\ell} - R_{i\ell o}$ (for pulsed irradiation), cm.
51. Strain due to interstitial loops, cm/cm.
52. Strain due to vacancy loops, cm/cm.
53. Equivalent void sink density (defined as $4\pi R_c N_c$), cm^{-2}.

Any one of the 53 variables can be plotted in the Z-direction as a function of two independent variables:

a. The x-axis that is chosen from one of the following:
   1. the irradiation dose measured after incubation.
   2. the irradiation time after incubation.
b. The y-axis that is chosen from one of the following:
   1. Temperature, °K
   2. Logarithm to the base 10 of dose rate; dpa/sec.
   3. Logarithm to base 10 of gas generation rate; at/at/sec.
   4. Initial gas content of voids; atoms/void.
   5. Applied stress; psi.

VI.F. Example of TRANSWELL and PL3D Application

To conclude this chapter, an example showing the combined usage of TRANSWELL and PL3D computer codes, will be given. The TRANSWELL Computer Code was run first to simulate

the swelling of ion irradiated solution treated stainless steel in a steady-state irradiation environment. The parameters of Table (5.1) were used while the cascade collapse efficiency (ε) was fixed to a 0.001. A dose rate of 10^{-3} dpa/sec was used in the calculations. Output from this run was stored on a file given the name 4. INPUT/OUTPUT (I/Ø) utility routines were used to store the output information on a tape for later use. The computer code PL3D was then used to extract, transfer and process the numeric information on file 4 to 3-dimensional and contour plots as demonstrated in Figures (6.5) and (6.6).

Figure (6.5) shows a 3-dimensional plot of percent swelling as a function of dose and temperature for ion irradiated solution treated stainless steel. The dose rate is 10^{-3} dpa/s and the cascade collapse efficiency is 0.001. It clearly shows the 'bell' shaped swelling curve as a function of temperature, while the percent swelling is an increasing function of dose. For precise quantitiative values, contours of constant swelling as a function of dose and temperature are valuable, as shown in Figure (6.6). One can also see the slight shift towards higher temperatures of the peak swelling temperature with increasing dose.

In this chapter, the numerical and computational aspects of the Fully Dynamic Rate Theory has been explained with an

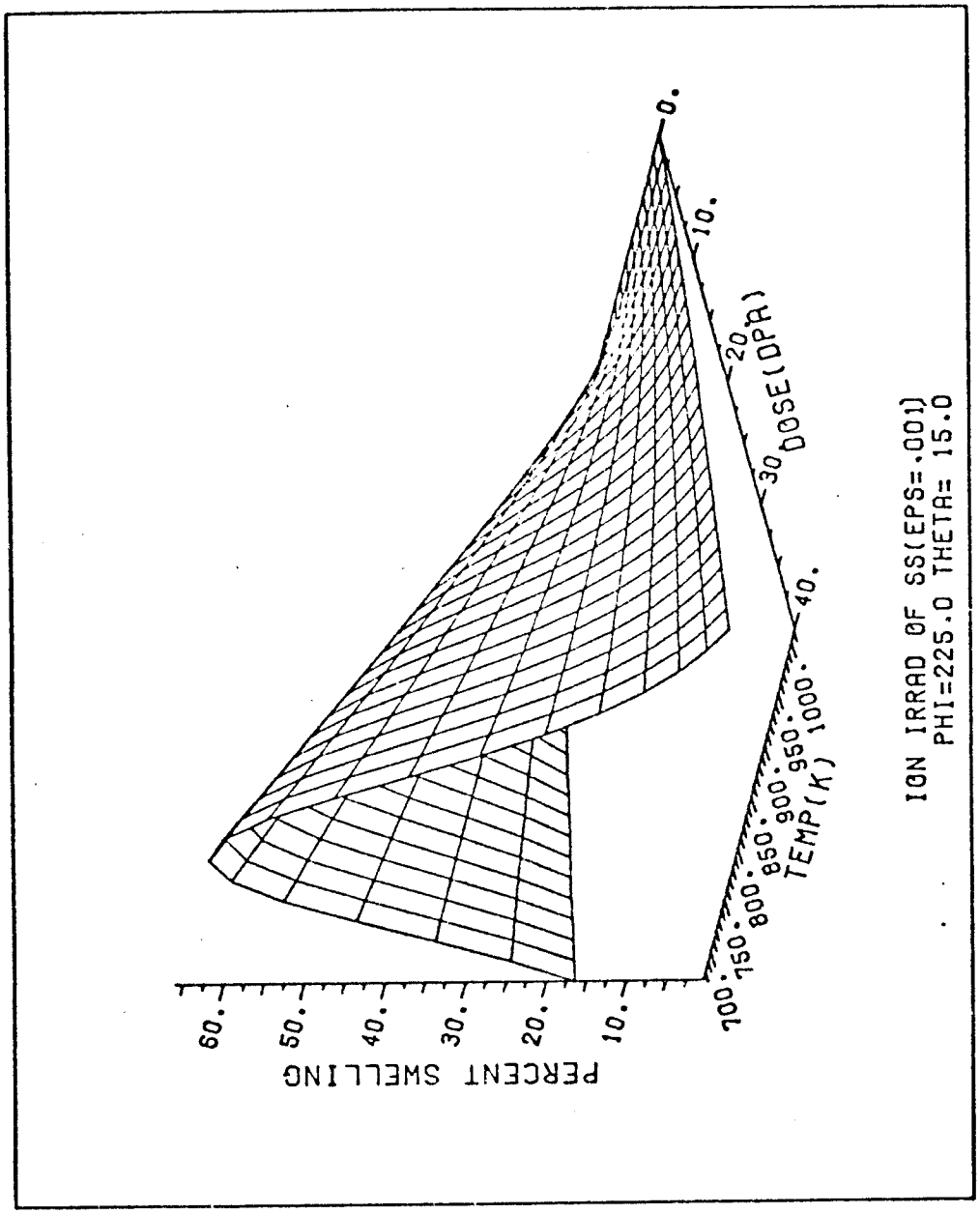

Fig. (6.5). 3-Dimensional plot of percent swelling as a function of dose and temp. for ion irradiated ST S.S. The dose rate is 10^{-3} dpa/sec and the cascade efficiency is 0.001.

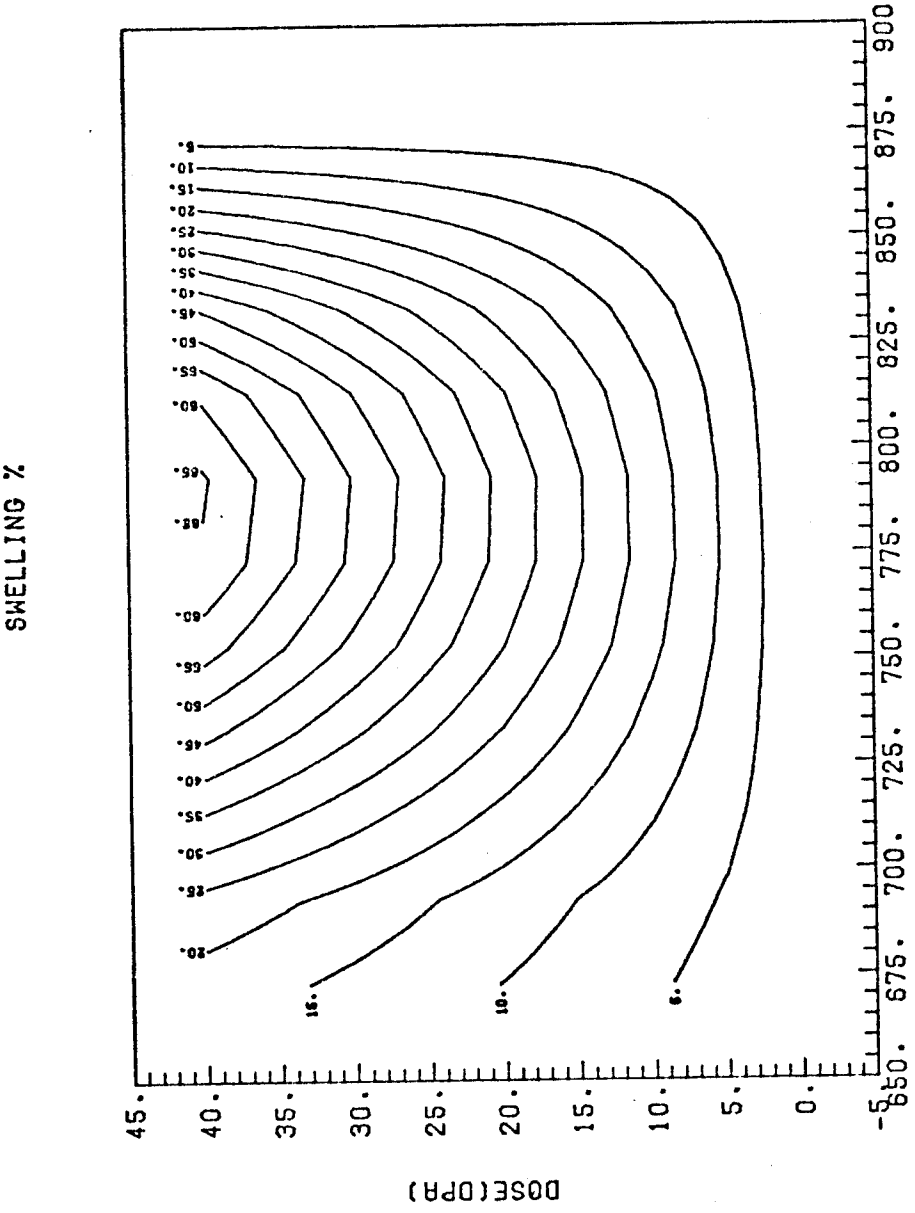

Fig. (6.6). Contour plot of percent swelling as a function of dose and temp. for ion irradiated ST S.S. The dose rate is 10^{-3} dpa/sec and the cascade efficiency is 0.001.

emphasis on versatility and the unique sides of the theory. The next chapter is devoted to some brief examples of the information available and the calibration of the theory against existing experimental data in different situations.

CHAPTER VII

GENERAL FEATURES AND CALIBRATION OF FDRT

The object of this chapter is two fold; first it is to illustrate some of the dynamic nature of the microstructural features in a metal, and secondly it is to demonstrate that TRANSWELL can accurately predict the experimentally measured amount of swelling in metals. The results of the first part of this chapter are meant to be illustrative in nature and more detail about the variables is given in Chapter XIII.

VII.A. Illustration of Typical TRANSWELL Outputs

In order to demonstrate the flexibility of the codes described in this work, we will examine the development of the microstructure in 316SS during steady-state electron and heavy ion bombardment. The main difference between the two types of radiation is the nature of the collision cascade; there essentially is no collision cascade for electron bombardment. Pulsed studies will be treated in Chapter IX.

VII. A.1. 1 MeV Electron Irradiations of M316 S.S.

Since collision cascades are not produced in electron irradiated metals, vacancy loop formation is not then expected and the cascade efficiency can be set equal to zero. In this case we have only four components of the vector $\vec{Y}$; Y(1), Y(2), Y(5) and Y(6).

The parameters for M316 steel (solution treated) listed

in Table 7.1 were adopted for these calculations [65]. To account for variable nucleation conditions, temperature dependent void and interstitial-loop concentrations were used. The temperature dependence of void concentration (eq. 7.1) is based on experimental observation[101] while the interstitial loop concentration (eq. 7.2) is a suitable fit between theory and experiment [65].

$$N_C = 6.5 \times 10^{8} \exp(1.0/kT) \tag{7.1}$$

$$N_{il} = 6.7 \times 10^{-3} \exp(2.8/kT) \tag{7.2}$$

The four equations for Y(1), Y(2), Y(5) and Y(6) are then solved numerically with the initial conditions

$$r_C(0) = 10 \text{ Å} \tag{7.3}$$

$$r_{i\ell}(0) = \sqrt{4r_C^3(0)N_C/3bN_{i\ell}}, \tag{7.4}$$

$$N_{v\ell}(0) = 0, \tag{7.5}$$

$$q_{v\ell}(0) = 0, \tag{7.6}$$

$$P_g(0) < 2\gamma/r_C(0). \tag{7.7}$$

The time dependent behavior of the vacancy and interstitial concentrations are shown in Figure (7.1). At irradiation times of the order of the first few microseconds, neither interstitials nor vacancies are mobile enough to migrate to neutral and biased sinks. Also their concentrations

TABLE (7.1)

SUMMARY OF MATERIALS CONSTANTS FOR 316 SS VOID GROWTH CALCULATIONS

Surface Energy, γ	$= 1.25 \times 10^{15}$ eV cm^{-2}
Vacancy formation Energy, E_f^v	= 1.6 eV
Vacancy migration Energy, E_m^v	= 1.3 eV
Interstitial formation Energy, E_i^f	= 4.0 eV
Interstitial migration Energy, E_i^m	= 0.2 eV
Vacancy diffusivity, D_v^o	$= 0.6$ cm^2 s^{-1}
$\frac{\text{recombination coefficient}}{\text{interstitial diffusion coefficient}}$, $\frac{\alpha}{D_i}$	$= 10^{16}$ cm^{-2}
stacking fault energy, γ_{sf}	$= 9.4 \times 10^{12}$ eV cm^{-2}
deformation produced dislocation density, ρ_d^o	$= 10^8$ cm^{-2}
Burgers vector, b	$= 2 \times 10^{-8}$ cm
dislocation bias for vacancies, Z_v	= 1.00
dislocation bias for interstitials, Z_i	= 1.08*
Effective modulus, $\mu' = \frac{\mu}{1-\nu}$	$= 4 \times 10^{11}$ dyne cm^{-2}

*The sensitivity of the calculations to the bias factor and correlation with experiments are explored later in this chapter.

will be so low that the mutual recombination is negligible. Under these conditions the rate of change of the concentration of vacancies and interstitials is almost equal to the production rate. In Figure (7.1) the initial slope of $C_i(t)$ and $C_v(t)$ is about 5×10^{-3} at/at/sec; the actual production rate. The build-up of the interstitial concentration coupled with their high mobility will cause the interstitial sink removal rate to be high after $\sim$10 microseconds. The concurrent build-up of the vacancy concentration also produces a high recombination rate. Consequently the total interstitial concentration passes through a maximum and then decreases in value as a function of time. As time progresses, the high vacancy concentration and the mobility of vacancies will produce a vacancy sink removal rate which increases with time. After a few vacancy mean lifetimes the vacancy concentration will decrease with time producing the broad maximum as shown in Figure (7.1).

The absolute defect removal rates are shown in Figure (7.2). As expected, the interstitial sink removal is high at short times ($\sim 10^{-5}$ seconds) while the recombination rates are low. The buildup of vacancy concentration causes the recombination rate to be dominant after $\sim 10^{-4}$ seconds. Eventually the buildup of the dislocation loop and void sinks causes the point defect removal rates to become dominant again after $\sim$100 seconds ($\sim$0.5 dpa). Note that in Figure (7.2) P_R is the point defect mutual recombination rate,

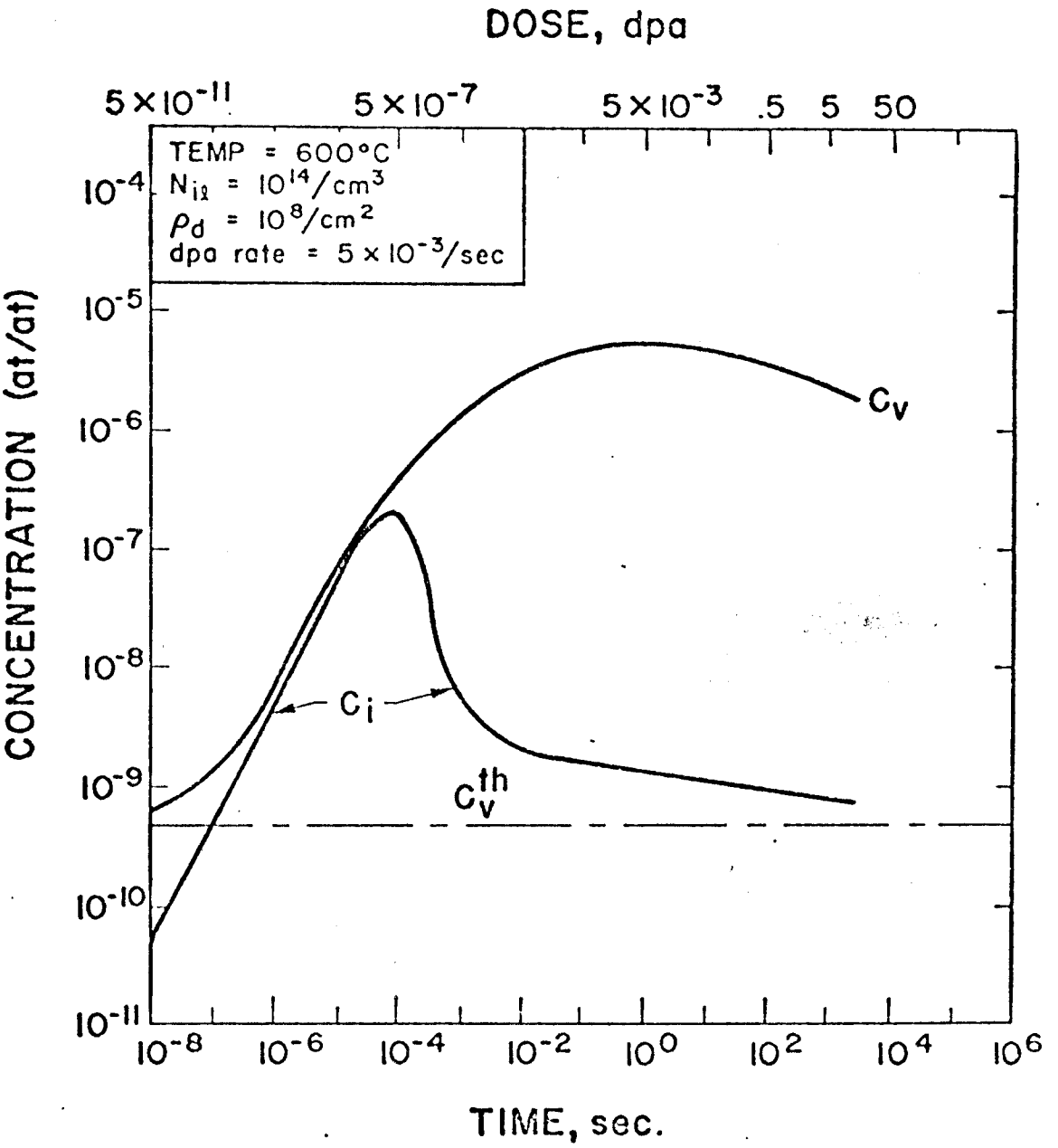

Point Defect Concentrations in electron irradiated M316 S.S. using the Fully Dynamic Rate Theory (FDRT)

Fig. (7.1)

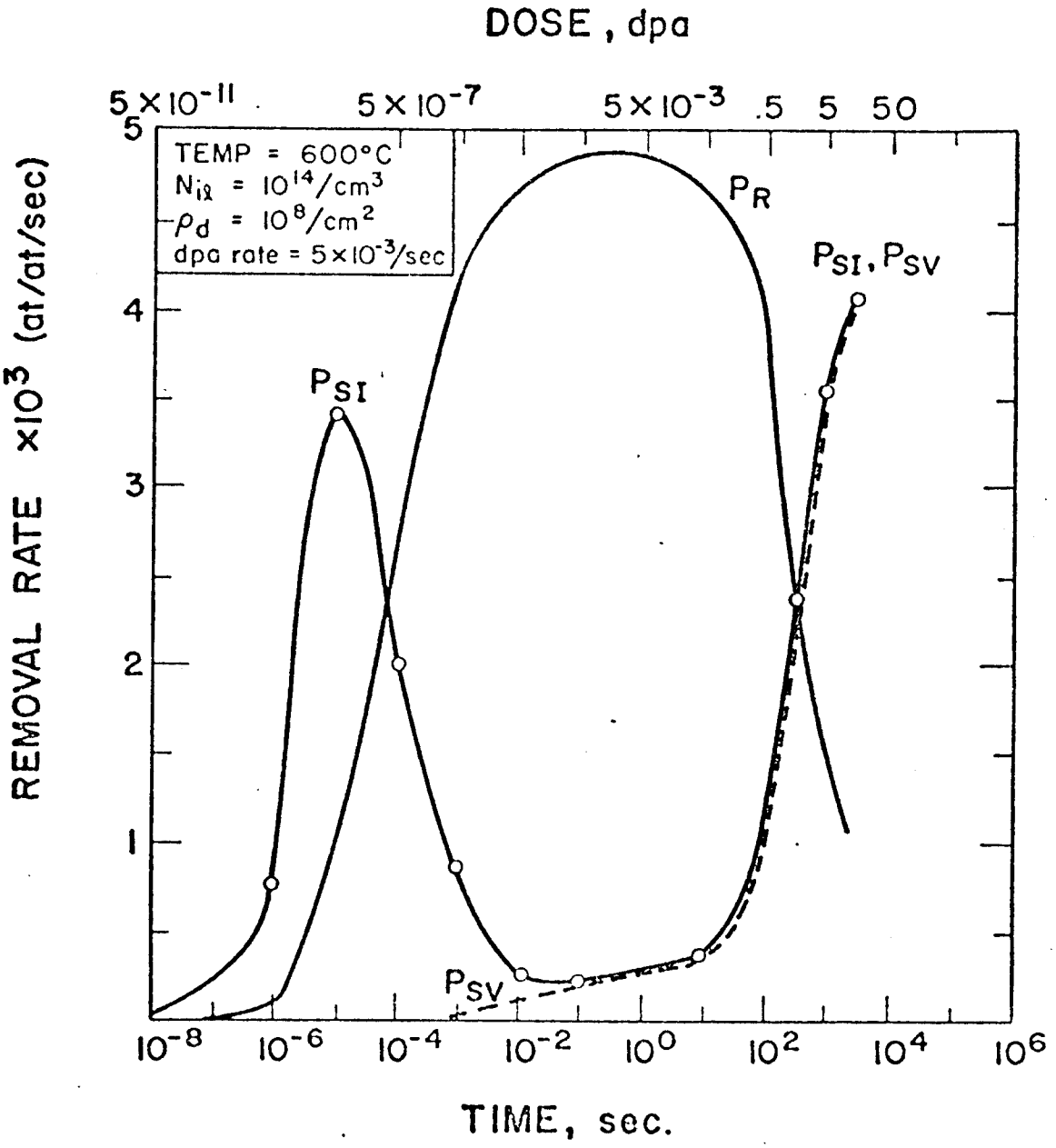

Removal Rates P_R, P_{SI}, P_{SV} in electron irradiated M316 S.S. using the Fully Dynamic Rate Theory (FDRT)

Fig. (7.2)

P_{SI} is the total sink removal rate for interstitials and P_{SV} is the total sink removal rate for vacancies in units of at/at/sec.

The significance of Figures (7.1) and (7.2) is that there is a complex time relation between point defect concentration rates and the dynamically changing microstructure. It is important to recognize the chronology of the defect structure development, because just concentrating on the end product at 10 or 100 dpa may yield an entirely different picture than during the early stages of irradiation. This is especially important for pulsed irradiation as we shall see later.

VII.A.2. 22 MeV C++ Ion Bombardment of M316 S.S.

Bombardment of metals with heavy ions will cause displacement spikes and collision cascades to collapse forming vacancy loops as described in Chapter IV. Therefore, we must take into account the 'loss' of free vacancies by signifying a fraction ε that is removed from the free defect production rate. We will use $\varepsilon = 0.044$ in the present example.

Void and interstitial loop concentrations at the end of the nucleation phase and the start of the growth phase were taken as

$$N_C = 3.15 \times 10^{11} \exp(0.625/kT) \qquad (7.8)$$

$$N_{il} = 1.34 \times 10^{-4} \exp(2.8/kT) \qquad (7.9)$$

The dose dependence of the average void and interstitial loop radii for 22 MeV C++ ion irradiated S.S., as predicted

by TRANSWELL, is shown in Figure (7.3). The irradiation temperatures are 450°C and 600°C. It is found that the close dependence of the void and loop radii is not strong at low temperatures because of the high recombination rate. Therefore, a smaller fraction of point defects will migrate to sinks to cause swelling and loop growth.

The higher temperature irradiation is characterized by low nucleation densities (eq. (7.5) and (7.9)) and large growth rates of voids and interstitial loops, hence higher swelling values. Shortly after the incubation dose, the average void radius starts to increase rapidly. However, as irradiation proceeds, the void (neutral) sink strength increases which renders the dislocation density somewhat less effective in removing point defects. The impact of the growing void sink strength then is to decrease the average void radius growth rate as a function of dose. It is also observed that the average interstitial loop growth follows that of the average void growth. One would expect this behavior because excess vacancies migrate to voids while excess interstitials migrate to interstitial dislocation loops.

Vacancy dislocation loops can significantly reduce the swelling during neutron or heavy ion irradiations. Their effect is to reduce the total production rate of free vacancies and to act as an additional biased sink for interstitials. Initially the number of vacancy loops increase linearly with time (Figure 7.4). The slope is temperature

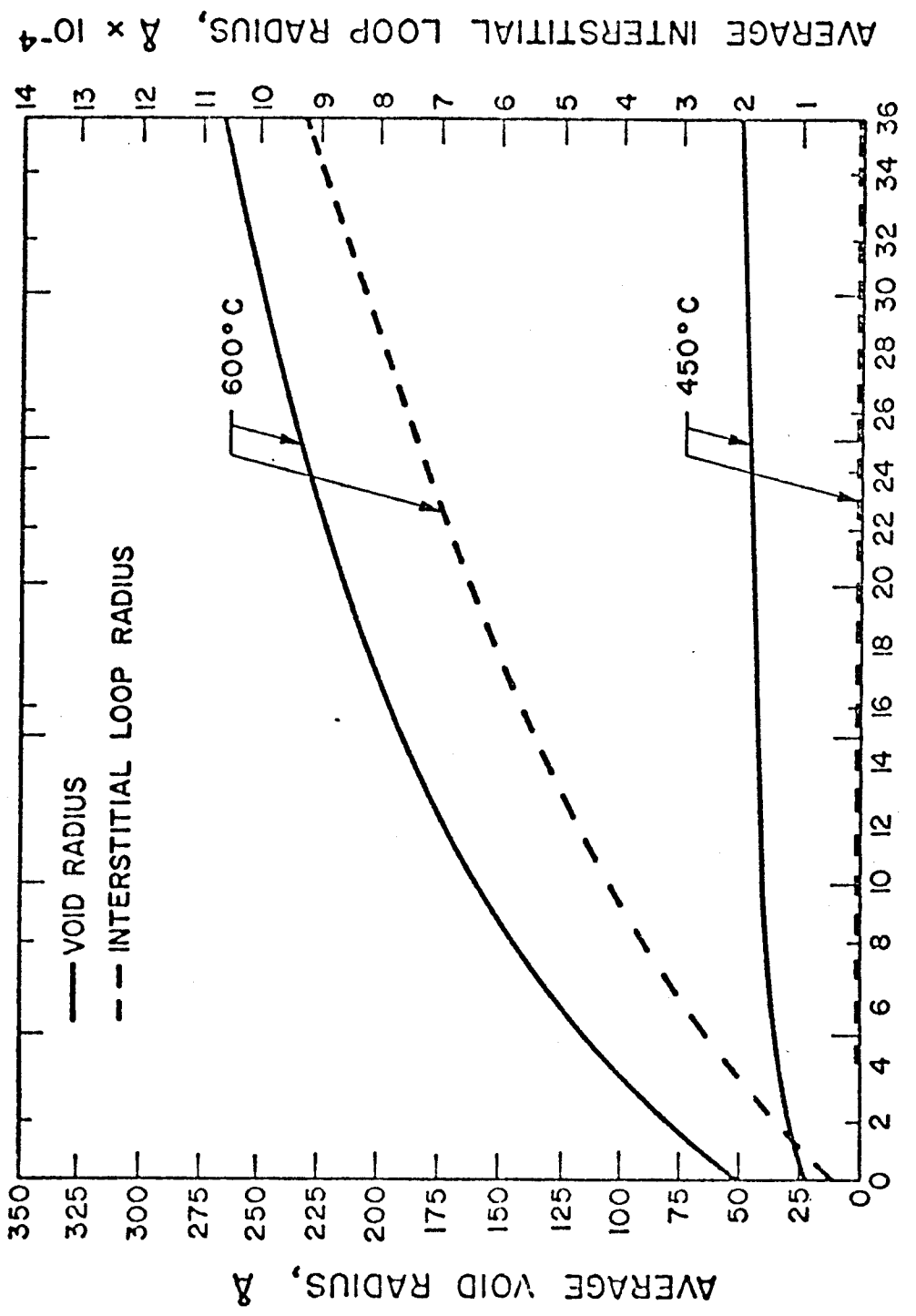

Fig. (7.3) THE PREDICTED DOSE DEPENDENCE OF THE AVERAGE VOID AND INTERSTITIAL LOOP RADII FOR 22 MeV C^{++} IRRADIATED S.S. dpa rate = 10 dpa/sec

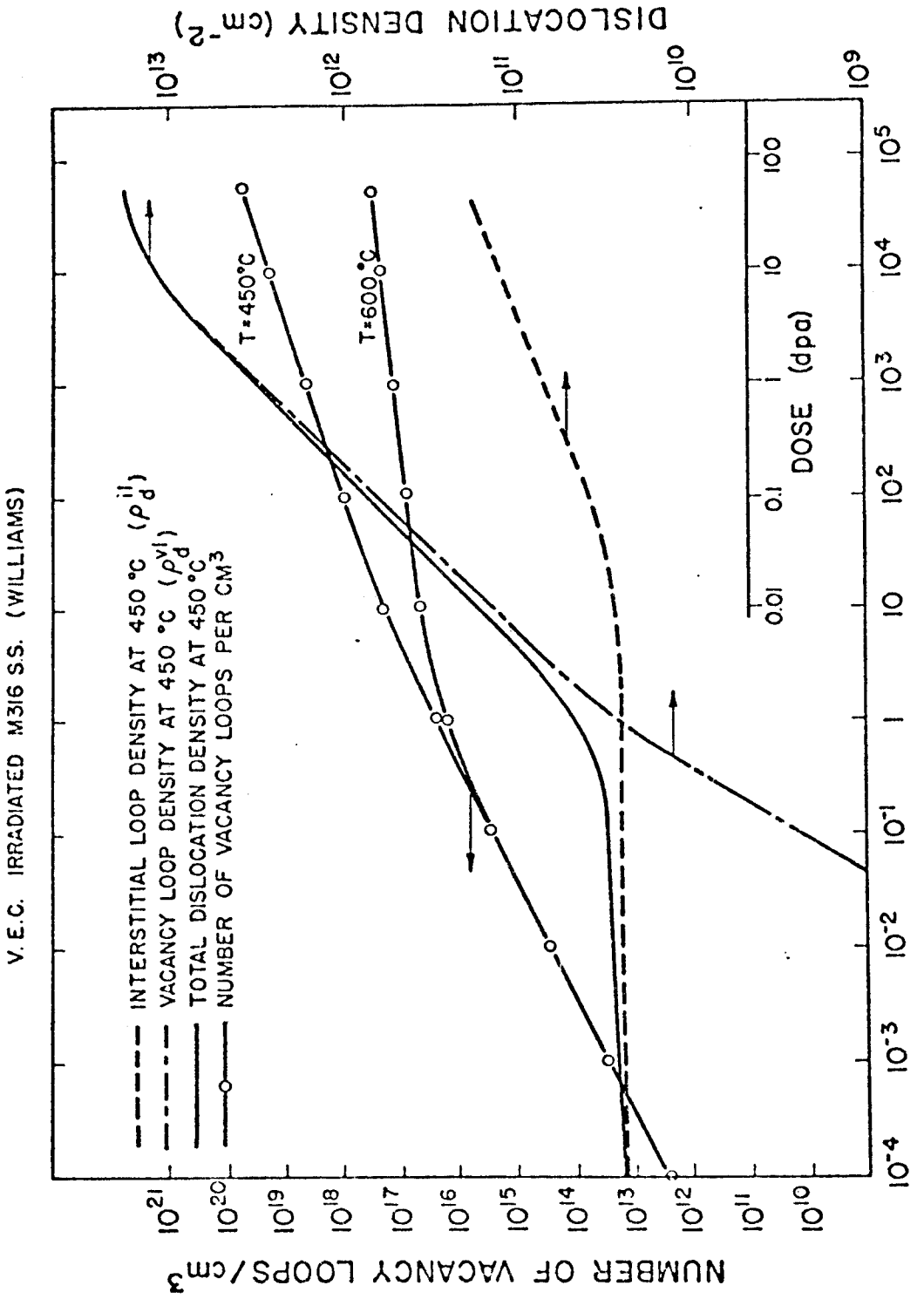

Fig. (7.4) THE DOSE DEPENDENCE OF DISLOCATION DENSITY AND VACANCY LOOP CONCENTRATION FOR 22 MeV C^{++} IRRADIATED S.S. dpa RATE = 10^{-3} dpa/sec

independent since the fraction of vacancies retained in vacancy loops was assumed to be temperature independent. However, the vacancy emission rates are both temperature and time dependent and eventually an approach to an equilibrium value is reached.

The results shown here in Figure (7.4) agree with the theoretical values of Bullough, et al.[65]. The only discrepancy is at short periods of times which is probably due to the transient conditions treated here versus quasi-steady state approximation used in their work. However, this graph shows the necessity to include recovery of dislocations as a part of the mathematical simulation because at low temperatures and high doses the dislocation densities approach an unrealistic level of 10^{12} to 10^{13} cm^{-2}.

A final comment about Figure (7.4) is that the dislocation sink at 450°C is dominated by the interstitial loops only at short times ($\sim$0.1 to 1 seconds or a dose of 10^{-3}dpa). The vacancy loops quickly become the major dislocation sink and continue in that role to higher damage levels. This curve illustrates the high sensitivity of the sink sturcture to the concept of cascade collapse and direct formation of vacancy loops.

VII.B. Calibration of the Rate Theory

Even though the qualitative features of the microstructural development during irradiation can be described by TRANSWELL, it is important to establish a quantitiative

relationship. Therefore, we will now try to match the experimental measurements of void and dislocation parameters with those predicted by TRANSWELL.

VII.B.1. Philosophy

Before examining the experimental data to be simulated and the actual simulation itself, it is worthwhile to state the philosophical approach taken here. It is certainly recognized that any successful theoretical model depends on a rather specific set of boundary conditions. In the case of the Brailsford and Bullough rate theory model, two of the most significant boundary conditions are:
(1) that nucleation of new voids and interstitial loops has ceased and the existing microstructure is merely in a state of growth (one important exception to this statement is the fact that vacancy loops are continually being formed and dissolving [65]); (2) all of the sinks are homogeneously distributed in the metal. The latter assumption is easy to justify when the defect density and dpa rates are high [71].

With these two conditions in mind, we proceed to select some data from the open literature on three metals (316 SS, Al and Ni) irradiated with neutrons, heavy ions and electrons. Even though there are a large number of studies on these materials (especially 316 SS) very few experimentalists measure and report all the data required to allow a reasonable comparison between theoretical models and the observed behavior. At a minimum, a successful growth model would

require the following input — the saturation interstitial dislocation loop and void density, dpa rate, temperature, something about the displacement spike efficiency (e.g., single atom displacements by electrons vs. large cascade spikes from neutron and heavy ions) and the appropriate material defect parameters.

Two other assumptions were used in the simulation study: (1) The dose used in the simulation study corresponds to an actual dose measured after the incubation period for voids, (2) to separate nucleation from growth effects, we assume that after nucleation had ceased, the irradiation was turned off, and the solid returns to thermal equilibrium. Then irradiation was turned on again to study the growth aspect of swelling. With this information, two of the main outputs from the model are the growth rates of voids and dislocation loops. The resultant swelling is easily calculated from the void density. Unfortunately, even though the TRANSWELL code will predict the above parameters, as well as many more, there is very little experimental data in the literature which correlates both the dislocation loop and void parameters as a function of temperature, dpa rate and total damage level. We have attempted to find such data in the literature and use it for our calibration; however, where such data is unavailable, we had to supplement the experimental results with information from other studies or with an emperical fit to existing data.

It is also important to understand what happens during

the transient stages when the irradiation is turned off, or on again. The buildup and decay of the vacancy and interstitial concentrations as well as the behavior of voids and loops between irradiation "pulses" can lend some understanding as to the ultimate response of the material. One of the crucial concepts in the application of FDRT to pulsed irradiation is that we allow voids to anneal out in between pulses when there is no damage produced. As part of the calibration procedure we have included a comparison between predicted and experimentally observed void annealing behavior.

VII.B.2. Sources of Data

The TRANSWELL Computer Code is designed primarily for dealing with metals under pulsed or transient irradiations. The Fully Dynamic Rate Theory (FDRT), as it stands now, is a combination of ideas, some of which are directly supported experimentally while others are still not. A few pulsed experiments have been performed to date (6-11) under a restricted set of conditions. Because the problem is so complex, it is difficult to assess pulsed experiments without investigating the constituents of FDRT independently. Therefore, we must rely on steady-state information.

In this section we will briefly present some experimental data on voids in metals which will be used to "calibrate" the FDRT and draw conclusions on the applicability of the theory as used in TRANSWELL. Experiments analyzed and presented here fall under two broad categories:

(1) Experiments to determine metal swelling under steady irradiation conditions. They include Fast Fission Reactor Irradiations and Simulation Experiments involving electron irradiation in high voltage electron microscope (HVEM) and irradiation with heavy ions or light particles using accelerators.

(2) Experiments to determine void annealing behavior. The first category of experiments will be invaluable in understanding microstructural changes during irradiation pulses, while the second will be important to assess void kinetics in between pulses.

A carefully chosen set of data is presented here and the application of the FDRT to explain the results is investigated in the next section.

VII.B.3. Steady-State Irradiation Experiments

VII.B.3.a. Solution Treated 316 S.S.

VII.B.3.a.i. Ion Irradiation

Williams[102] investigated the temperature dependence of void swelling in Type 316 austenitic stainless steel irradiated with carbon ions. Foils of Type 316 stainless steel containing 10 appm helium have been irradiated to a dose of 3×10^{17} ion/cm^2 at temperatures in the range of 400°-700°C using 20 MeV C^{++} ions from the Harwell Variable Energy Cyclotron. This ion dose produced an estimated maximum of 40 displacements/atom at 6.6 μm below the ion-incident surface. The void volume at each temperature was determined by

transmission electron microscopy. In solution treated Type 316 steel, the void swelling reached a maximum of 12% at 600°C for a dose of 40 displacements/atoms.

The void diameters and concentrations measured at a depth of 6.6 μm and therefore corresponding to a damage concentration of 40 displacements per atom are listed in Table (7.2) as a function of irradiation temperature. These are average values, as there was some variation not only between equivalent specimens, but also within a given specimen.

In all the computer simulations studied we assumed the following:

a. A simple temperature dependent nucleation relationship for the number densities of voids and interstitial loops at saturation is of the form:

$$N_C^s = N_C^o \exp \{E_C(eV)/kT\} \quad (7.10)$$

$$N_{i\ell}^s = N_{i\ell}^o \exp \{E_{i\ell}(eV)/kT\} \quad (7.11)$$

where N_C^o, $N_{i\ell}^o$, E_C and $E_{i\ell}$ are experimentally determined or computer fitted quantities.

b. Initial "free growth" void radius defined as that radius at which a void can freely grow at a certain temperature without the assistance of internal gas pressure.

c. Initial vacancy loop radius determined by the number of vacancies in a collison cascade (about 15 Å).

d. A dislocation interstitial bias factor (Z_i) adjusted to fit the metal's swelling behavior under all conditions.

Experimentally measured void concentrations as a function

TABLE (7.2)

Void sizes and densities in 20% cold worked and in 1050°C solution treated Type 316 steel resulting from a dose of 40 displacements per atom after prior implantation with 10^{-5} helium atoms per atom. (102)

Irradiation Temperature (°C)	Material Condition	Maximum Void Diameter (Å)	Minimum Void Diameter (Å)	Mean Void Diameter (Å)	Voids per cm^3
400	ST	∿50	∿30	50	*
	CW	∿50	∿30	40	*
450	ST	135	∿30	85	1.1×10^{16}
	CW	∿70	∿30	∿50	*
500	ST	300	65	210	3.0×10^{15}
	CW	310	80	180	4.2×10^{15}
550	ST	680	150	460	1.4×10^{15}
	CW	650	90	375	1.1×10^{15}
600	ST	800	200	490	1.4×10^{15}
	CW	680	100	385	1.0×10^{15}
650	ST	1100	170	710	4.2×10^{14}
	CW	1100	250	700	3.2×10^{14}
700	ST	1200	270	760	3.2×10^{14}
	CW	1200	300	800	2.8×10^{14}

*Insufficient voids resolved to make a realistic estimate.

of temperature were fitted to expression (7.8) while the interstitial loop number densities were generated from expression (7.9) given earlier in this chapter. Material parameters from Table (7.1) for stainless steel were used, with the following initial conditions.

initial void radius = 40 Å

initial vacancy loop radius = 15 Å

number of gas atoms in a void = 100

cascade efficiency [65] = 0.044

bias factor [65] = 1.08

*

The initial interstitial loop radius is calculated from the condition:

number of vacancies in visible defect clusters = number of interstitials in visible defect clusters

$$3.15\times10^{11}\exp[0.625/kT]\cdot\frac{4}{3}\pi r_c^3(0) = 1.34\times10^{-4}\exp[2.8/kT]\cdot\pi r_{i\ell o}^2 b \qquad (7.12)$$

where,

$r_c(0)$ = initial void radius

$r_{i\ell o}$ = initial interstitial loop radius

The temperature dependent swelling of ST 316 SS is compared with experiment in Figure (7.5). Notice that the computer results tend to be lower than experimentally measured

*The calibration is not dependent on the individual values of ϵ or Z_i but rather the combination of these values. For example, Z_i = 1.025 and ϵ = 1.2% would give roughly the same results (see Appendix B).

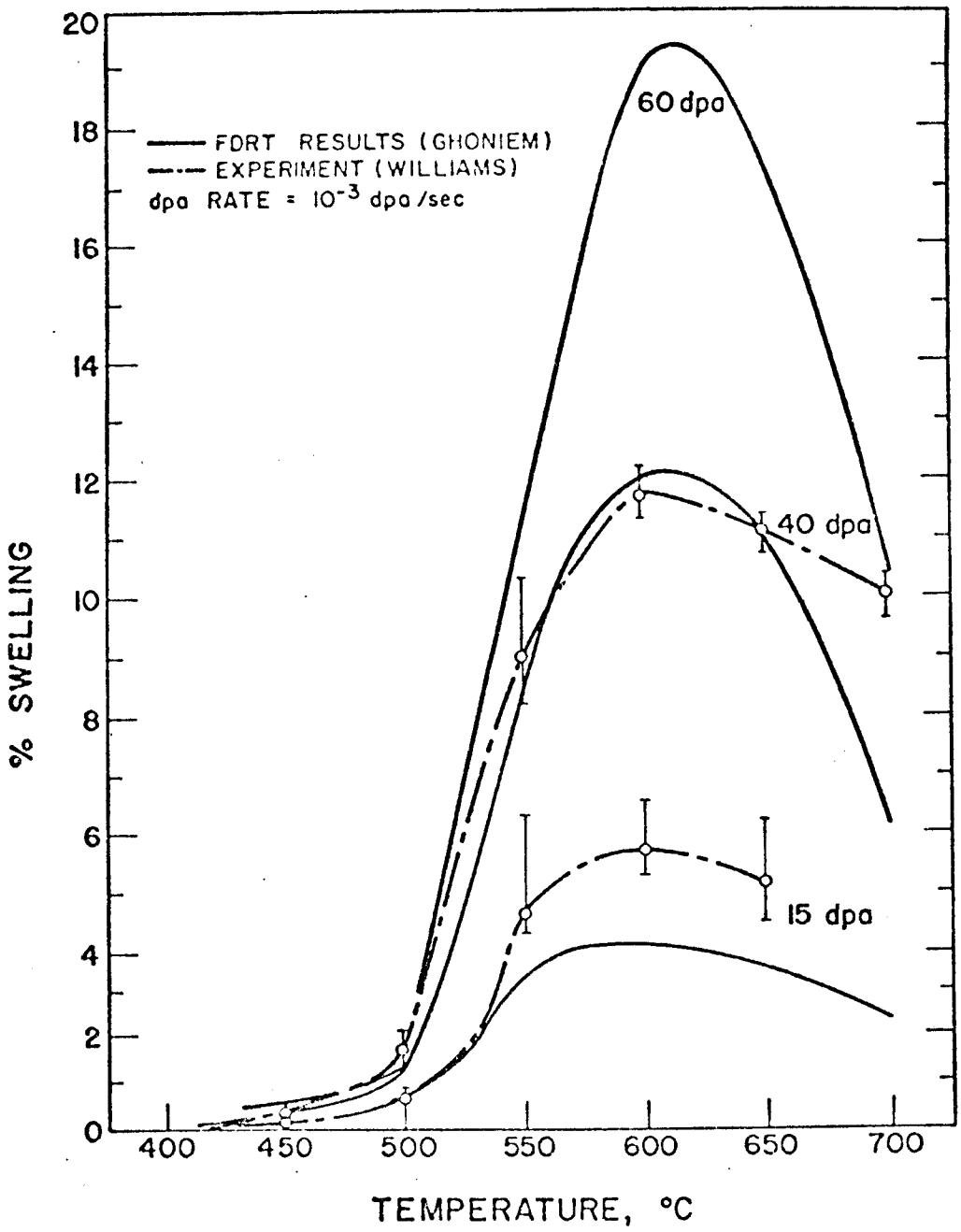

COMPARISON BETWEEN THE FULLY DYNAMIC RATE THEORY (FDRT) AND EXPERIMENTAL RESULTS FROM T.M. WILLIAMS (AERE HARWELL). THE TEMPERATURE DEPENDENCE OF VOID SWELLING IN M316 S.S. IRRADIATED WITH 22 MeV C^{++} IONS.

Fig. (7.5)

COMPARISON BETWEEN THE FULLY DYNAMIC RATE THEORY (FDRT) AND EXPERIMENTAL RESULTS FROM T.M. WILLIAMS (AERE HARWELL). THE TEMPERATURE DEPENDENCE OF VOID DIAMETER AS A FUNCTION OF TEMPERATURE AT 40 dpa IN SOLUTION TREATED M316 S.S. IRRADIATED WITH 22 MeV C^{++} IONS.

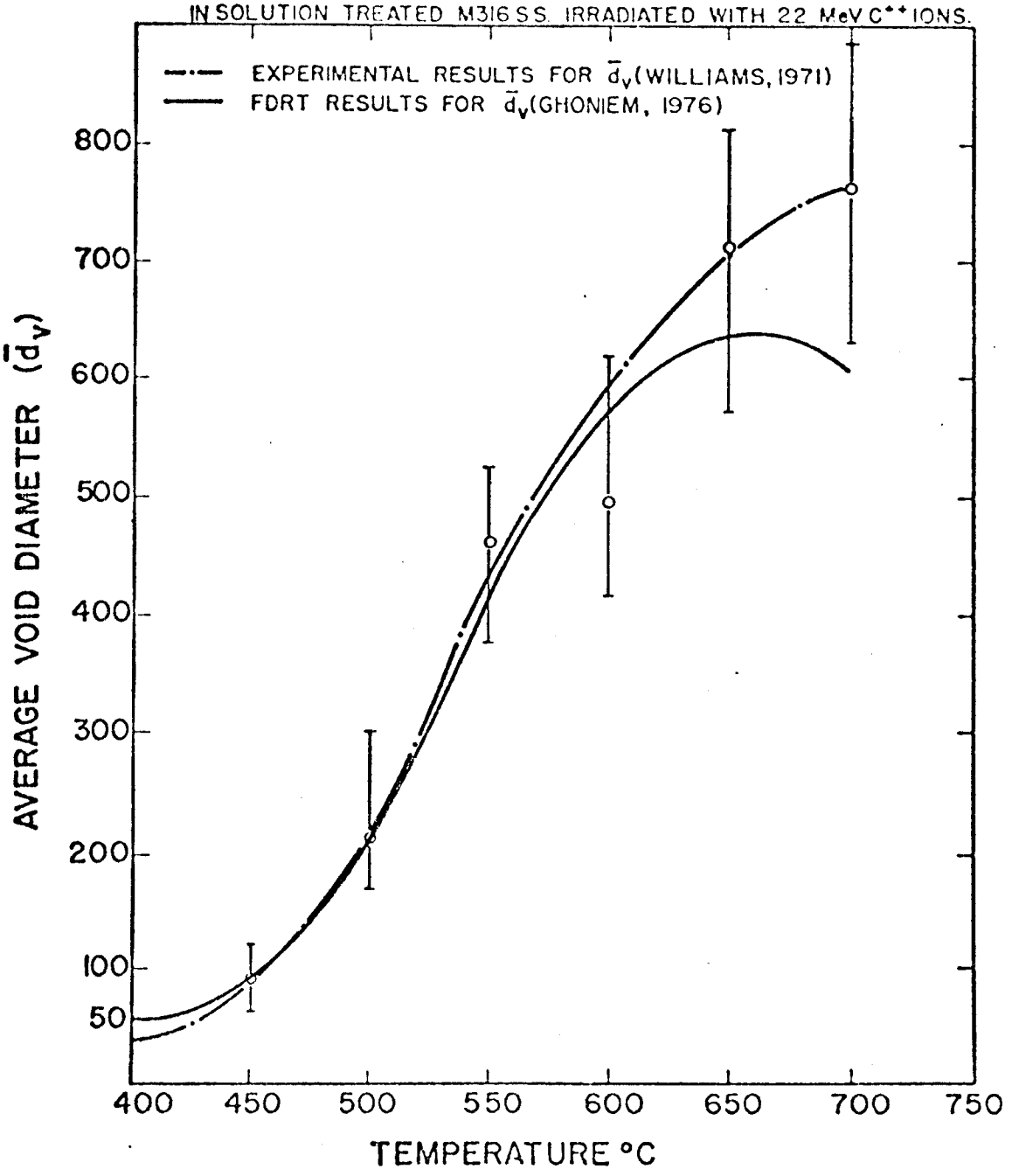

Fig. (7.6)

swelling at high temperatures. This is due to the fact that voids, starting with a small initial void radius, tend to shrink faster at high temperatures. This behavior at high temperature will be discussed in Appendix B. A comparison between computer simulations and experimentally measured void diameter as a function of temperature is shown in Figure (7.6) and it reveals that the agreement between TRANSWELL and the data is quite good.

VII.B.3.a.ii. Electron Irradiation

Makin and Walters[101] studied the effect of void density and carbon concentration on the swelling of type 316 austenitic steel irradiated in the HVEM. It is shown that the presence of carbon has the effect of reducing swelling of stainless steel. The particular results we will refer to later are those for low carbon concentration, $\sim$0.04%.

Experimentally measured void concentrations as a function of temperature were, in this study, fitted to expression (7.1), while interstitial loop number densities were calculated from expression (7.2).

Initial conditions were assumed as

initial void radius = 40 Å

number of gas atoms in a void = 0 (no doping)

cascade efficiency = 0

while initial interstitial loop radius was calculated as in the previous section.

The temperature dependence of the swelling of ST 316

stainless steel under electron irradiation is compared with experiment in Figure (7.7), while the temperature dependence of the mean void diameter is compared with experiment in Figure (7.8). The agreement in these figures is quite good but it must be emphasized that the results are sensitive to the value of Z_i used. Changing the bias factor from 1.08 to 1.02 would drop the swelling at 500°C and 30 dpa by a factor of 4. (See Appendix A).

VII.B.3.b. Aluminum Irradiation

VII.B.3.b.i. Neutron Irradiation

Packan [103] conducted neutron experiments on pure aluminum in HFIR irradiation environment. Void formation in high purity aluminum resulting from irradiation to fluences between 1.5×10^{19} and 1.6×10^{22} neutrons/cm^2 (E>0.1 MeV) at a temperature of 55 $\pm$ 5°C was studied, primarily by means of transmission electron microscopy. Void size distribution curves were obtained for all fluences, and from these the mean void radius was found to increase in proportion to the irradiation time raised to the one-sixth power. The void concentration displayed a fluence dependence best described by a power law, $N_v \sim (\phi t)^{\alpha}$, in which the exponent decreased from 2.0 at 10^{19} neutrons/cm^2 down to only 0.1 at 10^{22} neutrons/cm^2. Treating the swelling with an analogous power relation, $\Delta V/V_o \sim (\phi t)^b$, a similar saturation effect was observed, with the fluence component b decreasing roughly from $\frac{5}{2}$ to $\frac{1}{2}$ over the range of fluence studied.

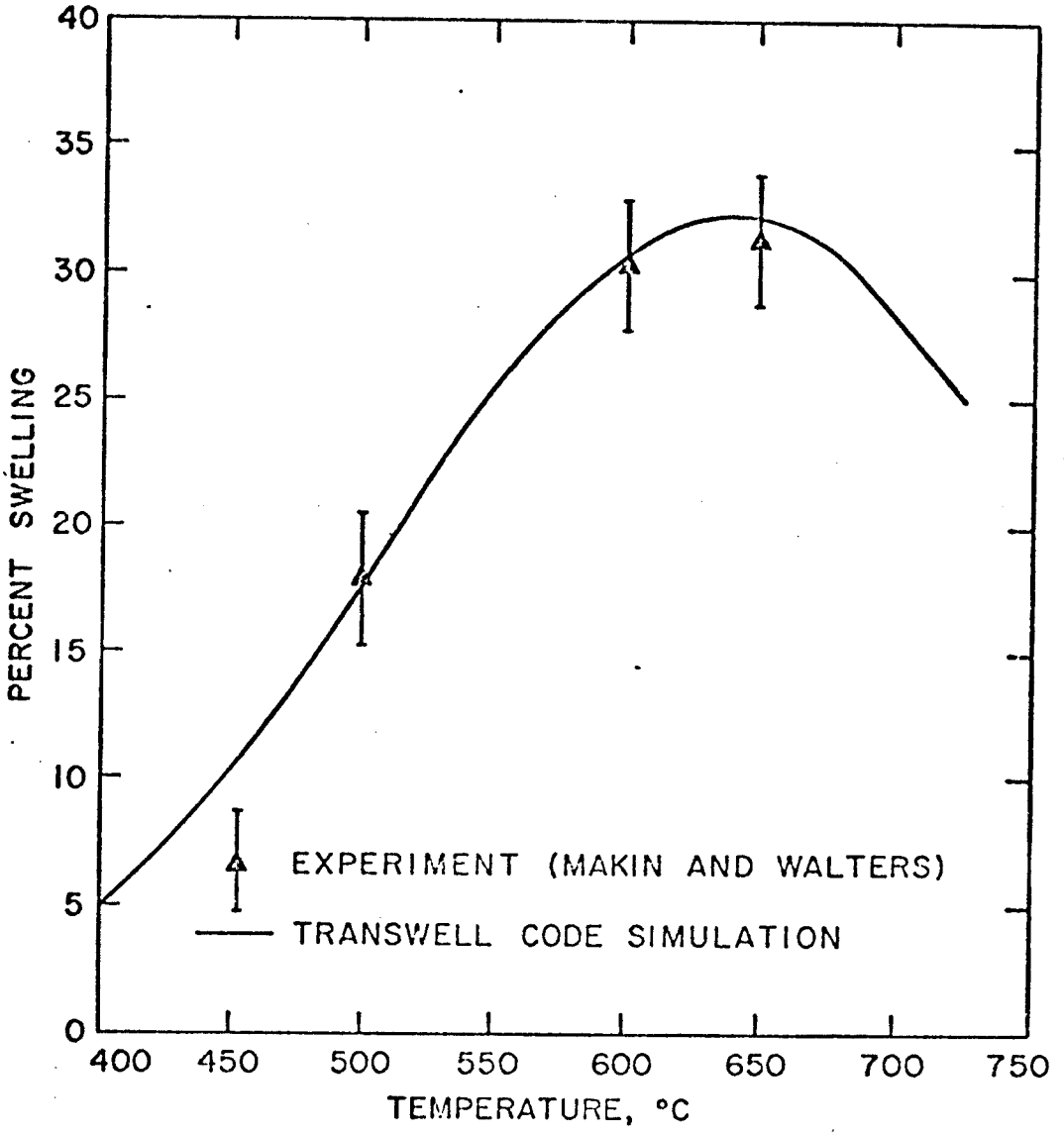

THE TEMPERATURE DEPENDENCE OF SWELLING IN ELECTRON IRRADIATED ST 316SS AT 30dpa AND A DOSE RATE OF 5×10^{-3} dpa/sec.

Fig. (7.7)

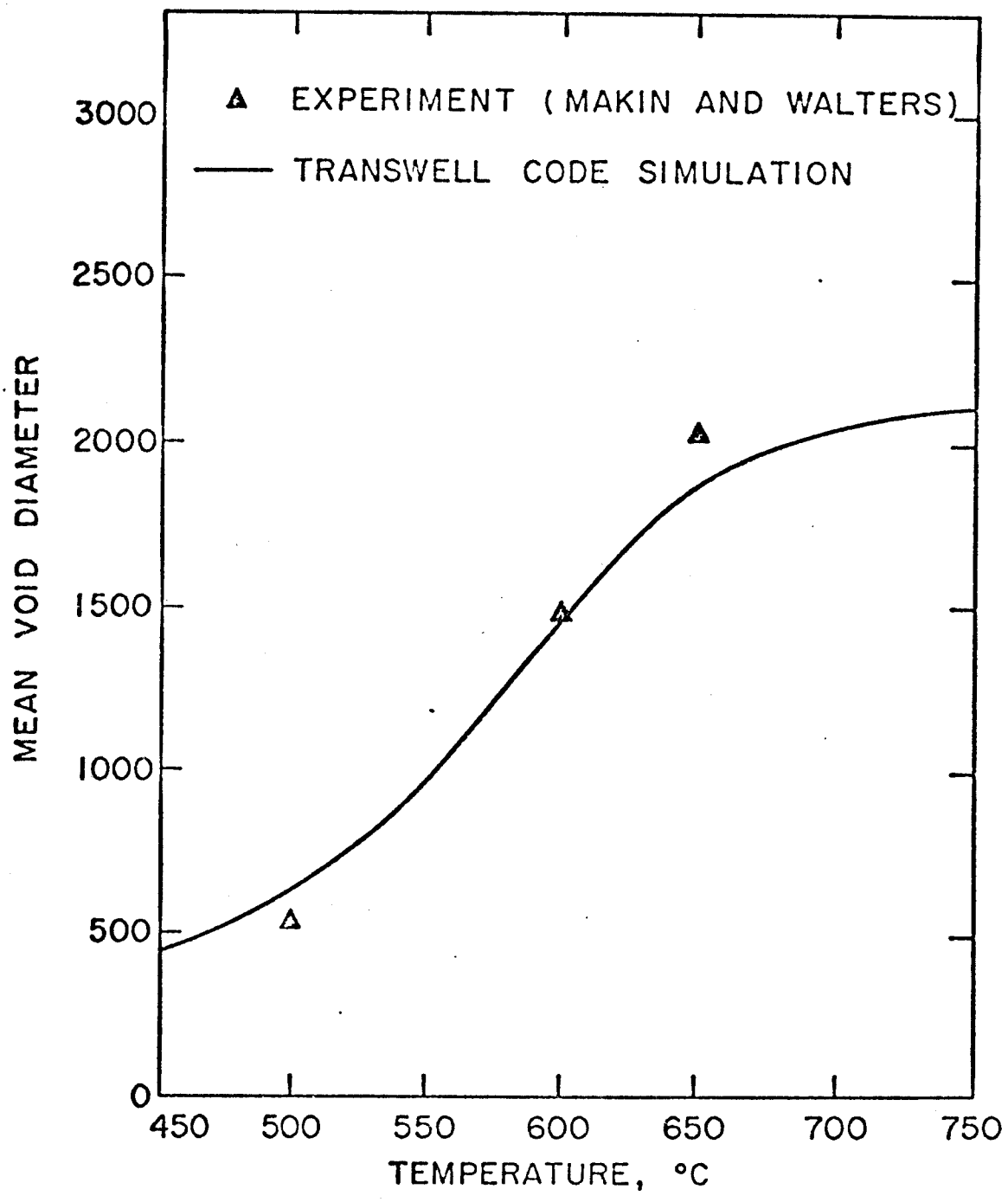

THE TEMPERATURE DEPENDENCE OF MEAN VOID DIAMETER IN ELECTRON IRRADIATED ST 316SS AT 30dpa AND A DOSE RATE OF 5×10^{-3} dpa/sec.

Fig. (7.8)

Experimental results of Packan's work are shown in Table (7.3). Calculations of displacements per atom were made using HFIR fluxes [104] and Doran's [105] displacement cross sections with a threshold displacement energy of 16 eV for Al [106]. A value of 1.3 dpa was found to correspond to a fluence of 10^{21} n/cm^2/sec of neutrons with energy greater than 0.1 MeV.

The displacement rate was found to vary between 9.88×10^{-7} and 1.547×10^{-6} dpa/sec. Therefore, an average value of 1.3×10^{-6} dpa/sec was used in the calculations. Experiments on neutron irradiated aluminum [107,108] indicated that the saturation void number density could be fitted to a simple expression as:

$$N_c^s = 2.8 \times 10^6 \exp\{0.55(eV)/kT\} \text{voids/cm}^3 \qquad (7.13)$$

which yields a value of $\sim 8 \times 10^{14}$ voids/cm^3 for aluminum at 55°C.

The following parameters were used in our TRANSWELL calculations:

number of density of interstitial loops at saturation	$= 10^{14}$ cm^{-3}
initial deformation produced dislocation density	$= 10^9$ lines/cm^2
initial number of gas atoms in a void	= 50
gas production rate	$= 3 \times 10^{-12}$ at/at/sec
cascade efficiency (ε)	$= 10^{-3}$

TABLE (7.3)

PERTINENT DATA ON IRRADIATION EFFECTS IN HIGH PURITY ALUMINUM [103] AT 55°C

Fluence ($neutrons/cm^2$ E>0.1 MeV)	Void max. size (Å)	Void mean size (Å)	Number of voids/ cm^3	Calc.total void vol. (%)	Number of loops/ cm^3
$1.5x10^{19}$	238	161	$\sim 1x10^{12}$	--	$2x10^{13}$
$7.7x10^{19}$	320	201	$2.1x10^{13}$	0.01	$8x10^{13}$
$1.6x10^{20}$	401	244	$3.8x10^{13}$	0.03	$1x10^{11}$
$5.2x10^{20}$	583	299	$1.1x10^{14}$	0.19	$3x10^{14}$
$1.6x10^{21}$	712	329	$3.9x10^{14}$	0.86	$\sim 2x10^{14}$
$1.6x10^{22}$	1020	495	$5.9x10^{14}$	7.4	--
$1.3x10^{20}$ (low flux)	609	323	$1.9x10^{13}$	0.04	$5x10^{13}$
$5.3x10^{20}$ (degassed material)	532	279	$1.0x10^{14}$	0.15	--

A dislocation loop-interstitial bias factor (Z_i) of 1.015 was found to fit very well both neutron irradiations and ion irradiations of aluminum and therefore, was used in these calculations.

Figure (7.9) shows the comparison between Packan's experiment and TRANSWELL calculations. Figure (7.10) shows the agreement between measured void sizes and computer calculated values if one starts with an observable void size (e.g., a radius of 100 Å). The agreement is shown to be still good even if the starting void radius is very small (e.g., 10 Å) indicating that the somewhat arbitrary choice of a free growth radius is not too restrictive in TRANSWELL.

VII.B.3.b.ii. Ion Irradiation

Irradiation of aluminum with 400 keV Al ions was carried out using the Harwell 500 KV Cockroft-Walton accelerator (Mazey [109]). The temperature-dependence of void swelling was investigated in non-helium doped 1100 grade aluminum by 400 keV Al^+ irradiation to 1×10^{17} ions/cm^2 at temperatures of 75, 100, 150, 200 and 250°C.

The dose-dependence of swelling was investigated at four dose levels in non-doped 1100 grade aluminum by irradiation with 400 keV Al^+ at 75°C. Details of void concentration and size and associated swelling are shown in Table (7.4).

The same set of material parameters used in neturon irradiated aluminum calculations (Table (6.1)) were used in ion irradiations of aluminum with experimental conditions

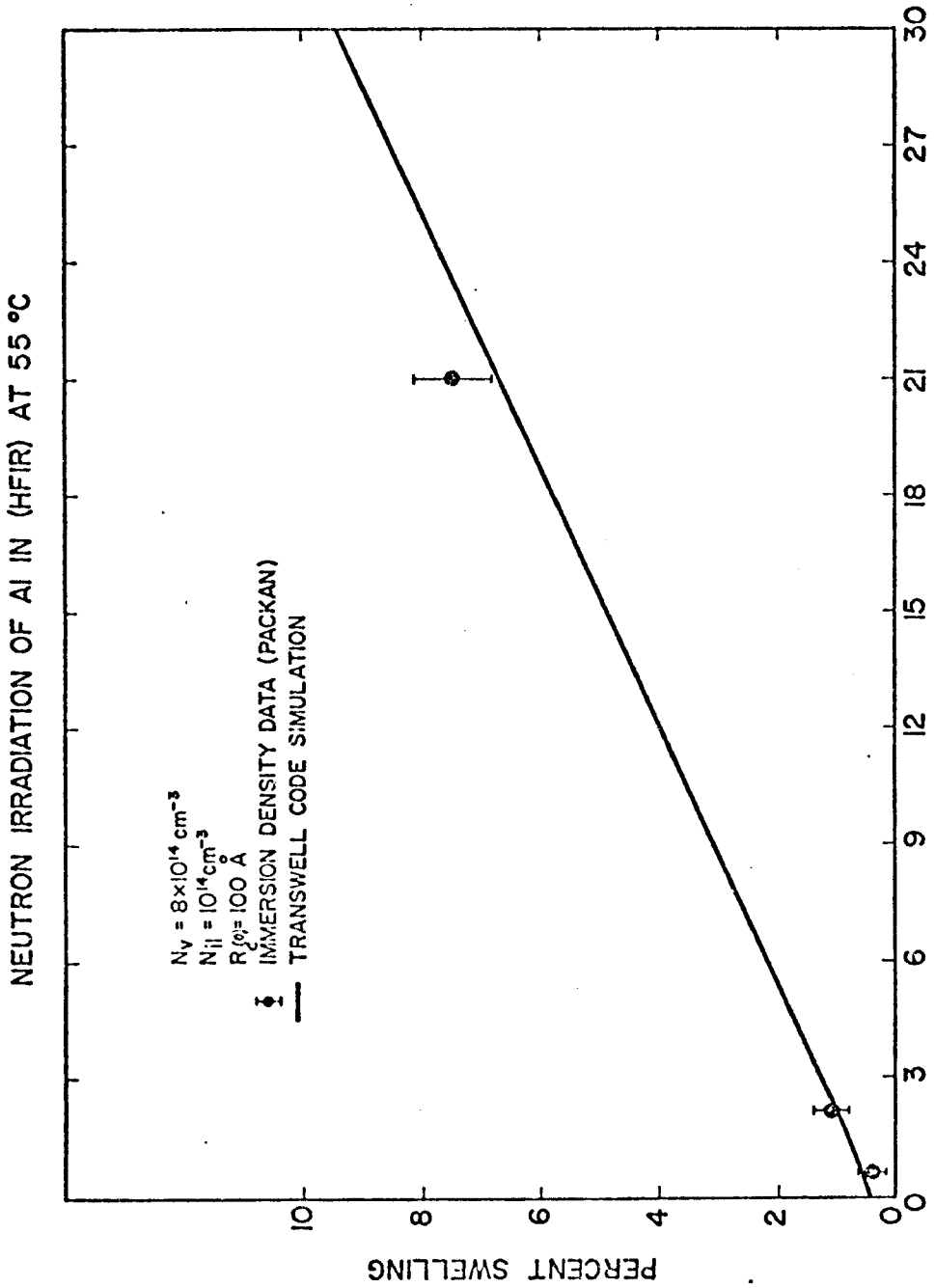

Fig. (7.9) Comparison between measured swelling of aluminum under neutron irradiation and theoretical predictions using TRANSWELL.

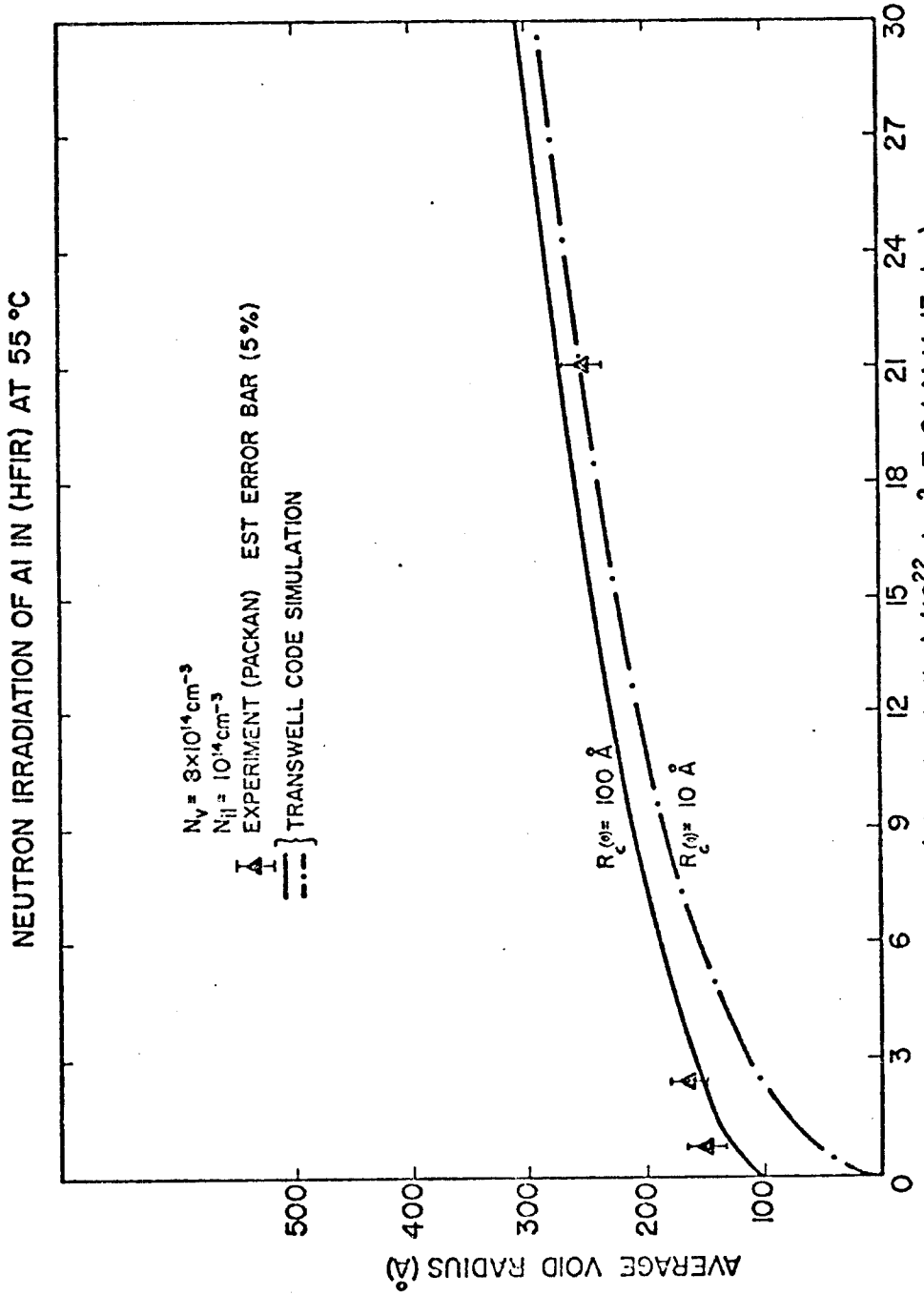

Fig. (7.10) Comparison between measured mean void radius of aluminum under neutron irradiation and theoretical predictions using TRANSWELL.

TABLE (7.4)

DOSE DEPENDENCE OF PEAK SWELLING IN Al AT 75°C[109]

Specimen Number	Pre-Doping Treatment	Total Ion Dose x 10^{-17} cm^{-2}	Calculated Peak Dpa	Void Concentration x $10^{-15} cm^{-3}$	$\bar{d}$ (Å)	Swelling %
C16	None	0.15	16	3.6	172	1.0
C3	None	0.625	65	4.6	219	2.6
C3	10^{-5}H	1.0	104	5.4	267	5.6
C17	None	1.5	156	12	227	8.4

corresponding to Mazey's experiment.

The following set of initial conditions were used in the calculations:

$$N_C^S = 1.26 \times 10^8 \exp\{0.55 \text{ (eV)}/kT\} \text{voids/cm}^3 \quad (7.14)$$

$$N_{i\ell}^S = 7.6 \times 10^8 \exp\{0.25 \text{ (eV)}/kT\} \text{loops/cm}^3, \quad (7.15)$$

and

defect production rate	$= 10^{-3}$ dpa/sec
total displacements	= 104 dpa
initial deformation produced dislocation density	$= 10^9$ lines/cm^2
cascade efficiency	$= 10^{-3}$
initial number of gas atoms in a void	= 0
gas production rate	= 0 at/at/sec
initial void radius	= 40 Å
Z_i	= 1.015

A comparison of TRANSWELL results to the experimentally determined swelling is shown in Figure (7.11). The results of the work on aluminum seem to indicate the following, if reasonable agreement is to be attained:

a. A bias factor (Z_i) in the order of 1.015.

b. Aluminum is not as efficient as steel retaining vacancies in collision cascades.

c. Interstitial dislocation loop density changes slowly with temperature.

VII.B.3.c. Nickel Irradiations

VII.B.3.c. Ion Irradiation

The temperature dependence of void and dislocation loop

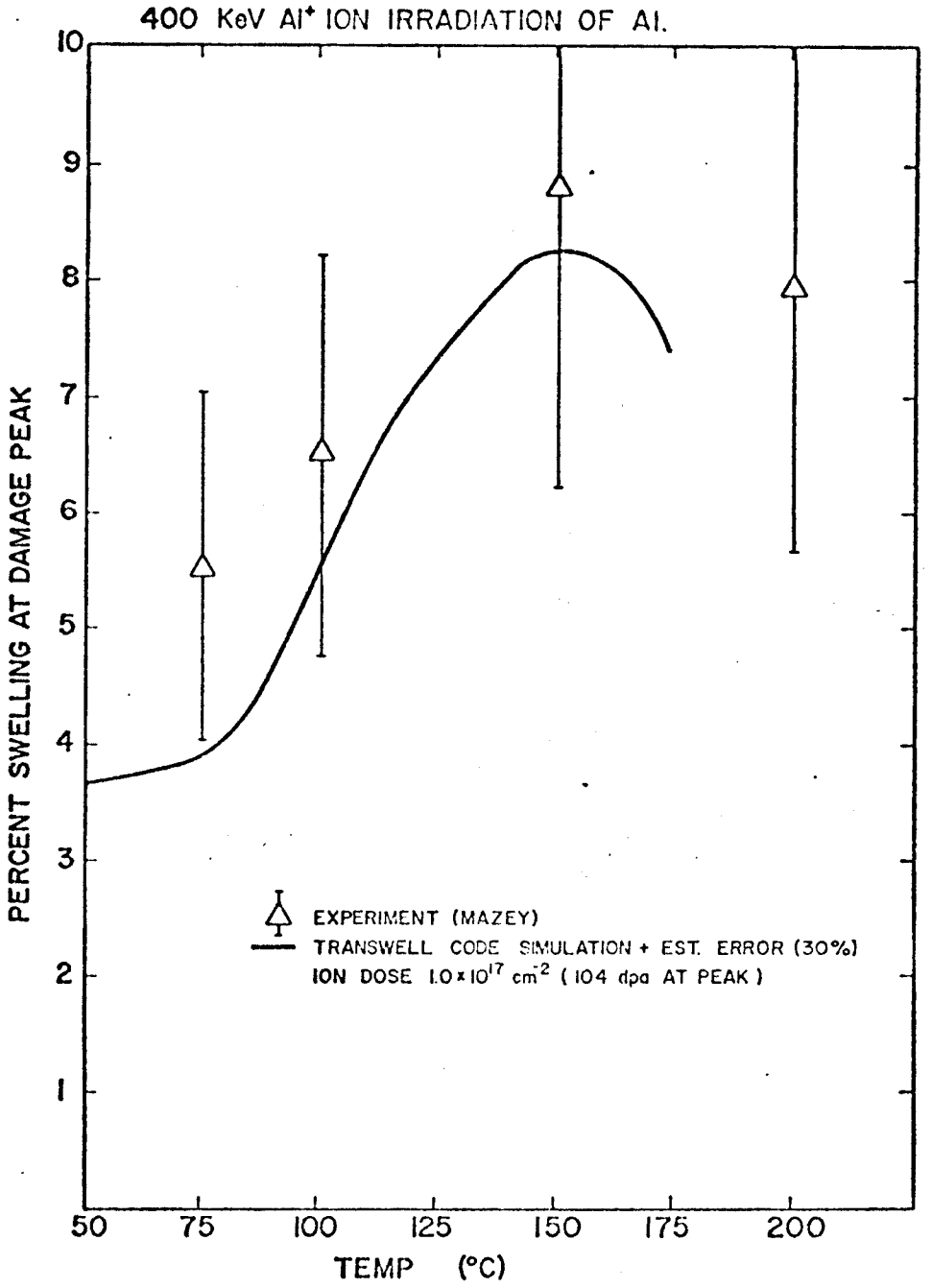

Fig. (7.11) Comparison between measured swelling in ion irradiated aluminum and theoretical predictions using TRANSWELL.

structures was studied by Sprague et al.[110] in high-purity nickel irradiated with 2.8 MeV $^{58}Ni^{+}$ ions to a displacement density of 13 displacements per atom (dpa) at a displacement rate of 7×10^{-2} dpa/sec over the temperature range 325°C to 625°C. Dislocation loops with no significant concentrations of voids were observed in specimens irradiated at 475°C and below. Specimens irradiated between 525°C and 725°C contained both voids and dislocations. The maximum swelling was measured as 1.2% at 625°C. Results obtained from this experiment are summarized in Table (7.5). No helium doping was used in this work.

The following set of conditions were used in the computer simulation of swelling in nickel:

$$N_{i\ell}^{s} = 10^{9} \exp\{1\ (eV)/kT\} cm^{-3} \qquad (7.8)$$

total displacements	= 13 dpa
production rate	= 7×10^{-2} dpa/sec
initial void radius	= 30 Å
cascade efficiency	= 0.01
initial number of gas atoms	= 0
gas production rate	= 0
initial deformation produced dislocation density	= 10^{8} lines/cm^{2}
interstitial-dislocation bias factor (Z_i)	= 1.022

TABLE (7.5)

EFFECT OF IRRADIATION TEMPERATURE ON VOIDS AND DISLOCATIONS IN NICKEL [110]

Irrad. Temp.	Void Density (cm^{-3})	Mean Void Diameter (Å)	Std. Dev. of Diameter (Å)	Swelling (%)	Dislocation Density (cm^{-2})
375	--	--	--	--	7.8×10^{10}
425	--	--	--	--	4.5×10^{10}
475	--	--	--	--	4.5×10^{10}
525	7.6×10^{15}	100	20	0.48	2.9×10^{10}
575	6.9×10^{15}	130	20	0.90	2.0×10^{10}
625	1.8×10^{15}	225	45	1.2	5.6×10^{9}
675	3.0×10^{13}	725	145	0.62	2.8×10^{9}
725	1.4×10^{13}	800	120	0.40	1.6×10^{9}

The experimentally measured void densities were used in all the computer calculations.

As shown in Figure (7.12) there is good agreement between calculated swelling values and experimentally measured ones. Curve (2) shows the better agreement at high temperatures if the starting void radius was taken to be 200 Å. It was observed from all the calculations that small voids find it difficult to grow in ion or neutron irradiations without the assistance of gas for temperatures above the peak temperature. This suggested that the present growth theory could be better correlated with data at high temperatures if one starts with a "free-growth radius" as defined before. This radius, which is the radius of voids when nucleation has ceased, is obviously temperature as well as irradiation and microstructure dependent.

The important point to note from Figure (7.12) is that TRANSWELL comes remarkably close to predicting the swelling in ion bombarded Ni form 500°C to 650°C under relatively high displacement rates (7×10^{-2} dpa/sec.).

VII.B.3.c.ii. Electron Irradiations

Voids in nickel electron irradiated at 450°C were studied by Norris [111,112]. The specimen was previously bombarded with 6×10^{17} He^+ ions/m^2 at 50 keV and then annealed at 640°C to remove the vacancy clusters. A calculated displacement rate of 2.06×10^{-3} dpa/sec with an error of $\pm$20% was used. Figure (7.13) shows the results of this experiment

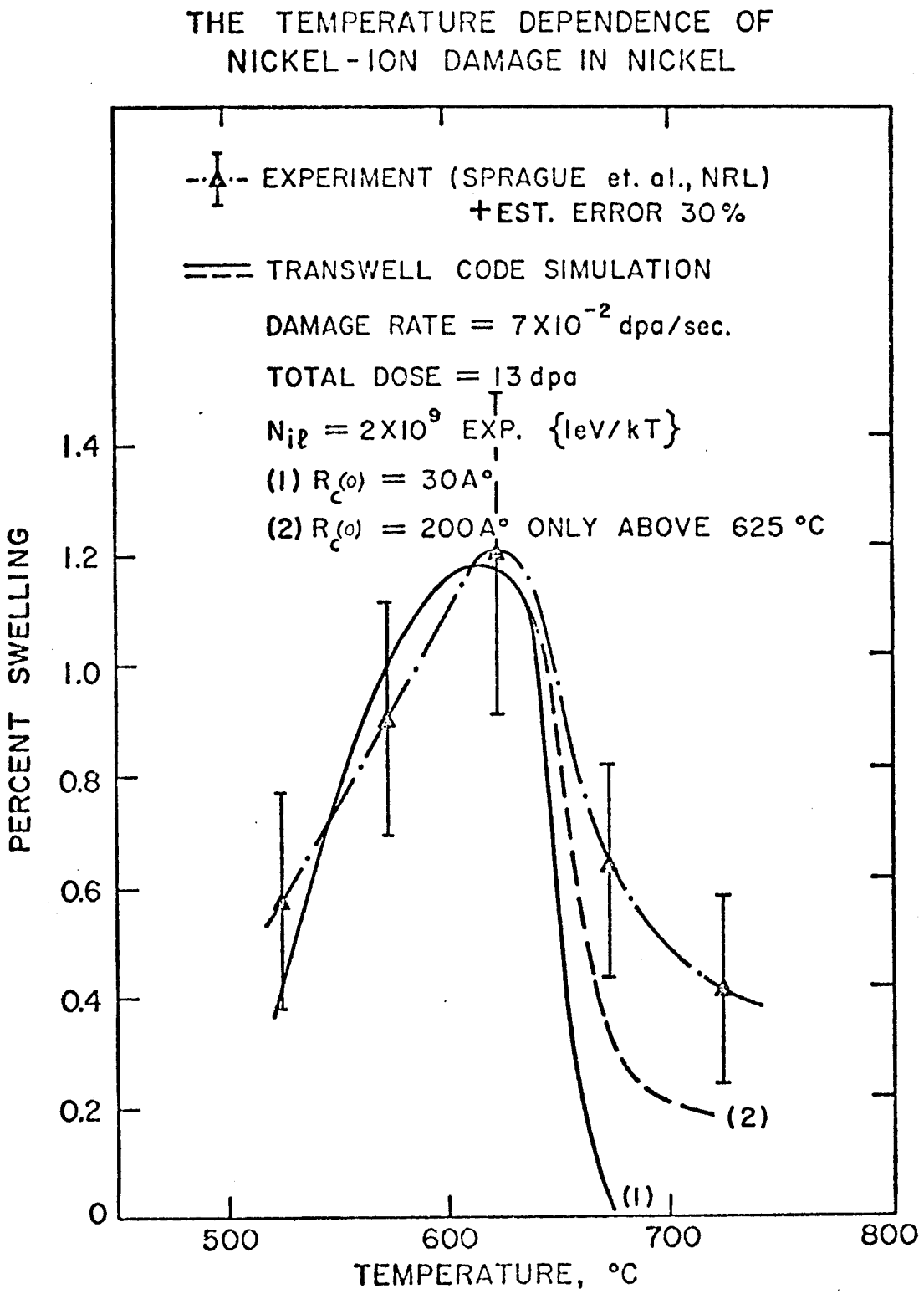
THE TEMPERATURE DEPENDENCE OF
NICKEL-ION DAMAGE IN NICKEL
EXPERIMENT (SPRAGUE et. al., NRL)
+EST. ERROR 30%
TRANSWELL CODE SIMULATION
DAMAGE RATE = 7X10^-2 dpa/sec.
TOTAL DOSE = 13 dpa
N_il = 2X10^9 EXP. {1eV/kT}
(1) R_c(o) = 30A°
(2) R_c(o) = 200A° ONLY ABOVE 625 °C
PERCENT SWELLING
0
0.2
0.4
0.6
0.8
1.0
1.2
1.4
500
600
700
800
TEMPERATURE, °C
(1)
(2)

Fig. (7.12)

with dose uncertainty of ±20% and swelling uncertainty of ±30%. Swelling saturation at high doses is suspected to be due to surface effects in thin foils.

Unfortunately, only total void induced swelling was reported in the electron irradiation studies of Ni, no void density, size or interstitial loop information was given. We have tried to simulate some of the irradiation parameters with those of steel at the same temperature even though we realize that there may be some significant differences. At 450°C the following conditions were assumed for electron irradiated Ni.

number of voids per cm^3 (saturation)	$= 8 \times 10^{15}$
number of interstitial loops per cm^3 (saturation)	$= 1 \times 10^{15}$
initial deformation produced dislocation density	$= 10^8$ lines/cm^2
production rate	$= 2.06 \times 10^{-3}$ dpa/sec
total dose	= 40 dpa
initial void radius	= 10 Å
interstitial-dislocation loop bias factor (Z_i)	= 1.022
number of He gas atoms in a void	= 50

With this set of parameters we found that computer simulations produce reasonable agreement with experimentally measured swelling values as shown in Figure (7.13). At large doses, foil surface effects impose artificial saturation limits on the swelling data so we would not expect TRANSWELL to agree in that region.

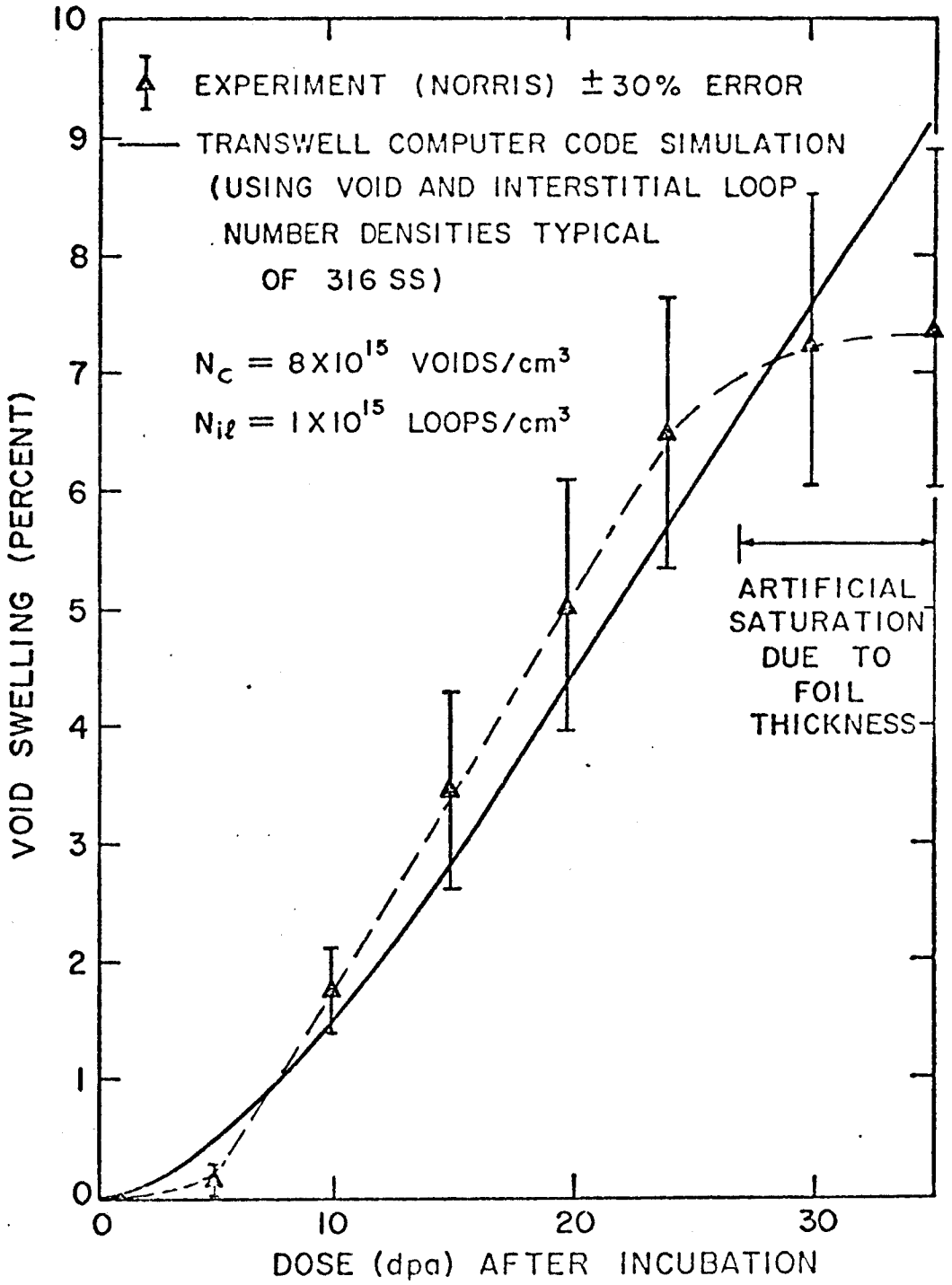

VOID SWELLING VERSUS DOSE AT 450°C IN NICKEL AT A DOSE RATE OF $2X10^{-3}$ dpa/sec (ELECTRON IRRADIATED)

Fig. (7.13)

VII.B.4. Annealing Experiments

a) Westmacott, Smallman and Dobson's Experiment [84].
Octahedral voids up to 500 Å in diameter were produced in thin foils of spectroscopically pure aluminum by quenching. Transmission electron microscopy has been used to investigate the thermal stability of these voids and it was observed that they anneal out rapidly in the range of 150-200°C. The annealing treatments were performed outside the microscope in a silicon-oil bath controlled to an accuracy of ± 0.25°C. At best, the error in their method was estimated to an accuracy of ±10 Å in diameter. By adopting a value of the diffusion coefficient determined by Volin and Baluffi [83], they were able to estimate a surface energy of γ_s = 1140 ± 200 ergs/cm^2.

b) Volin and Balluffi's Experiment [83]

The annealing kinetics of voids in 99.9999 wt % pure aluminum were studied over the temperature range of 85 to 209°C in thin specimens by transmission electron microscopy. The isothermal shrinkage of individual voids was measured and interpreted on the basis of a self-diffusion annealing model. The self-diffusion coefficient of aluminum, as determined from the data, was given by $D_s = 0.176\ (-1.31\ eV/kT)\ cm^2 s^{-1}$. The activation energy, Q = 1.31 eV, was found to be significantly lower than the value Q = 1.48 eV determined by Lundy and Murdock [113] at temperatures near the melting point in a radioactive tracer technique. In all their

calculations, the surface energy of aluminum was assumed to be $\gamma_s = 1500$ ergs/cm^2, and the atomic volume was taken as $\Omega = 16.6 \times 10^{-24}$ cm^{-3}.

On major constituent idea in pulsed irradiation studies is the allowance of voids to anneal out in between consecutive pulses. The accuracy of the model to predict this annealing behavior is crucial to the success of TRANSWELL in a pulsed simulation. The present section is aimed at focusing on this particular aspect and treating different factors that influence the annealing kinetics of voids.

If there is no production of point defects, their concentrations will be the thermal equilibrium concentrations. In the annealing mode of voids in between pulses, the equation for the time rate of change of the void radius (R_c) takes the simple form:

$$\frac{dR_c}{dt} = -D_v C_v^e \{\exp(\frac{2\Omega\gamma}{R_c kT}) - 1\}/R_c \qquad (7.16)$$

provided that the void contains no gas atoms and the sink density is low in the metal.

Individual shrinkage curves in the previous experiment were obtained for a number of voids at each temperature. This allowed isolation of a multitude of factors to affect void shrinkage, and was used to directly verify the last equation.

The presence of a void inside a crystal introduces an additional surface so that the surface energy provides a

driving force to eliminate the voids. Annealing at temperatures high enough to permit self-diffusion causes the voids to shrink by emitting vacancies. The energy of a void, radius R_C, is reduced by an amount $(\frac{2\gamma\Omega}{R_C})$ per vacancy emitted. This leads to a concentration gradient of vacancies between the void and the vacancy sinks. In thin foils the foil surfaces are perfect sinks for vacancies and are thus able to maintain the vacancy concentration away from the voids at the thermal equilibrium level.

Using the parameters of Table (7.6), Figure (7.14) shows the results of the TRANSWELL Computer Code simulations for voids in Al at 126°C (typical of Volin and Balluffi's experiments). A remarkably good agreement between experimental and computer simulation values is obtained with a surface energy of γ = 1000 ergs/cm^2 and a vacancy formation energy E_v^f = 0.645 eV. Figure (7.15) shows the predicted annealing behavior at a higher temperature (175°C) and a comparison with the experimental results of Westmacott, et al.[84]. Values of γ = 1000 ergs/cm^2 and E_v^f = 0.665 eV are again found to produce good agreement. It is noted that the void anneals out about 30 times faster at the higher temperature than at the lower temperature.

A surface energy value of γ = 1000 ergs/cm^2 and a vacancy formation value of $E_v^f \tilde{=}$ 0.66 eV are established from the previous two experiments and substantiate the values that are used in the previous TRANSWELL equations for Al.

TABLE (7.6)

PARAMETERS USED FOR ANNEALING CALCULATIONS IN ALUMINUM

E_v^m(eV)	= 0.57 (114)
E_v^f(eV)	= 0.645 - 0.665*
D_v^o(cm^2/sec)	= 0.045 (114)
γ(ergs/cm^2)	= 1000*
b(Å)	= 2.32
Ω(cm^3)	= 1.25×10^{-23}
C_v^e(at/at) at 126°C	= 6.159×10^{-9}*
C_v^e(at/at) at 175°C	= 3.302×10^{-8} *

*Used in present work

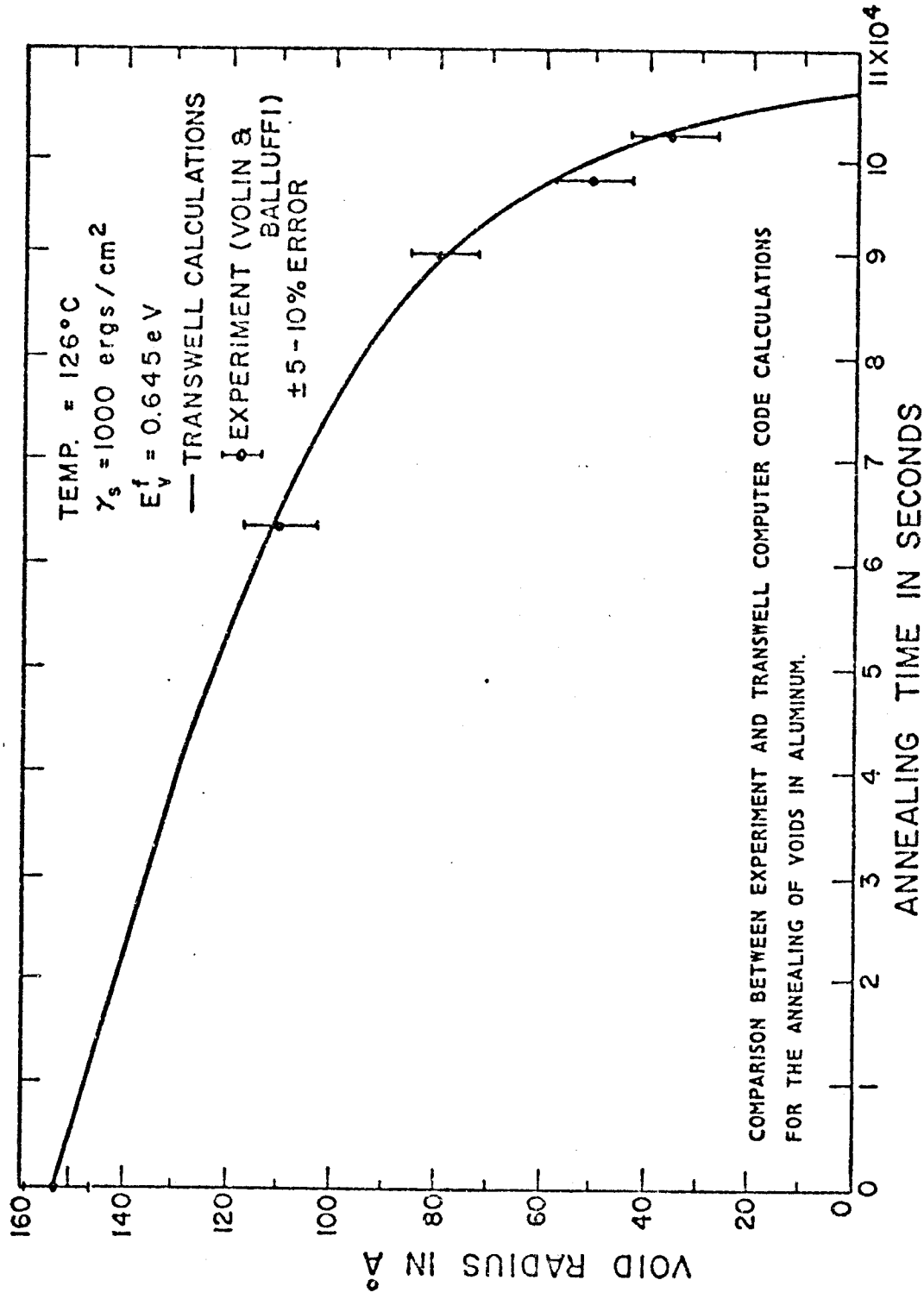
TEMP. = 126°C
γ_s = 1000 ergs / cm^2
E_v^f = 0.645 eV
TRANSWELL CALCULATIONS
EXPERIMENT (VOLIN & BALLUFFI)
± 5 - 10% ERROR
COMPARISON BETWEEN EXPERIMENT AND TRANSWELL COMPUTER CODE CALCULATIONS
FOR THE ANNEALING OF VOIDS IN ALUMINUM.
VOID RADIUS IN Å
ANNEALING TIME IN SECONDS
0
20
40
60
80
100
120
140
160
1
2
3
4
5
6
7
8
9
10
11X10^4

Fig. (7.14)

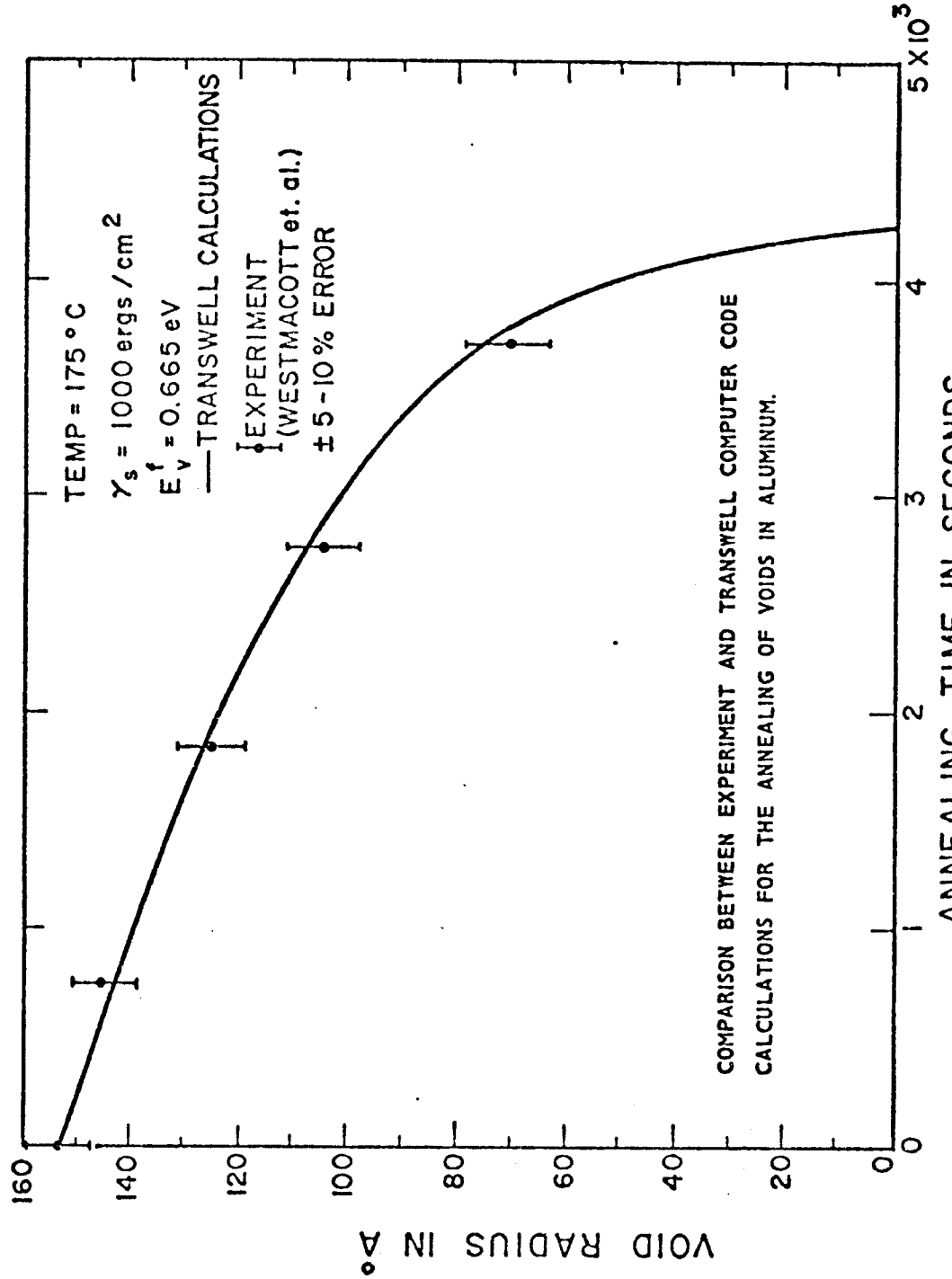
TEMP = 175 °C
γ_s = 1000 ergs / cm^2
E_v^f = 0.665 eV
—TRANSWELL CALCULATIONS
EXPERIMENT (WESTMACOTT et. al.)
± 5 - 10 % ERROR
COMPARISON BETWEEN EXPERIMENT AND TRANSWELL COMPUTER CODE CALCULATIONS FOR THE ANNEALING OF VOIDS IN ALUMINUM.
VOID RADIUS IN Å
ANNEALING TIME IN SECONDS
0
20
40
60
80
100
120
140
160
1
2
3
4
5 X 10^3

Fig. (7.15)

Neutron irradiated aluminum [115] showed a slower annealing behavior than quenched aluminum. There are numerous factors that could affect annealing kinetics such as transmutation products (both gaseous and solid) and absorption of vacancies by other microstructural components [116]. Due to the importance of inter-pulse annealing in Pulsed Systems, study of the sensitivity of annealing kinetics to those factors are investigated in Chapter IX.

VII.C. Discussion and General Remarks

The fundamental reason for the growth of three dimensional cavities (voids) in irradiated materials is believed now to be understood [72] and many of the contributory physical mechanisms have been identified. By adopting a more systematic approach and relating theory to experiments, as attempted in this chapter, the dominant mechanisms affecting the void swelling problem can be qualitatively parametrized.

The results of the present comparison between TRANSWELL and experimental data have shown that the FDRT can do a remarkably good job of predicting the high temperature void swelling behavior of both pure elements and alloys. The fact that TRANSWELL can predict the temperature dependence of defect parameters over a wide range of displacement rates ($\sim 10^{-6}$ to $\sim 10^{-1}$ dpa/sec) and with different bombarding species (neutrons, heavy ions and electrons) is also very satisfying. However, the reader must remember that this FDRT only applies to the situation when an equilibrium void and interstitial

loop density has already been established, i.e., it does not apply to the initial stages of irradiation when nucleation is still dominant.

At high temperatures (>0.4-0.45 T/Tm), it is noted that TRANSWELL predicts lower swelling. This difficulty arises because the initial void size has to be relatively large to withstand the emission of vacancies which is proportional to 1/r. One way to remedy that would be to use an empirically determined void size at saturation, which is a function of temperature (Appendix B). It is clear that initial radii of 10 Å is satisfactory at low temperature (∿0.3 T/Tm), but at temperatures above T/Tm = 0.4 this should increase to several hundred angstroms.

The use of different spike collapse efficiencies (1.2-4.4% for steel, 0.1% for Al and 1% for Ni) to achieve agreement between theory and experiment reveals that the displacement cascade in Al is rather diffuse and inefficient at retaining vacancies. It also demonstrates that future research is required to understand the underlying phenomena that control the collision cascade collapse mechanism.

It will also be noticed that slightly different values of the bias factor of dislocations for interstitials were used.

Material	Zi
316 SS	1.025-1.08
Al	1.015
Ni	1.022

However, one would expect that since the interaction depends on the strain energy, and since that depends on the shear modulus, different values of Z_i should be assigned different materials.

The results of this study show that TRANSWELL can accurately predict the post incubation growth behavior of voids and dislocation loops as a function of temperature in a wide variety of materials irradiated over a factor of 10^5 in steady-state displacement rates with two widely, different types of irradiation. The TRANSWELL code also accurately predicts the annealing of voids in dilute solutions indicating that it can adequately predict the behavior between pulses of irradiation.

The calibration of the theory against existing experimental results showed the need for specifically designed calibration experiments that augment the present qualitative capability of the theoretical model as a means of both extrapolating existing swelling data and tailoring suitable new materials.

CHAPTER VIII

DYNAMIC RESPONSE OF METALS DURING STEADY STATE POINT DEFECT PRODUCTION

VIII.A.Introduction

The phenomenon of void growth in metals is known to be a strong function of both the intrinsic properties and the irradiation envrionment. Two of the most common parameters studied are the temperature and the fluence dependence of the swelling. However, there are many more parameters which influence the production, migration and agglomeration of point defects and in the Brailsford and Bullough rate theory model[71] and the Fully Dynamic Rate Theory (FRDT)[53] there are at least 16 materials and 5 irradiation parameters which need to be considered.

The object of this chapter is to use the FDRT to examine the significance of two of the more important irradiation parameters, the displacement rate and cascade collapse efficiency, on the swelling of 316 stainless steel over a range of temperatures and fluences[126,127].

There is a great deal of experimental evidence on the effect of displacement rate on the swelling in metals[117]. In general, the higher the displacement rate, the higher the supersaturation level of both vacancies and interstitials. These higher defect concentrations can affect both the nucleation (which is assumed to have ceased in the rate theory

approach) and the growth of clustered defects. Aside from the obvious interest in void growth, it is important to know what effect changing displacement rate has on the other sink removal rates and the recombination rates. We will examine displacement rates from 10^{-6}dpa s^{-1} typical of fast reactor conditions to 10^{-3}dpa s^{-1} typical of heavy ion simulation experiments.

The concept of cascade collapse efficiency (ε) was first introduced into the void growth theories by Straalsund [118] and Bullough, Eyre and Krishan [65]. The value of ε is defined as the fraction of vacancies that are produced directly into vacancy loops. This factor (ε) has two effects on the growth of voids.

1) A certain fraction of the vacancies is tied up in vacancy loops, thus reducing the total number of vacancies going to voids.
2) The vacancy loops represent a new sink in the matrix which now must be considered in the dynamics of the point defect behavior (sink removal and recombination rates).

Qualitatively one expects the value of ε to be zero for electron irradiation and it has been estimated to be $\sim$0.044 for heavy ion irradiation of 316 SS [65]. We will investigate values of ε from 0.001 to 0.1 in this study.

The organization of this chapter is as follows. First, a brief description is given about the calculational procedure

and assumptions used in this work. The next section describes the results of the calculation on a variation of ε from 0.001 to 0.1 at P = 10^{-3}dpa s^{-1} and a variation of P from 10^{-6} to 0.1 dpa s^{-1} at ε = 0.044 (see Figure (8.1)). We have chosen to be very explicit about the data from one calculation, ε = 0.01 and P = 10^{-3}dpa s^{-1} and display the results in great detail. However, only the most interesting points and trends will be quoted from the other ε-P combinations. Following a discussion of the results, a comparison between this work and the fixed microstructure calculations is made. Finally, we make some concluding remarks about this work and suggestions for future work.

VIII.B. Calculational Procedure and Assumptions

All calculations were made with the TRANSWELL computer program in conjunction with the recently developed plotting routine, PL3D. This latter code allows the information to be plotted in three dimensional form or as contour plots as will be explained later.

The physical parameters of Table (6.1) were used, and the following assumptions were made:

(1) There is only one average void size at a given temperature that starts to grow under irradiation. At high temperatures, nucleated voids must start growing from a bigger size to withstand surface emission of vacancies. In the present computations, we determined the size at which a void survives at the highest temperature. Also we determined another size at the lowest temperature of interest and linearly interpolated

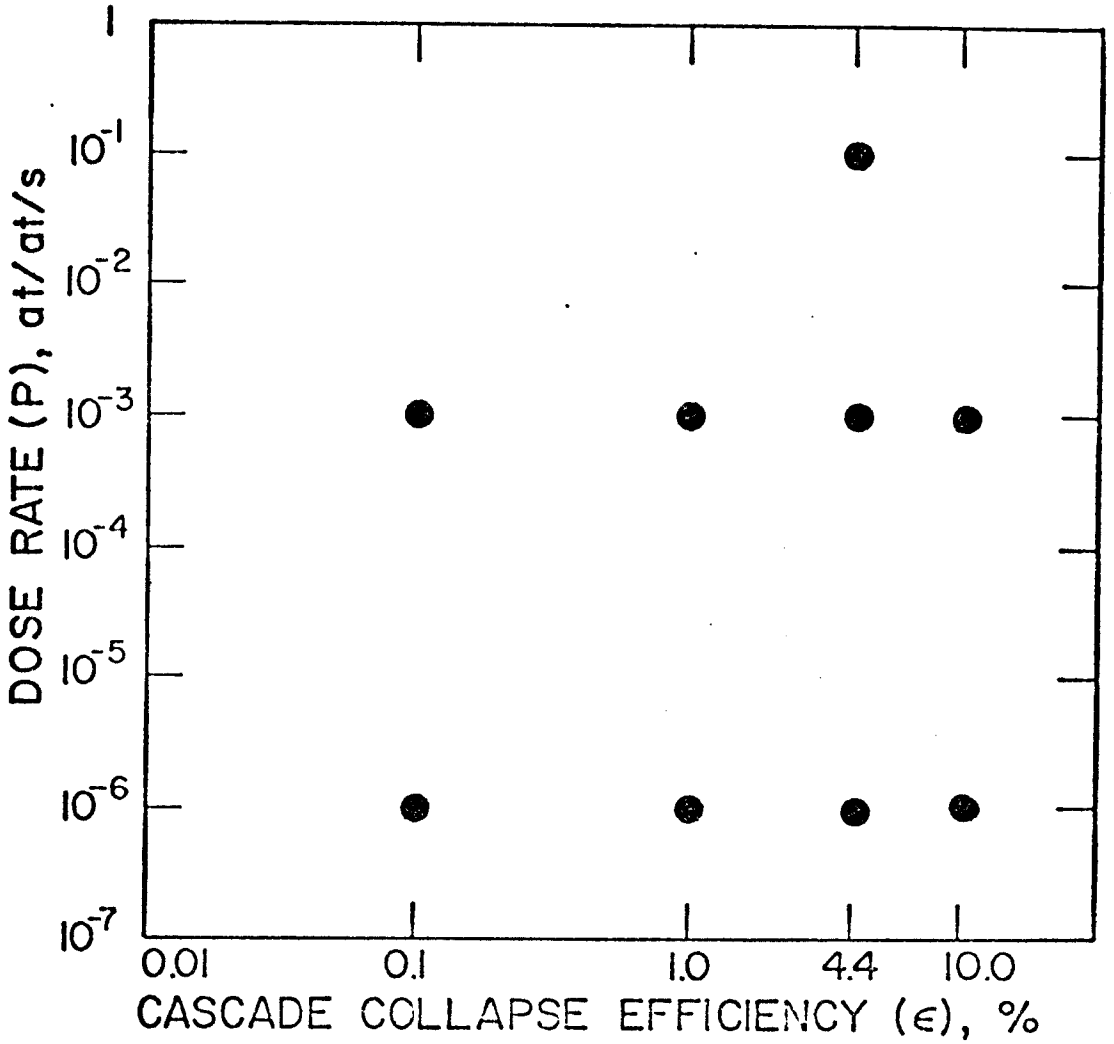

Fig.(8.1) INVESTIGATED COMBINATIONS OF DOSE RATE AND COLLISION CASCADE COLLAPSE EFFICIENCY FOR 316 SS.

$r_{co}(T)$ in between.

(2) The initial dislocation density is set at $\rho_d^0 = 10^8$ cm/cm^3. This value is not changed with dose and is appropriate for solution treated steels.

(3) No gas generation during irradiation was included.

(4) A temperature dependent interstitial loop density as:

$$N_{i\ell} = 1.3 \times 10^{-4} \exp\{2.8 \text{ eV/kT}\}, \text{ cm}^{-3} \quad (8.1)$$

(5) A temperature dependent void density as:

$$N_c = 3.15 \times 10^{11} \exp\{0.625 \text{ eV/kT}\}, \text{ cm}^{-3} \quad (8.2)$$

(6) The previous two nucleation functional dependencies, which were determined at $P \tilde{=} 10^{-3}$dpa s^{-1}, <u>were not changed</u> with dose rate or collapse efficiency to keep the effects of nucleation separate from those of growth.

(7) Finally, a total dose of 40 dpa was studied in all cases and represents the total dose beyond the end of the nucleation phase.

Cases studied in this chapter may be conveniently divided into two broad categories:

(A) Reactor conditions in which the production rate of point defects is 10^{-6}dpa/sec.

(B) Simulation conditions (accelerator or HVEM) in which the production rate of point defects is in the range 10^{-3} to 10^{-1}dpa/sec.

The results presented here are classified into four different groups:

1. Point defect concentrations and fluxes.
2. Resultant average void size and percent swelling.
3. Rate processes:
   a. Vacancy thermal emission rates.
   b. Sink removal rates.
   c. Point defect recombination rate.
4. Microstructural information:
   a. Vacancy loop line dislocation density.
   b. Interstitial loop line dislocation density.
   c. Total dislocation density.
   d. Effective void sink strength ($4\pi R_c N_c$).

VIII.C. Results for Accelerator Conditions

VIII.C.1. ($\varepsilon = 0.01$ and $P = 10^{-3}$ dpa s^{-1})

VIII.C.1.a. Point Defect Concentrations and Fluxes

VIII.C.1.a.i. Vacancy and Interstitial Concentrations

The vacancy concentration in at/at is shown in Figures (8.2) and (8.3). It can be seen that, at any given temperature, the vacancy concentration is decreased as the damage level increases. The reason for this behavior is primarily due to (as we shall see later) the rapid buildup of vacancy loops in the matrix in the early stages of irradiation (see Figure (8.11)). This effect is more pronounced at lower temperatures where the vacancy loop lifetime is the longest.

The vacancy concentration behavior with respect to

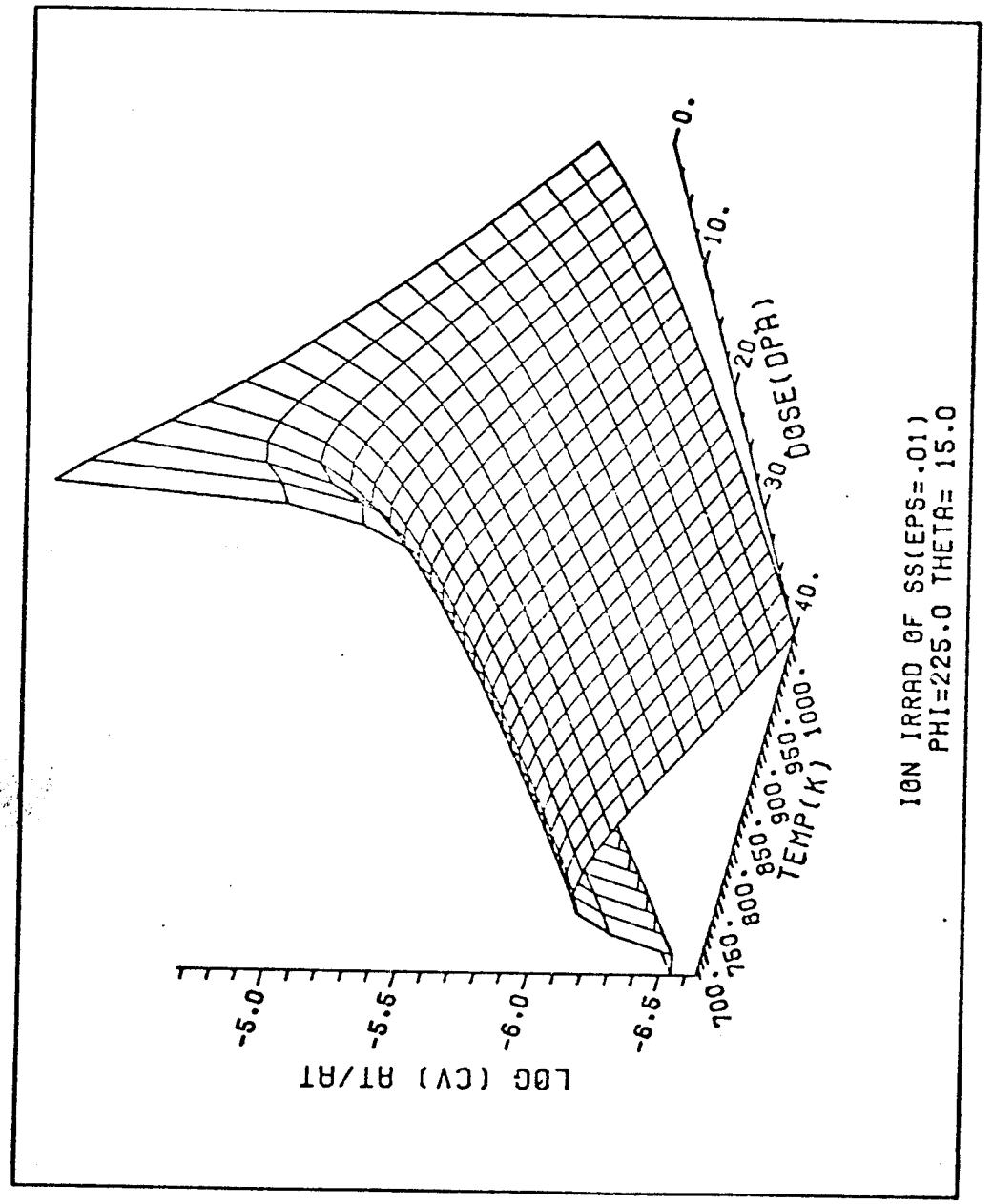

Fig. (8.2). 3-Dimensional plot of vacancy concentration (at/at) as a function of dose and temp. for ion irradiated ST S.S. The dose rate is 10^{-3} dpa/sec and the cascade efficiency is 0.01.

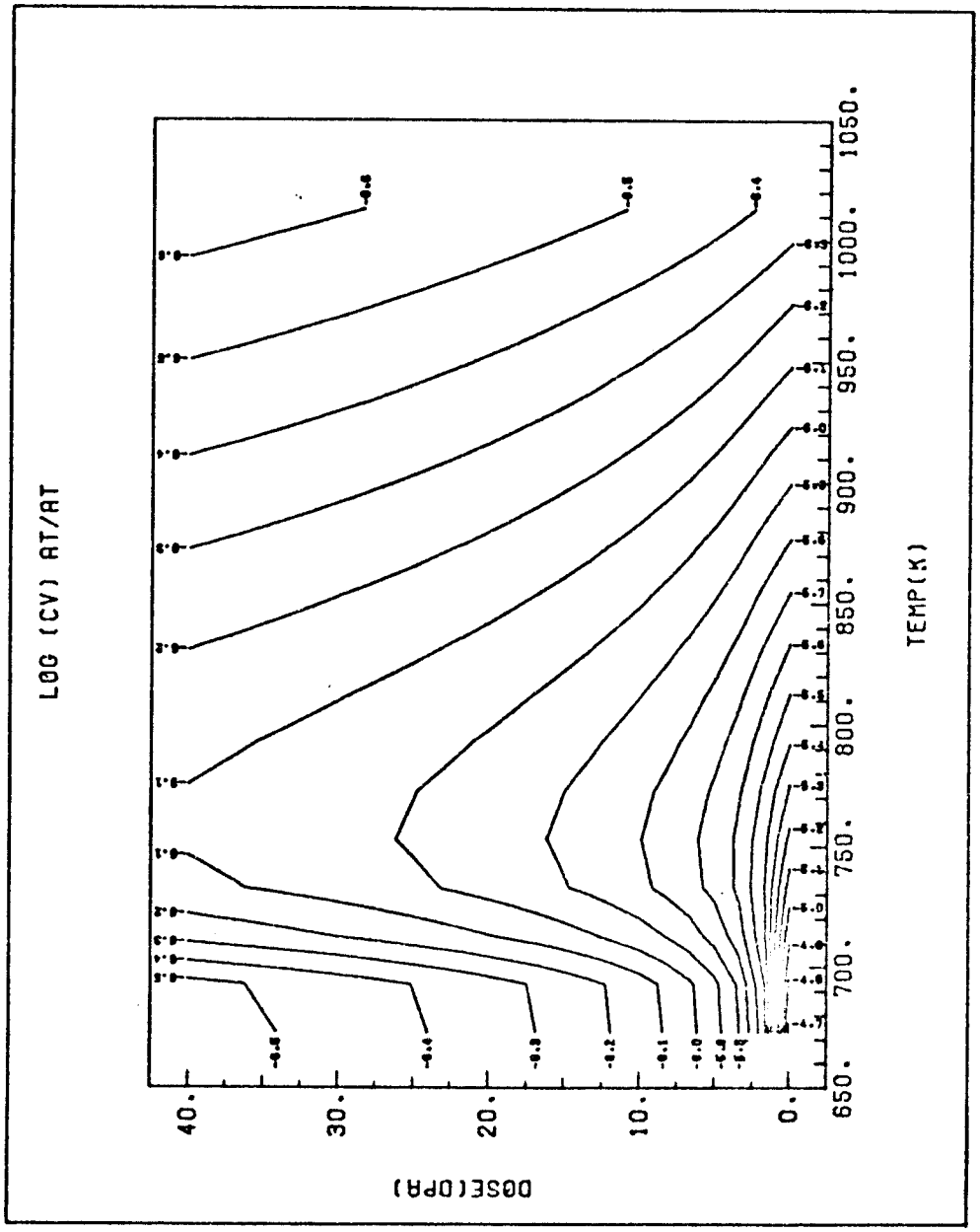

Fig. (8.3). Contour plot of vacancy concentration (at/at) as a function of dose and temp. for ion irradiated ST S.S. The dose rate is 10^{-3} dpa/sec and the cascade efficiency is 0.01.

temperature is more complex. At any given dose, the vacancy concentration exhibits a peak at the intermediate temperatures. Physically, this behavior is attributed to the following:

1) The increase in C_v up to $\sim$750°K is due to the drop in the density of both interstitial and vacancy loops which then drastically reduces the loop line density (Figures (8.22) and (8.24)). The matrix is then much "cleaner" and both the vacancy and interstitial concentrations can build up to higher values.

2) The decrease in the point defect concentrations is due to the increased mobility of vacancies about 750°K which in turn promotes more recombination (Figures (8.20) and (8.21)) and migration to different sinks.

The interstitial concentration also decreases with dose at any given temperature because of the buildup in the loop sink density which causes more interstitials to be removed from the matrix. However, in contrast to the vacancy concentration, the interstitial concentration does not reach a maximum with temperature as could be seen from Figures (8.4) and (8.5). This is due to the low activation energy for migration and the fact that an interstitial is only twice as mobile at 1000°K as it is at 750°K. In contrast, the vacany at 1000°K is over 200 times more mobile than at 750°K.

VIII.C.1.a.ii. Defect Fluxes

Although vacancy concentration is order of magnitude

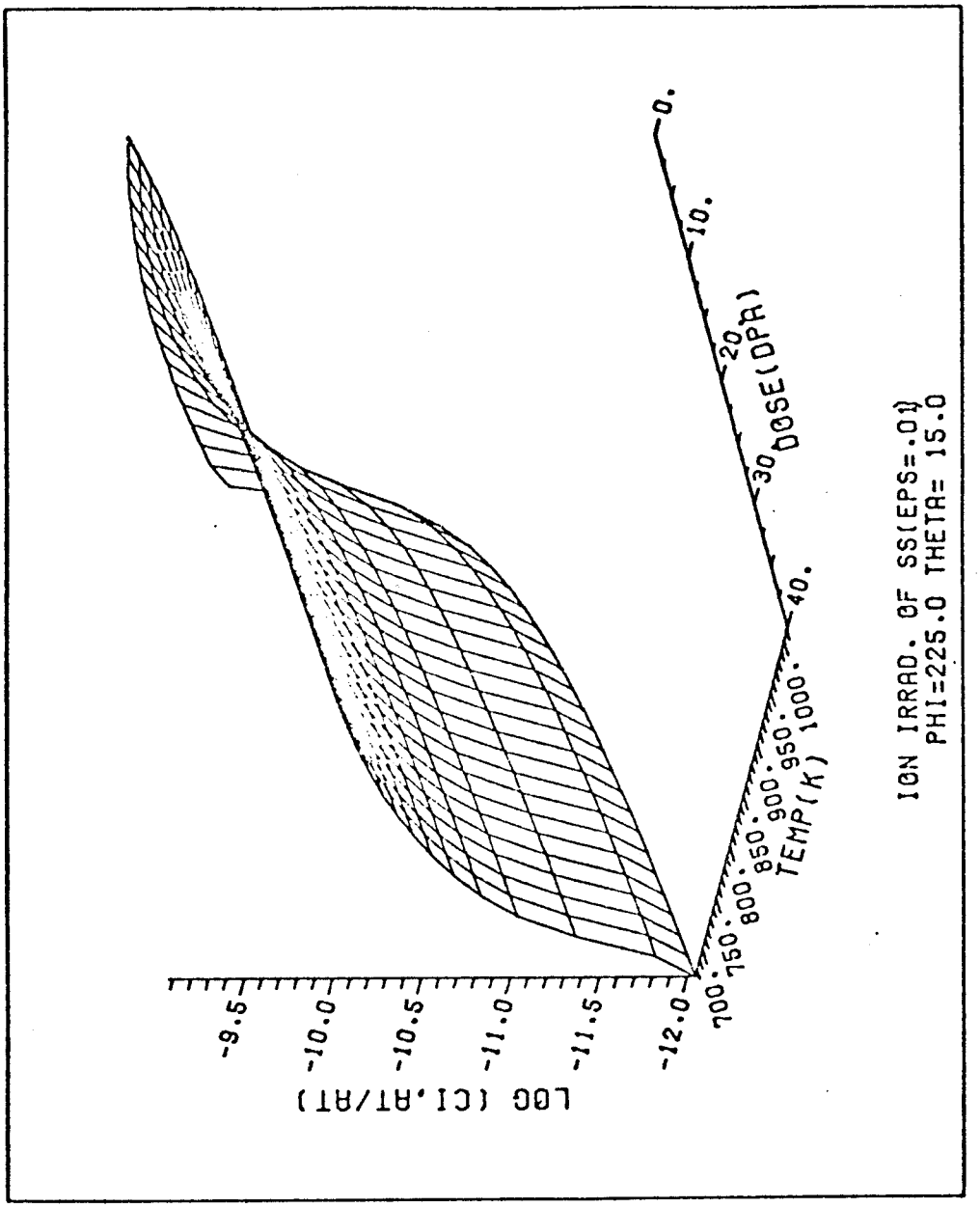

Fig. (8.4). 3-Dimensional plot of interstitial concentration (at/at) as a function of dose and temp. for ion irradiated ST S.S. The dose rate is 10^{-3} dpa/sec and the cascade efficiency is 0.01.

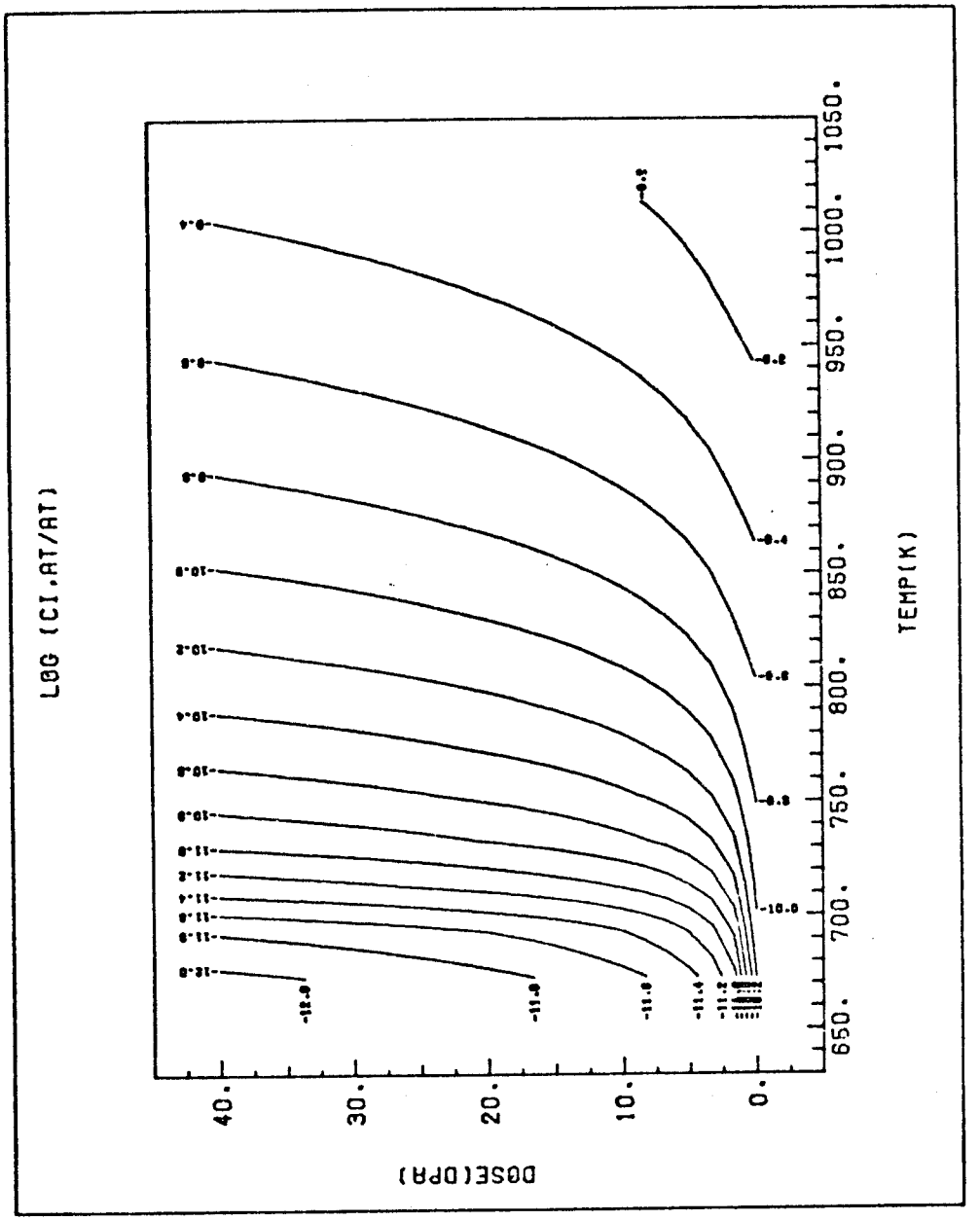

Fig. (8.5). Contour plot of interstitial concentration (at/at) as a function of dose and temp. for ion irradiation ST S.S. The dose rate is 10^{-3} dpa/sec and the cascade efficiency is 0.01.

greater than interstitial concentration, the flux of defects arriving at surfaces of voids and dislocations are only slightly different due to the much higher mobility of interstitials. A vacancy flux is defined as (D_vC_v) while an interstital flux is defined as (D_iC_i). The slightly larger vacancy flux to voids is in fact the driving force causing them to grow.* This small difference in fluxes is also the reason for the sensitivity of the void growth problem to slight changes in material and irradiation variables.

Figure (8.6) and (8.7) show the vacancy flux as a function of dose and temperature. As the dose increases, the flux decreases slowly due to a higher probability of vacancy absorption by the sink density which is building up. At higher temperatures, vacancies are more mobile causing the flux to increase with temperature even though the concentration of vacancies is decreasing. In Figures (8.8) and (8.9) the same behavior of interstitial flux is displayed and from the values on the contour plots one can see the very small difference from vacancy flux.

VIII. C.1.a.iii. Fractions of Vacancies in Loops:

The fraction of vacancies in vacancy loops is shown in Figures (8.10) and (8.11) and is a balance between the production rate (which is constant) and the removal rate (which depends on the number and size of loops). This fraction increases slowly with dose but decreases sharply as the temper-

*The reason interstitial loops grow despite the fact that the interstitial flux in the matrix is less than the vacancy flux can be attributed to the bias factor Z_i.

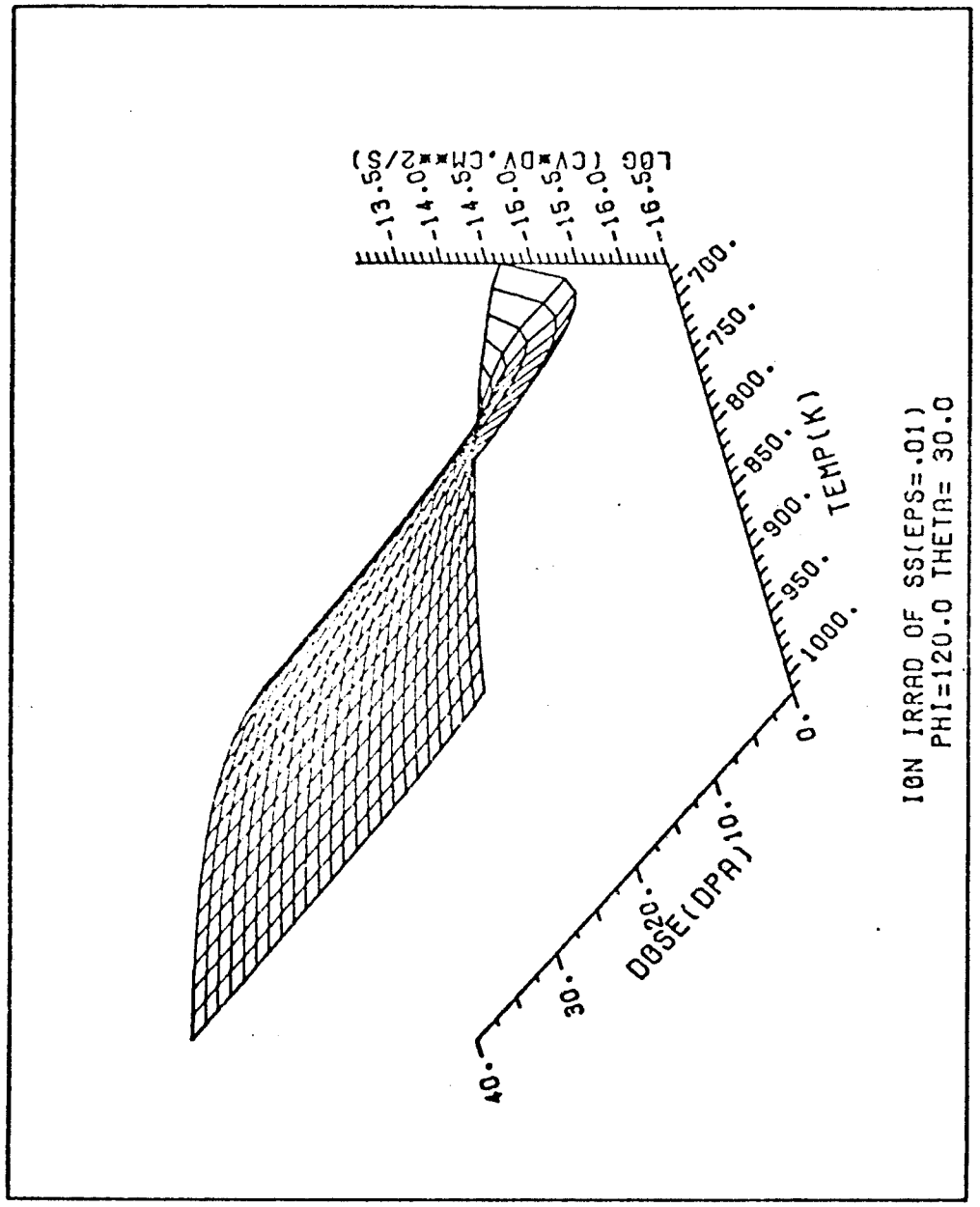

Fig. (8.6). 3-Dimensional plot of vacancy flux ($D_v C_v$, cm^2/sec) as a function of dose and temperature for ion irradiated ST S.S. The dose rate is 10^{-3} dpa/sec and the cascade efficiency is 0.01.

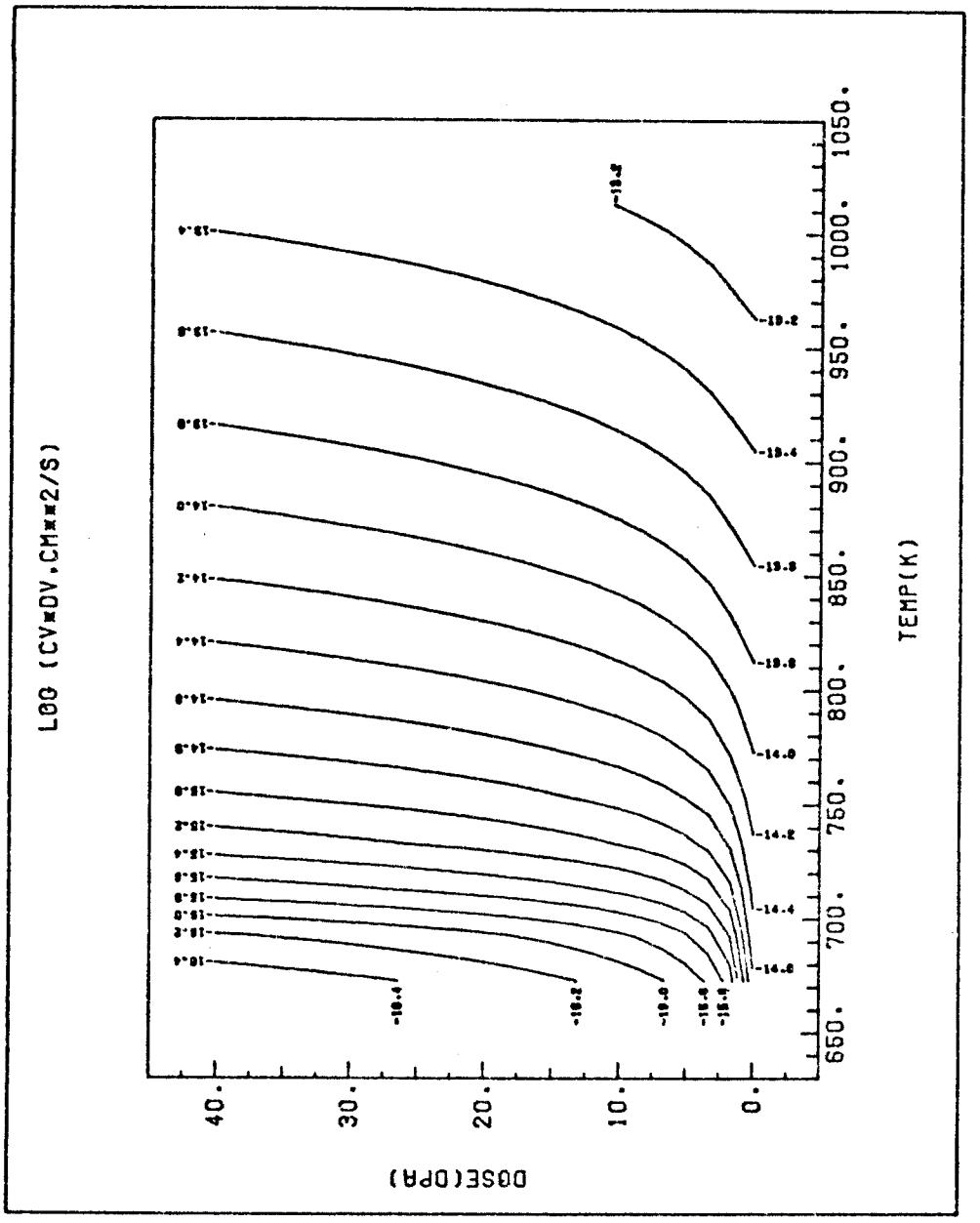

Fig. (8.7). Contour plot of vacancy flux ($D_v C_v$, cm^2/sec) as a function of dose and temp. for ion irradiated ST S.S. The dose rate is 10^{-3} dpa/sec and the cascade efficiency is 0.01.

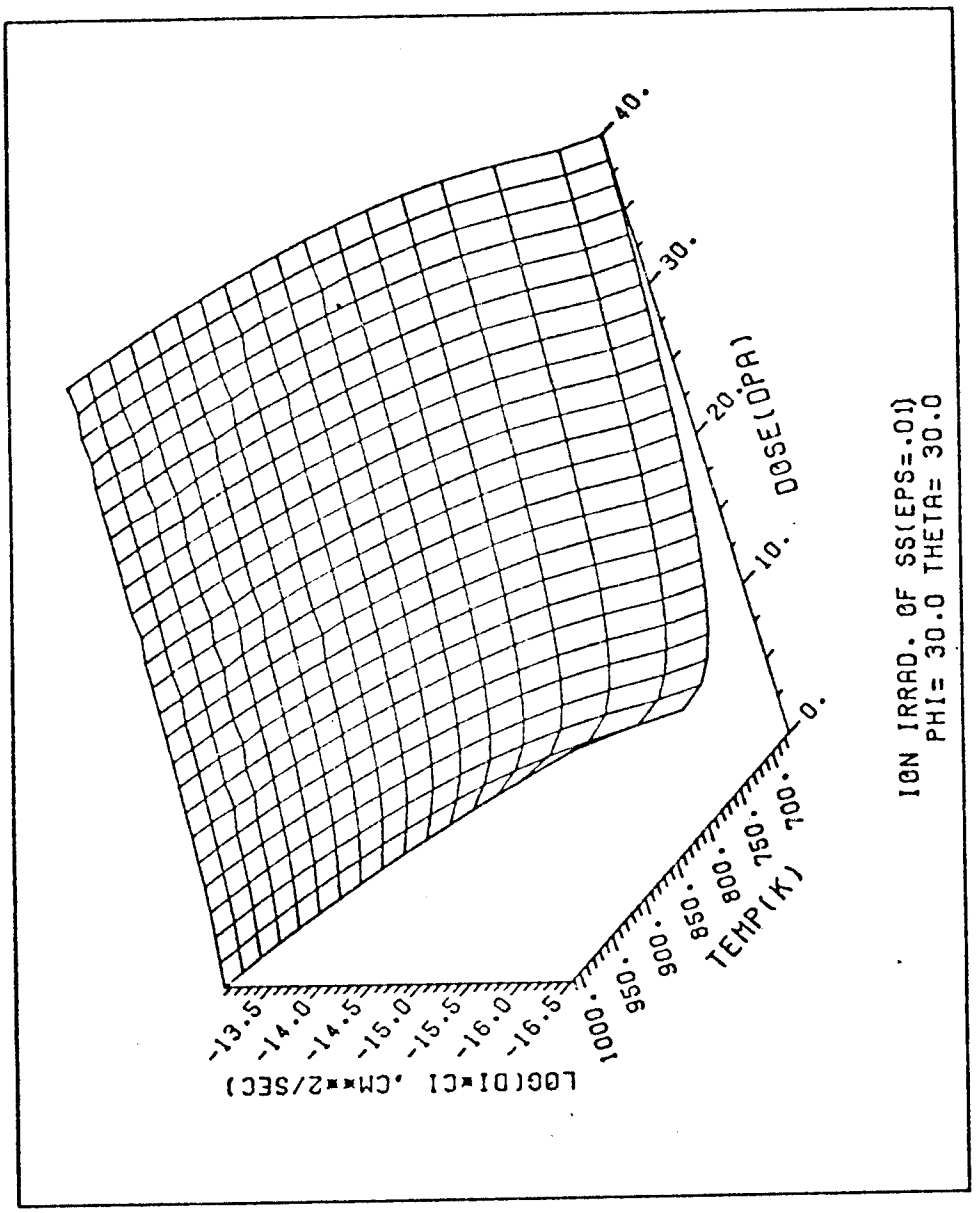

Fig. (8.8). 3-Dimensional plot of interstitial flux (D_iC_i,cm^2/sec) as a function of dose and temp. for ion irradiated ST S.S. The dose rate is 10^{-3} dpa/sec and the cascade efficiency is 0.01.

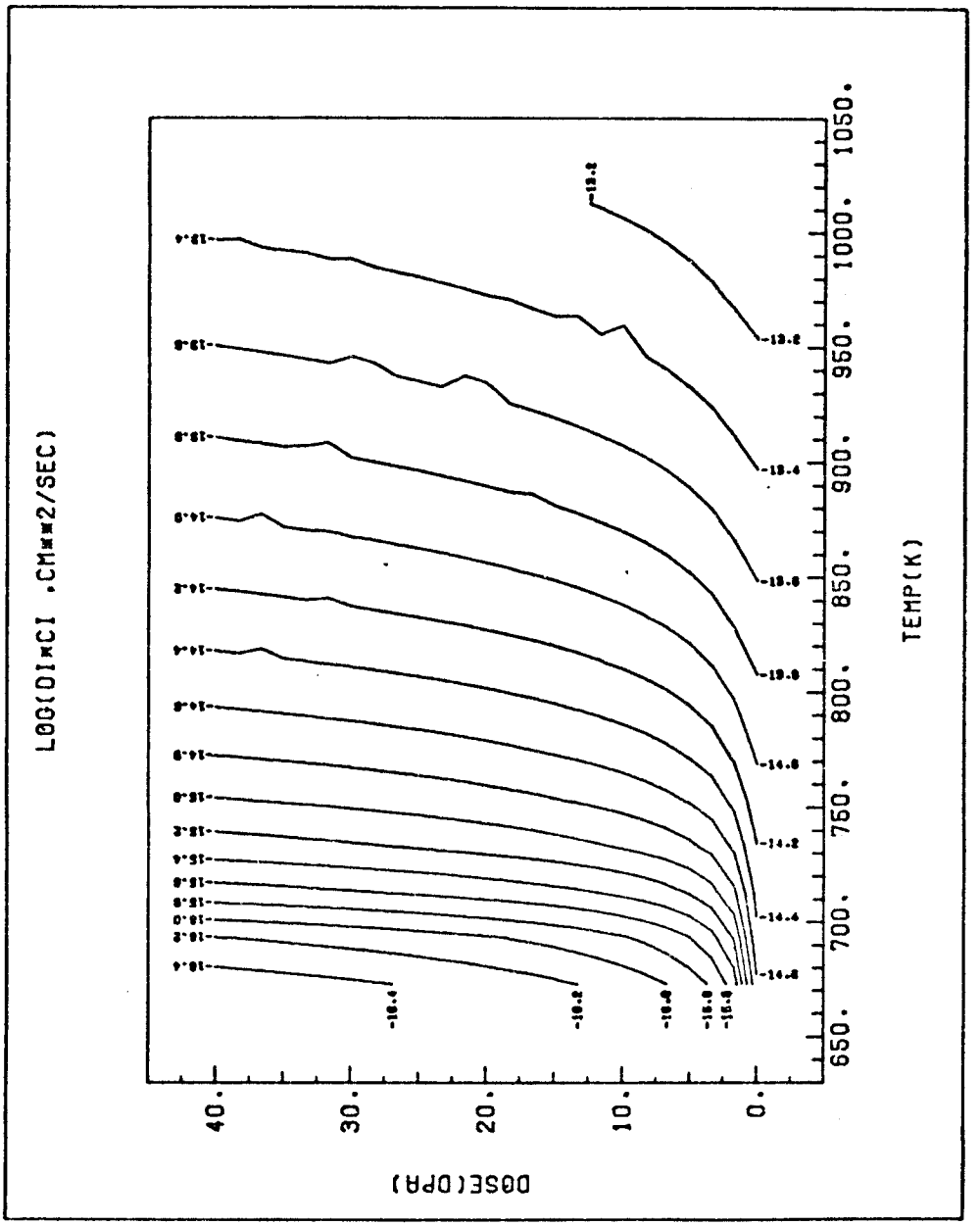

Fig. (8.9). Contour plot of interstitial flux (D_iC_i,cm^2/sec) as a function of dose and temp. for ion irradiated $ST^1S.S$. The dose rate is 10^{-3} dpa/sec and the cascade efficiency is 0.01.

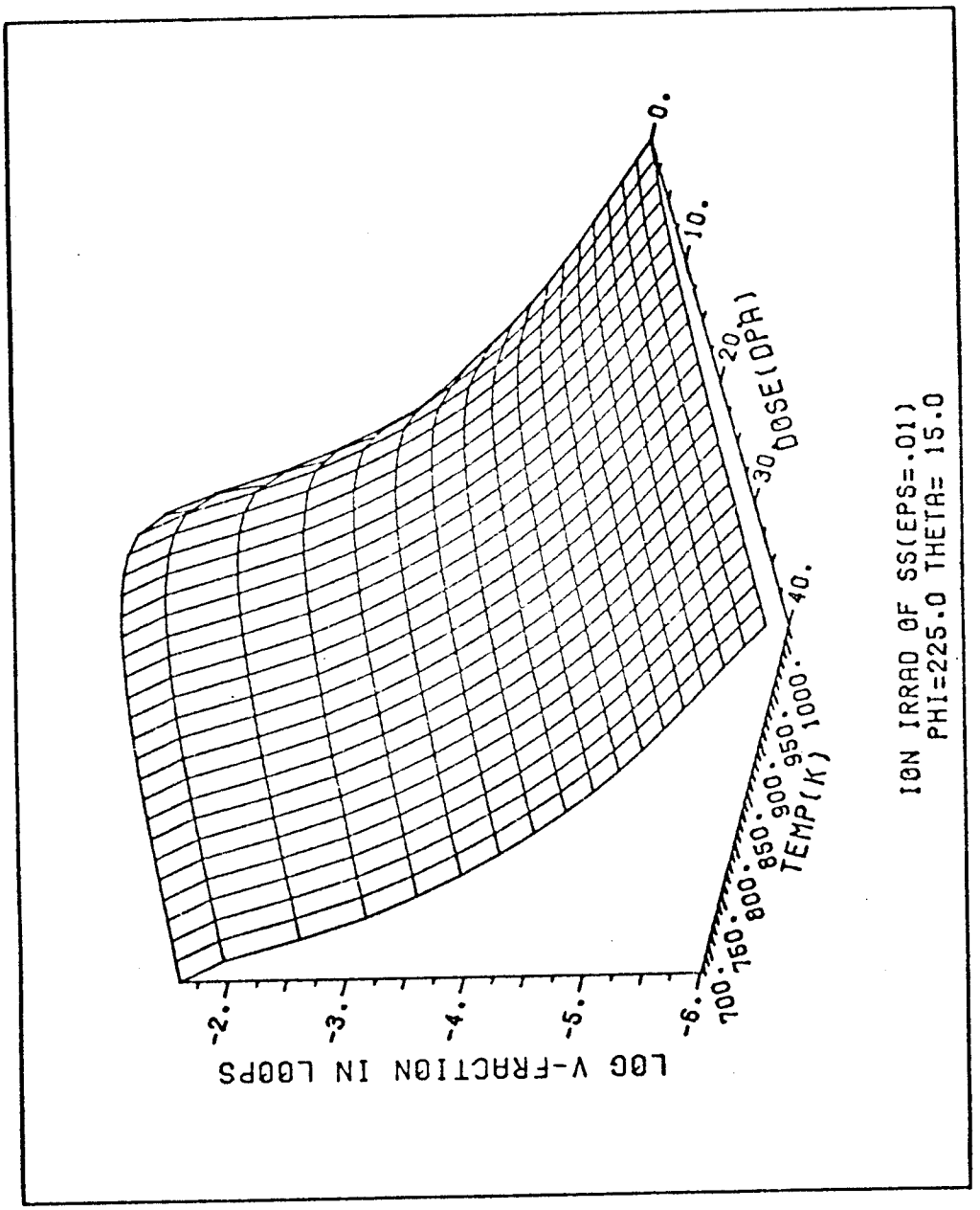

Fig. (8.10). 3-Dimensional plot of vacancy fraction in vacancy loops (at/at) as a function of dose and temp. for ion irradiated ST S.S. The dose rate 10^{-3} dpa/sec and the cascade efficiency is 0.01.

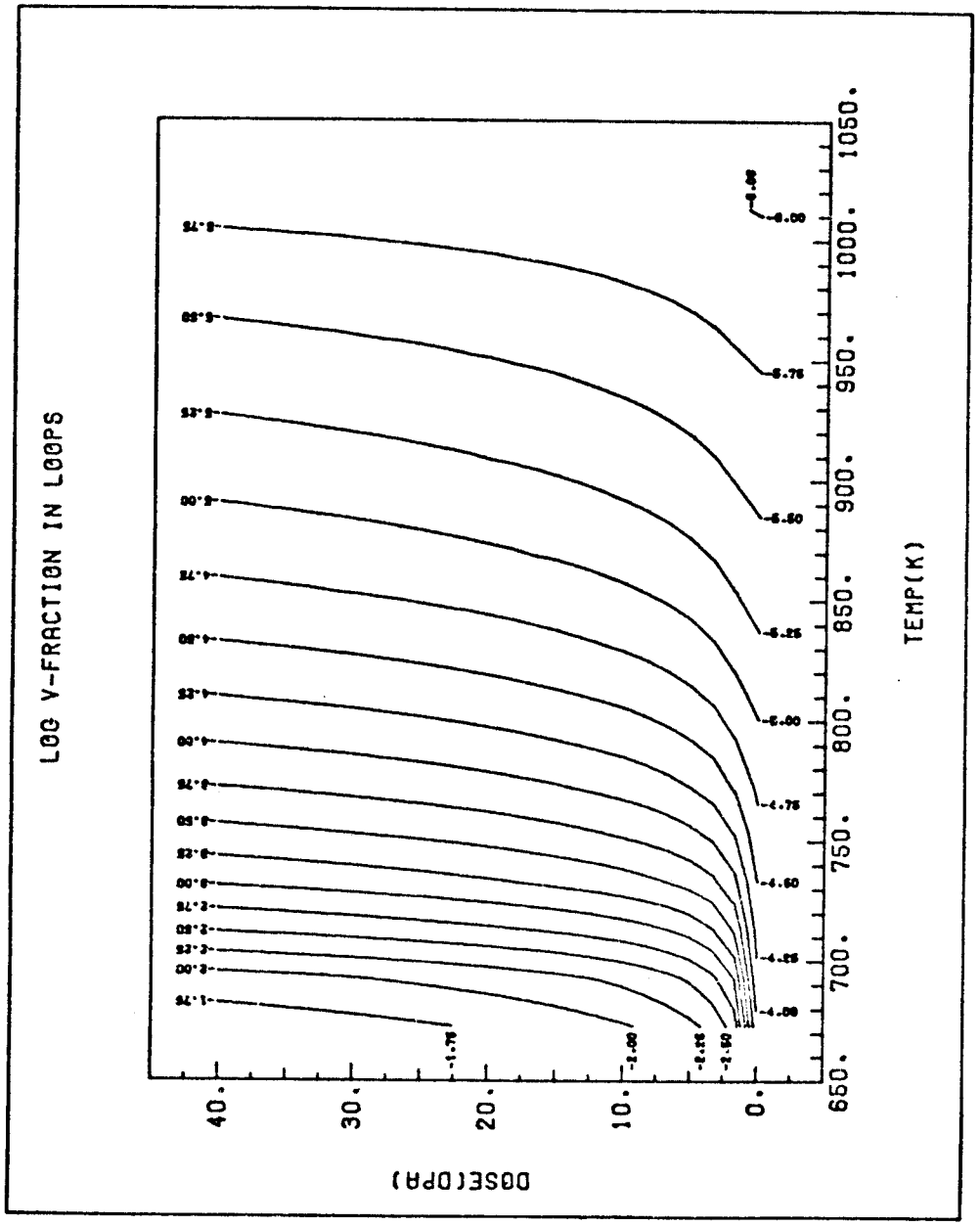

Fig. (8.11). Countour plot of vacancy fraction in vacancy loops (at/at) as a function of dose and temp. for ion irradiated ST S.S. The dose rate is 10^{-3} dpa/sec and the cascade efficiency is 0.01.

ature is increased. The decrease is due to the emission of vacancies at high temperature. The effect of this fraction of vacancies tied up in vacancy loops is to decrease the free vacancy concentration thus decreasing the vacancy flux.

VIII.C.1.b. Resultant Average Void Size and Percent Swelling

Figure (8.12) shows the temperature and dose dependence of the average void radius. Due to the excess flux of vacancies arriving at the voids ($D_vC_v > D_iC_i$), they start to grow immediately upon irradiation. Figure (8.13) shows the contours of constant void radius. At low temperatures the growth rate is not as pronounced as at intermediate temperatures (between 500 and 650°C) due to the lower vacancy flux. At 500 to 650°C the vacancy flux is sufficiently high and the vacancy emission rate sufficiently low that the growth rates are very high. At high temperatures vacancies are more readily emitted from voids (see Figures (8.16) and (8.17), and this has the effect of slowing down the growth of voids since the difference between the vacancy flux (D_vC_v) and the sum of interstitial and emitted vacancy flux ($D_iC_i + D_vC_v^e \exp\{(\frac{2\gamma}{R_c} - P_g)\frac{\Omega}{kT}\}$) is very small. At still higher temperatures the vacancy flux falls farther and eventually the vacancy emission rate in conjunction with the interstitial absorption rate exceeds the vacancy flux and the voids will shrink.

The percent swelling is shown in Figure (8.14) in a 3-dimensional form while it is displayed as constant swelling contours in Figure (8.15). It is interesting to note that

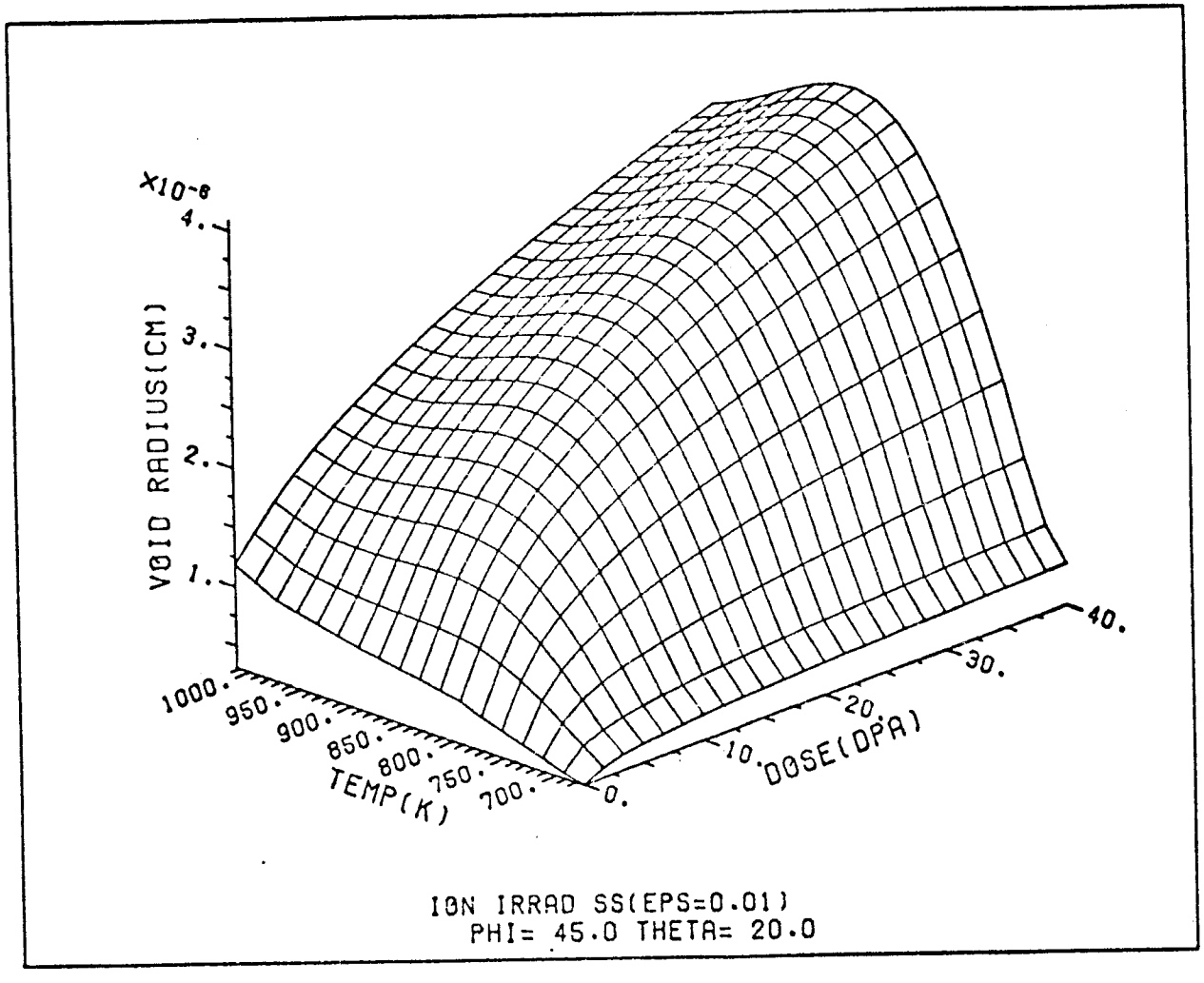

Fig. (8.12). 3-Dimensional plot of mean void radius (cm) as a function of dose and temp. for ion irradiated ST S.S. The rate is 10^{-3} dpa/sec and the cascade efficiency is 0.01.

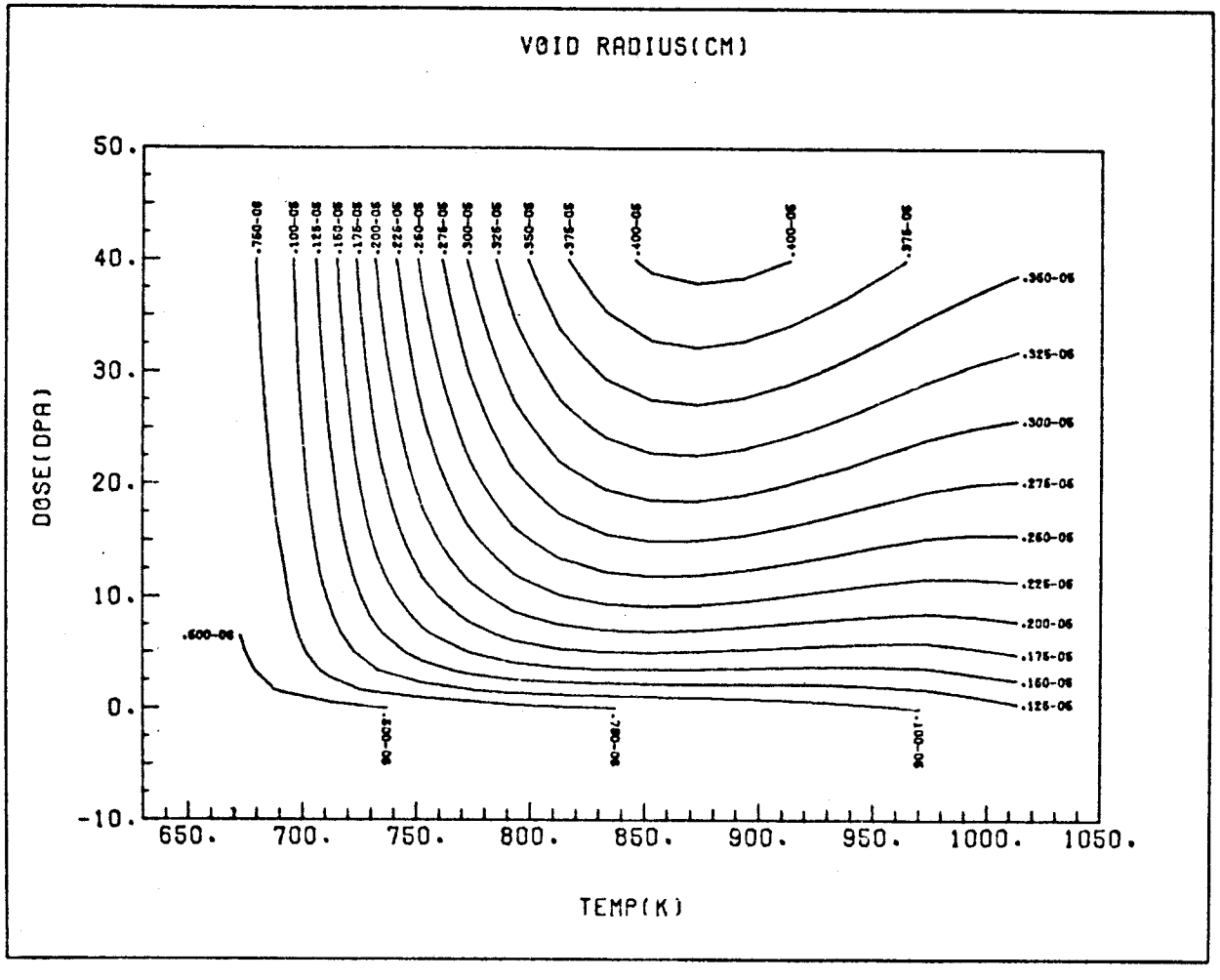

Fig. (8.13). Contour plot of mean void radius (cm) as a function of dose and temp. for ion irradiated ST S.S. The rate is 10^{-3} dpa/sec and the cascade efficiency is 0.01.

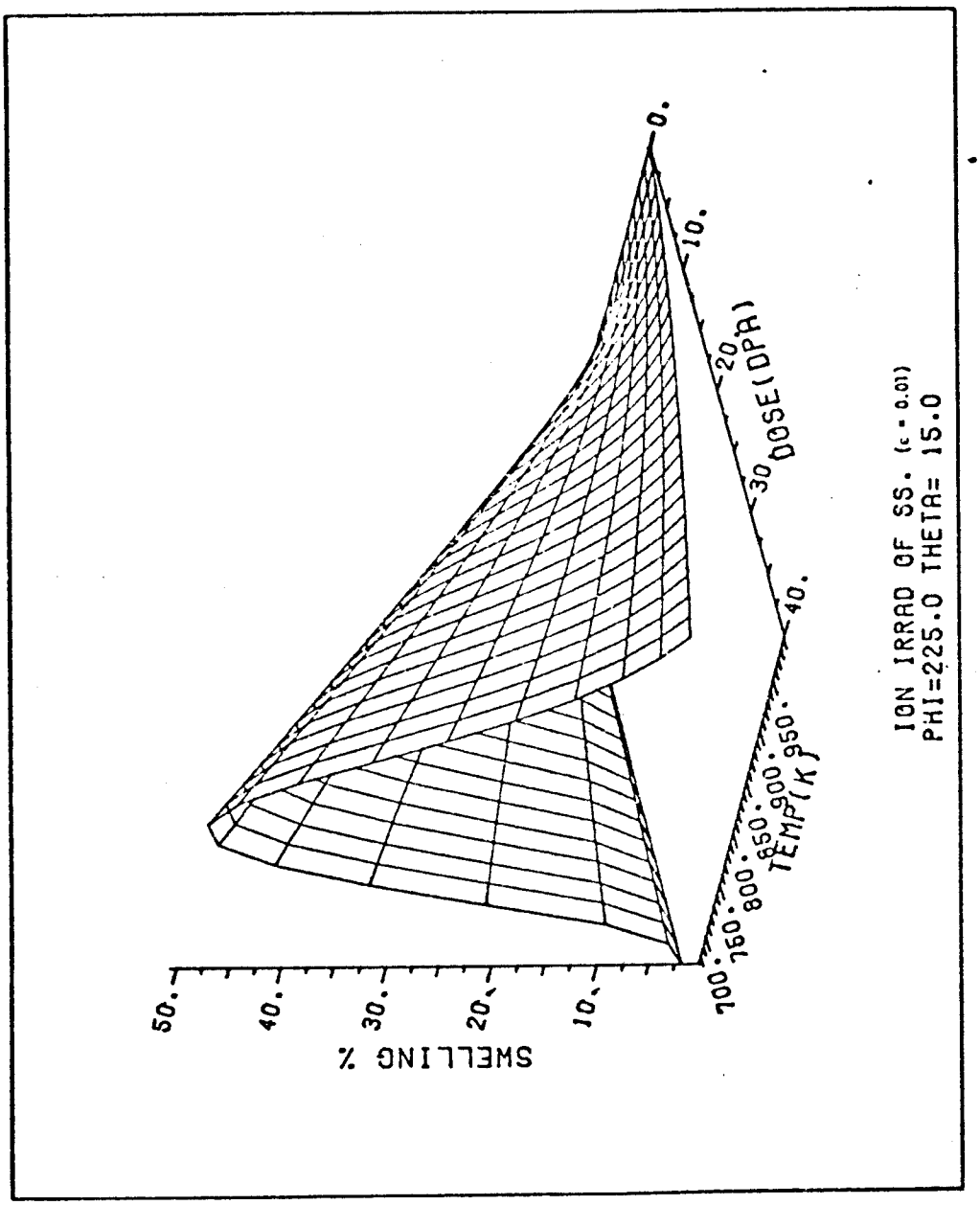

Fig. (8.14). 3-Dimensional plot of percent swelling as a function of dose and temp. for ion irradiated ST S.S. The rate is 10^{-3} dpa/sec and the cascade efficiency is 0.01.

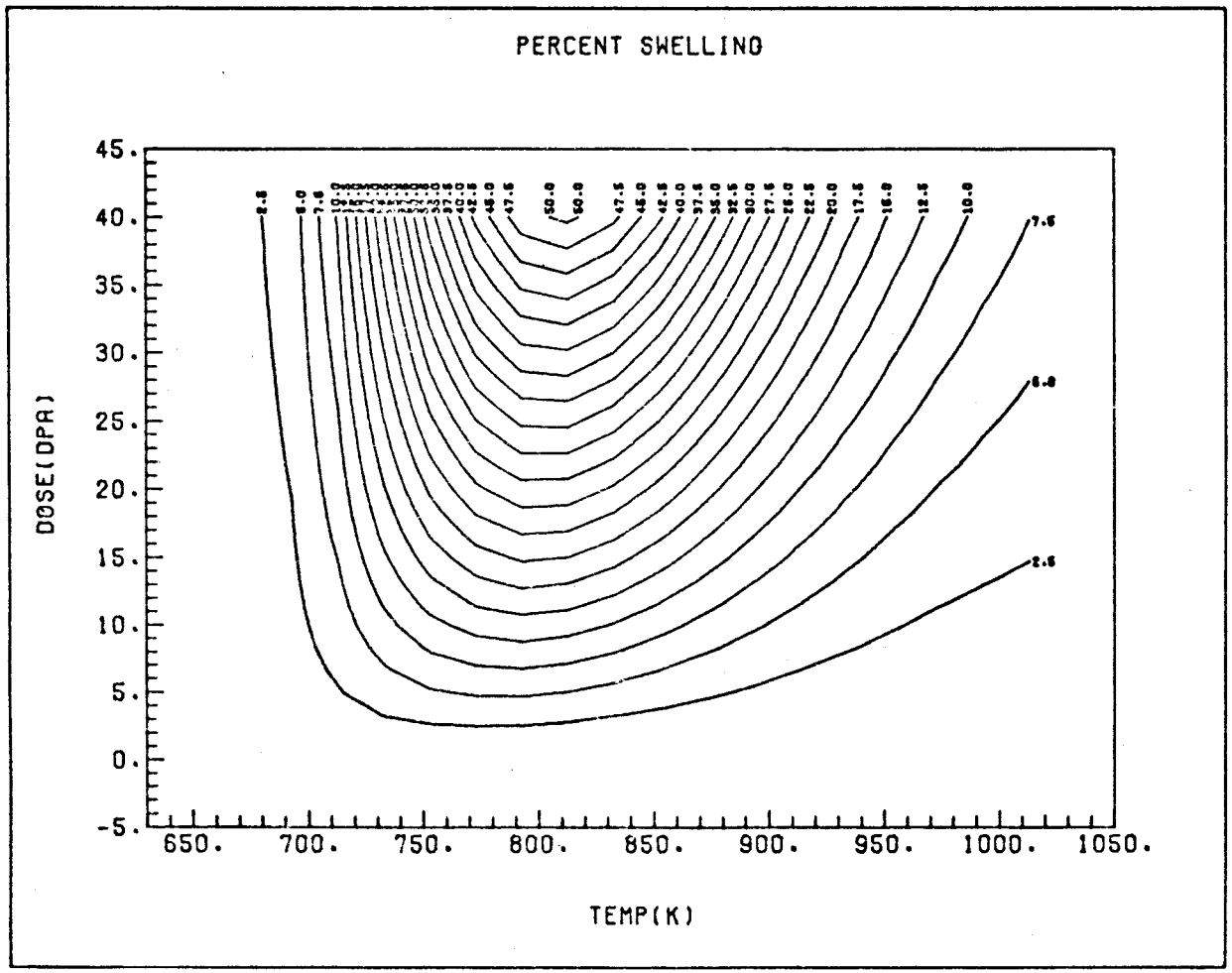

Fig. (8.15). Contour plot of swelling as a function of dose and temp. for ion irradiated ST S.S. The rate 10^{-3} dpa/sec and the cascade efficiency is 0.01.

swelling goes "almost" linear as a function of dose. This is the consequence of a fixed void density and an increasing void size(Figure (8.12)). On the other hand, swelling is temperature dependent in the fashion shown in Figure (8.14) with a slightly dose-dependent peak value. There are two reasons for this temperature dependence which can be understood by examining the simple swelling expression:

$$S = \frac{4}{3} \pi R_c^3 N_c \qquad (8.1)$$

i - The void number density goes down exponentially with temperature (nucleation).

ii - The mean void radius goes up with temperature to 800-850°K and then drops very slowly at high temperatures.

The obvious result would be a "bell shaped" swelling curve as frequently observed experimentally.

A large peak swelling value is obtained here (∿50% at 40 dpa) compared to the smaller swelling for the same steel (∿12% at 40 dpa) reported in reference (65). The only difference between the two cases is the cascade collapse efficiency (ε) being 1% in this case versus 4.4% in the case studied in reference (65).

VIII.C.1.c. Rate Processes

VIII.C.1.c.i. Vacancy Thermal Emission Rate

The vacancy thermal emission rate from edge dislocations is equal to $(D_v^s \rho_d^e)$ where D_v^s is the self diffusion coefficient

of vacancies and ρ_d^e is the deformation produced dislocation density (assumed to be constant at the low value of 10^8 lines/cm^2 commensurate with solution treated steel). The temperature dependence of this quantity is obviously exponential while it is constant as a function of dose. It is found that thermal emission of vacancies from edge dislocations does not become significant until $\sim$900°K and even then the absolute value of $\sim 10^{-7}$ at/at/sec is much smaller than the production rate of 10^{-3} at/at/sec.

The emission rate of vacancies from the surfaces of voids in at/at/sec is; $\{D_v^s\ (4\pi R_c N_c)(\exp[(\frac{2\gamma}{R_c} - P_g)\ \frac{\Omega}{kT})]\}$. The temperature dependence of this function is mainly controlled by the self diffusion coefficient D_v^s with small contribution from the total void surface and the driving force to emit vacancies. The emission term does not become important until $\sim$900°K and it is only slightly dose dependent through the R_c term. Note that the absolute value of a few times 10^{-5} at/at/sec is much larger than the emission from edge dislocations.

The total vacancy emission rate is plotted in Figures (8.16) and (8.17). Calculations reveal that vacancy emission in this particular system is mainly controlled by voids alone. The contribution to vacancy emission from voids seems to be roughly 80% and that from the rest of the microstructure (i.e., i-loops, v-loops and edge dislocations) is dominated by the vacancy loops. A final feature of note is that the

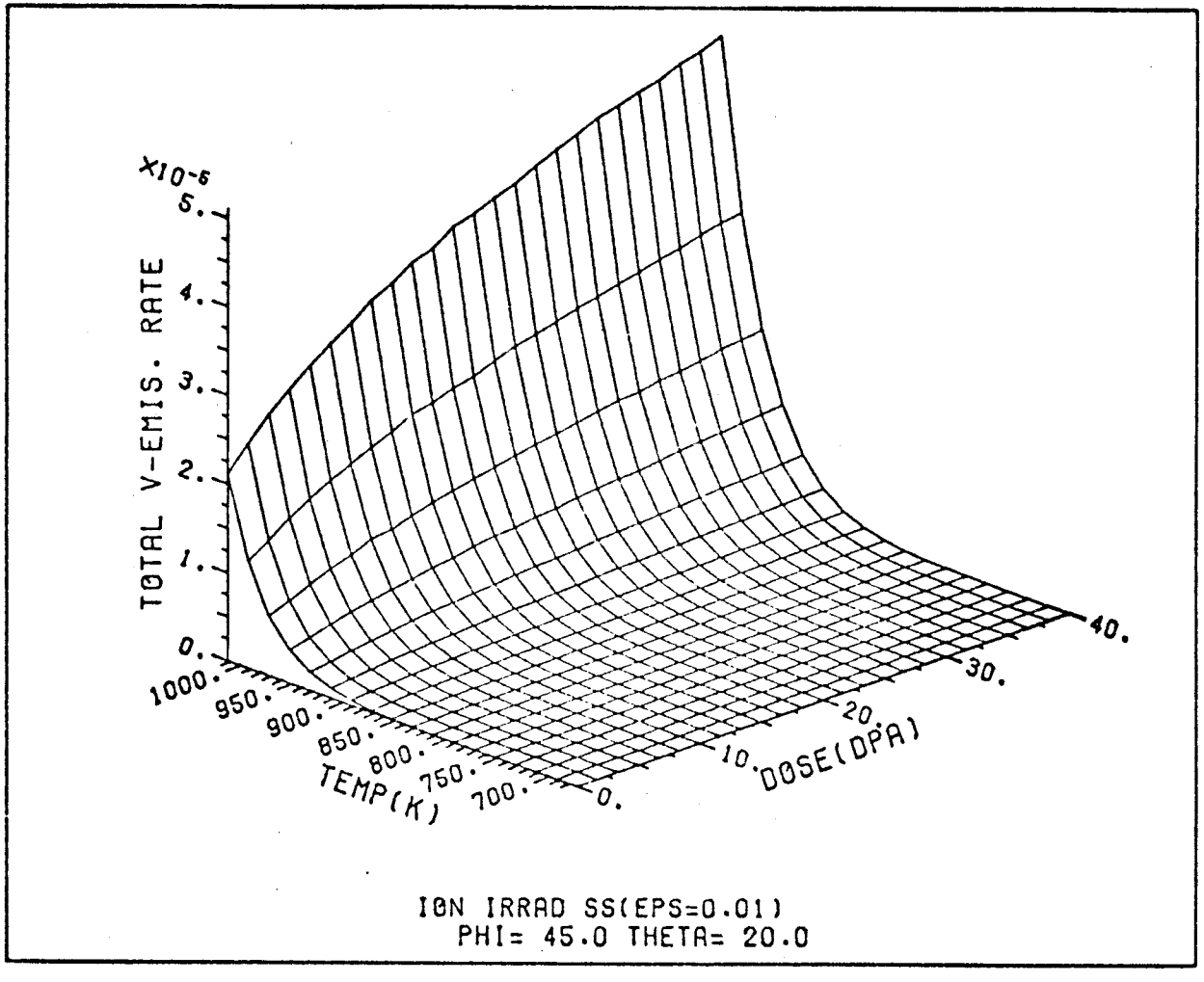

Fig. (8.16). 3-Dimensional plot of total vacancy thermal emission rate (at/at/sec) as a function of dose and temp. in ST S.S. The dose rate is 10^{-3} dpa/sec and the cascade efficiency is 0.01.

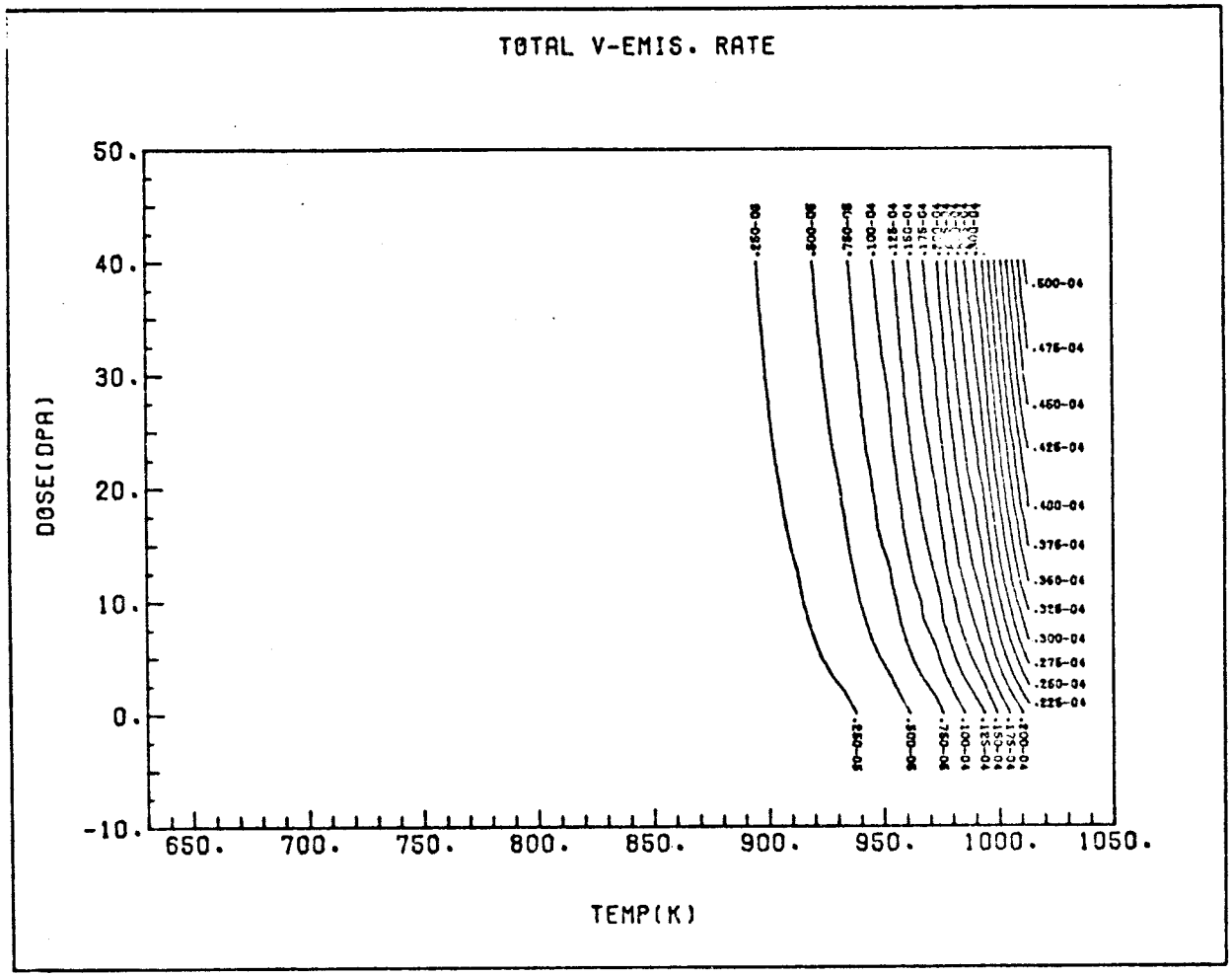

Fig. (8.17). Contour plot of total vacancy thermal emission rate (at/at/sec) as a function of dose and temp. in ST S.S. The dose rate is 10^{-3} dpa/sec and the cascade efficiency is 0.01.

total vacancy emission rate can approach 5% of the gross production rate.

VIII.C.1.c.ii. Point Defect Sink Removal Rates

Sink removal rates are defined as the rates at which different types of sinks (i.e., i-loops, edge dislocations, v-loops, voids,...,etc.) remove point defects from the matrix. Point defect concentrations are determined by the balance between their production (via irradiation or thermal emission) and their removal (via different sinks or recombination).

We will concentrate here on the total rate at which various sinks remove point defects. The quantity displayed in Figure (8.18) and (8.19) is given by:

$$\text{Vacancy Removal Rate} = D_v C_v \{4\pi N_c R_c + \rho_d\} \qquad (8.2)$$

where ρ_d is the total dislocation density.

The results of the present work show that the vacancy removal rate is not a strong function of temperature or dose except for a transient at ∿650-750°K up to a few dpa. This transient occurs because of the rapid buildup of vacancy loops in the first few hundredths of a dpa followed by rapid vacancy emission which adds vacancies to those already being produced by irradiation. The time steps between the updating of defect concentrations needs to be very small to fully illustrate the initial buildup and then the longer decay of the defect concentrations.*

*In Figures (8.18) and (8.19) the dose axis starts at ∿0.5dpa to remove the artifical peaks due to the integration process.

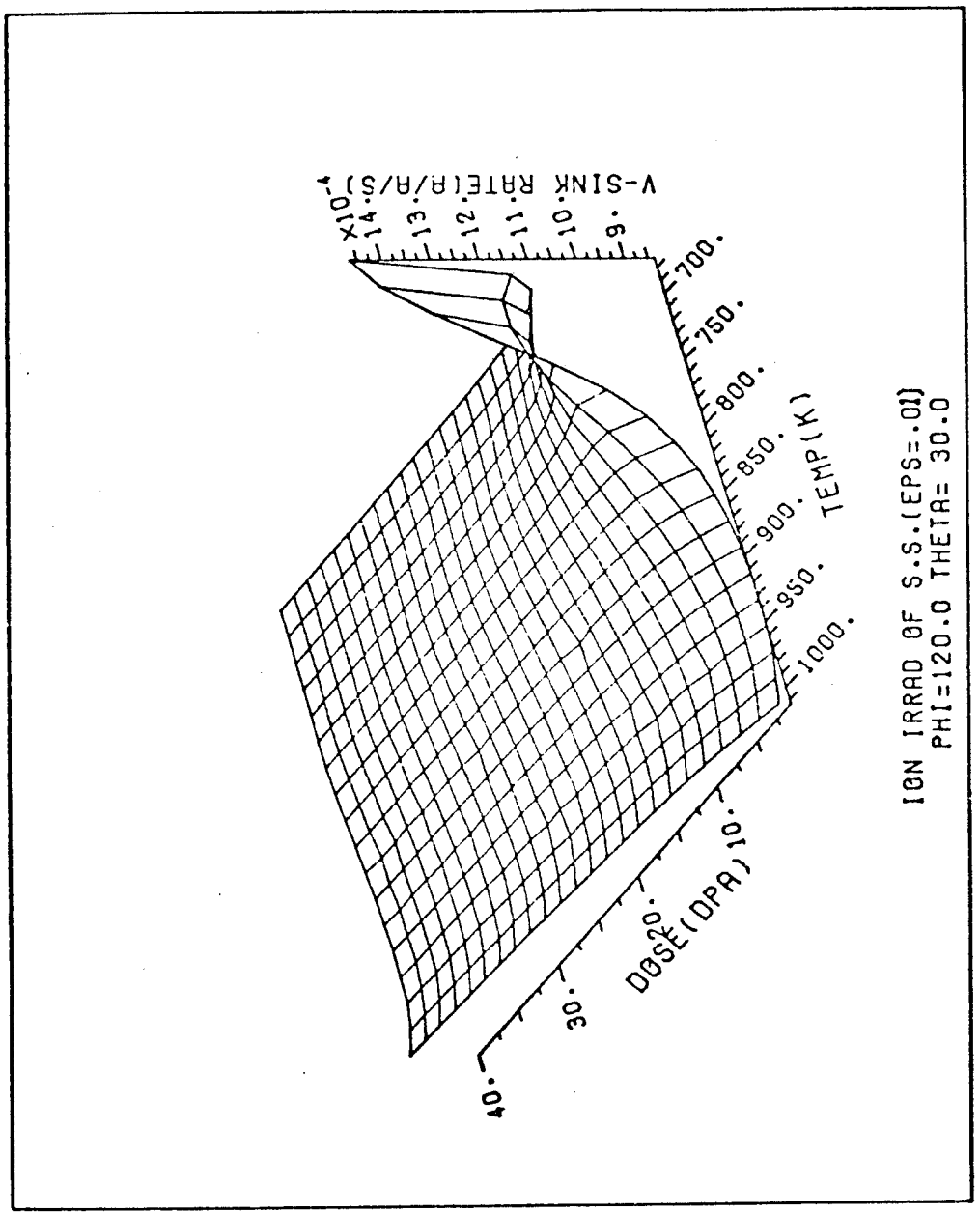

Fig. (8.18). 3-Dimensional plot of vacancy sink removal rate (at/at/sec) as a function of dose and temp. for ion irradiated ST S.S. The dose rate is 10^{-3} dpa/sec and the cascade efficiency is 0.01.

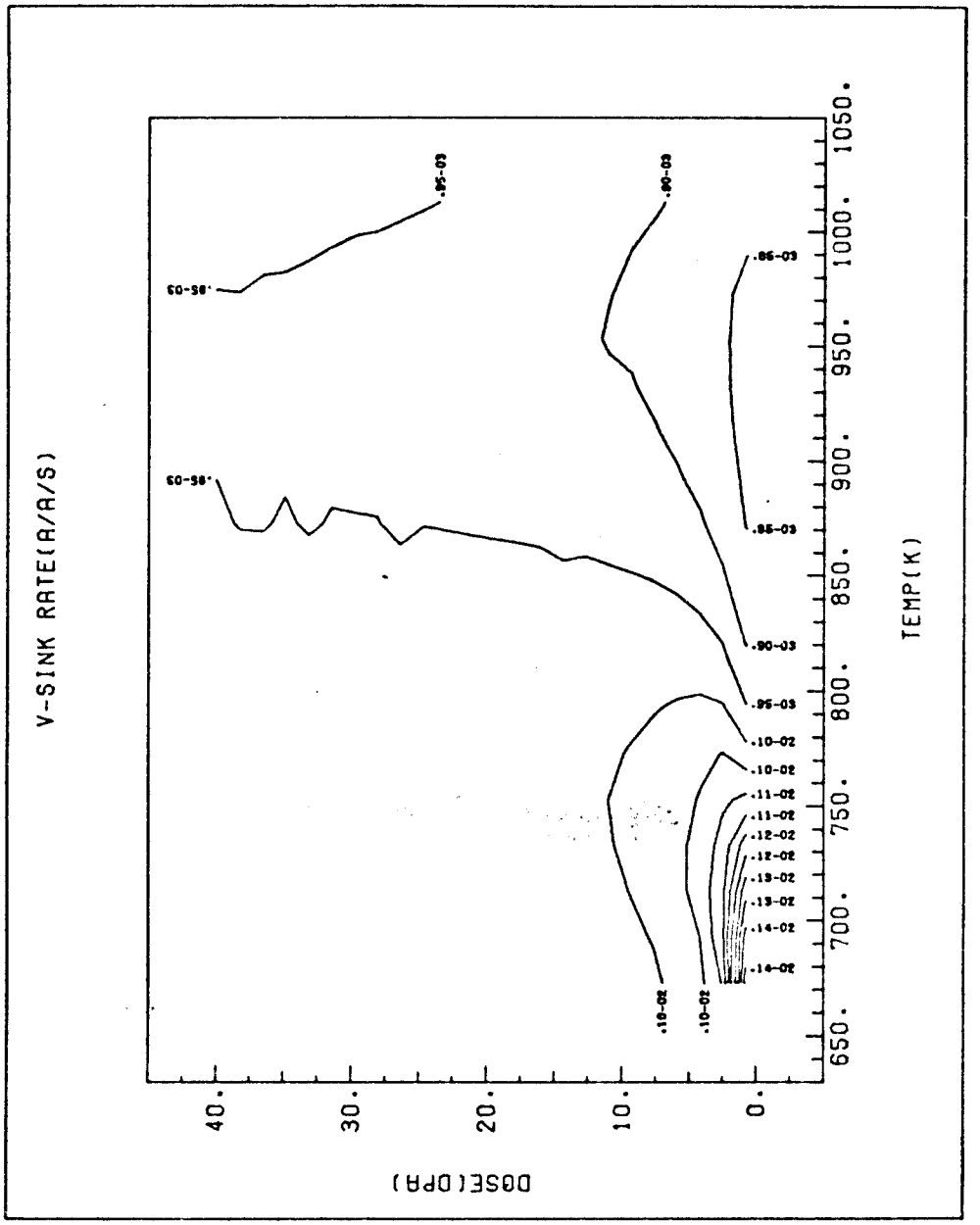

Fig. (8.19). Contour plot of vacancy sink removal rate (at/at/sec) as a function of dose and temp. for ion irradiated ST S.S. The dose rate is 10^{-3} dpa/sec and the cascade efficiency is 0.01.

The slight decrease of this removal rate with temperature is due to the dominance of the temperature dependence of the sink term in Equation (8.2) over the vacancy flux ($D_v C_v$). The increase of the removal rate with increasing dose is due to growth of voids and loops with irradiation dose. This feature is seen more clearly at high temperatures in Figure (8.19).

Total interstitial sink removal rate is given by:

$$\text{Interstitial Removal Rate} = D_i C_i \{4\pi N_c R_c + Z_p \rho_d\} \qquad (8.3)$$

The behavior of the interstitial sink removal rate is similar to that of the vacancies, the only difference being the thermal vacancy population.

It will be shown later (Figures (8.28) and (8.29) that the void equivalent sink strength ($4\pi N_c R_c$) is about 2 order of magnitude lower than the dislocation sink strength ($Z_i \rho_d$) and, therefore, anything that influences the number and size of dislocation loops (i.e., ε or nucleation agents) will greatly affect the vacancy and interstitial sink strengths.

VIII.C.1.c.iii. Point Defects Recombination Rate

The recombination rate for point defects, as shown in Figures (8.20) and (8.21) reveals a sharp recombination rate transient at low temperatures. Quantitatively, this behavior is described in Table (8.1).

The fraction of defects removed by recombination is about equal to 1/2 of the total sink removal rate at the start of the irradiation, but it drops rapidly after that at

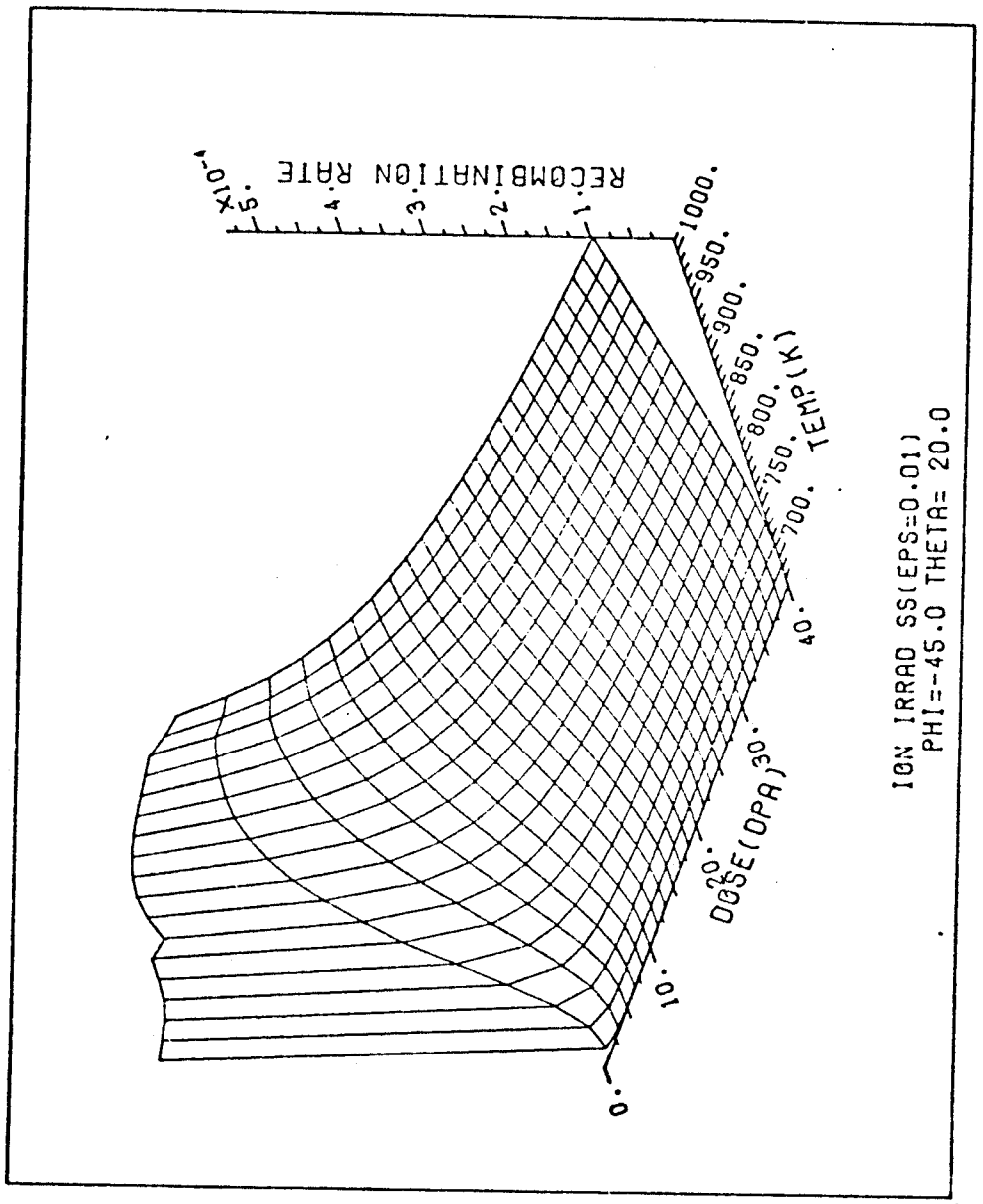

Fig. (8.20). 3-Dimensional plot of point defect recombination rate (at/at/sec) as a function of dose and temp. for ion irradiated ST S.S. The dose rate is 10^{-3} dpa/sec and the cascade efficiency is 0.01.

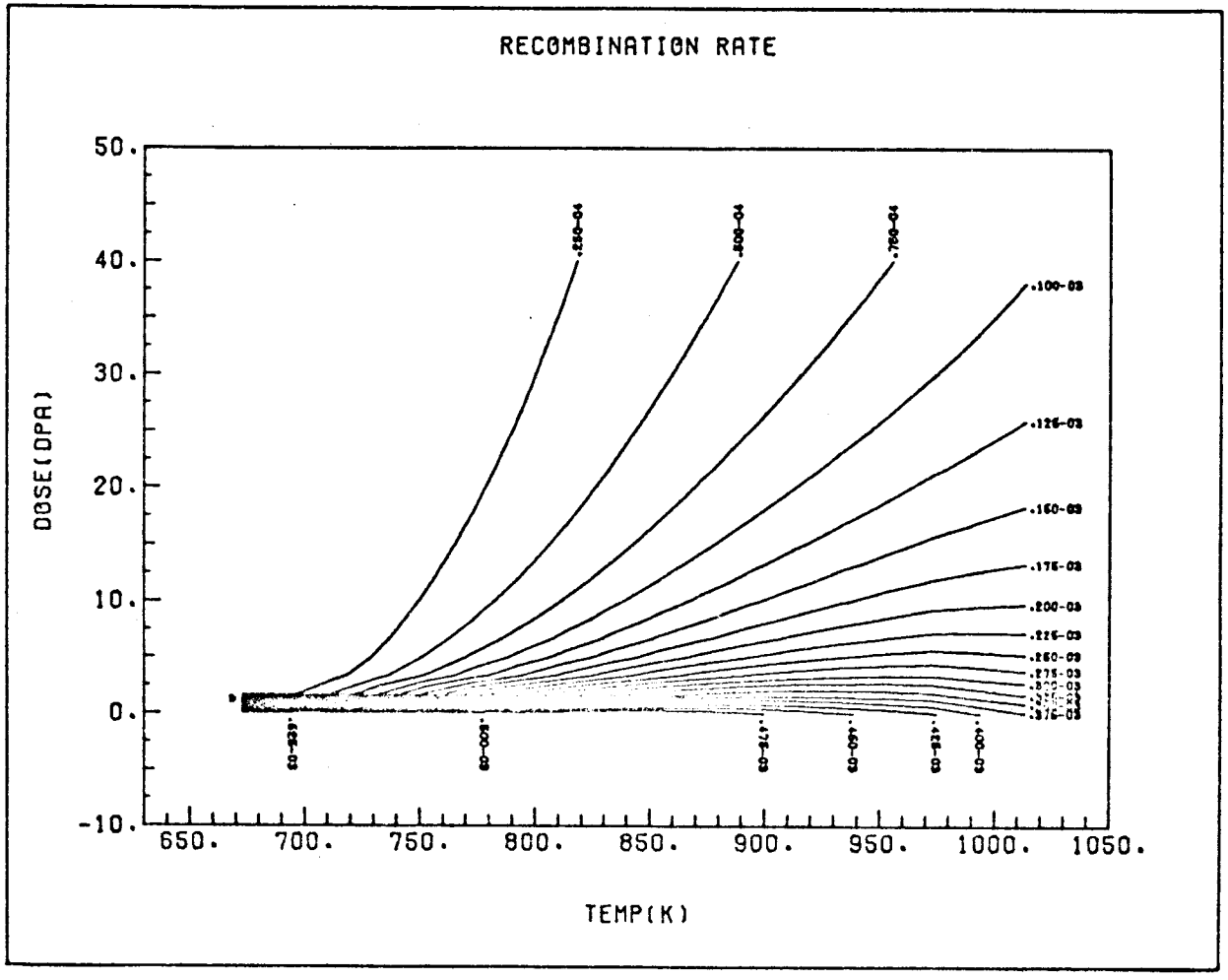

Fig. (8.21). Contour plot of point defect recombination rate (at/at/sec) as a function of dose and temp. for ion irradiated ST S.S. The dose rate is 10^{-3} dpa/sec and the cascade efficiency is 0.01.

TABLE (8.1)

Effectiveness of Recombination as a Means of Removing Point Defects

Temperature °C	% Point Defect Removal by Recombination		
	0 dpa	2.5 dpa	40 dpa
400	50	2	∿0
700	40	30	8

low temperatures. Basically, the introduction of a high density of vacancy loops makes it more likely that vacancies and interstitials will find the loops before they find each other. At higher temperatures the drop off in recombination rate with dose also occurs, but it is much less pronounced. This behavior is due to the lower loop line density at the higher temperatures and the higher mobility of the defects.

VIII.C.1.d. Microstructural Information

VIII.C.1.d.i. Vacancy Loop Line Dislocation Density

The production rates of vacancy loop number density and vacancy fraction in vacancy loops are constant with irradiation (κ_1 and κ_2) while the decay rates (Λ_1 and Λ_2) are acutely temperature dependent. Once vacancy loops are born, they tend always to shrink because of the preferential attraction of interstitials and vacancy emission (evaporation of vacancies from their surfaces). Vacancy emission is also very sensitive to temperature as was pointed out in the section on rate processes (Figure (8.16)). The net result is that the

vacancy loop line density is only important at low temperatures (Figures (8.22) and (8.23)). Another important point is that it takes a long irradiation time for the vacancy dislocation density to saturate at low temperatures while it saturates quickly at high temperatures due to increased shrinkage rates.

VIII.C.1.d.ii. Interstitial Loop Dislocation Density

The temperature dependence of interstitial loop line density is essentially exponential due to the previously chosen nucleation condition for the number density. Interstitial loops always grow by either receiving an excess flux of interstitials (biased growth) or by thermally emitting vacancies. They exhibit no net shrinkage behavior (except at very high temperatures due to abundance of thermal vacancies) because thermal emission of interstitials has a diminishingly small value due to the large interstitial formation energy. As a consequence of the described physical behavior, interstitial loop dislocation density goes up with increasing dose. The behavior is illustrated in Figures (8.24) and (8.25).

VIII.C.1.d.iii. Total Dislocation Density

The total dislocation density (Figures (8.26) and (8.27) is the sum of three components: (1) Initial deformation produced dislocations (10^8 lines/cm^2 in this case), (2) vacancy loop line dislocation density (Figures (8.22) and (8.23)), and (3) interstitial loop line dislocation density (Figures (8.24) and (8.25)). A comparison of Figures (8.22) and (8.26)

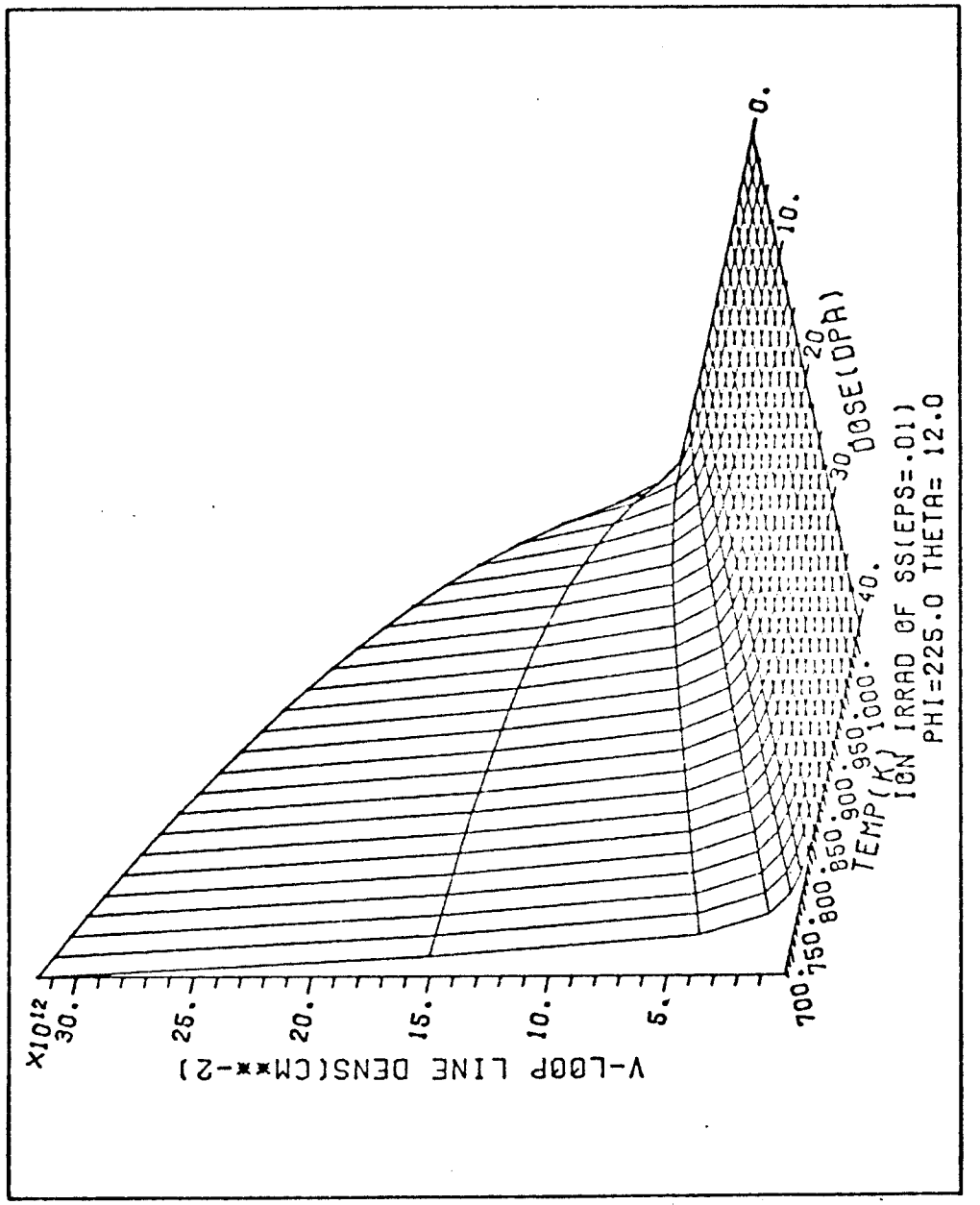

Fig. (8.22). 3-Dimensional plot of vacancy loop line dislocation density (cm/cm^3) as a function of dose and temp. for ion irradiated ST S.S. The dose rate is 10^{-3} dpa/sec and the cascade efficiency is 0.01.

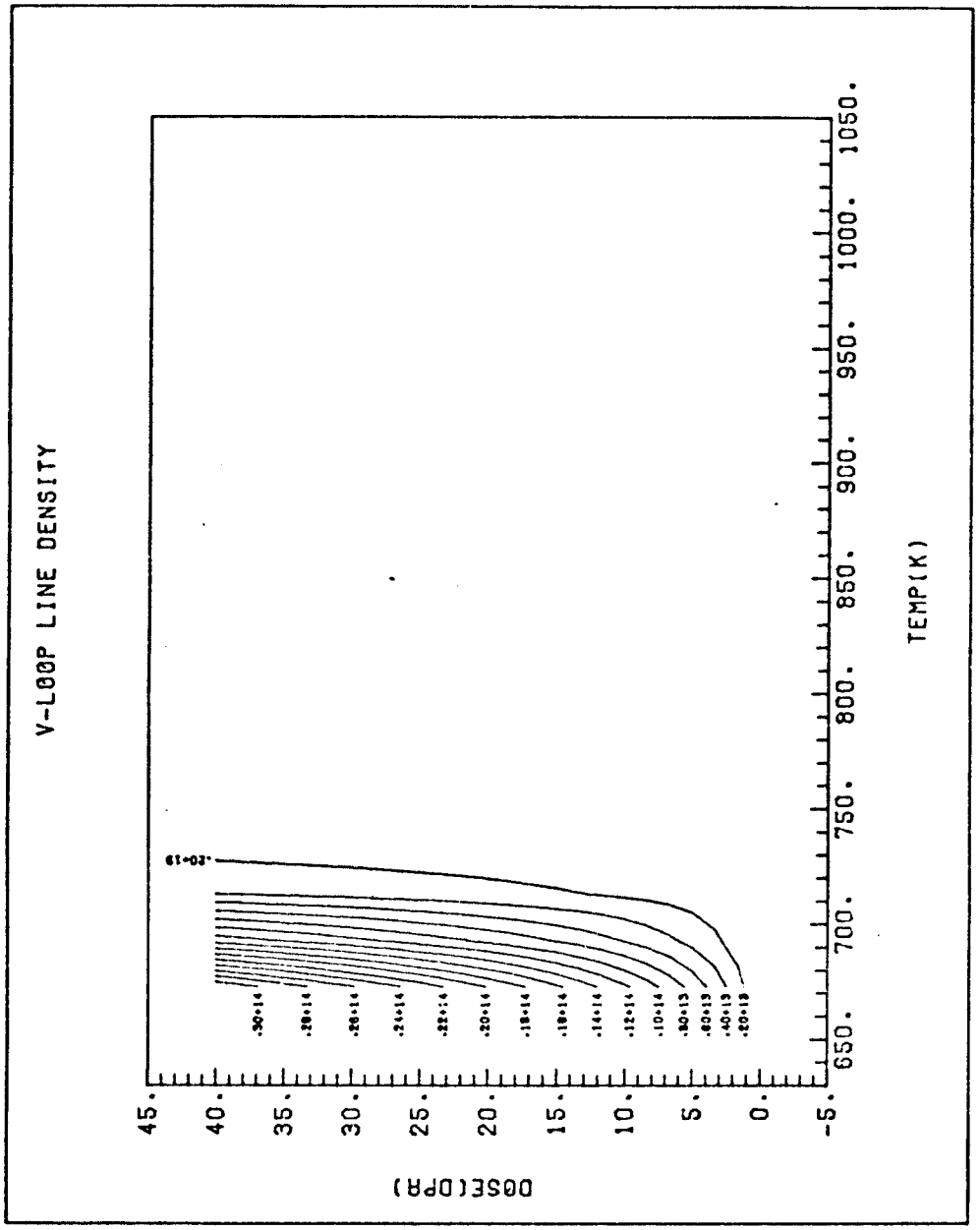

Fig. (8.23). Contour plot of vacancy loop line dislocation density (cm/cm^3) as a function of dose and temp. for ion irradiated ST S.S. The dose rate is 10^{-3} dpa/sec and the cascade efficiency is 0.01.

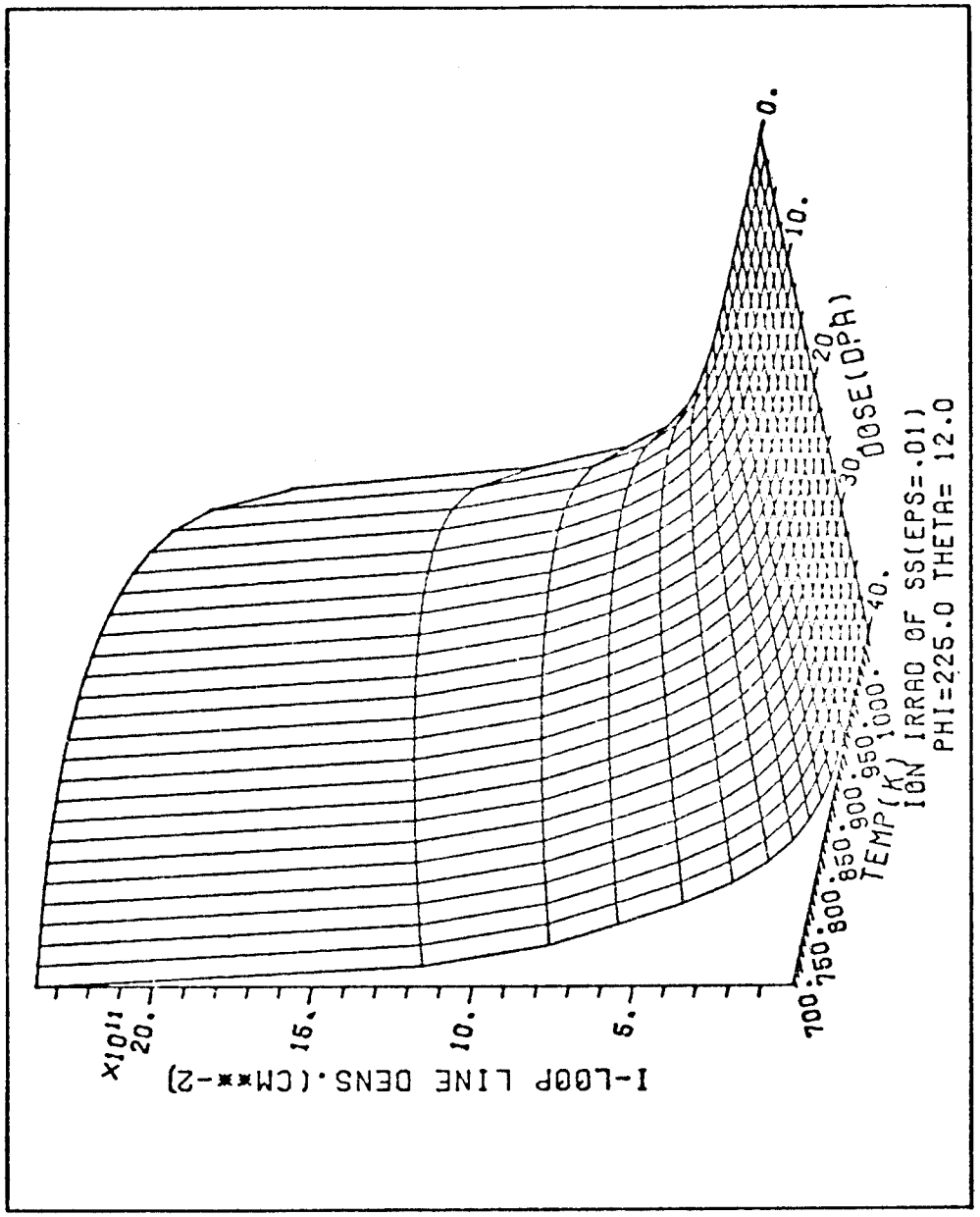

Fig. (8.24). 3-Dimensional plot of interstitial loop line density (cm/cm^3) as a function of dose and temp. for ion irradiated ST S.S. The dose rate is 10^{-3} dpa/sec and the cascade efficiency is 0.01.

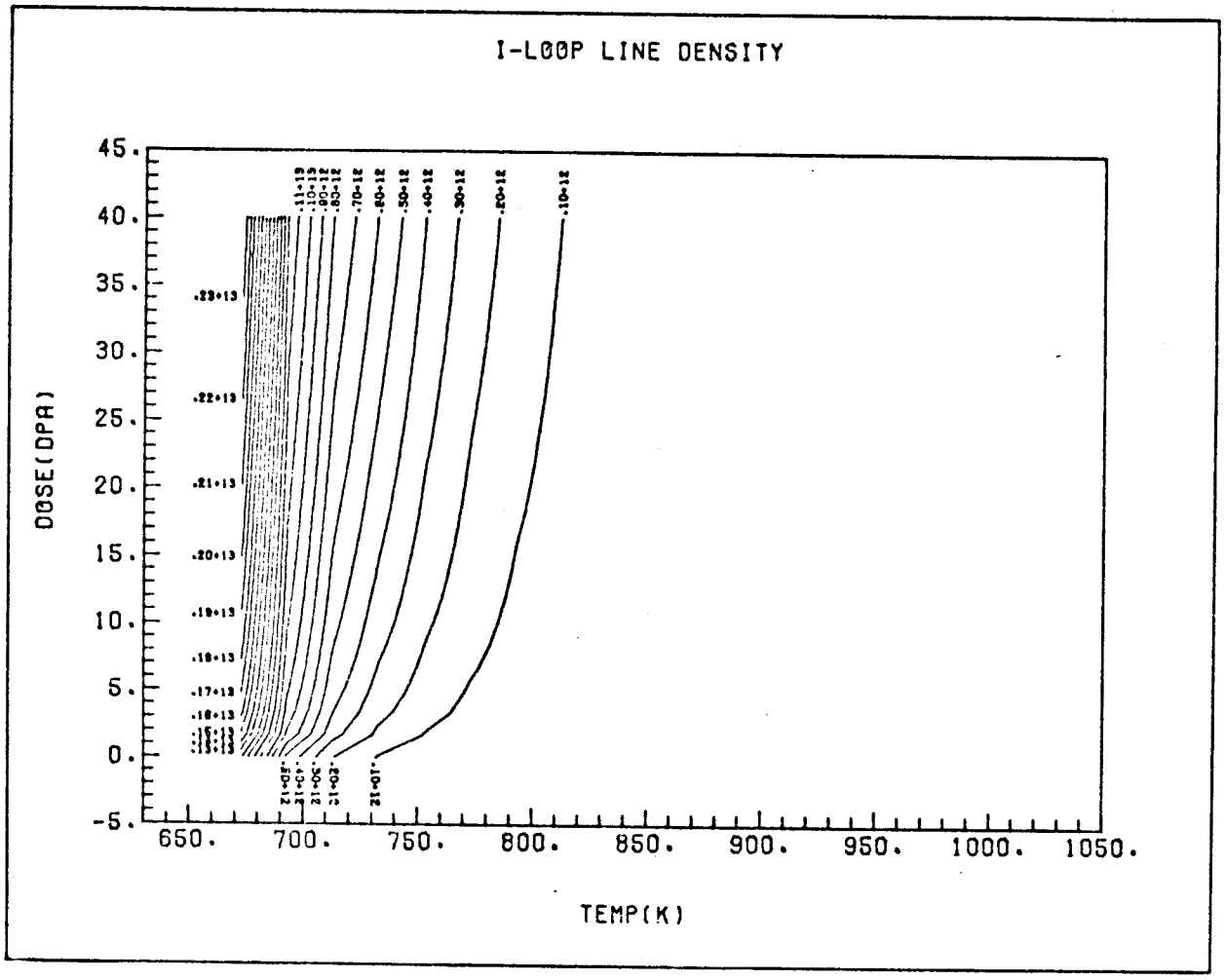

Fig. (8.25). Contour plot of interstitial loop line density (cm/cm^3) as a function of dose and temp. for ion irradiated ST S.S. The dose rate is 10^{-3} dpa/sec and the cascade efficiency is 0.01.

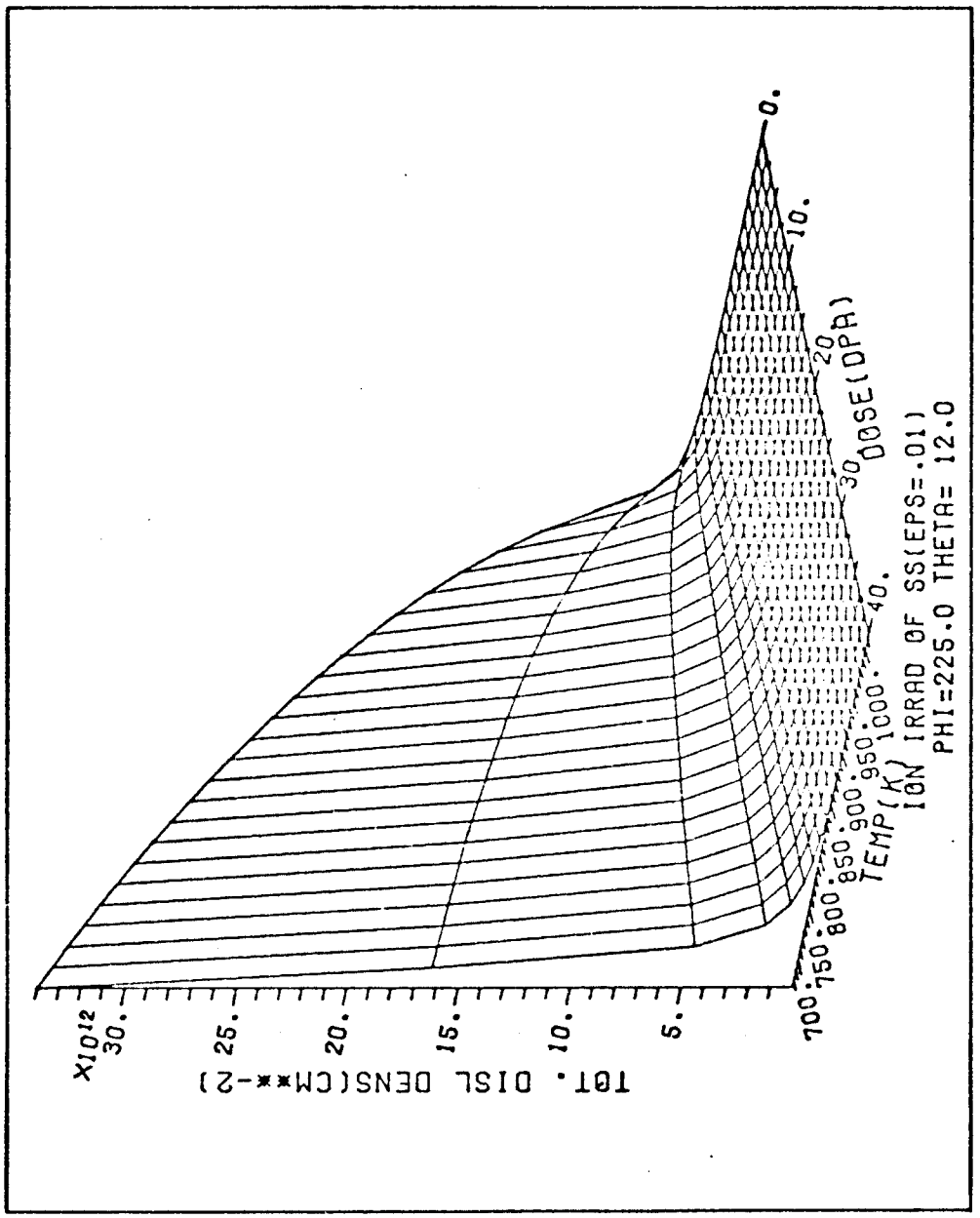

Fig. (8.26). 3-Dimensional plot of total dislocation line density (cm/cm^3) as a function of dose and temp. for ion irradiated ST S.S. The dose rate is 10^{-3} dpa/sec and the cascade efficiency is 0.01.

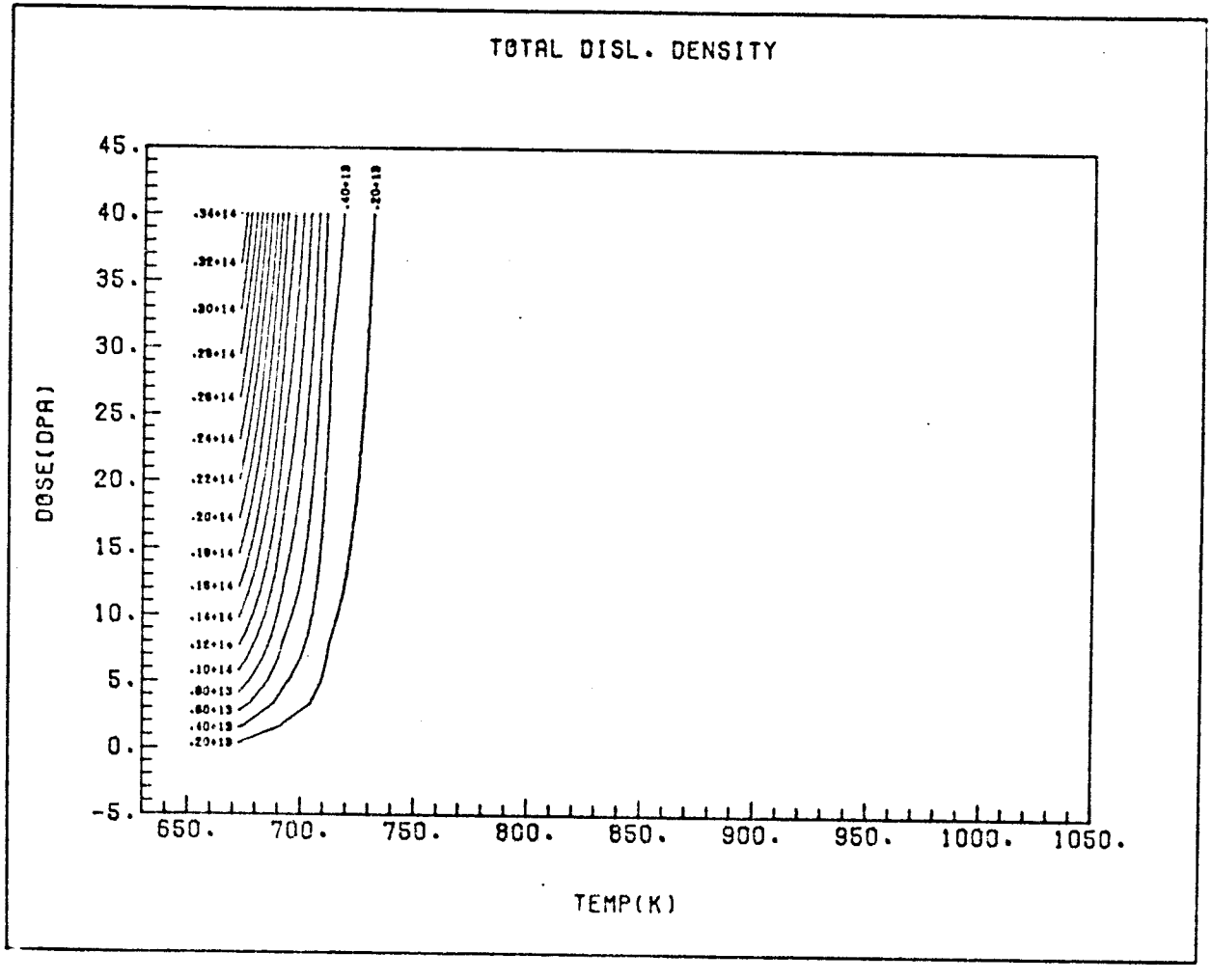

Fig. (8.27). Contour plot of total dislocation line density (cm/cm^3) as a function of dose and temp. for ion irradiated ST S.S. The dose rate is 10^{-3} dpa/sec and the cascade efficiency is 0.01.

shows that the major contribution to the total dislocation density is from vacancy loops. Obviously, it is extremely important as to what value of ε is used for the growth calculation.

VIII.C.1.d.iv. Effective Void Sink Strength ($4\pi R_{c-c} N_{c-c}$)

This quantity is of special importance in the analysis of metal swelling under irradiation because ;

(1) It represents the total non-biased sink through which vacancies and interstitials are lost.

(2) It competes with biased sinks in the matrix (mainly dislocations) to remove point defects.

If this quantity is large compared to the total dislocation density, the swelling rate will be small. This is intuitively understandable since "almost" equal numbers of point defects are dumped into voids and the effect of bias is small. From Figures (8.28) and (8.29) one can see that the void equivalent sink is only a moderate function of temperature. If one compares Figures (8.26) and (8.28) it is clear that at low temperatures total dislocation line density is 2 orders of magnitude greater than void equivalent sink causing a high growth rate. However, at high temperatures, the dislocation density drops much faster than void equivalent sink.

VIII.C.2. Accelerator Conditions with Low Cascade Production Efficiency ($\varepsilon = 0.001$ and $P = 10^{-3}$ dpa/sec)

Reducing the cascade collapse efficiency leads to releasing more free vacancies with the consequence of enhanced void

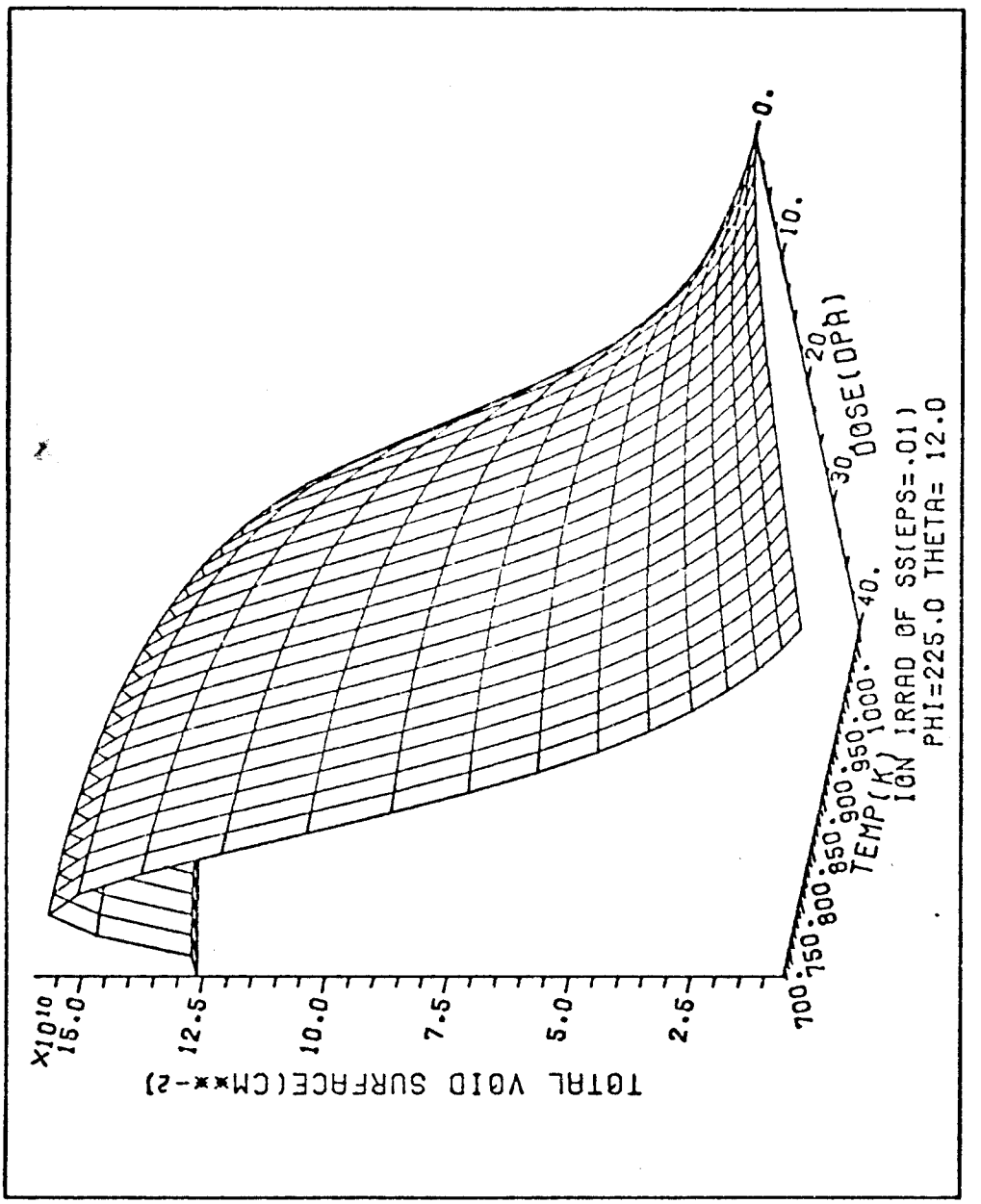

Fig. (8.28). 3-Dimensional plot of equivalent void sink (cm/cm^3) as a function of dose and temp. for ion irradiated ST S.S. The dose rate is 10^{-3} dpa/sec and the cascade efficiency is 0.01.

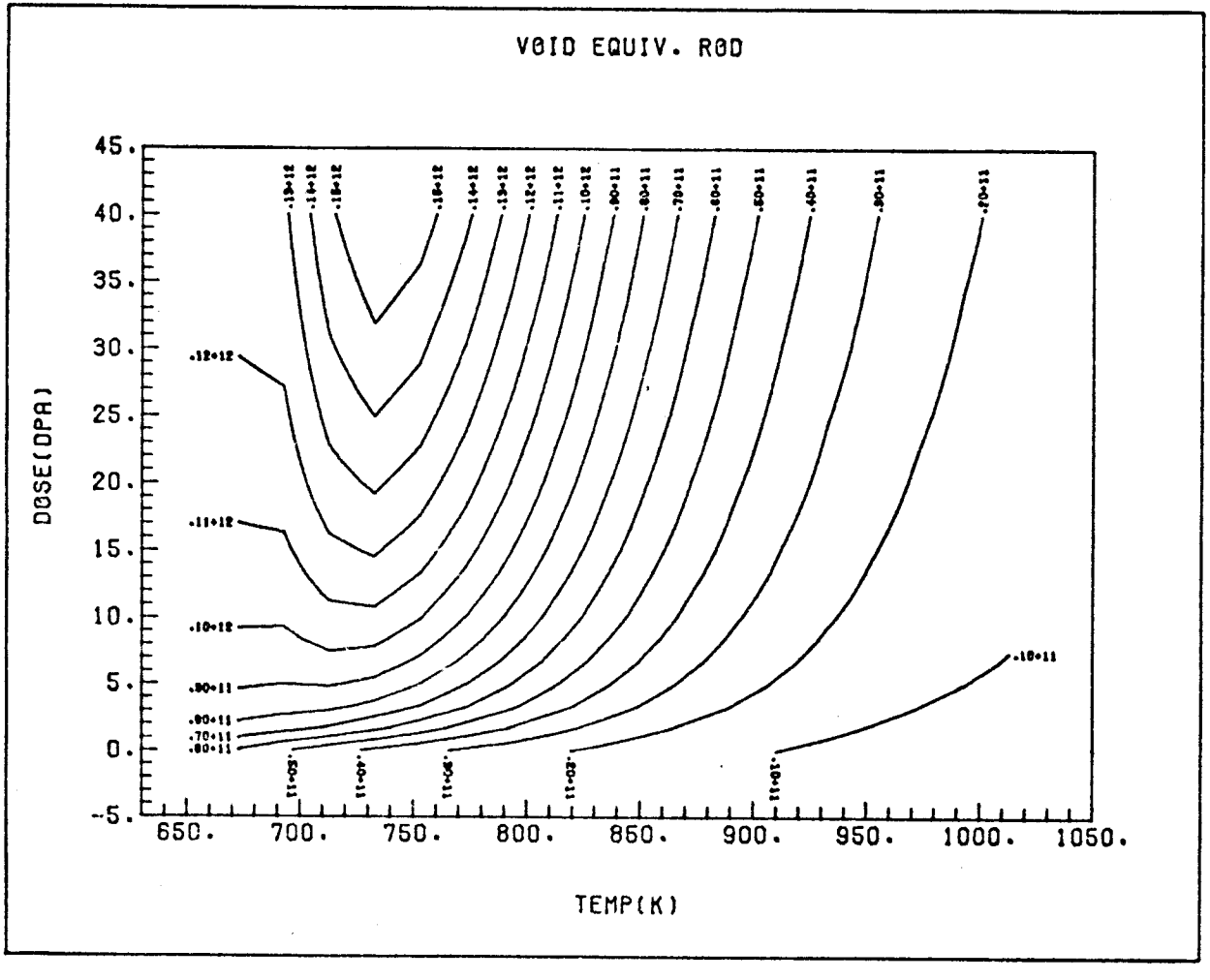

Fig. (8.29). Contour plot of equivalent void sink (cm/cm^3) as a function of dose and temp. for ion irradiated ST S.S. The dose rate is 10^{-3} dpa/sec and the cascade efficiency is 0.01.

swelling.

The swelling behavior is qualitatively the same as before, as a function of temperature and dose. However, there is a 15% enhancement of swelling at the peak over the $\varepsilon = 0.01$ value as shown in Figures (8.30) and (8.31).

Interstitial loop dislocation density is shown to be larger than the $\varepsilon = 0.01$ case (Figures (8.24) and (8.25)). This is expected because interstitial loops receive the flux of interstitials, which would have normally gone to the vacancy loops. For the same reason, there are now more vacancies in the matrix and these cause more swelling.

Although we have reduced the cascade collapse efficiency by only an order of magnitude, the vacancy loop line density is found to go down by a factor of $\sim$30. Besides the reduction in the vacancy loop generation rate, their chance of destruction is increased with the presence of a higher interstitial flux in the matrix.

The total vacancy emission rate is reduced by 10-20% from the value associated with $\varepsilon = 0.01$ displayed in Figures (8.16) and (8.17). This slight reduction is due to a smaller number of vacancy loops that thermally emit vacancies.

VIII.C.3. Accelerator Conditions with High Cascade Efficiency ($\varepsilon = 0.044$ and $P = 10^{-3}$ dpa/sec)

Detailed computer calculations show that increasing the cascade efficiency by a factor of 4.4 from the reference case

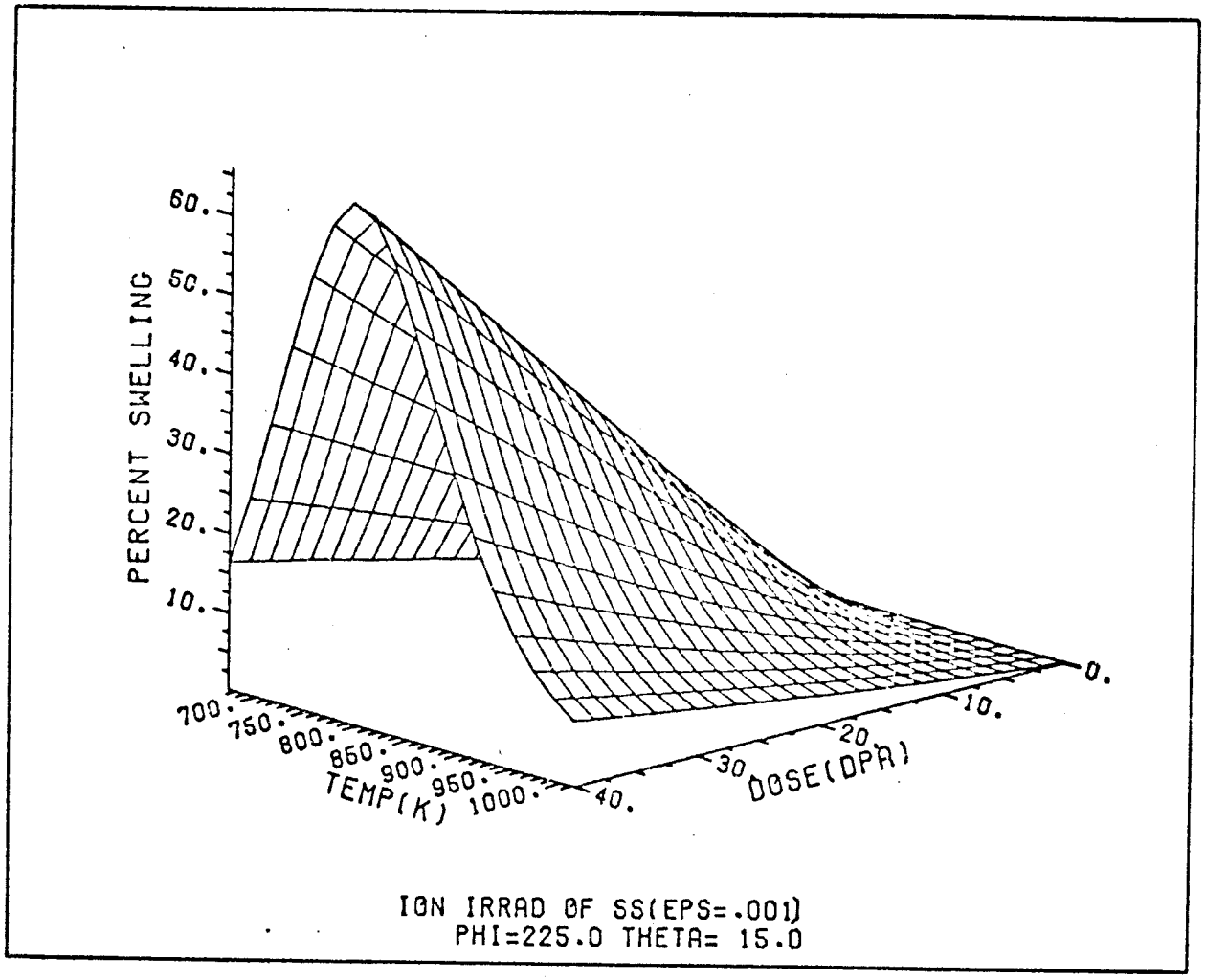

Fig. (8.30). 3-Dimensional plot of percent swelling as a function of dose and temp. for ion irradiated ST S.S. The dose rate is 10^{-3} dpa/sec and the cascade efficiency is 0.001.

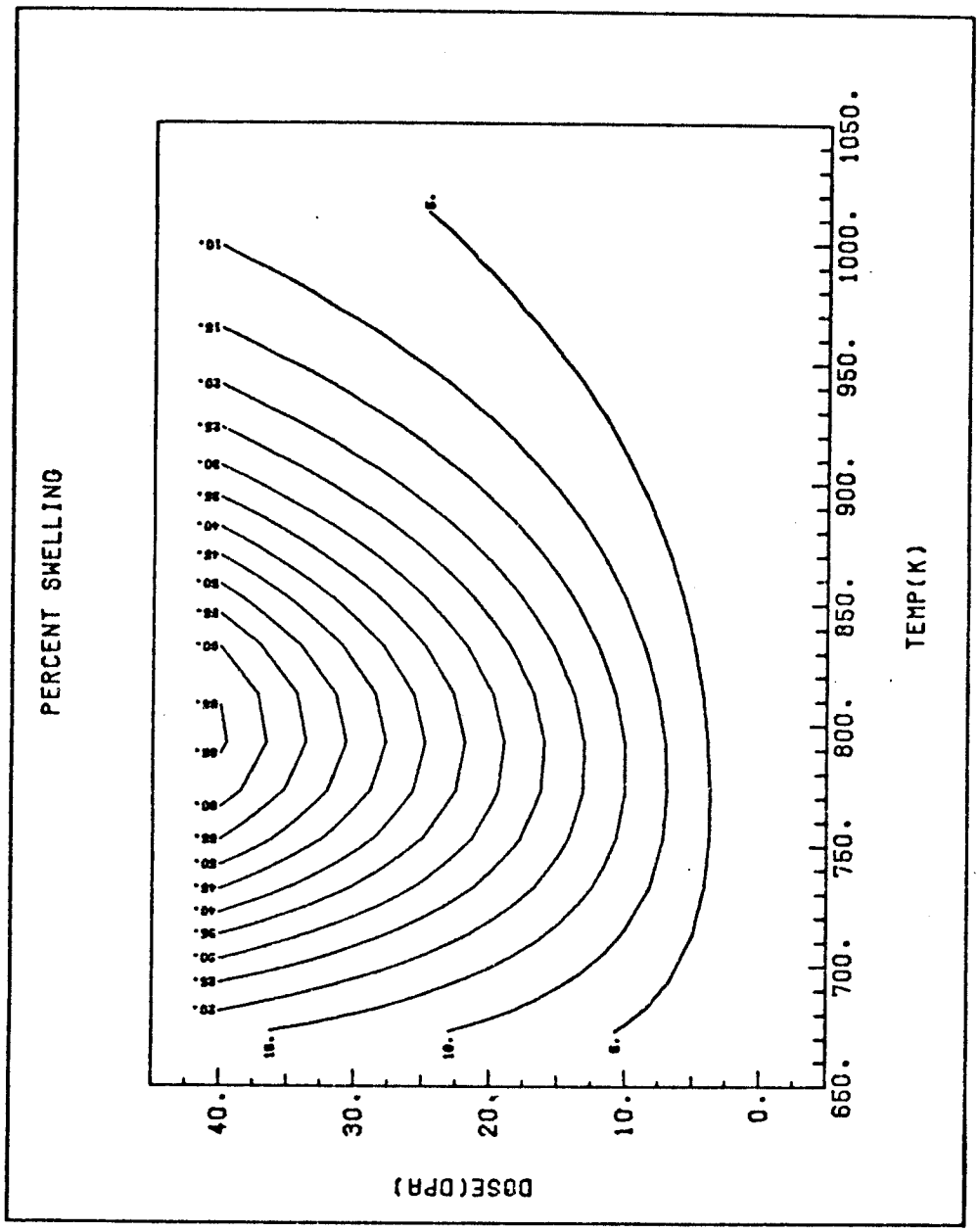

Fig. (8.31). Contour plot of percent swelling as a function of dose and temp. for ion irradiated ST S.S. The dose rate is 10^{-3} dpa/sec and the cascade efficiency is 0.001.

of $\varepsilon = 0.01$ reduces the recombination coefficient by about a factor of 2-3. The use of a higher cascade efficiency tends to remove more defects from the matrix, thus lowering the vacancy concentration. The increased absorption of vacancies and interstitials by dislocation loops (especially vacancy loops) completely dominates the defect removal process and one can safely neglect the recombination rates.

Due to the lower vacancy flux, the maximum swelling at 40 dpa and 600°C is inhibited roughly by a factor of 4-5 compared to the $\varepsilon = 0.01$ case.

The equivalent void sink ($4\pi R_c N_c$) shows the same general characteristics as before but its absolute level is reduced in this case by the presence of a large biased sink (mainly vacancy loops).

The swelling values for this case ($\sim$12% at 40 dpa) agree with the experimental values of reference (102). A 3-dimensional and contour plotting display of the results is shown in Figures (8.32) and (8.33).

VIII.D. Results for Reactor Conditions

VII.D.1. Reactor Conditions with Low Cascade Efficiency ($\varepsilon = 0.001$ and $P = 10^{-6}$ dpa/sec)

Under reactor conditions a major item of concern is the vacancy thermal emission rate because it is in the same order of magnitude as the vacancy production by irradiation. This behavior is highly sensitive to temperature and at high temperatures (above >550°C) irradiation at 10^{-6} dpa s^{-1} is comparable to the thermal generation of vacancies from the

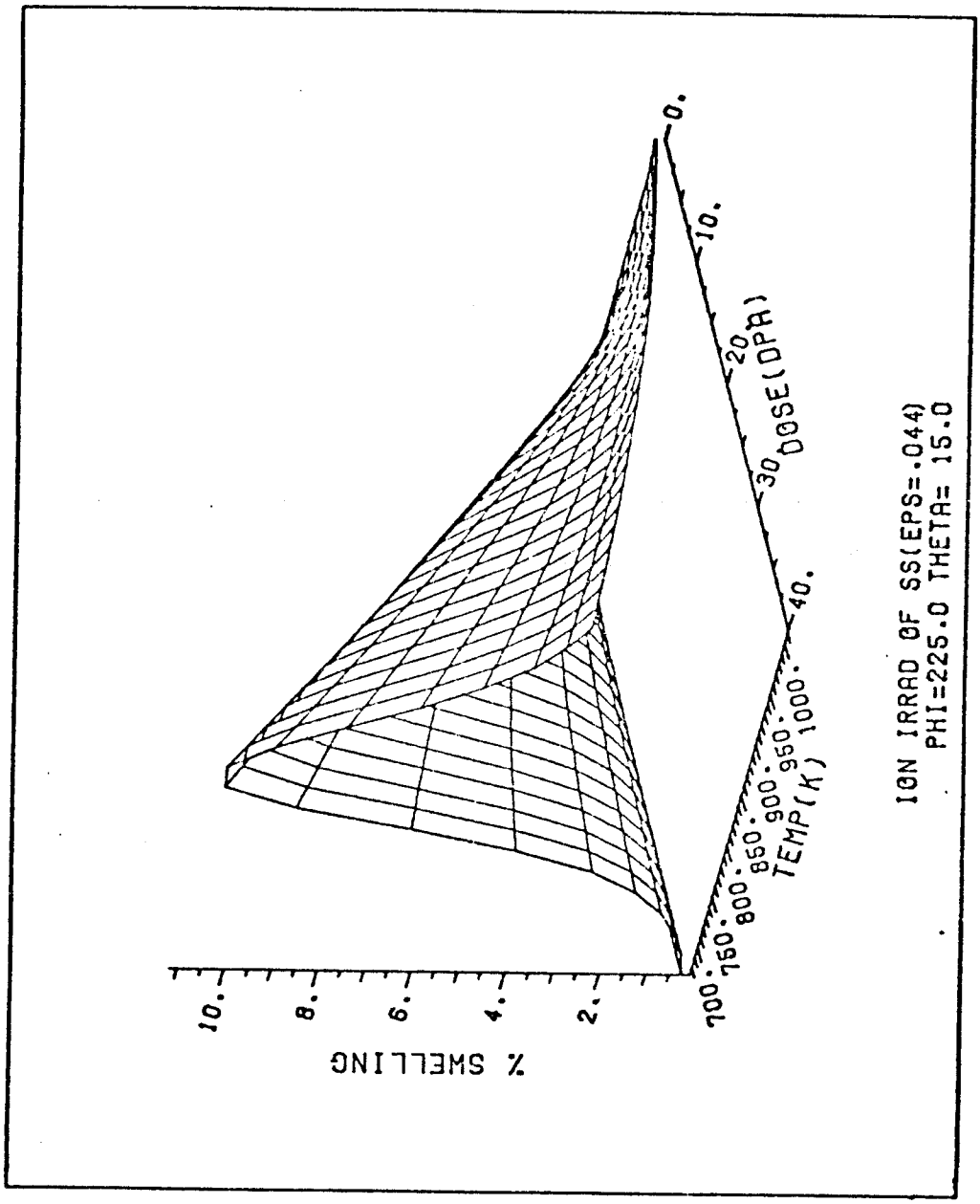

Fig. (8.32). 3-Dimensional plot of percent swelling as a function of dose and temp. for ion irradiated ST S.S. The dose rate is 10^{-3} dpa/sec and the cascade efficiency is 0.044.

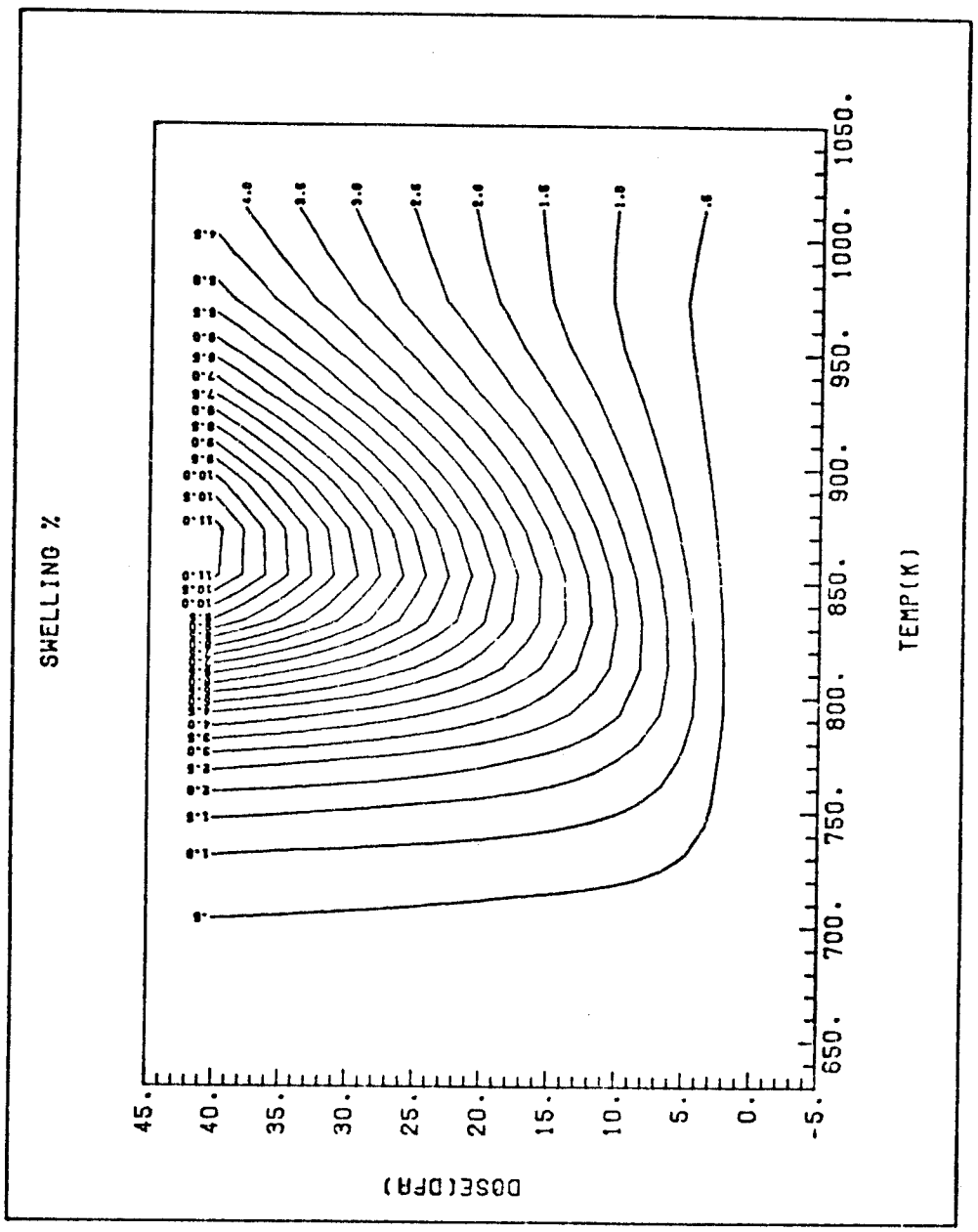

Fig. (8.33). Contour plot of percent swelling as a function of dose and temp. for ion irradiated ST S.S. The dose rate is 10^{-3} dpa/sec and the cascade efficiency is 0.044.

microstructure.

Voids have a much more difficult time growing at high temperatures than the corresponding case of 10^{-3} dpa/sec because of thermal emission. As a result, swelling as shown in Figures (8.34) and (8.35) shows a sharp drop in magnitude at high temperature. It is worthwhile to notice that no gas generation was assumed in this particular set of calculations. The presence of a large amount of gas atoms in voids would lead to gas driven swelling at high temperatures under reactor conditions.

The total vacancy emission rate (at/at/sec) is found to contribute largely to the vacancy population in the matrix. It reaches the high value of $\sim$40% of the irradiation produced vacancies at a temperature of 600°C. As demonstrated in all the previously studied cases, void vacancy emission rate was found to constitute the largest portion of total vacancy emission rate. Calculations showed that almost all irradiation produced point defects get absorbed by sinks (voids as well as dislocation loops), and that recombination is negligible in this particular case.

VIII.D.2. Reactor Conditions with High Cascade Efficiency (ε = 0.044 and P = 10^{-6} dpa/sec)

As was established previously, the swelling in this case can be reduced by increasing the cascade efficiency. Comparing the swelling curves in Figures (8.36) and (8.37) with Figures (8.32) and (8.33) we find a temperature shift for the peak swelling of about 50°C. (T_{max} is lower at the lower displacement rate). Another feature to be noticed is the higher

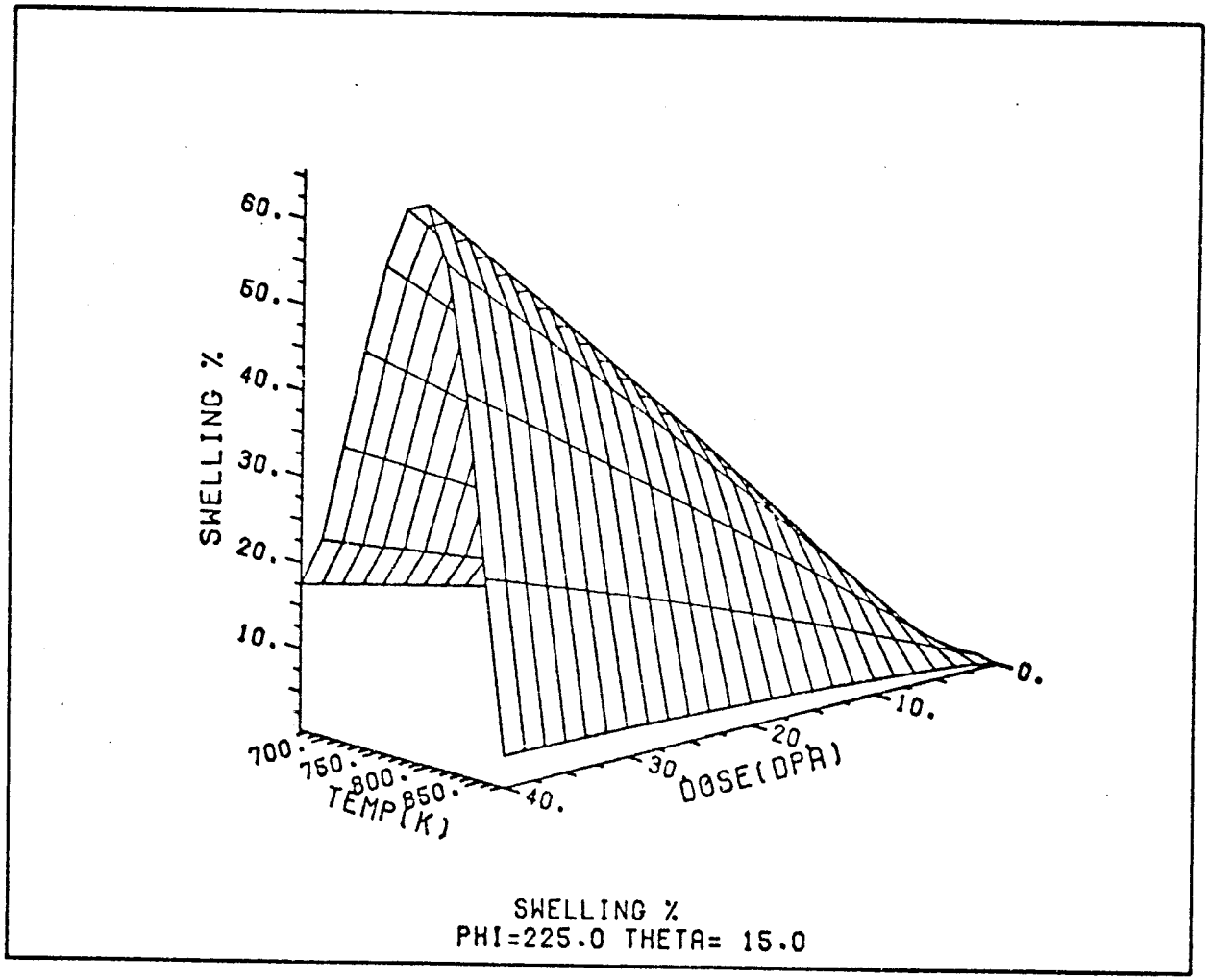

Fig. (8.34). 3-Dimensional plot of percent swelling as a function of dose and temp. for neturon irradiated ST S.S. The dose rate is 10^{-6} dpa/sec and the cascade efficiency is 0.001.

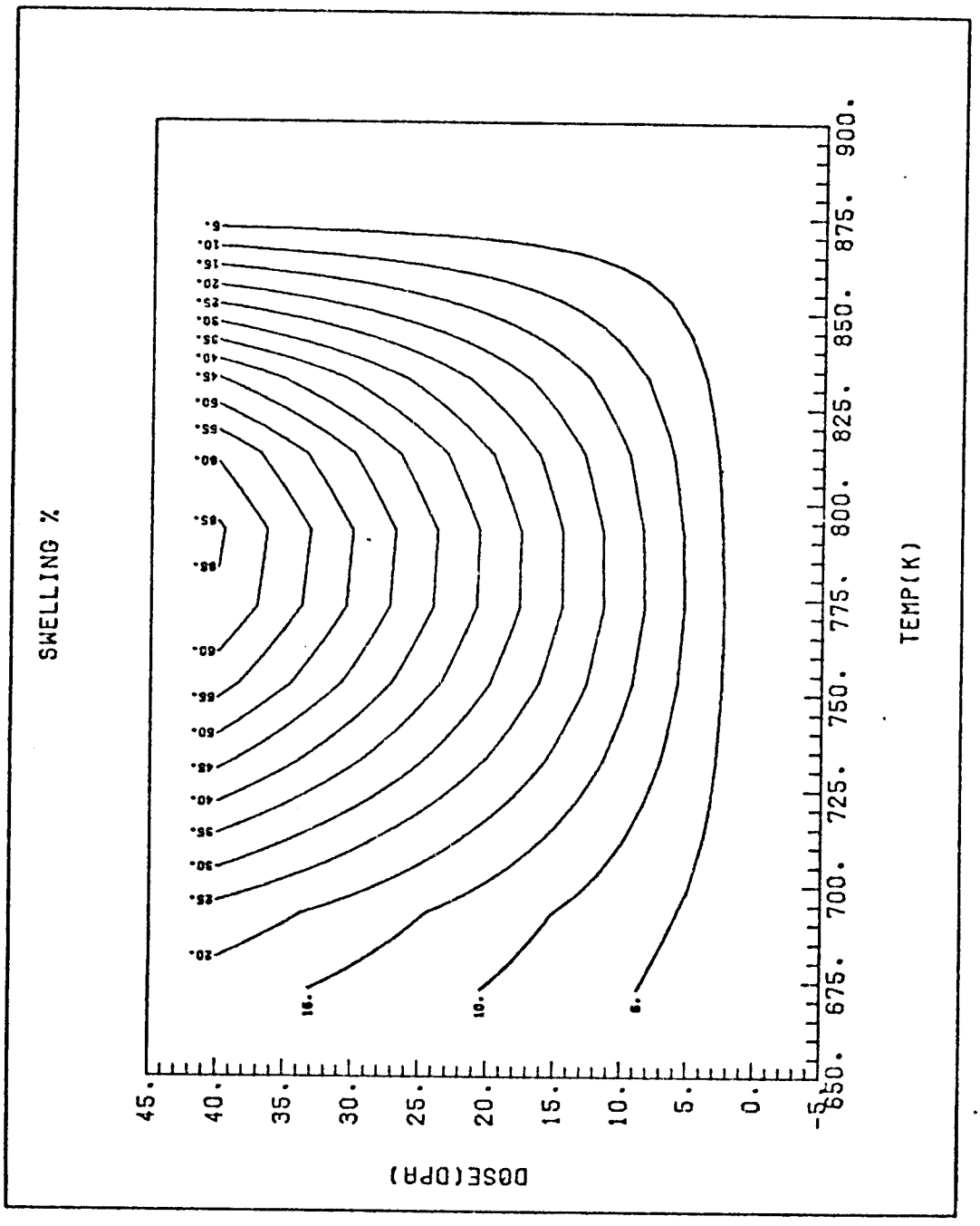

Fig. (8.35). Contour plot of percent swelling as a function of dose and temp. for neutron irradiated ST S.S. The dose rate is 10^{-6} dpa/sec and the cascade efficiency is 0.001.

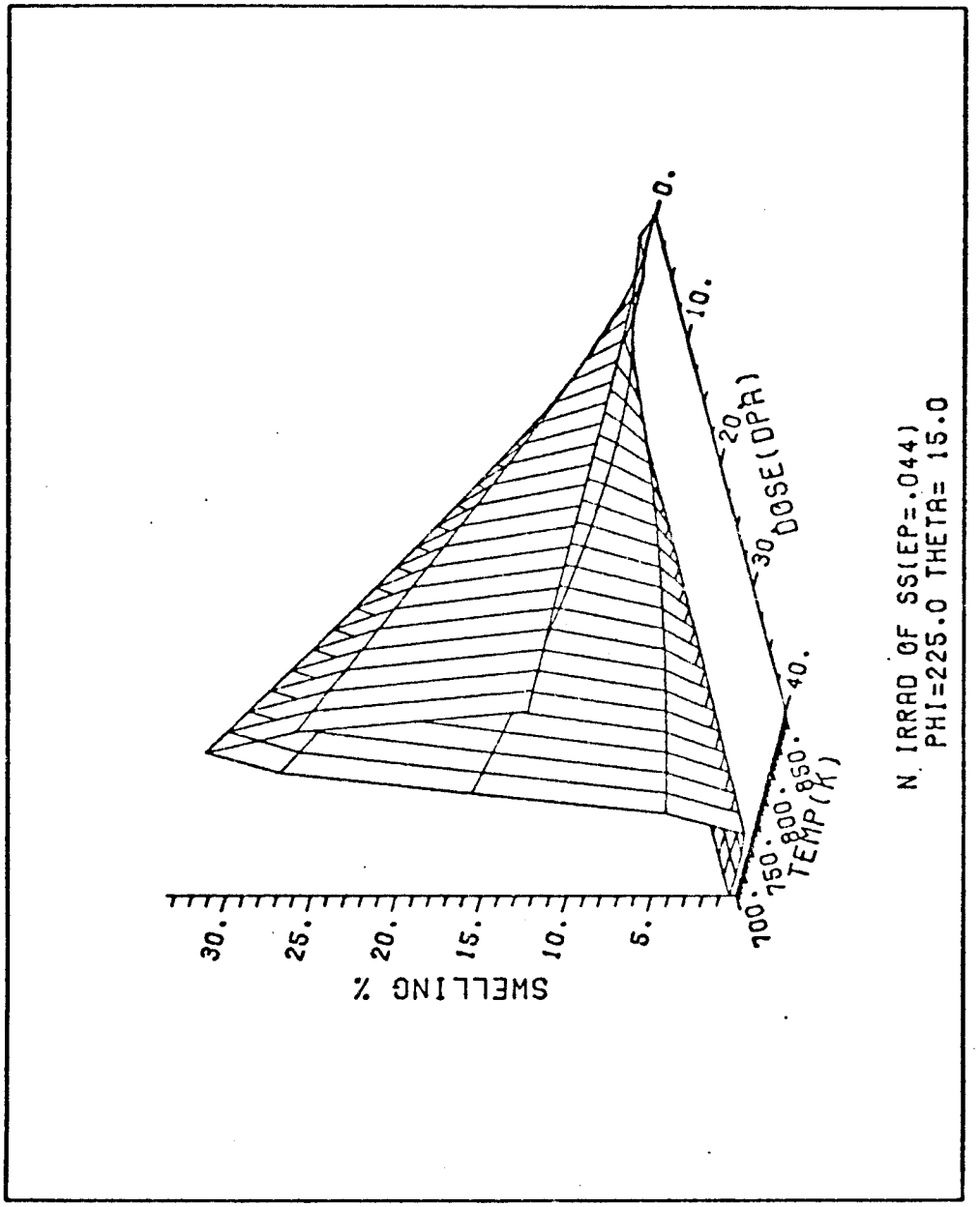

Fig. (8.36). 3-Dimensional plot of percent swelling as a function of dose and temperature for neutron irradiated ST S.S. The dose rate is 10^{-6} dpa/sec and the cascade efficiency is 0.044.

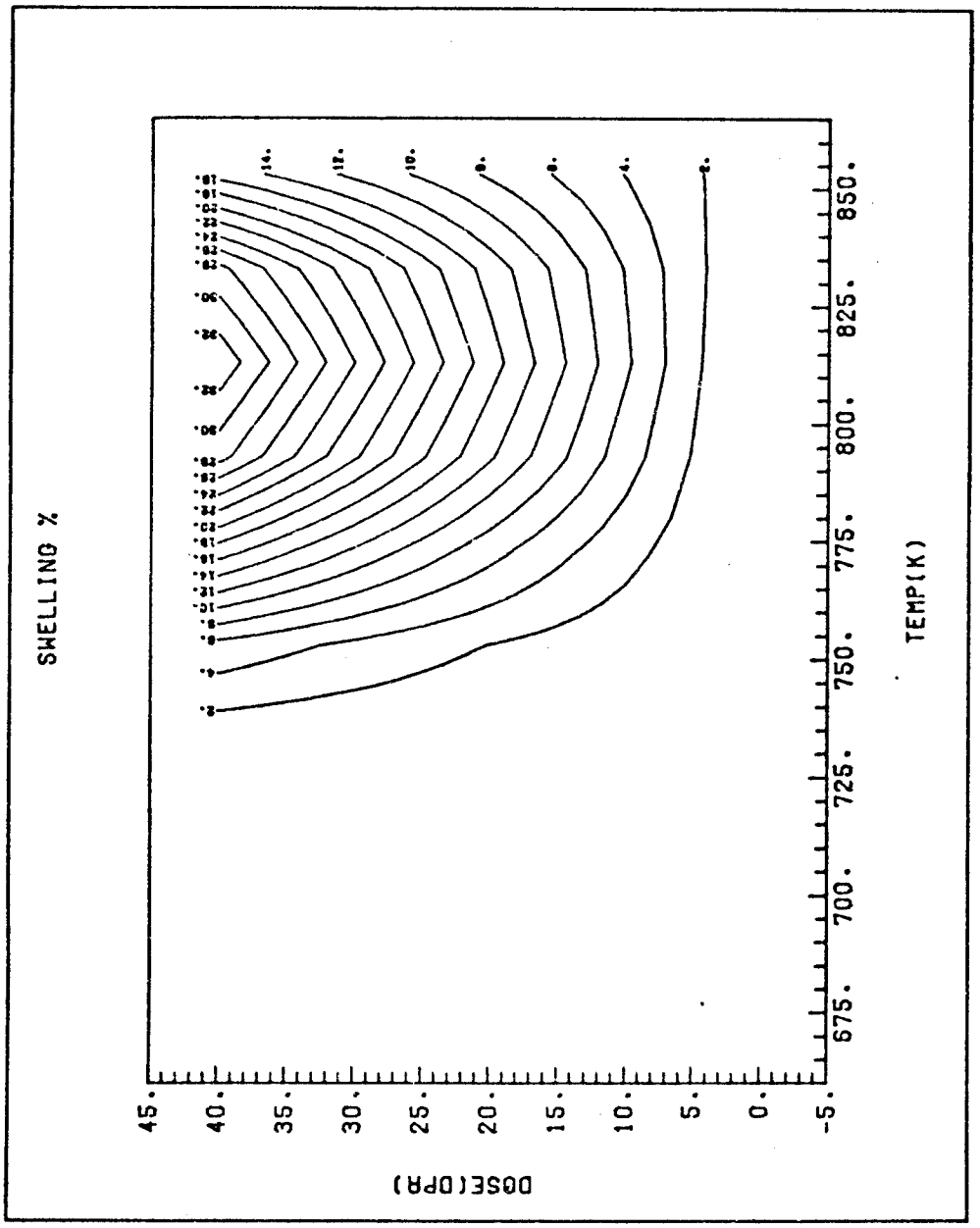

Fig. (8.37). Contour plot of percent swelling as a function of dose and temperature for neturon irradiated ST S.S. The dose rate is 10^{-6} dpa/sec and the cascade efficiency is 0.044.

peak swelling value in a reactor condition compared to the corresponding accelerator condition. These differences are attributed to the greater importance of point defect mutual recombination under accelerator conditions due to their higher concentrations.

Again, it should be noticed that the void vacancy thermal emission is over 2/3 of the total emission rate. The total thermal vacancy emission rate is also considerable (30-40% of irradiation point defect production rate, at high temperatures and high doses). At even higher temperatures, the voids will be emitting more vacancies than produced and hence would shrink signifying the upper temperature limit on void swelling.

VIII.E. Combined Effect of Cascade Collapse Efficiency and Dose Rate on Void Growth

The previous analysis related, in great detail, the fundamental point defect and microstructure processes that contribute to the phenomenon of void growth and subsequent metal swelling. The effect of the cascade collapse efficiency was established to reduce swelling for higher values of this collapse efficiency. Increasing the collapse efficiency reduces the vacancy flux that causes swelling, and it is expected that for certain values of ε, void growth will be completely inhibited. A demonstration of the boundary between void growth and no growth regimes as a function of ε and P is shown in Figure (8.38). It is seen that for stainless steel and a value of $Z_i = 1.08$, values of ε over the range 5% to 7.5% will

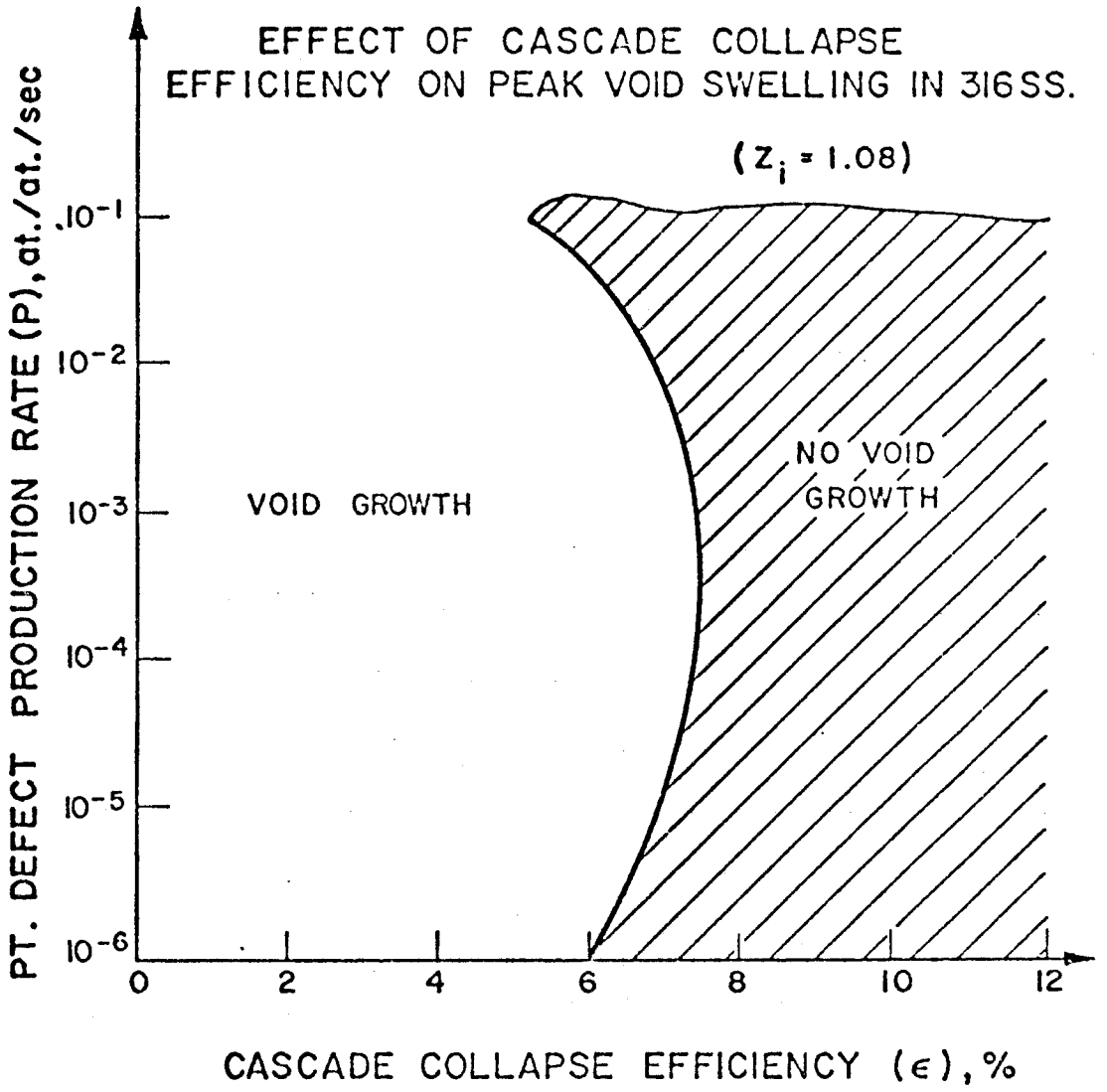
EFFECT OF CASCADE COLLAPSE
EFFICIENCY ON PEAK VOID SWELLING IN 316SS.
(Z_i = 1.08)
PT. DEFECT PRODUCTION RATE (P), at./at./sec
10^{-1}
10^{-2}
10^{-3}
10^{-4}
10^{-5}
10^{-6}
VOID GROWTH
NO VOID GROWTH
0
2
4
6
8
10
12
CASCADE COLLAPSE EFFICIENCY (ϵ), %

Fig. (8.38)

completely inhibit swelling. (The effect of Z_i on this void growth and no growth boundary is explained in Appendix (B)).

This may cast some light on why metals which may have high collision cascade efficiencies (Au, Ti and Zr), do not form voids and form vacancy loops instead. Alloying metals to increase the collision cascade efficiency may be a very useful potential to reduce or inhibit swelling of metals under irradiation.

VIII.F. Effect of Surface Energy and Temperature Dependent Microstructure on Swelling

The previous analysis has considered the details of point defect source and sink variations as a function of time and temperature. In this section we will study the displacement rate effects on swelling with a microstructure that does not change as a function of temperature. The materials parameters and the microstructure used in these calculations are those of Brailsford and Bullough[71].

Figure (8.39) shows point defect average concentrations as a function of temperature for two different dose rates. As the temperature is increased, vacancy mobility increases and more vacancies are absorbed by sinks. This causes a drop in vacancy concentration with temperature. The interstitial concentration, on the other hand, shows an increase as a function of temperature. This behavior is due to the dominance of recombination at lower temperatures which depends on the product of point defect concentrations. Thus, when vacancies

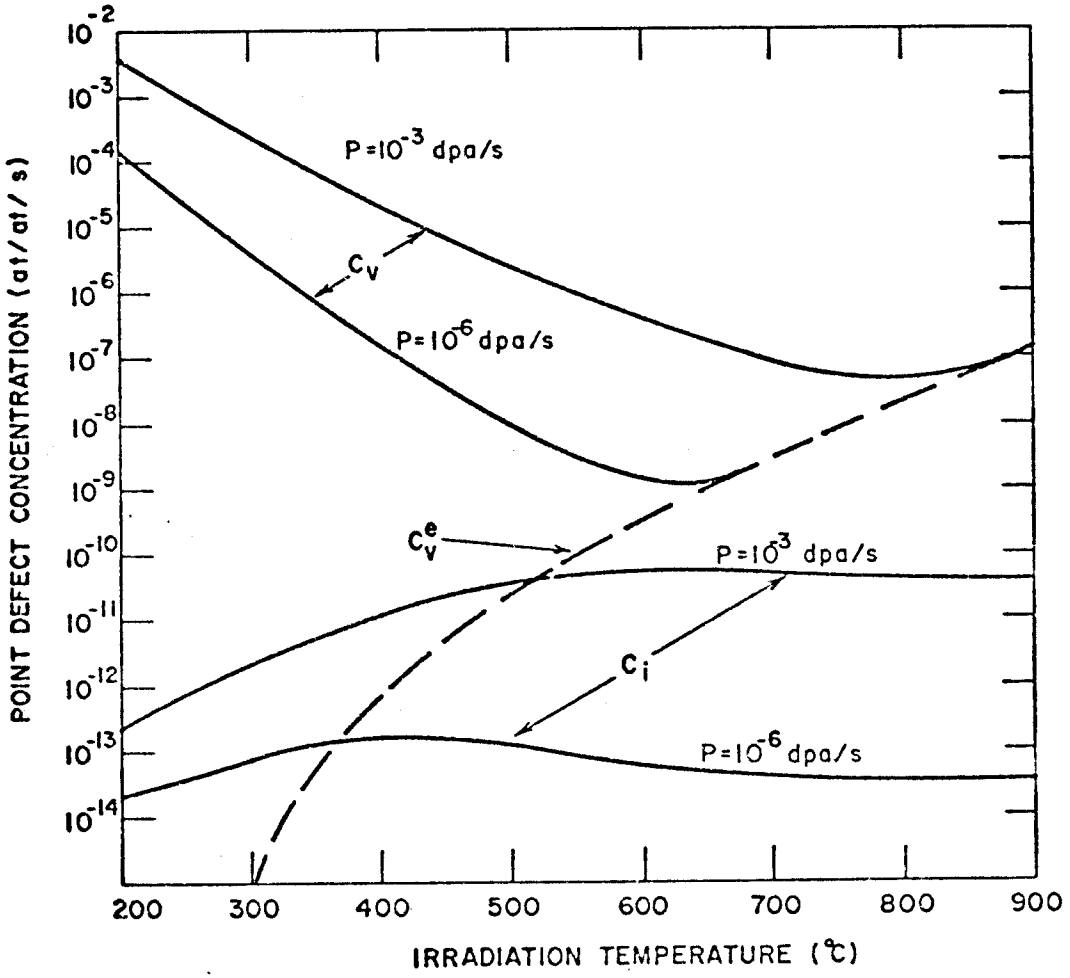

Fig. (8.39). Point defects average concentration as a function of temperature for a temperature independent microstructure in 316 S.S.

disappear from the matrix, interstitials find a better chance to survive. At higher temperatures, recombination is unimportant as depicted in Figures (8.40) and (8.41). In this temperature region, concentrations are not functions of the dose. Vacancy concentration decreases due to a higher mobility and interstitial concentration saturates because of an almost constant mobility.

At even higher temperatures, the vacancy concentration becomes the thermal equilibrium value (Figure (8.39)) and the interstitial concentration becomes constant as a function of temperature. It is apparent that for lower dpa rates the vacancy concentration approaches the thermal equilibrium value at a lower temperature, which causes the maximum temperature at which swelling is observed to be lower (Figure (8.41)).

Figures (8.40) and (8.41) show that at low temperatures, point defects recombine faster than their removal by existing sinks. At higher temperatures, vacancies are more mobile which give rise to a higher removal rate by sinks and a lower recombination rate. At even higher temperatures, the contribution of thermally emitted vacancies from the preexisting microstructure becomes appreciable. It is important to notice that as the point defect production rate goes up, the temperature range over which recombination rate dominates also increases.

A comparison between vacancy concentration calculated with a temperature independent microstructure, and that calculated with a dynamic and temperature dependent microstructure

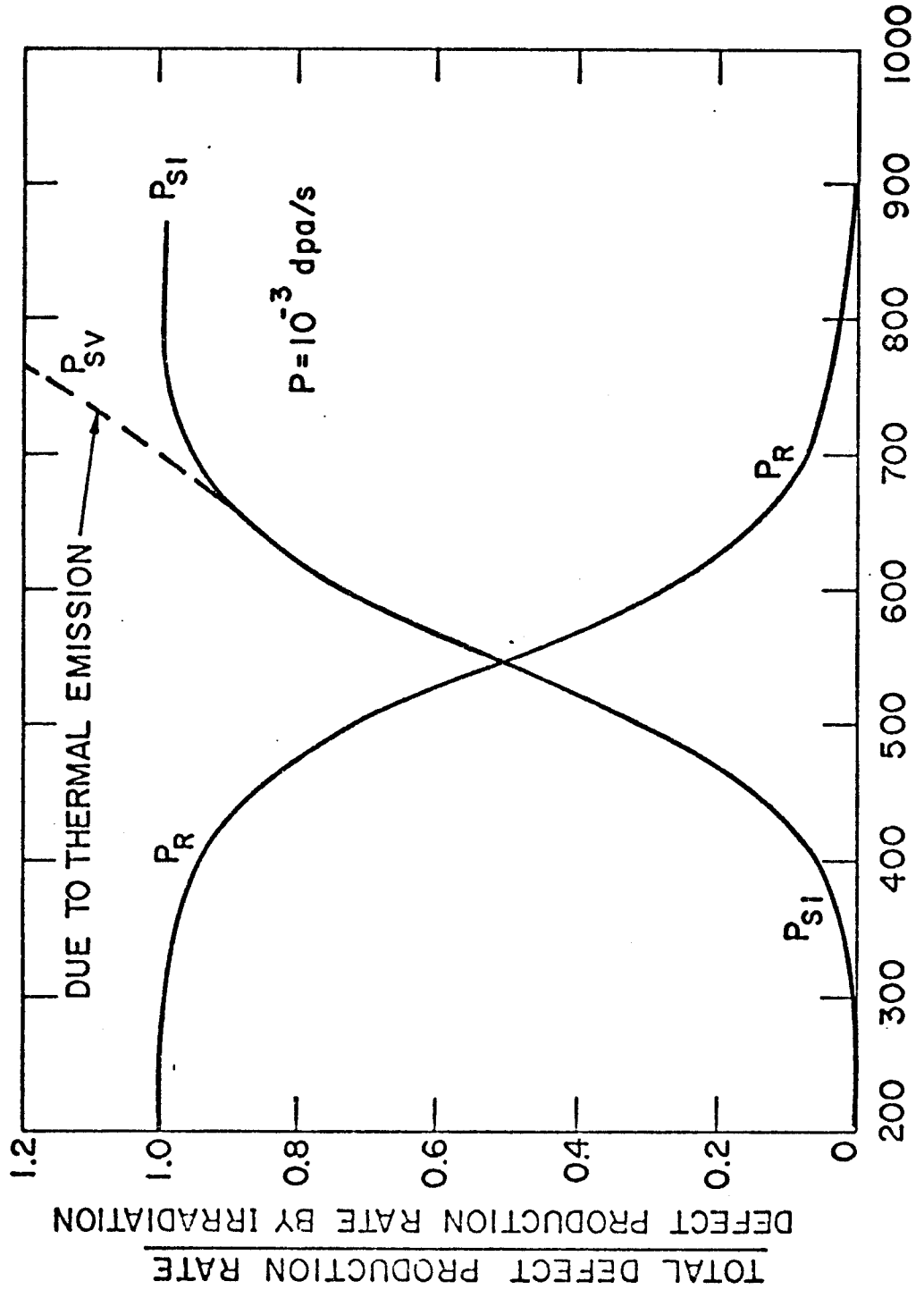

Fig. (8.40). Relative removal rates of point defects as a function of temperature for temperature independent microstructure of 316 S.S. (Accellerator conditions).

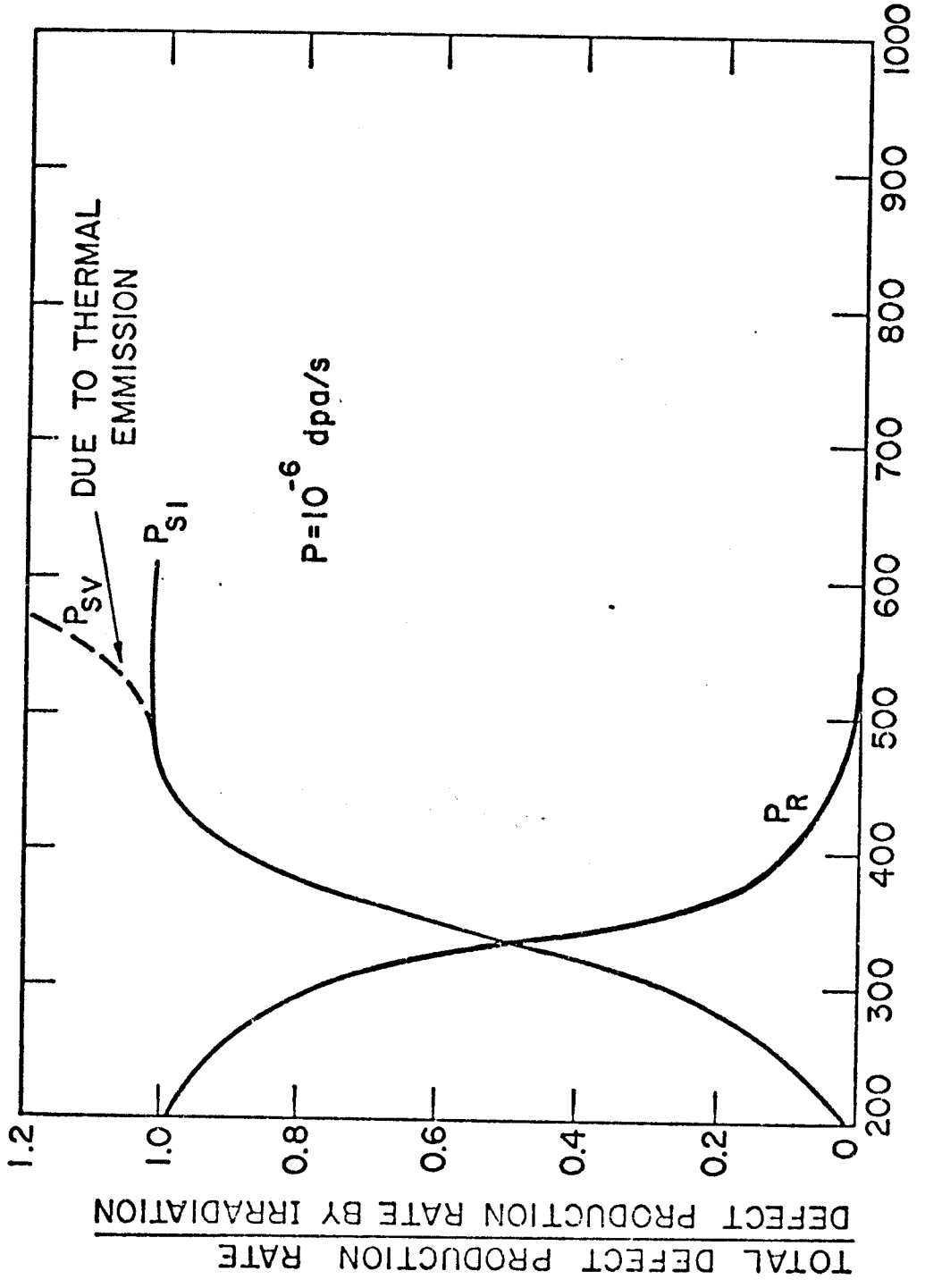

Fig. (8.41). Relative removal rates of point defects as a function of temperature for fixed microstructure of 316 S.S. (Reactor conditions)

is shown in Figure (8.42). In the case of a dynamic microstructure the high sink density (especially vacancy loops) at low temperatures will force the vacancy concentration to go down. As the temperature is increased, the sink density becomes less important and the vacancy concentration also increases. As the vacancies become more mobile with further increases in temperature, their concentration decreases because they now migrate to other sinks (i.e., voids and interstitial loops) that are left in the matrix. The contribution of thermal vacancies from the rest of the microstructure eventually increases vacancy concentration again with increasing temperature.

The relative swelling under neutron and ion irradiations for a temperature independent microstructure is shown in Figure (8.43). The Brailsford and Bullough model which used a void surface energy of 0 ergs/cm^2 and a temperature, as well as irradiation dose independent, microstructure, predicts a peak temperature shift of 190°C for 316 S.S. between 10^{-6} dpa/s and 10^{-3} dpa/s, (see Table 8.2). The computer code TRANSWELL was used to calculate relative swelling for a temperature independent microstructure that varies as a function of dose, but corresponds, on the average, to the Brailsford and Bulough conditions.

When a surface energy of 0 ergs/cm^2 is used, a peak temperature shift of 200°C, between 10^{-6} dpa/s and 10^{-3} dpa/s, is obtained. On the other hand, a surface energy of 1000 ergs/cm^2

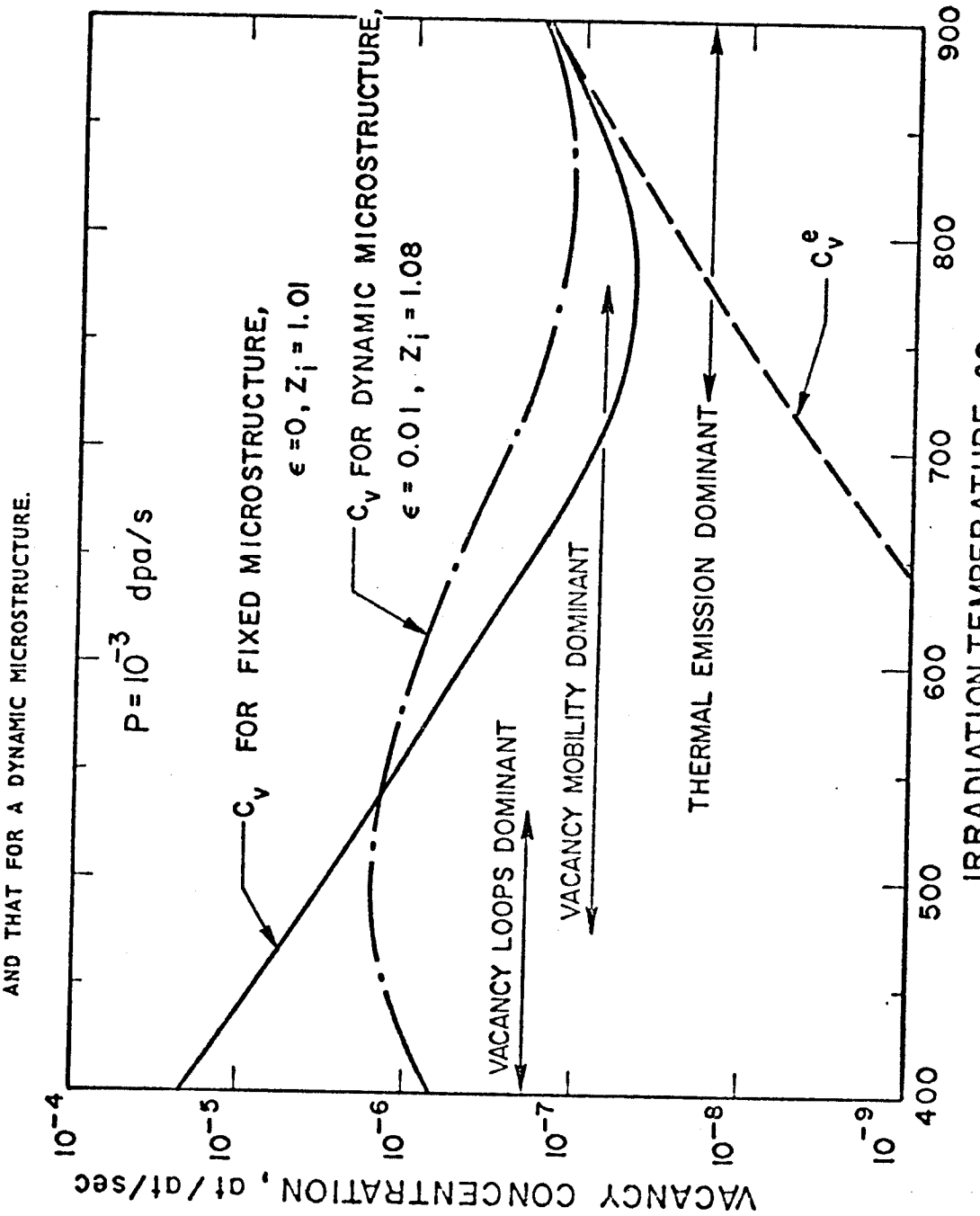

COMPARISON BETWEEN VACANCY CONCENTRATION CALCULATED FOR A FIXED MICROSTRUCTURE AND THAT FOR A DYNAMIC MICROSTRUCTURE.

Fig. (8.42)

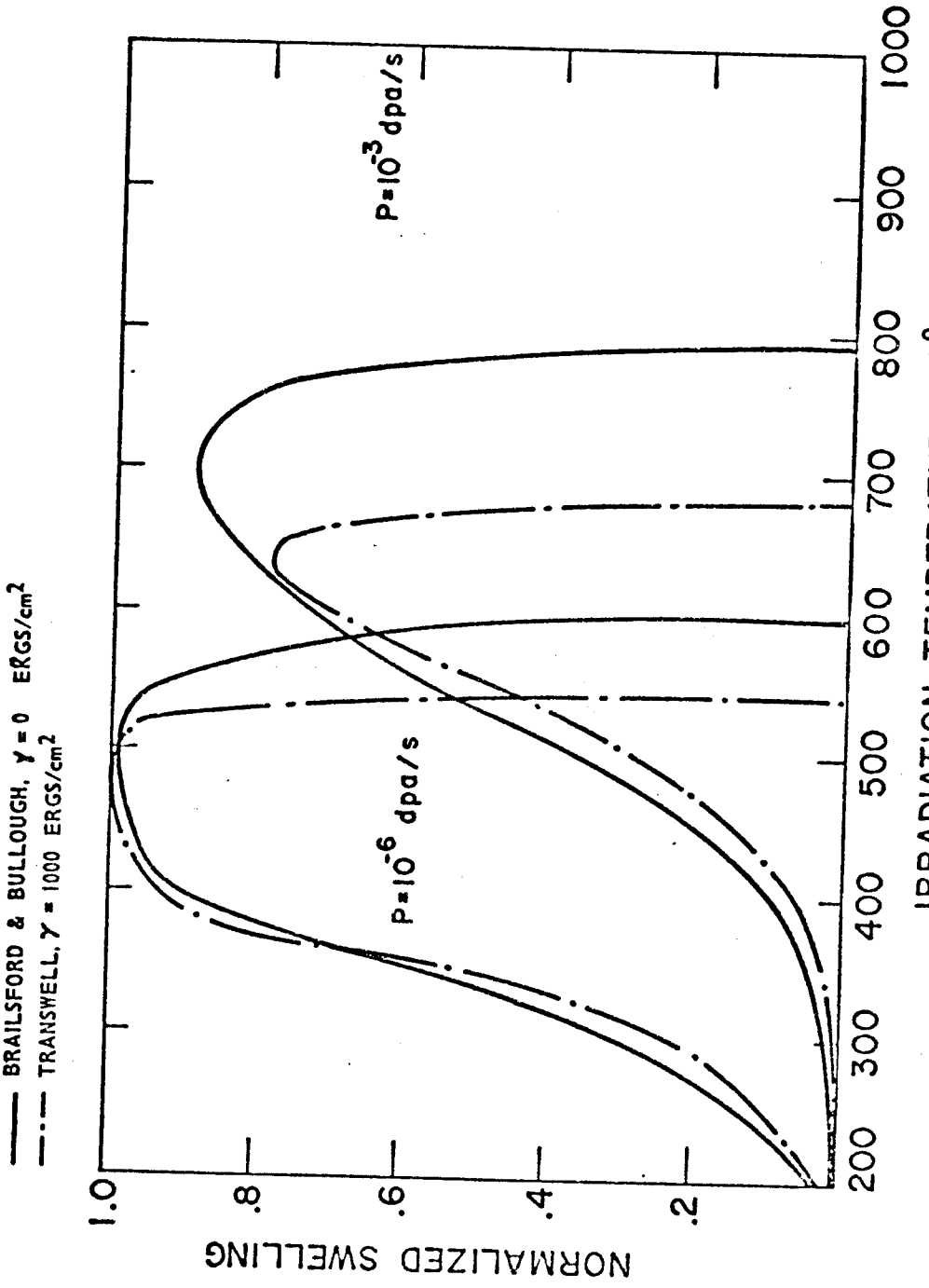

Fig. (8.43). Relative swelling of 316 S.S. for a temperature independent microstructure.

TABLE (8.2)

Comparison Between Theoretical Predictions of the Peak Temperature Shift and Experimental Observations for ST 316 S.S.

Lower Dose Rate, dpa/s	Higher Dose Rate, dpa/s	Peak Temp. Shift, °C	Investigator	
10^{-6}	10^{-3}	190	Brailsford and Bullough	Theoretical with temperature and dose independent microstructure, $\gamma = 0$ ergs/cm^2, $\varepsilon = 0$, $Z_i = 1.01$.
10^{-6}	10^{-3}	200	Ghoniem and Kulcinski	Theoretical with temperature independent microstructure, $\gamma = 0$ ergs/cm^2, $\varepsilon = 0$, $Z_i = 1.01$.
10^{-6}	10^{-3}	140	Ghoniem and Kulcinski	Theoretical with temperature independent microstructure, $\gamma = 1000$ ergs/cm^2, $\varepsilon = 0$, $Z_i = 1.01$.
10^{-6}	10^{-3}	50	Ghoniem and Kulcinski	Theoretical with temperature and dose dependent microstructure, $\gamma = 2000$ ergs/cm^2, $\varepsilon = 4.4\%$, $Z_i = 1.08$.
10^{-6}	10^{-3}	60	Bates and Straalsund (n irrad. [119]), and Williams (ion irrad. [102]).	Experimental; reactor versus 22 MeV C^{++} ion irradiations.

produces a peak swelling temperature shift of 140°C between reactor and accelerator conditions, reflecting the sensitivity of the calculations to the value of the surface energy. One can see from Table (8.2) that:

(1) The calculations for the temperature shift are sensitive to the value of the surface energy, and a change of its value from 0 ergs/cm^2 to 1000 ergs/cm^2 reduces the temperature shift from 200°C to 140°C.

(2) The inclusion of a temperature and dose dependent microstructure further reduces the temperature shift from 140°C to 50°C.

(3) The experimental observations of the peak swelling temperature shift (see Williams[102] and Bates and Straalsund[119]) are far less than would be predicted by a fixed microstructure model. The observations of ∿60°C temperature shift between reactor and accelerator conditions agree reasonably well with the dynamic calculations of 50°C.

VIII.G. Concluding Remarks

A fully dynamic rate theory approach has been utilized to analyze in detail the dynamics of point defects as well as voids, interstitial and vacancy loops. The following major features emerge from this chapter:

1. The vacancy concentration exhibits a peak value at intermediate temperatures due to the competition between a drop in sink density and a vacancy mobility increase with temperature. This behavior could have an appreciable effect

on void nucleation rates calculated at intermediate temperatures since they are sensitive to vacancy supersaturation ratios.

2. The fraction of vacancies retained in vacancy loops has a great influence on void growth kinetics. However, this fraction is very sensitive to temperature and decreases sharply as the temperature increases becoming of negligible importance in 316 S.S. above about 550°C.

3. Recombination of point defects can take place either on microstructural defects or by free collisions of vacancies and interstitials in the bulk. The latter mechanism is referred to as bulk recombination. For temperature independent and dose dependent microstructures, with no vacancy loops, bulk recombination is dominant at low temperatures and sink removal is the major annealing mechanism at high temperatures. On the other hand, if the microstructure is both temperature and dose dependent and contains vacancy loops, annealing at sinks dominates over the entire void production range. Point defect bulk recombination, at low temperatures (0.3-0.4 T_m) is effectively replaced by their mutual recombination at vacancy loops. However, as the metal matrix becomes 'cleaner' of sinks at high temperatures ($\sim$0.4-0.5 T_m), point defect bulk recombination rates become appreciable.

4. Vacancy thermal emission from existing microstructure can be neglected compared to point defect production rates for high dose rates (10^{-3} dpa/sec), but it is very important

for low dose rates (10^{-6} dpa/s).

5. For ion or neutron irradiation, vacancy loop line density is around 2 orders of magnitude higher than interstitial loop line density for temperatures approximately below the swelling peak. Therefore, it is a dominant sink of point defects that should be taken into consideration.

6. There exists a temperature and microstructure dependent free growth void radius. This is defined as the minimum radius at which a void can grow without the assistance of internal gas pressure. For simplicity, we have taken a 10 Å void radius to be the critical size at 400°C, determined the free growth void radius at the highest temperature, and linearly interpolated in between.

7. A temperature and dose independent microstructure model does not predict the correct shift for the peak swelling temperature, while a fully dynamic model comes closer to experimental observations of the peak swelling temperature shift.

8. There is a delicate balance in a metal's matrix between the vacancy flux (D_vC_v) and the interstitial flux (D_iC_i). For void growth under irradiation, D_vC_v is greater than D_iC_i. The formation of vacancy loops influences this balance by reducing the free vacancy flux and for high collapse efficiencies the vacancy flux can be less then the interstitial flux. Should more interstitials than vacancies go to voids,

void growth is inhibited and voids shrink instead of grow. For a value of $Z_i = 1.08$, collision cascade efficiencies greater than 5% to 7.5% will inhibit void growth over a wide range of dose rates.

This chapter has been entirely devoted to the different aspects of the theory when applied to steady-state irradiations. The next chapter will concentrate on the void growth problem in systems where the irradiation is time dependent.

CHAPTER IX

SWELLING OF METALS UNDER PULSED IRRADIATION

In the past 10 years investigators have been directing increasing efforts towards the understanding of the relationships between microstructural behavior and mechanical responses of metals under irradiation. The fundamental motive for such studies has been the increasing dependence on nuclear reactors for energy production. The use of large material testing reactors as well as experimental simulation techniques (i.e., particle accelerators and high voltage electron microscopes) has helped to supply the experimental data for both reactor designs and theory development. But there is a complete absence of Fusion materials testing reactors at the present time, and the need for experimental and mathematical simulation techniques is readily apparent. The planning of a well defined strategy[120] for both theoretical developments and fundamental experiments is vital to achieve a greater understanding of materials responses to different irradiation environments. This chapter is aimed particularly at the temporal performance of metals under pulsed irradiation.

IX.A. Scope of Pulsed Irradiation

Pulsed irradiation environment is encountered in a wide range of situations of both practical and experimental value. Chapter III considered the time performance of pulsed irradiation facilities. Since point defect behavior is important

in the understanding of a variety of irradiation induced phenomena, we will consider the dynamic nature of these defects in the different irradiation environments.

IX.A.1. Tokamak Fusion Reactors

Tokamak Fusion Reactors are designed to have long confinement times and relatively shorter times between burns to achieve maximum plant efficiency. Burn cycles with durations in the range of (30-90) minutes and cooling cycles of about (5-10) minutes are considered in the design of these devices [121,122]. Recent advances in the conceptual designs consider burn and cooling cycles duration of only a few minutes long [123]. As an illustrative example of a Tokamak reactor, we will consider a burn cycle of 10^4 seconds and a cooling cycle of 400 seconds, to study point defect behavior.

With the parameters of Table (7.1) for 316 SS, point defect calculations were performed to study their general behavior as a function of time. Figure (9.1) shows the vacancy and interstitial concentrations, at 400°C, in the stainless steel first-wall of a typical Tokamak reactor where the average rate of point defect production is 10^{-6} dpa/sec (which corresponds to few MW/m^2 wall loading). It is seen that in the first few tenths of a microsecond, interstitials reach an equilibrium with the sink structure present at this temperature, while vacancies essentially maintain their thermal equilibrium values. The interstitial concentration remains constant at a value of $\sim 3 \times 10^{-14}$ at/at, as a result of an

POINT DEFECT CONCENTRATIONS IN 316SS IN A TOKAMAK FUSION REACTOR

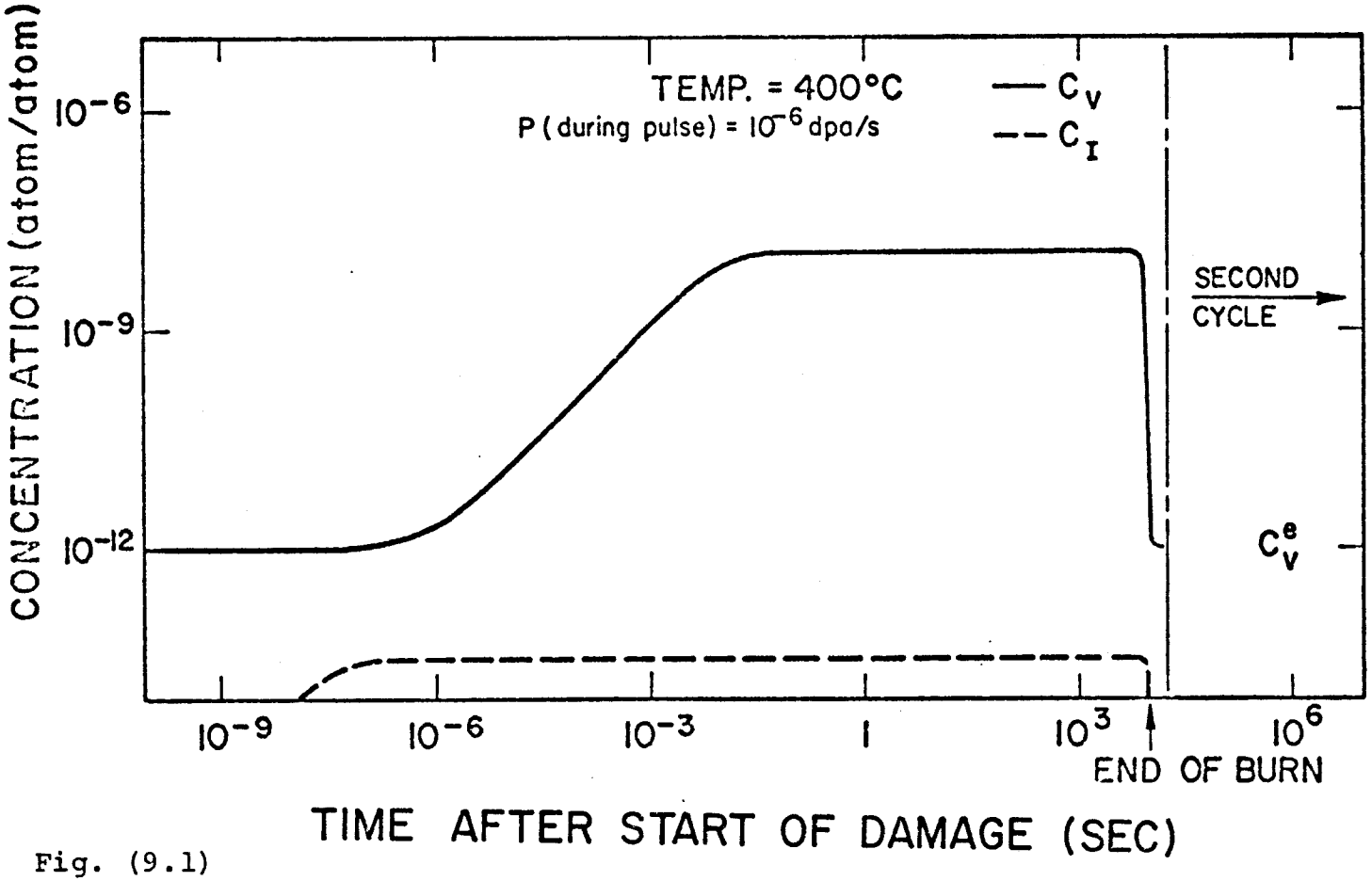

Fig. (9.1)

equilibrium between a constant production rate and a steady absorption rate by present sinks. The microstructure doesn't change appreciably at the end of the burn cycle, because of the small dose achieved (10^{-2} dpa) per cycle. On the other hand, the lower mobility of vacancies at this temperature causes the vacancy population to increase linearly from its thermal equilibrium value ($\sim 10^{-12}$ at/at) to its irradiation equilibrium value ($\sim 10^{-8}$ at/at), only by accumulation in the matrix of the metal. Around a vacancy mean lifetime ($\sim$2 milliseconds), vacancies reach various sinks and are removed from the matrix causing the state of equilibrium between production and sink removal. Point defect mutual recombination rate is not a significant means of point defect removal, because of the high sink density at low temperatures.

At higher temperatures, other factors influence point defect dynamics, Figure (9.2) shows point defect concentrations as functions of irradiation time during one burn cycle, at 600°C. Owing to lower sink densities at higher temperatures, point defects experience lower sink removal rates, causing generally higher defect concentrations. The interstitial mean lifetime increases by two orders of magnitude (to about 4 microseconds) at 600°C because of the drop in the sink density at higher temperatures. Therefore, the interstitials achieve complete equilibrium with the sinks after about 10 microseconds and their concentration reaches the value of 1.8 x 10^{-12} at/at.

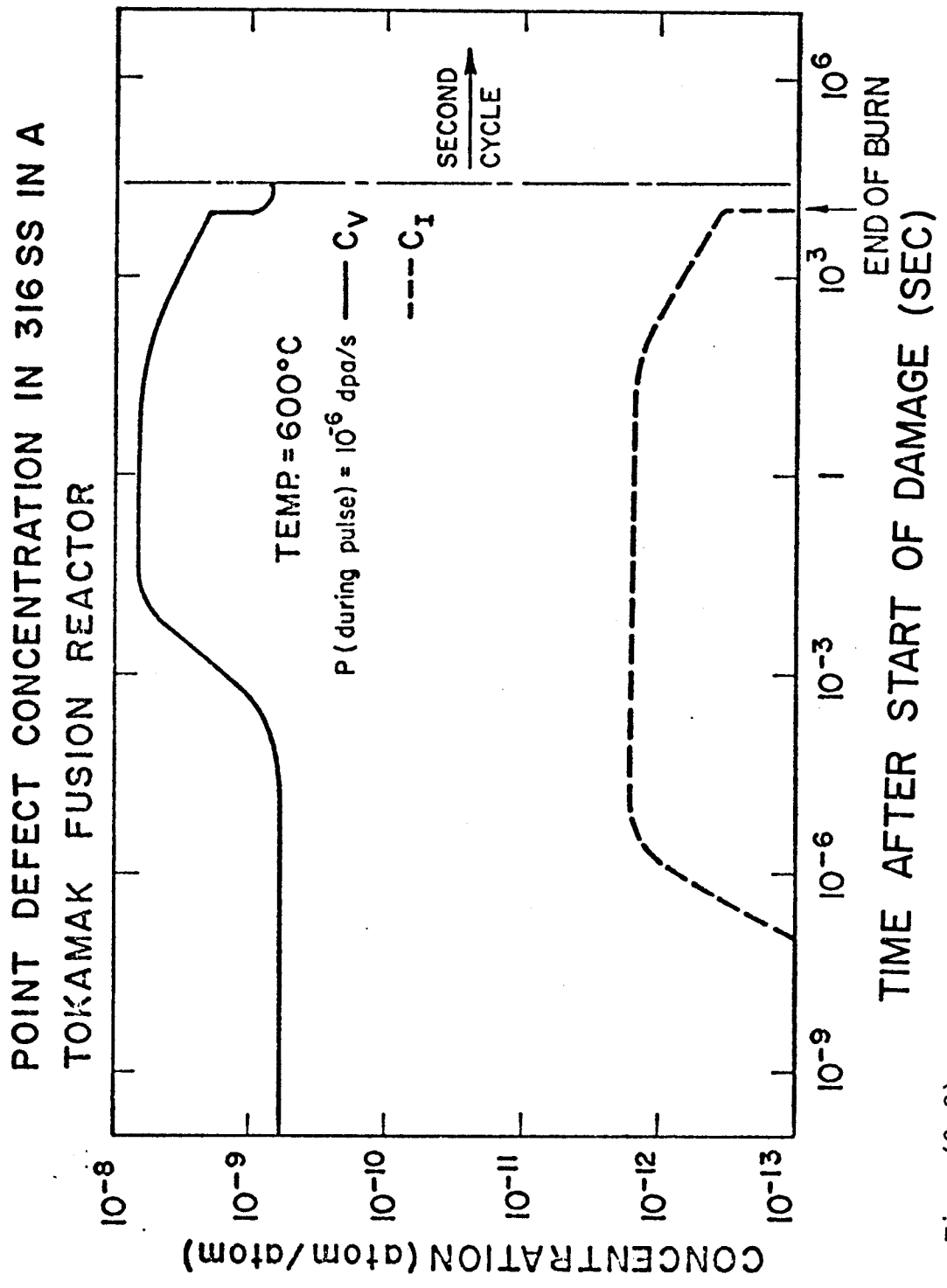
POINT DEFECT CONCENTRATION IN 316 SS IN A
TOKAMAK FUSION REACTOR
TEMP. = 600°C
P (during pulse) = 10⁻⁶ dpa/s
C_V
C_I
SECOND CYCLE
END OF BURN
CONCENTRATION (atom/atom)
TIME AFTER START OF DAMAGE (SEC)
10⁻⁸
10⁻⁹
10⁻¹⁰
10⁻¹¹
10⁻¹²
10⁻¹³
10⁻⁹
10⁻⁶
10⁻³
1
10³
10⁶

Fig. (9.2)

The effects of the irradiation produced vacancies at 600°C are not felt in the system before a relatively longer time (∿1 millisecond); the higher thermal equilibrium vacancy concentration at 600°C ($6x10^{-10}$at/at) constitutes almost all of the vacancy population before such time is reached. There is also a shorter period of vacancy accumulation before they diffuse to sinks, because of their much higher mobility at this temperature. Therefore, vacancy concentration quickly reaches the value of 7×10^{-9} at/at. The lower sink density at 60°C increases interstitial concentrations, which renders mutual point defect recombination rate an important role. This leads to the drop in point defect concentrations around 100 seconds as shown in Figure (9.2). At the end of the burn cycle point defect concentrations drop to their thermal equilibrium values with their characteristic time constants, which is much shorter than the cooling cycle duration.

IX.A.2. Theta Pinch Fusion Reactors

High magnetic fields are required for Theta Pinch Reactors to produce burn times of a sufficiently short duration to be free from plasma instabilities. Besides their effects on first-wall swelling, point defects behavior is connected to the dielectric properties of the insulator. A pulse duration of 0.1 seconds and pulse period of 1 second was assumed in this study. Figures (9.3) and (9.4) show the time behavior of point defects in a Theta Pinch Fusion first-wall. A point defect generation rate of 10^{-5} dpa/sec was assumed during the

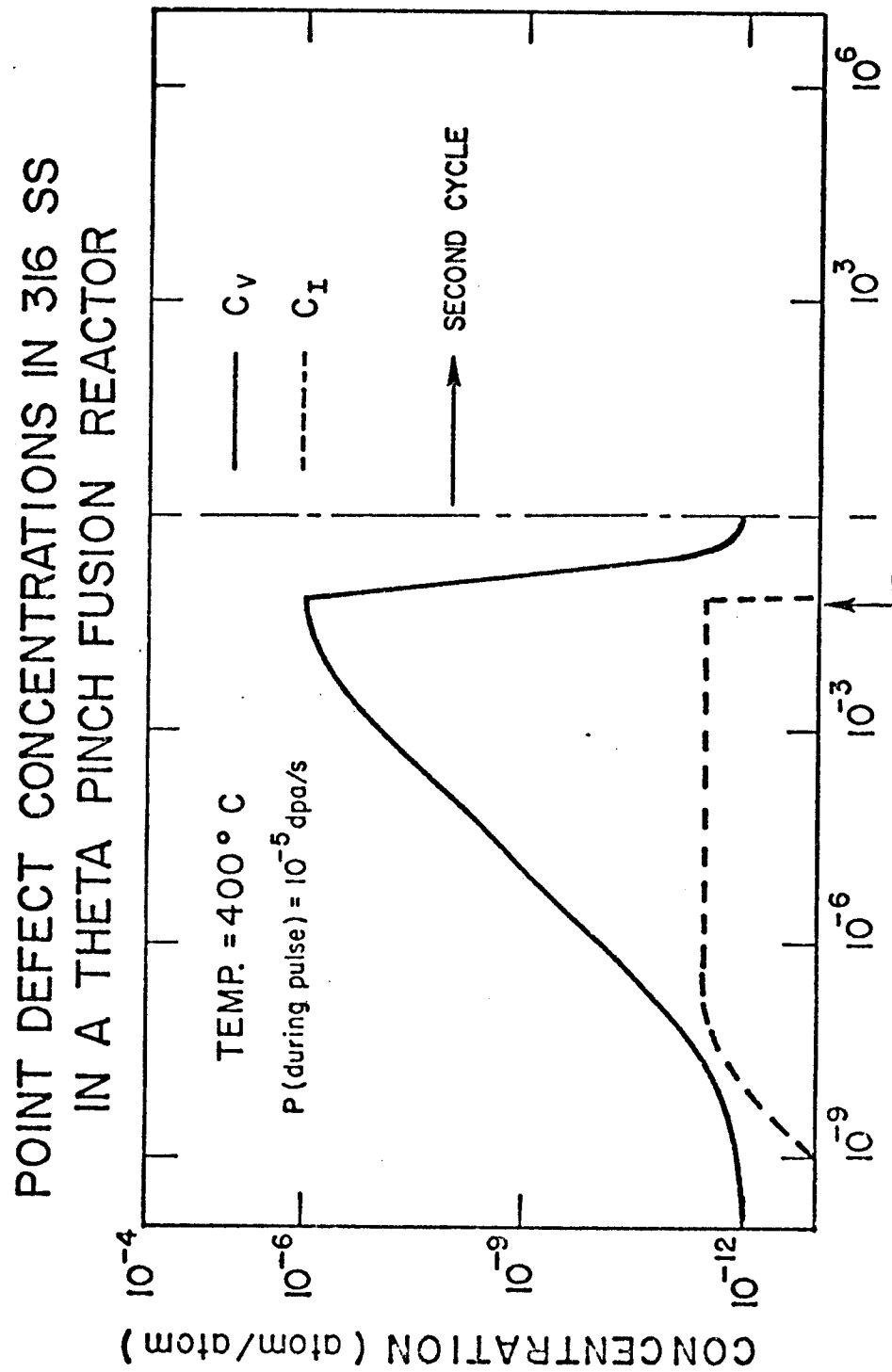
POINT DEFECT CONCENTRATIONS IN 316 SS
IN A THETA PINCH FUSION REACTOR
TEMP. = 400 ° C
P (during pulse) = 10^{-5} dpa/s
C_V
C_I
SECOND CYCLE
END OF BURN CYCLE
CONCENTRATION (atom/atom)
TIME AFTER START OF DAMAGE (SEC)
10^{-4}
10^{-6}
10^{-9}
10^{-12}
10^{-9}
10^{-6}
10^{-3}
10^{3}
10^{6}

Fig. (9.3)

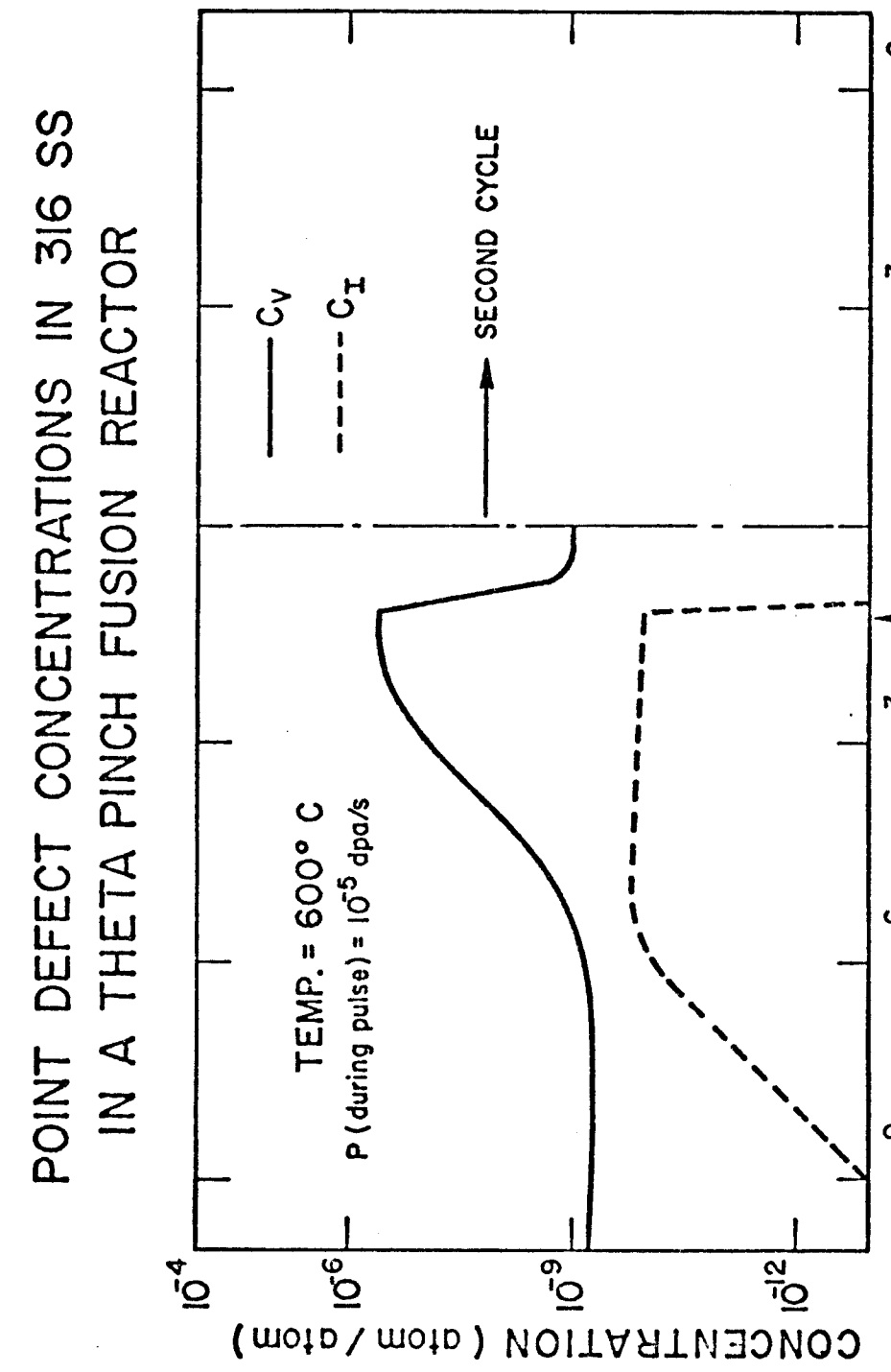
POINT DEFECT CONCENTRATIONS IN 316 SS
IN A THETA PINCH FUSION REACTOR
TEMP. = 600° C
P (during pulse) = 10^-5 dpa/s
C_V
C_I
SECOND CYCLE
END OF BURN CYCLE
CONCENTRATION (atom / atom)
TIME AFTER START OF DAMAGE (SEC)
10^-4
10^-6
10^-9
10^-12
10^-9
10^-6
10^-3
1
10^3
10^6

Fig. (9.4)

burn cycle, and 0 dpa/sec for the cooling cycle.

At 400°C, as shown in Figure (9.3), interstitials quickly reach an equilibrium with sinks and achieve a concentration of 3×10^{-12}. On the other hand, vacancies do not achieve equilibrium conditions at the end of the burn cycle with values as high as 10^{-6} at/at at the end of the burn cycle. Point defect concentrations in this case are about 2 orders of magnitude higher than the corresponding Tokamak reactor case.

Figure (9.4) shows point defect concentrations, as a function of time, at 600°C. Vacancy concentration is lower than the 400°C case, of the higher vacancy mobility. Although interstitial concentration is higher at 600°C than at 400°C ($\sim 10^{-10}$ at/at), it starts to slowly drop with time because of mutual point defect recombination. At the end of the burn cycle, point defect concentrations begin to decline very rapidly to their thermal equilibrium values with greatly different time constants (about 4 microseconds for an interstitial and 15 milliseconds for a vacancy). It is obvious from the previous analysis that point defect time behavior is far from steady-state equilibrium values, encountered in normal steady-state analysis.

IX.A.3. Rastered Ion Beam Experiments

Obtaining a uniformly bombarded surface is one of the main objectives of ion simulation studies experimentalists, this reduces the number of experimental variables that have to be

studied in the final analysis of the results. It was previously mentioned in Chapter II that scanning the ion beam across the specimens surface and holding a defocused beam in one position over the specimen showed to produce very different microstructures [11]. The following section will concentrate on some time domain aspects of point defects behavior in the two cases. It also points out the reasons for such differences in the microstructural behavior.

IX.A.3.a. Experimental Results:

At the Naval Research Laboratory (NRL), experiments were conducted to study the effects of the methods used to obtain a uniform ion dose across the surface of the bombarded specimens. Specimens of >99.99% nickel were examined by transmission electron microscopy following bombardment with 2.8 MeV $^{58}Ni^{+}$ ions to a fluence of 5.68×10^{15} ions/cm^2 at temperatures between 365°C and 775°C. Two methods of bombardment were used to produce these specimens. One set of irradiations was performed with a focused ion beam scanned over the specimen surface in a raster pattern with a horizontal scan frequency of 10 kHz and a vertical scan frequency of 100 Hz. The other set of irradiations was made with the central portion of a defocused ion beam which was held in one position over the specimen.

The temperature dependence of the damage produced by these two modes of bombardments was very different as shown in Figure (9.5); which is a plot of the mean void diameter as

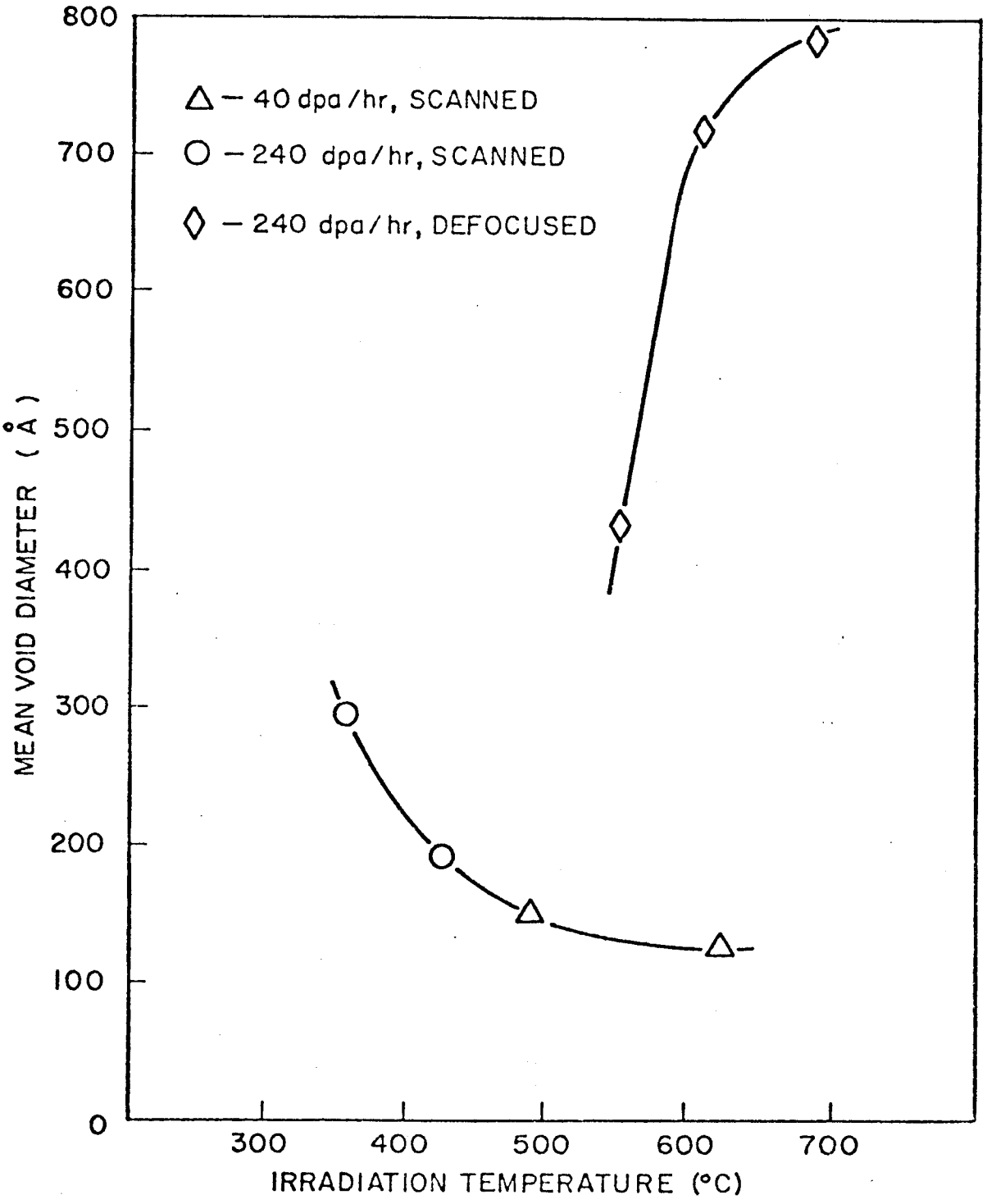

Fig. (9.5). Experimental results of Ni ion irradiated Ni for steady defocused and scanned beams.

a function of the irradiation temperature. The mean diameter of the voids produced by the defocused beam irradiations increased with increasing bombardment temperature which is the typical dependence normally observed in neutron-irradiated metals. The mean diameter of the voids in the scanned-beam specimens, on the other hand, decreased with increasing bombardment temperature. Both methods of bombardment produced the highest swelling near 600°C, and all of the data points were found to fall near the same swelling curve, although the swelling of the defocused beam specimen at 620°C was significantly higher than that observed in the scanned beam specimen at the same temperature.

The square cross-section beam was assumed to have uniform intensity and was scanned in a raster pattern as shown in Figure (9.6.a). This produced an ion flux at the center of the specimen as shown in Figure (9.6.b): A series of 50 pulses, 2.5×10^{-5} sec; no ion flux for 2.5×10^{-3} sec; then repetition of this sequence. The point defect production rate during each pulse of ions were chosen to be 0.32 dpa/sec, to give time-averaged production rates of 8×10^{-2} dpa/sec.

IX.A.3.b. Theoretical Analysis

Using the dislocation and void densities for Nickel given in Chapter VII, and the Nickel parameters from Table (6.1), a set of calculations was performed at 525°C and 725°C, to study the theoretical aspects of the rastered beam experiment.

Table (9.1) shows some of the main features of steady

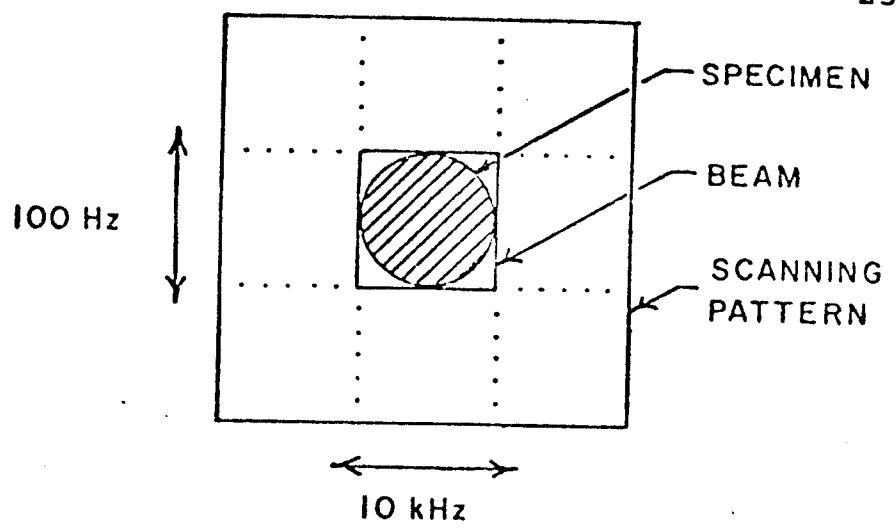

(a) IDEALIZED SCANNING PATTERN

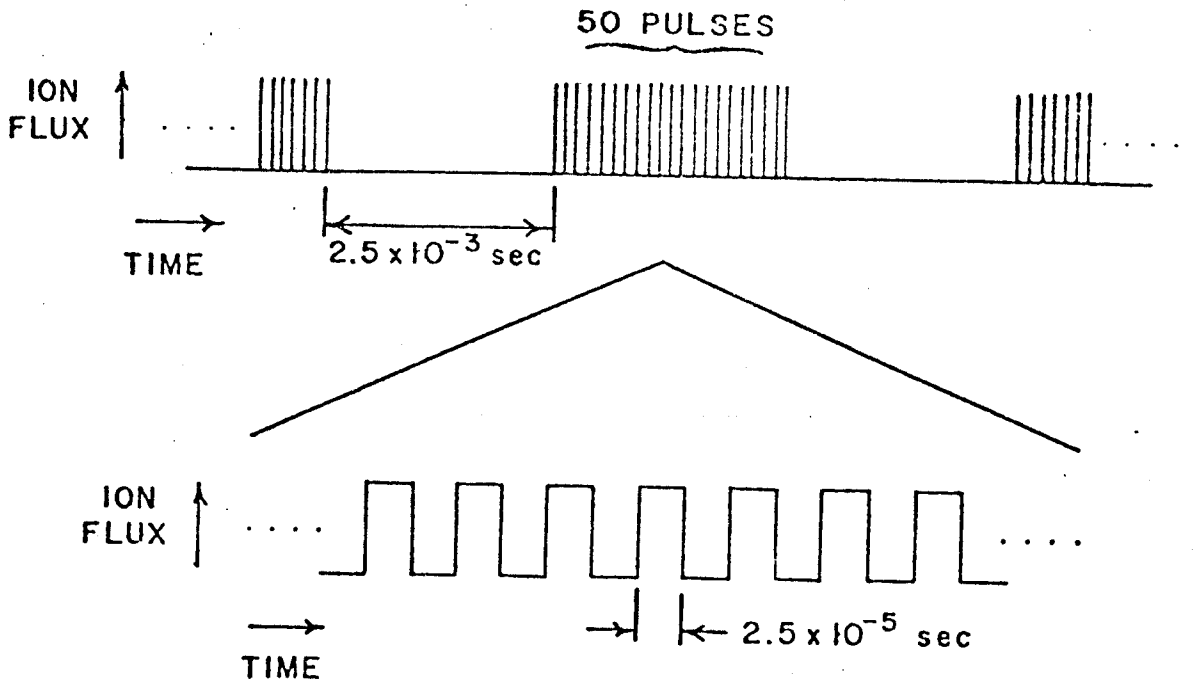

(b) IDEALIZED ION FLUX

Fig. (9.6). Idealized scanning pattern and ion flux for the scanned Ni ion beam experiment.

TABLE (9.1)

RESULTS OF RASTERED Ni ION BEAM EXPERIMENT CALCULATIONS

PROPERTY	525°C	725°C
Vacancy thermal equilibrium concentration, (at/at)	1.66×10^{-9}	9.56×10^{-8}
Interstitial thermal equilibrium concentration (at/at)	1.7×10^{-26}	2.49×10^{-21}
Vacancy mean lifetime (seconds)	8.07×10^{-2}	0.125
Interstitial mean lifetime (seconds)	1.12×10^{-9}	6.28×10^{-8}
Void number density (cm^{-3})	7.6×10^{15}	1.4×10^{13}
Interstitial loop number density (cm^{-3})	2.07×10^{15}	1.12×10^{14}
Steady-state vacancy concentration, (at/at)	3.1×10^{-4}	6.95×10^{-5}
Steady-state interstitial concentration, (at/at)	4.4×10^{-12}	3.48×10^{-11}

state calculations with an average dose rate of 8×10^{-2} dpa/sec. Vacancy mean lifetime increases only slightly while interstitial mean lifetime increases by over an order of magnitude when the temperature is changed from 525°C to 725°C. One can also observe the decrease in the steady-state vacancy concentration with increasing temperature, mainly because of the increase in vacancy mobility over this range of temperature. The interstitial concentration, on the other hand, increases with increasing temperature, essentially because of the saturation of interstitial mobility and the drop of the sink density with temperature.

The calculations for the experimental conditions are demonstrated in Figures (9.7); Figures (9.7.a) and (9.7.b) show the overall (envelope) point defect concentrations during and after 50 cycles (2.5×10^{-3} sec), whereas Figures (9.7.c) and (9.7.d) show the fine structure of point defect concentrations as a function of time in one individual cycle (2.5×10^{-5} sec).

Figures (9.7.a) and (9.7.b) show the gross behavior of point defects. Since vacancy mean lifetime is much greater than the pulse period, little vacancy diffusion takes place during these cycles. On the converse, considerable diffusion of interstitials occurs during the initial stages of the cycle leading to an early maximum in their concentrations. Due to the high concentration of point defects, mutual recombination is very important and the interstitial

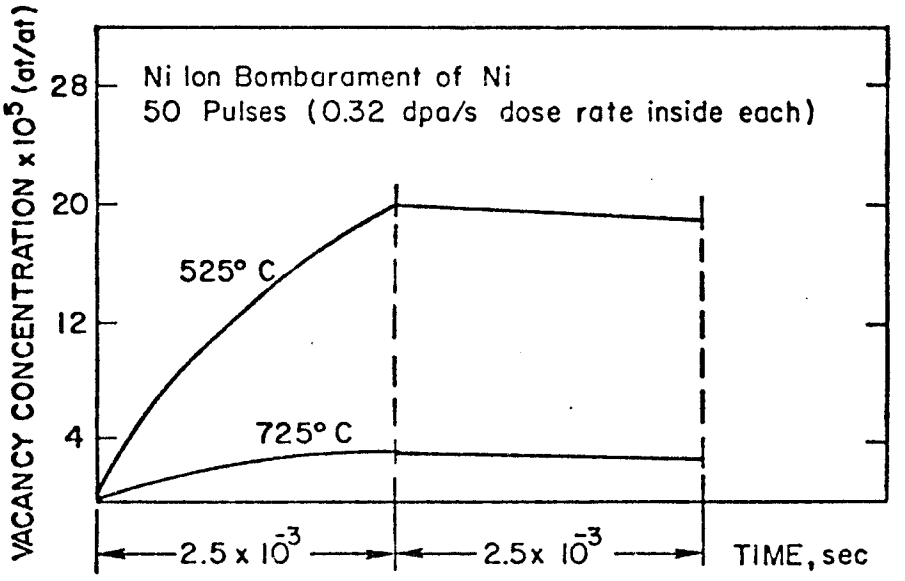

Fig. (9.7.a). Vacancy concentration for 50 pulses.

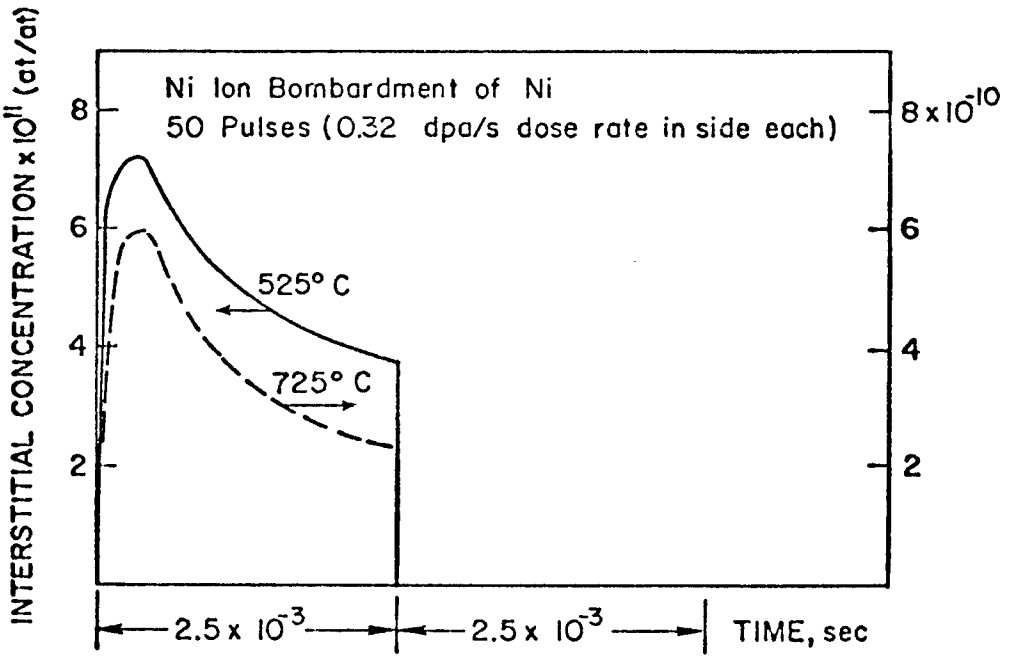

Fig. (9.7.b). Interstitial concentration for 50 pulses.

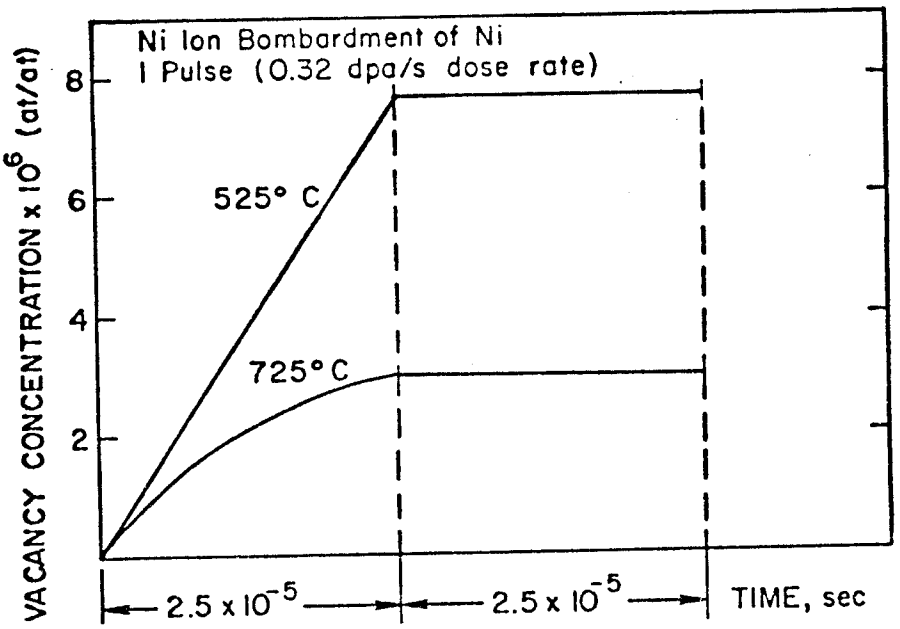

Fig. (9.7.c). Vacancy concentration for one individual pulse.

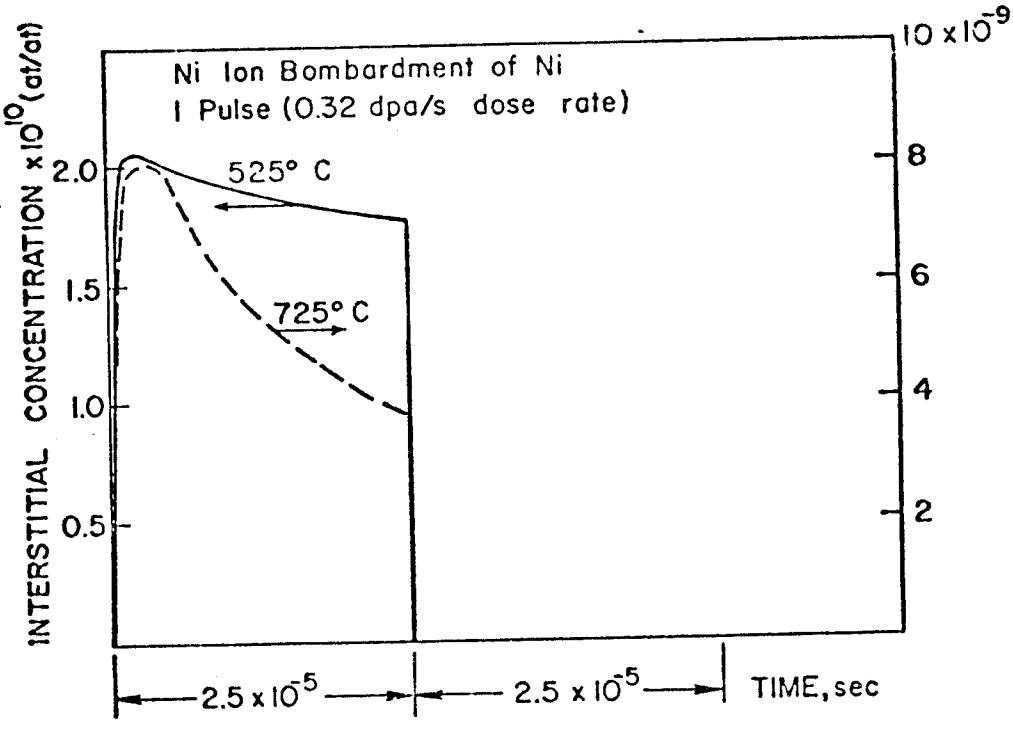

Fig. (9.7.d). Interstitial concentration for one individual pulse.

concentration is reduced as a function of time after the first microsecond. The individual pulse characteristics are shown in Figures (9.7.c) and (9.7.d). Interstitials show the same time characteristics as in the 50 pulses especially at high temperatures where their concentration is considerably higher. At 525°C the vacancy concentration does not greatly deviate from linearity because mutual recombination of point defects, (which is almost the only operative removal process), is not strong enough to affect its concentration. Interstitials are affected to a larger degree by this mechanism, because of their relatively smaller concentration as a function of time, as shown in Figure (9.7.d). However, at the higher temperature (725°C) mutual point defect recombination shows a stronger influence on their concentrations.

The kinetic growth behavior of a 50 Å radius void was also studied under the previously described point defect steady-state and fluctuating concentrations. Under steady-state conditions, voids of 50 Å average radius continued to grow at 525°C and 725°C. On the other hand, the same voids experienced shrinkage after 100 long cycles, in the rastered beam case at the two temperatures. This result is in qualitative agreement with the experiments as shown in Figure (9.5). A main reason for the inhibited growth of voids in the rastered-beam mode is the higher interstitial flux which rushes to the voids during the ion pulses, and the void annealing

that occurs in between the pulses.

IX.4. Inertial Controlled Thermonuclear Reactor (ICTR)

This category of pulsed fusion reactors include the Laser Controlled Thermonuclear Reactors, Electron Beam and Ion Beam Controlled Thermonuclear Reactors. These types of reactors differ in the basic operational methods, and there is a wide variety of design concepts that try to alleviate some of the connected technological problems. In the following, we describe, in a generic sense, the time frames for the damage analysis related to ICTR's. Then point defect behavior in ICTR's first-wall is explained to furnish the groundwork for a discussion of pulsed irradiation swelling results, given later in this chapter.

IX.A.4.a Microexplosion Time Characteristics

The pulse widths of neutrons from microexplosions as well as the repitition rates and damage rates can vary considerably depending on the specific designs. The particular structure of the DT pellet exploded in the center of the cavity affects the method by which neutrons are generated. Neutrons travel through the space of the cavity, experience different reactions in the structural components and finally deposit their energy and resulting damage in the first-wall as well as other reactor parts. Therefore, the design concept affects the period of time over which bulk neutron damage is produced. The following schemes correspond to conditions that embrace the different design concepts as far as neutron pulse width

is concerned.

(1) A bare DT pellet, in which neutrons experience no collisions during the burn time, but are born with a Doppler broadening of a few tenths of an MeV and traverse a small cavity radius. The pulse width in this case is in the order of a nanosecond.

(2) A low ρR pellet (ρR is an indication of the degree of compression during the burn), in which neutrons experience no collisions during the burn time, but are born with a Doppler broadening of about ±1 MeV and traverse a cavity of about 6 meters in radius[124]. The neutron pulse width at the first-wall is on the order of 10 nanoseconds.

(3) An intermediate ρR pellet, in which neutrons experience collisions in the pellet during the burn time. Neutrons are born with a broadening due to Doppler shift and on the average downscatter by a few MeV and traverse a cavity of about 10 meters in radius. The neutron pulse width at the first-wall is on the order of 100 nanoseconds.

(4) A high ρR pellet, in which neutrons experience significant collisions in the pellet during the burn time. Neutrons are born with a broadening due to Doppler shift, downscatter by a few MeV and traverse the cavity. The neutron pulse width at the first wall is in the order of a microsecond.

IX.A.4.b. Generic Damage Analysis of ICTR

The many variations in design concepts make the damage

analysis of a particular design rather arbitrary. Another useful approach is a parameteric study with a wide range of pellet yields and reactor design concepts. Due to the Doppler broadening and the downscattering of neutrons, the pellets output neutron spectrum will have a Gaussian-like shape [125] centered around 14.1 MeV. The details of the spectrum depend on the pellet structure and implosion hydrodynamics. In general, a broader spectrum is expected to accompany high yield pellets. Neutrons of different energies will then arrive at the first-wall at different times which causes the neutron pulse to have a time spread. Results of peak damage calculations as a function of pellet yield, expressed in Mega Joule/shot, are shown in Figure (9.8). The calculations were performed for a 5 m radius cavity with two different Gaussian spectra. It is obvious that a broader pulse carrying the same amount of energy will result in a lower peak dose rate. For example, a 1000 MJ yield pellet will result in a damage rate in stainless steel of about 9 dpa/sec peak value for a 10 $\pm$ 4 MeV Gaussian, while the sharper 14 $\pm$ 1 MeV Gaussian pulse results in about 60 dpa/sec peak value.

Adopting a reference value of 5 m for the cavity radius, the effect of changing cavity radius and of the corresponding neutron spread on the peak damage rate is shown in Figure (9.9). Besides the definite effect of increasing the surface area on the peak damage in the first-wall ($1/r^2$), there is a neutron pulse spreading effect due to the differences in the

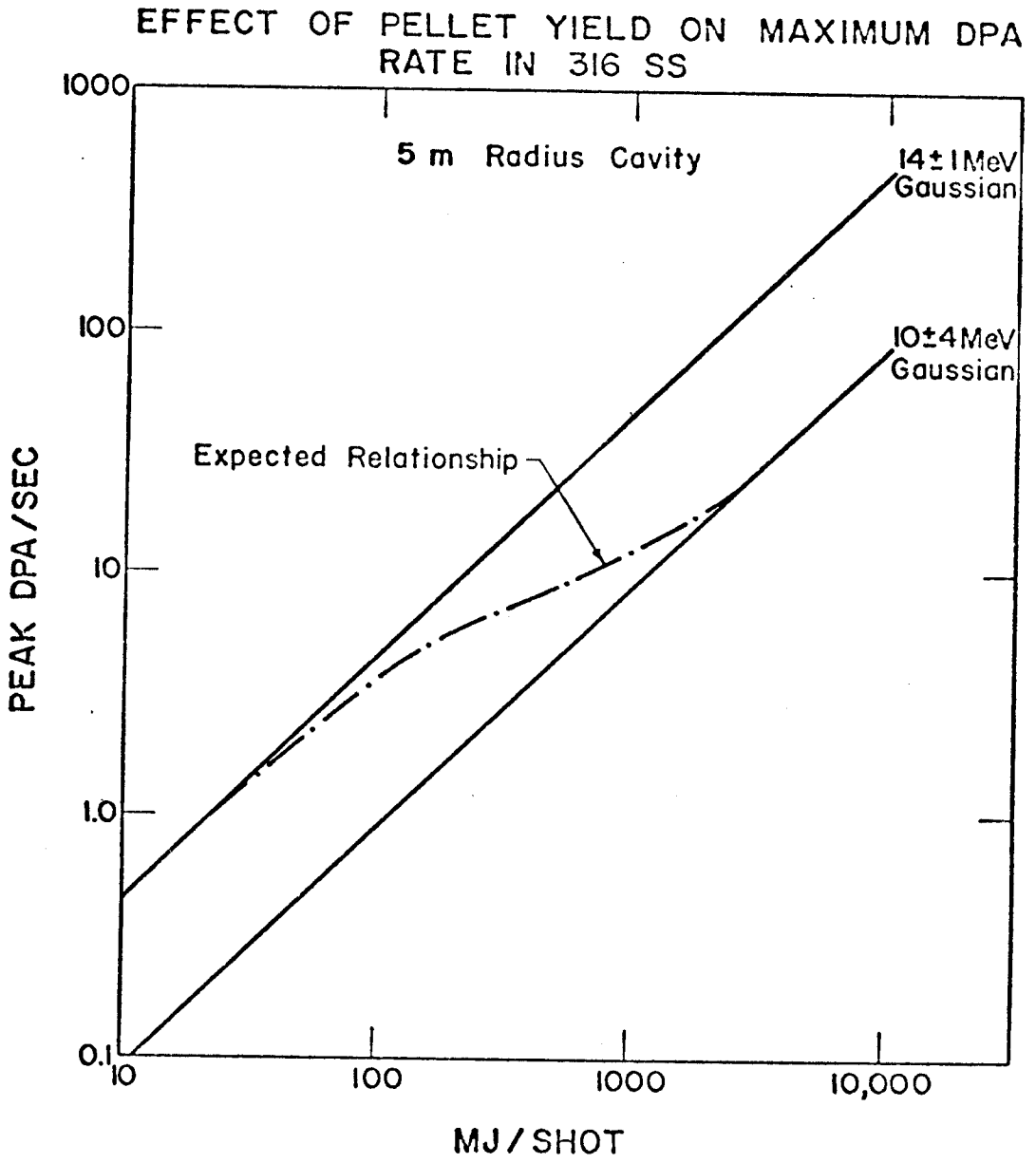

Fig. (9.8). Neutron spectrum effect on peak dap rate as a function of pellet yield.

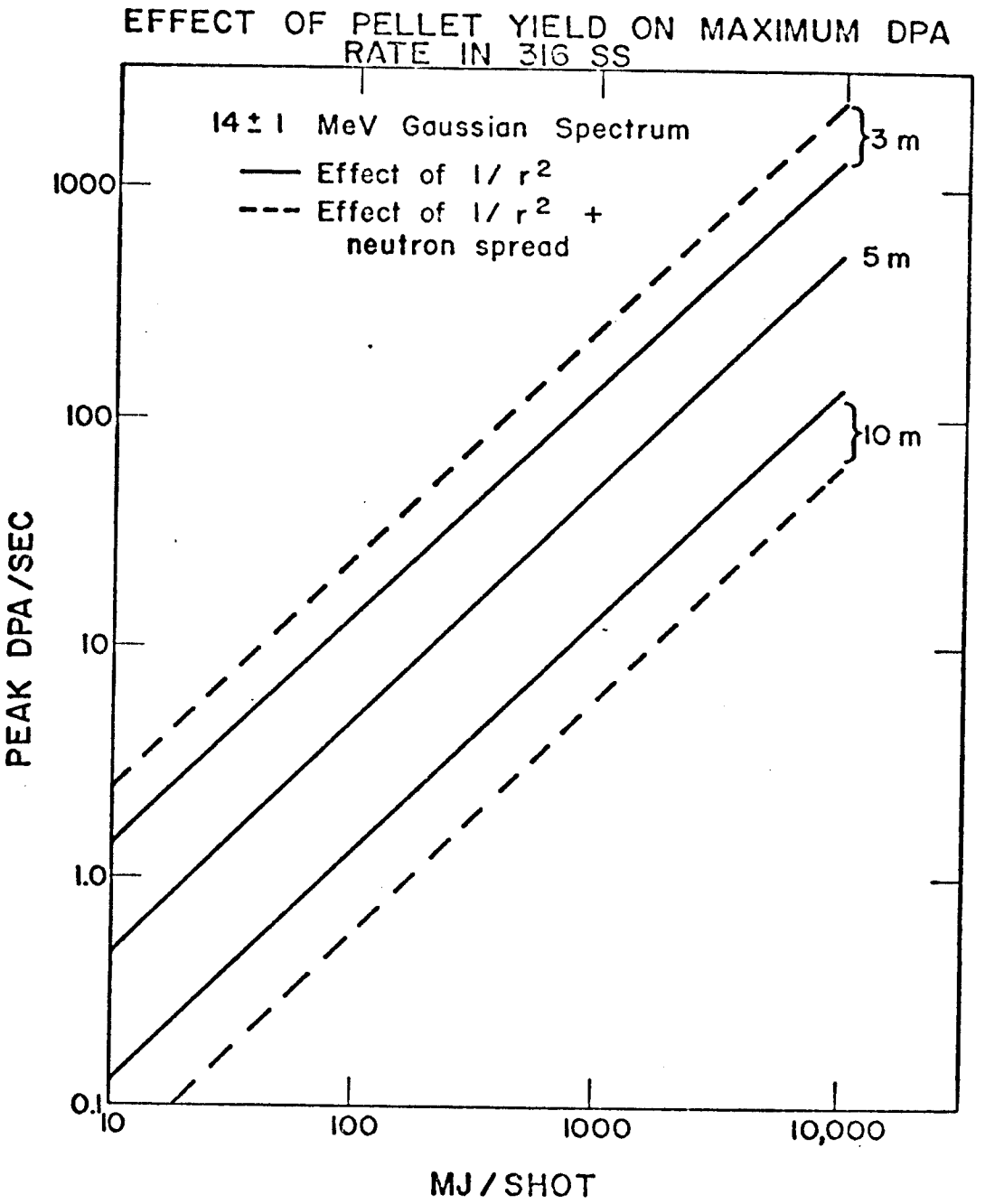
EFFECT OF PELLET YIELD ON MAXIMUM DPA RATE IN 316 SS
14 ± 1 MeV Gaussian Spectrum
Effect of 1/ r²
Effect of 1/ r² + neutron spread
3 m
5 m
10 m
PEAK DPA/SEC
1000
100
10
1.0
0.1
10
100
1000
10,000
MJ / SHOT

Fig. (9.9)

flight times between the more energetic and less energetic neutrons. Taking into account the different mechanisms for neutron pulse spreading, Figure (9.10) shows how the peak damage rate inside the pulse is expected to vary as a function of pellet yield. One can see that for a pellet yield of 10000 MJ/shot and a cavity radius of 5 m, dose rates as high as 70 dpa/s are experienced, while for a pellet yield of 100 MJ/shot and a radius of 10 m, the peak damage rate is only about 0.5 dpa/s.

A summary of the timescales, energy considerations and accumulated dose per pulse is given in Table (9.2), while possible pulse widths and corresponding average dose rates for the 4 different cases of Table (9.2), are shown in Table (9.3). One can notice that the accumulated dose per pulse is not large (10^{-5} dpa maximum), while the average dose rate in the pulse reaches a maximum value of 10^{4} dpa/s, as shown in Table (9.3). A common feature of all the studied cases is the average dose rate over many pulses, which is fixed to the value of 10^{-6} dpa/s.

IX.A.4.c. Point Defect Behavior in ICTR's

Point defect dynamic behavior is closely related to their mean lifetimes. A vacancy mean lifetime can vary between 10^{-4} seconds, at high temperatures ($\sim 0.5\ T_m$) and high sink densities, and 1 second at low temperatures ($\sim 0.3\ T_m$) and low sink densities. On the other hand, interstitial mean lifetime can vary between 10^{-7} seconds at high temperatures and high sink

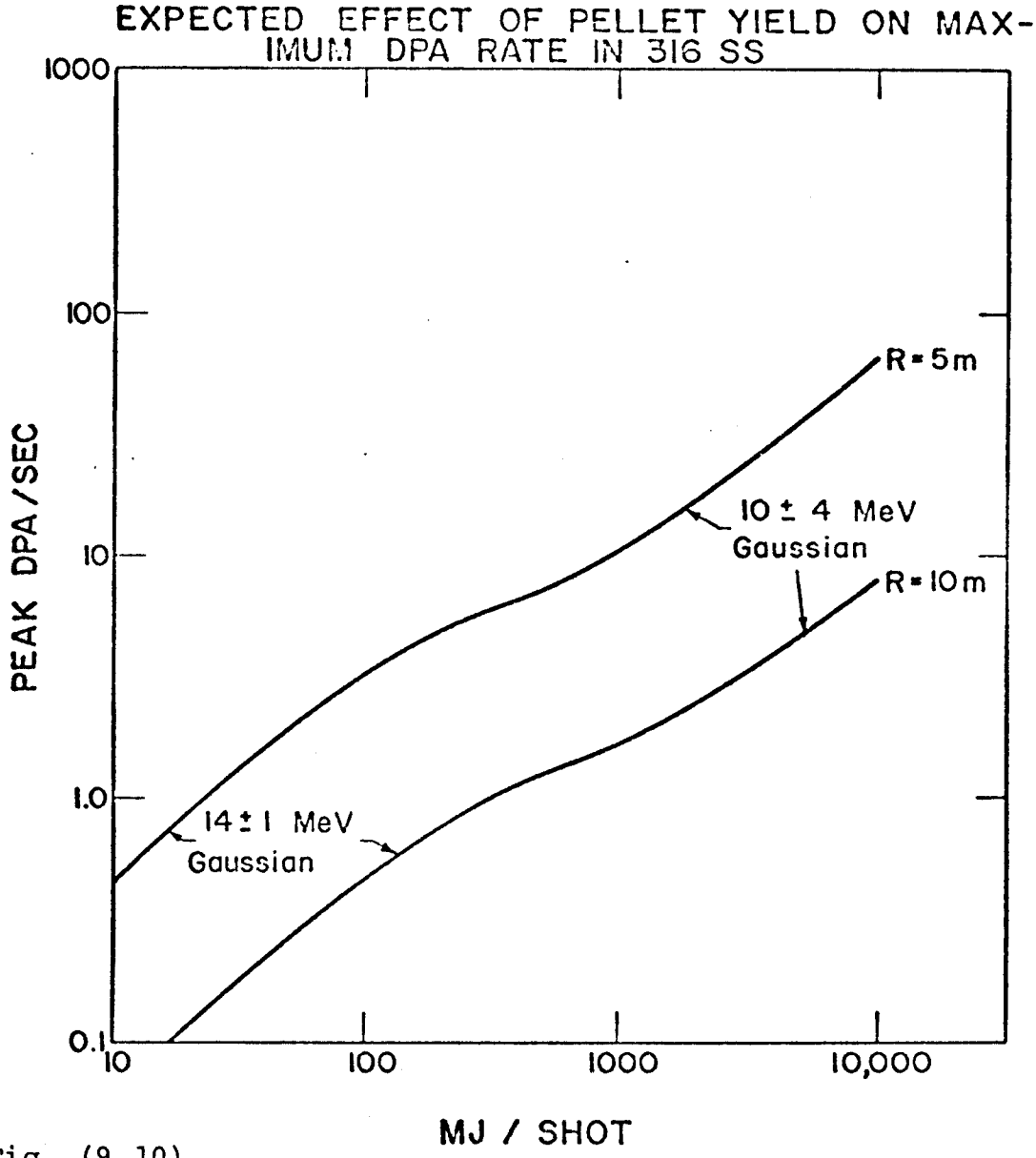
EXPECTED EFFECT OF PELLET YIELD ON MAX-IMUM DPA RATE IN 316 SS
1000
100
10
1.0
0.1
PEAK DPA/SEC
R=5m
10 ± 4 MeV
Gaussian
R=10m
14 ± 1 MeV
Gaussian
10
100
1000
10,000
MJ / SHOT

Fig. (9.10)

TABLE (9.2)

SUMMARY OF TIME AND ENERGY CONSIDERATIONS OF PULSED SYSTEMS

Case	Time Between Seconds, Pulses	Repetition Rate; Hz	Energy Per Pulse, MJ	Accumulated dpa/shot
1	10	0.1	10000	10^{-5}
2	1	1	1000	10^{-6}
3	0.1	10	100	10^{-7}
4	0.01	100	10	10^{-8}

TABLE (9.3)

SUMMARY OF PULSE WIDTH AND DAMAGE RATE

CONSIDERATIONS FOR PULSED SYSTEMS

Case	Pulse Width, Seconds	Av. Dose Rate in Pulse, dpa/sec
1	10^{-9}	10000
	10^{-8}	1000
	10^{-7}	100
	10^{-6}	10
2	10^{-9}	1000
	10^{-8}	100
	10^{-7}	10
	10^{-6}	1
3	10^{-9}	100
	10^{-8}	10
	10^{-7}	1
	10^{-6}	0.1
4	10^{-9}	10
	10^{-8}	1
	10^{-7}	0.1
	10^{-6}	0.01

densities and 10^{-5} seconds at low temperatures and low sink densities. The following notation will be used throughout this chapter:

τ_i; interstitial mean lifetime in seconds (9.D.1)

τ_v; vacancy mean lifetime in seconds (9.D.2)

P_w; pulse width in seconds (9.D.3)

Δt; pulse period in seconds (9.D.4)

Then, a combination of two of the following 4 conditions is satisfied in a practical pulsed system.

(1) $P_w < \tau_i < \tau_v$

(2) $\tau_i < P_w < \tau_v$

(3) $\tau_i < \Delta t < \tau_v$

(4) $\tau_i < \tau_v < \Delta t$

We will now study the case of 1 pulse every 10 seconds (case 4) with two different pulse widths corresponding to cases (1) and (2). As an example, neutron irradiated 316 SS, with the conditions previously established in Chapter VII, will be examined. At low temperatures (400°C) the vacancy concentration during the pulse increases rapidly with time irrespective of pulse width as displayed in Figure (9.11). Vacancy concentration starts to decline from the high value achieved during the pulse ($\sim 10^{-5}$ at/at) to its equilibrium concentration around a vacancy mean lifetime ($\sim$2 milliseconds at 400°C). These results indicate that the pulse width, and hence the details of the damage rates inside the pulse, have no effect on the vacancy concentration after the end of the

pulse. On the other hand, interstitial concentration increases linearly with time only for short pulses (10^{-9} seconds), while the concentration levels off at the end of long pulses (10^{-6} seconds), because of the high interstitial mobility. Therefore, the interstitial concentration is dependent on the pulse width, but the concentrations tend to be the same after about 10^{-6} seconds as shown in Figure (9.11). At higher temperatures (600°C) the metals matrix contains less voids and dislocations, which in turn increases interstitial concentrations. As shown in Figure (9.12), interstitials and vacancies exist with almost equal concentrations until the end of the pulse. This aspect enhances point defect mutual recombination, and causes a considerable decrease in the vacancy concentration around 10 microseconds. It is easily observed from Figure (9.12) that there is no effect of pulse width on point defect behavior after about a microsecond. The vacancy mean lifetime is a little longer at the higher temperature ($\sim$15 milliseconds at 600°C) which produces the relatively rapid drop in vacancy concentration around 10^{-2} seconds.

The vacancy concentration in the matrix does not reach the thermal equilibrium value, C_v^e, for a long time after the irradiation is turned off. Rather, it takes an average value, $\bar{C}_v$, determined by the existing microstructure and temperature, as will be explained later in this chapter. The vacancy concentration on the surface of a void of radius R_c, in the

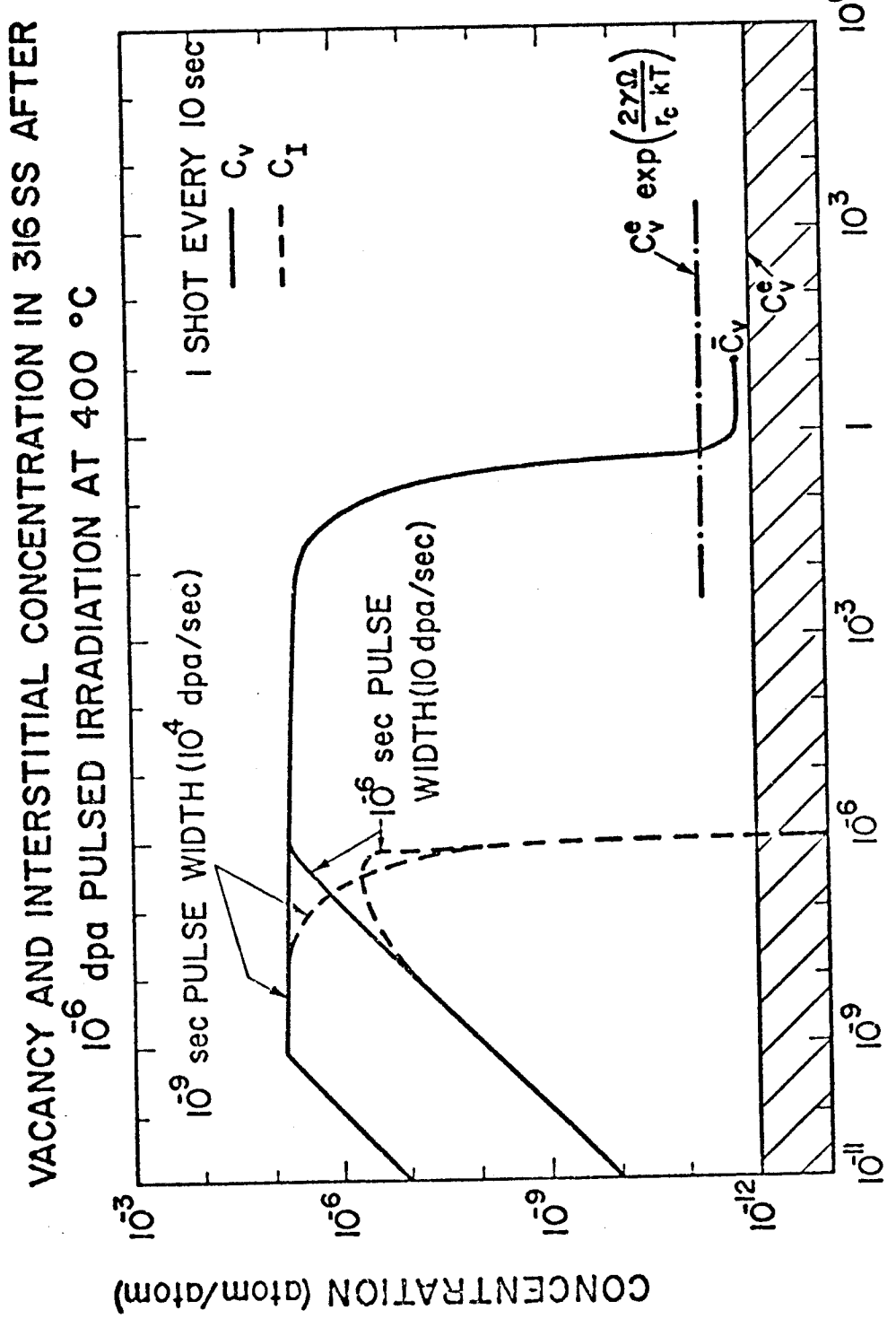
VACANCY AND INTERSTITIAL CONCENTRATION IN 316 SS AFTER
10^{-6} dpa PULSED IRRADIATION AT 400 °C
1 SHOT EVERY 10 sec
C_V
C_I
10^{-9} sec PULSE WIDTH (10^4 dpa/sec)
10^{-6} sec PULSE WIDTH (10 dpa/sec)
$C_V^e \exp\left(\frac{2\gamma\Omega}{r_c kT}\right)$
$\bar{C}_V$
C_V^e
CONCENTRATION (atom/atom)
TIME AFTER NEUTRON ARRIVAL (SEC)
10^{-3}
10^{-6}
10^{-9}
10^{-12}
10^{-11}
10^{-9}
10^{-6}
10^{-3}
1
10^{3}
10^{6}

Fig. (9.11)

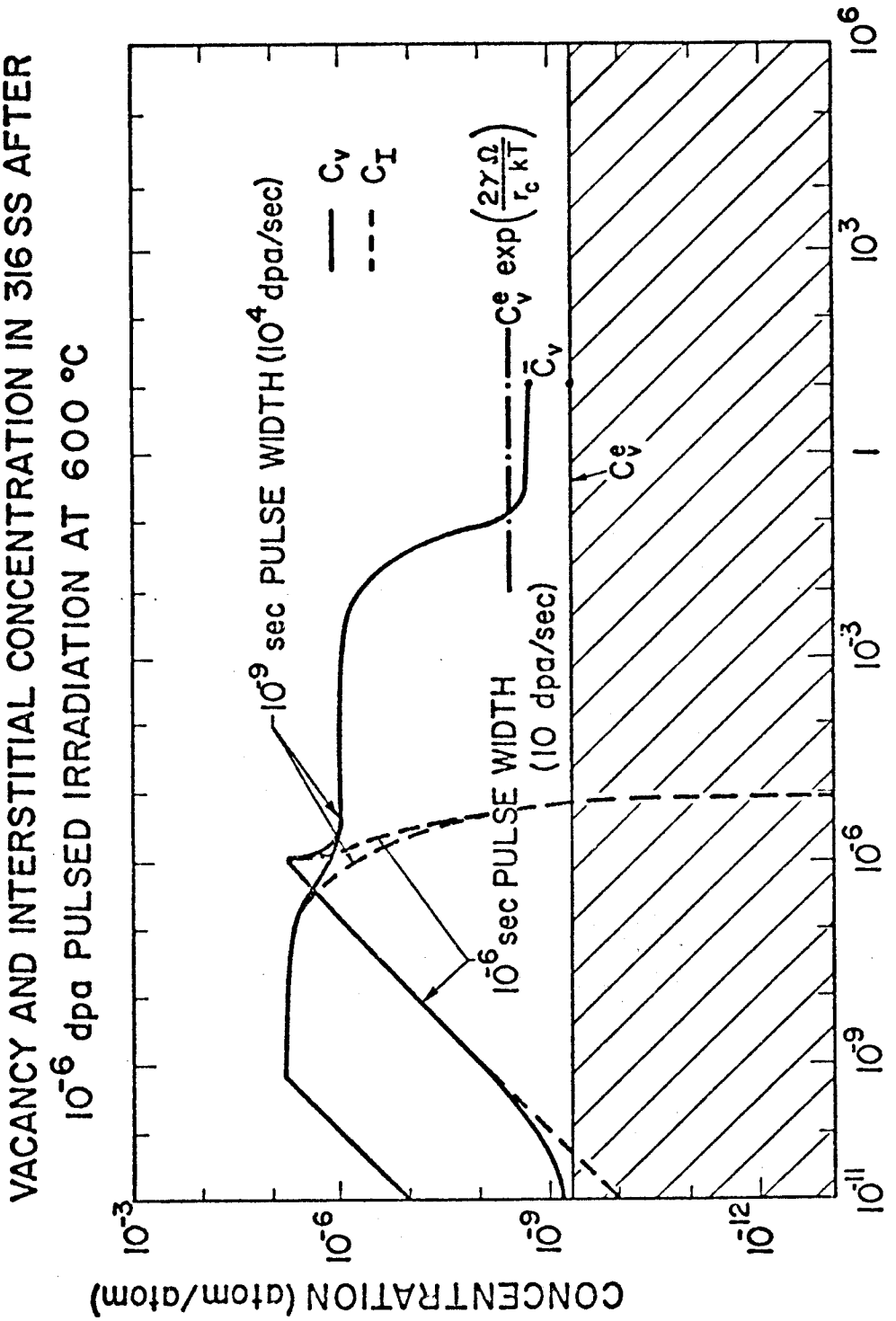
VACANCY AND INTERSTITIAL CONCENTRATION IN 316 SS AFTER
10^-6 dpa PULSED IRRADIATION AT 600 °C
CONCENTRATION (atom/atom)
TIME AFTER NEUTRON ARRIVAL (SEC)
10^-3
10^-6
10^-9
10^-12
10^-11
10^-9
10^-6
10^-3
1
10^3
10^6
10^-9 sec PULSE WIDTH (10^4 dpa/sec)
10^-6 sec PULSE WIDTH (10 dpa/sec)
C_v
C_I
C_v^e exp(2γΩ / r_c kT)
C̄_v
C_v^e

Fig. (9.12)

absence of stresses and gas atoms inside, is determined by the simple expression:

$$C_v = C_v^e \exp\{\frac{2\gamma\Omega}{R_c kT}\} \qquad (9.1)$$

Due to the presence of dislocations, grain boundaries and free surfaces, the average matrix thermal vacancy concentration is smaller than the value given by expression (9.1). This creates a vacancy concentration gradient between the void surface and the bulk of the metal. A flow of vacancies from the void surface to the bulk of the metal is then set up, tending to reduce the void size. From Figure (9.11), one can notice that at low temperature (400°C) the gradient (proportional to concentration difference) between the void and the matrix is small and the time available for void annealing is short, compared to the larger gradient and longer annealing time at 600°C, as can be seen from Figure (9.12). The effects of the different irradiation and materials variables on void annealing are explained later in this chapter, and a study of the consequences of pulsed irradiation variables on metal swelling is also described.

IX.B. Approximate Solution of the Void Growth Problem

The general solution of time dependent void growth under pulsed irradiation ensues from the application of the (FDRT), previously described in Chapter V. Although the theory is based on the fundamental behavior of defects, FDRT does not give a simple picture of the void behavior under irradiation.

In this section, we present a simple example applicable under a restricted set of circumstances, to guide the general understanding of the different aspects of point defect and microstructure behavior under pulsed irradiation.

IX.B.1. Analysis

The following assumptions are adopted for the approximate analysis given in this section.

(1) High dislocation density such that point defect bulk recombination is ignored.

(2) Low void sink density compared to the total dislocation density.

(3) Low precipitate concentration compared to void concentration.

(4) Large grain sizes.

(5) Low vacancy loop production rate such that their effect on point defects and microstructure could be ignored.

A simplification of mathematical difficulties can be made with these assumptions. Assumption (1) will always be satisfied if:

$$\left.\begin{aligned} & D_v C_v Z_v \rho_d >> \alpha C_i C_v \\ \text{and} \quad & D_i C_i Z_i \rho_d >> \alpha C_i C_v \end{aligned}\right\} \tag{9.2}$$

or in other words,

$$\rho_d >> \frac{\alpha C_i}{D_v} >> 10^{16} \frac{\phi_i}{D_v} \tag{9.3}$$

where ϕ_i is the interstitial flux ($D_i C_i$), and $\frac{\alpha}{D_i} \sim 10^{16}$.

The thermal vacancy emission rate is then simply given by:

$$P^e = D_v Z_v \rho_d C_v^e + 4\pi R_c N_c D_v C_v^e \exp\{\frac{2\gamma\Omega}{R_c kT}\} \quad (9.4)$$

and under the previous assumptions, Eq. 9.4 boils down to:

$$P^e \tilde{=} D_v Z_v \rho_d C_v^e \quad (9.5)$$

The two governing equations for the time behavior of point defects (5.62) and (5.63), will now reduce to the following uncoupled first order linear differential equations:

$$P(t) - Z_i D_i \rho_d C_i(t) = \frac{dC_i(t)}{dt} \quad (9.6)$$

$$P(t) + Z_v D_v \rho_d C_v^e - Z_v D_v \rho_d C_v(t) = \frac{dC_v(t)}{dt} \quad (9.7)$$

From the definitions given by equations (5.36) and (5.38) in Chapter V, equations (9.6) and (9.7) will take the simple form

$$\dot{C}_i = P - \lambda_i C_i \quad (9.8)$$

$$\dot{C}_v = P - \lambda_v (C_v - C_v^e) \quad (9.9)$$

IX.B.2. Solutions for a Delta Function Generation of Point Defects

As pointed out before in the previous section, point defect generation rate is a function of many design and neutron source variables. However, an insight into the problem is gained by investigating the solution of equations (9.8) and (9.9) for a delta function generation of point defects. In this case the point defect production rate is given by:

$$P(t) = \varepsilon P_o \delta(t - t_p) \quad (9.10)$$

where εP_o is the strength of the δ-function (this product is actually the accumulated dose per pulse), t_p is the starting time of the pulse, and ε is the small time interval during which a constant generation of P_o dpa/sec takes place.

The rate of change of a void radius, R_c, as given by equation (5.58) is now simplified to:

$$\frac{dR_c}{dt} = \frac{1}{R_c}\,(D_v C_v - D_i C_i) - \frac{D_v C_v^e}{R_c}\exp\left\{\frac{2\gamma\Omega}{R_c kT}\right\} \tag{9.11}$$

Combining equations (9.8) and (9.9) and (9.11), one gets

$$\frac{d}{dt}\begin{bmatrix} C_v \\ C_i \\ R_c \end{bmatrix} = \begin{bmatrix} -\lambda_v & 0 & 0 \\ 0 & -\lambda_i & 0 \\ \frac{D_v}{R_c} & -\frac{D_i}{R_c} & 0 \end{bmatrix}\begin{bmatrix} C_v \\ C_i \\ R_c \end{bmatrix} + \begin{bmatrix} P(t) + \lambda_v C_v^e \\ P(t) \\ -\frac{D_v C_v^e}{R_c}\exp\{\frac{F_m\Omega}{kT}\} \end{bmatrix} \tag{9.12}$$

where F_m is given by, $F_m = \frac{2\gamma}{R_c}$. If just the fluctuations around the void radius R_c are studied, the void radius R_c could be considered to be a constant in the right hand side of equation (9.11). This assumption linearizes the system of equations (9.12), and consequently gives the following solution for a delta function generation of point defects:

$$C_i(t) = \varepsilon P_o \exp\{-\lambda_i (t-t_p)\}\, U(t-t_p) \tag{9.13}$$

$$C_v(t) = C_v^e + \varepsilon P_o \exp\{-\lambda_v (t-t_p)\}\, U(t-t_p) \tag{9.14}$$

$$R_c(t) = R_c(0) + \frac{\varepsilon P_o}{R_c} U(t-t_p) \left\{ \frac{D_v}{\lambda_v} [1-\exp(-\lambda_v(t-t_p)] \right.$$

$$\left. - \frac{D_i}{\lambda_i} [1-\exp(-\lambda_i(t-tp))] \right\} - \frac{D_v C_v^e}{R_c} \left\{ \exp(\frac{F_m \Omega}{kT}) - 1 \right\} t \qquad (9.15)$$

where $U(t-t_p)$ is the unit step function at t_p.

IX.B.3. General Time-Behavior of Voids and Point Defects

The detailed analysis resulting from equations (9.13), (9.14) and (9.15) is given in reference (99), but the general features of the solution will briefly be given here.

It is appropriate at this point to define two different times relevant to the kinematic behavior of a pulse; the recovery time (t_r) and the pulse annealing time (t_a), as follows:

t_r = The time at which the void regains its initial radius.

t_a = The time at which the void loses the volume increase due to the pulse, by emitting excess vacancies, i.e., when the void comes back to its original radius.

With reasonable approximations*, it is possible to derive the following simple expressions for t_r and t_a:

$$t_r = \tau_v \ell n \left\{ \frac{Z_i}{Z_i - 1} \right\} \qquad (9.16)$$

*It is readily seen that at times near t_r, interstitial and annealing effects can be neglected. While for times in the range of t_a, no time dependent vacancy and interstitial contributions have to be considered.

$$t_a = \frac{\varepsilon P_o (Z_i - 1)/Z_i}{\rho_d D_v^s \{\exp(\frac{F_m \Omega}{kT}) - 1\}} \qquad (9.17)$$

where D_v^s is the vacancy self-diffusion coefficient in cm^2/sec.

As an example, we will study 316 SS at 400°C, with $\varepsilon P_o = 10^{-7}$ dpa and $\rho_d = 5 \times 10^{11}$ cm^{-2}. Point defect concentrations and void radius change after a short irradiation pulse (delta function) are shown in Figure (9.13). Interstitials and vacancy concentrations decay after the pulse with their respective time constants.

One should notice in Figure (9.13) that the time scale is logarithmic until ∿10 seconds and then becomes linear. Point defects simply migrate to voids and dislocations, governed by their time constants. The 40 Å void in this example experiences a large flux of interstitials around an interstitial mean lifetime reducing its radius by about 4×10^{-5} Å. Since the process is statistical in nature, this small change is considered as an average value over many voids. Around a vacancy mean lifetime, the void receives a vacancy flux, which is slightly larger than the interstitial flux due to the fact that more interstitials than vacancies were absorbed at dislocations.

The void regains its original radius at a time t_r that is approximately given by equation (9.16), and it is shown in Figure (9.13). Once the bulk vacancy concentration is lower than the vacancy concentration at the void surface,

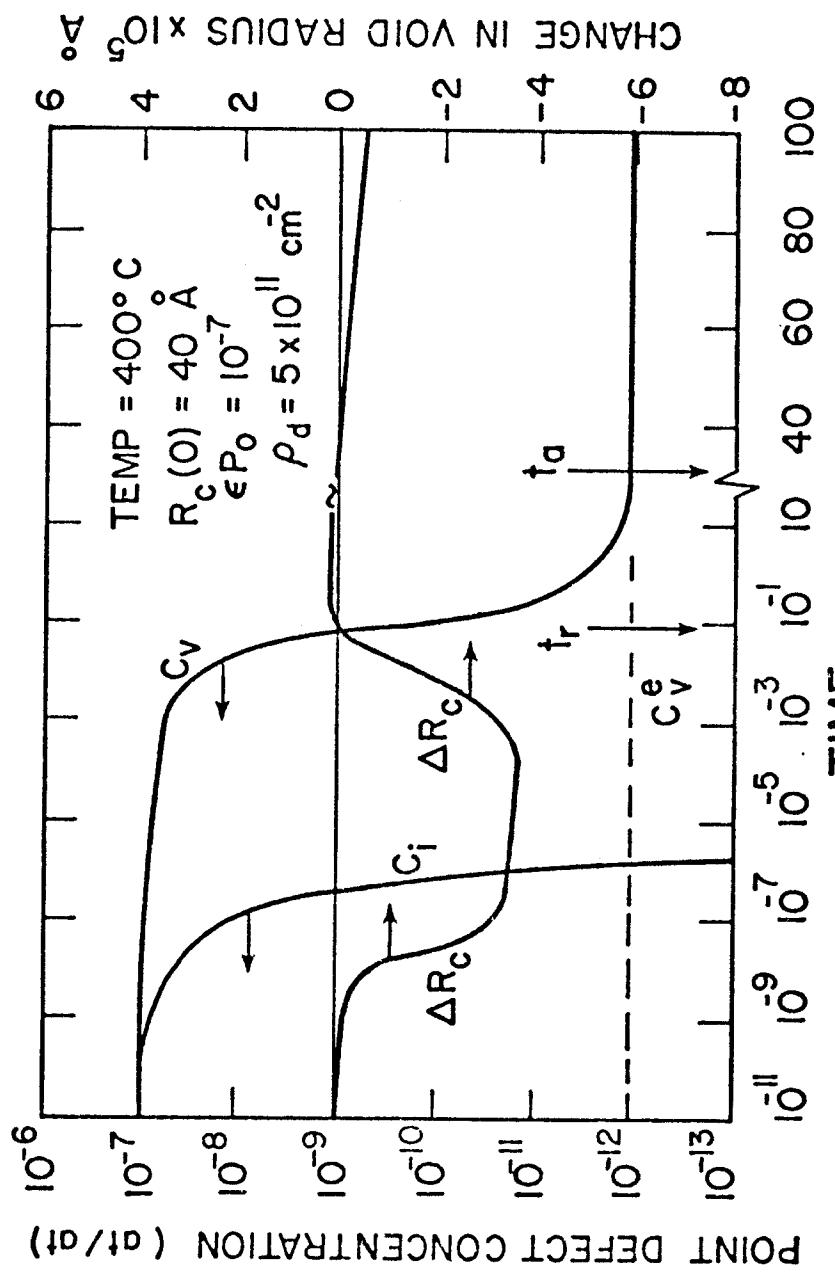

Fig. (9.13). Point defect concentrations and change in void radius as a function of time after a pulse of irradiation.

the void starts to thermally emit vacancies. This tends to continually reduce its size. The void anneals out all the vacancies gained from the damage pulse around the time t_a, given by equation (9.17) and shown in Figure (9.13), and starts to shrink thereafter.

IX.C. Results of FDRT for Annealing Studies

A key requirement of the FDRT is to accurately describe the annealing behavior of voids between successive damage pulses. A precise assessment of the void growth due to the damage pulse and its shrinkage between pulses is needed to determine the final fate of this void. This section focuses on this particular aspect and investigates the major parameters that influence the annealing kinetics of voids. A detailed analysis is given in Reference (116) for a few void annealing experiments carried out on aluminum [83,84]. The agreement between the theory and the results of these experiments was shown to hold in Chapter VII. Here, void annealing kinetics is studied further in aluminum because of its relation to experimental findings. The parameters of Tables (6.1) and (7.6) were used throughout these calculations.

IX.C.1. Temperature Effects

The void annealing calibration experiments of Chapter VII showed the great sensitivity of void annealing to temperature. At higher temperatures voids anneal out much faster than at lower temperatures as can be seen from Figures (7.14)

and (7.15). At 175°C voids in aluminum anneal out about 30 times faster then at 126°C. It can be seen from the same figures that the void radius versus time curve is almost linear for the first stages of the annealing time. However, it becomes heavily non-linear as the void size decreases. This means that smaller size voids anneal out much faster than large size voids.

IX.C.2. Surface Energy

The value of void/matrix surface energy is known to have a great effect on calculated void nucleation rates in metals under irradiation. Void annealing is controlled by the surface energy as one of its variables, therefore, it is of considerable interest to study the sensitivity of annealing kinetics to the value of the surface energy. Annealing curves with different values of the surface energy for a 152 Å radius void, at a temperature cf 126°C, are shown in Figure (9.14). It can be seen that quite large changes in the surface energy do not substantially influence the kinetics in the early stages of annealing, at least in the period of seconds to minutes which might be typical of the time between bursts of irradiation.

IX.C.3. Void Gas Content

Cavities in neutron irradiated aluminum showed slower annealing behavior than quenched in voids[84]. This behavior was attributed to the presence of gas atoms in the cavities. Using Van der Waal's gas equation (Equation 5.15)

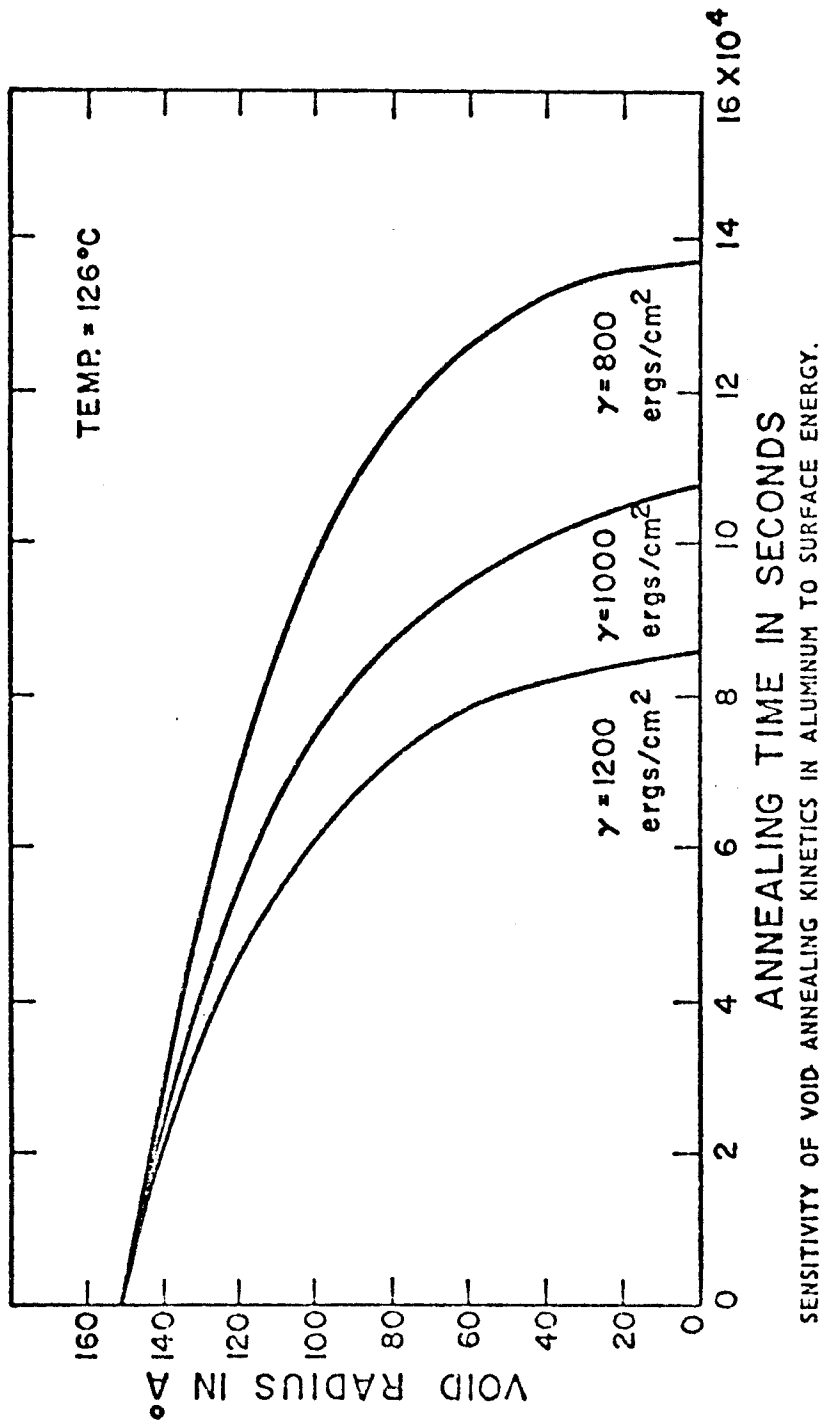

SENSITIVITY OF VOID ANNEALING KINETICS IN ALUMINUM TO SURFACE ENERGY.

Fig. (9.14)

for He gas, the annealing kinetics of a 152 Å cavity is studied in Figure (9.15). It is observed that the annealing behavior becomes slower as the number of He gas atoms is increased in the cavity. For a larger number of gas atoms, a longer time is needed for the cavity to come to its equilibrium radius. If the number of gas atoms in a cavity is greater than the equilibrium value for this particular radius, the cavity becomes an overpressurized gas bubble. For example, if a cavity of 152 Å radius contains 1.5×10^5 He gas atoms at 120°C, it actually grows by vacancy absorption to an equilibrium radius of 165 Å. The driving force for the growth is the fact that the vacancy concentration at the cavity surface is lower than that in the bulk. This situation creates a flow of vacancies from the matrix to the void relieving the internal gas pressure and the gas bubble grows as shown in Figure (9.15).

IX.C.4. Microstructure Effect on Annealing

The previous analysis indicated that void annealing kinetics can be substantially altered by different material parameters. The analysis was based on the existence of surfaces that maintain a thermal equilibrium vacancy concentration such as straight dislocations, grain boundaries or specimen surfaces. This provides enough driving force for voids to lose their vacancies to these surfaces by thermal emission. In this section we will concentrate on the effect of existing planar surfaces, interstitial loops, vacancy loops and voids

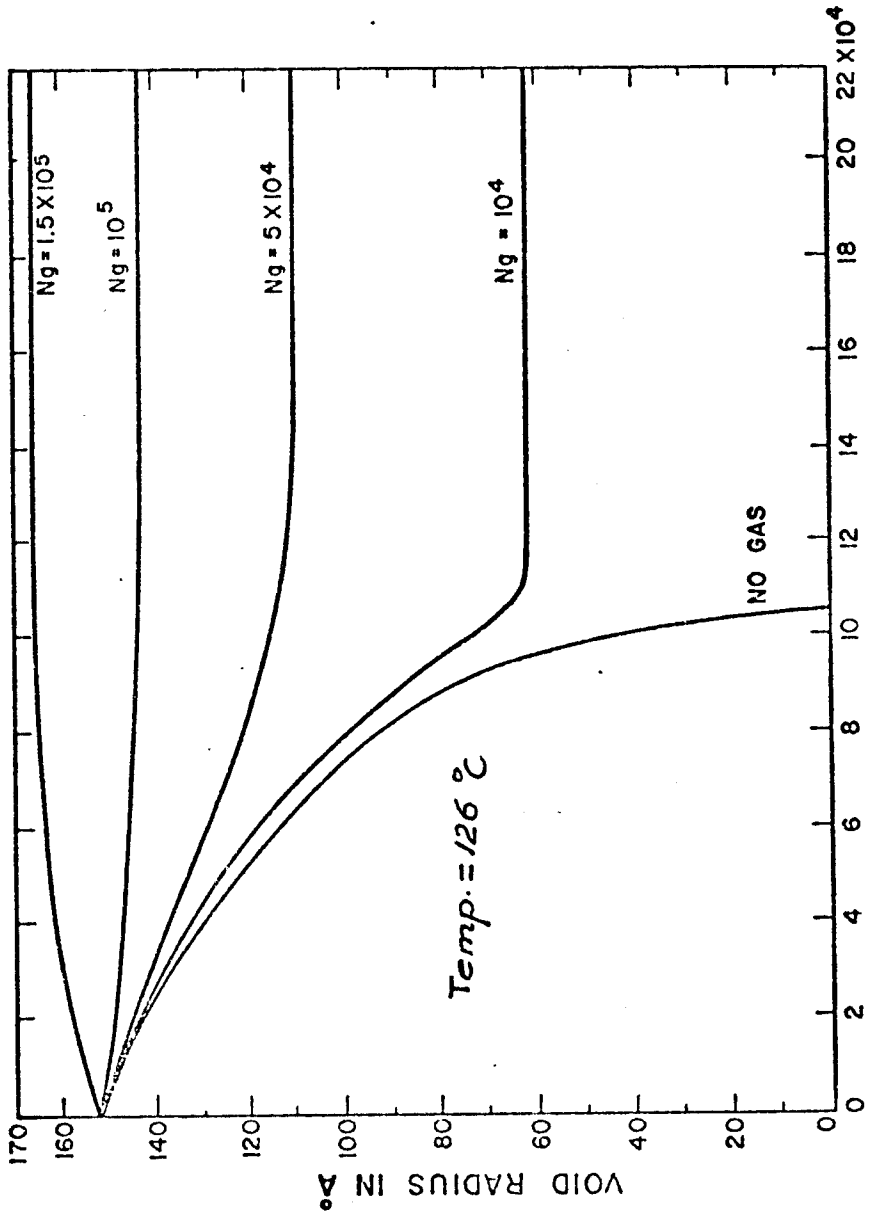

EFFECT OF NUMBER OF He GAS ATOMS IN THE VOID (Ng) ON THE ANNEALING KINETICS OF VOIDS IN ALUMINUM.

Fig. (9.15)

on the annealing behavior of voids.

IX.C.4.a. Analysis and Results

When irradiation is turned off, as in post irradiation annealing experiments, or in the annealing mode of voids in between pulses, thermal vacancies are emitted from different components of the microstructure and absorbed by others. If the time between pulses is longer than a vacancy mean lifetime, or in a post irradiation annealing experiment, a simple point defect balance situation can be described. Since thermal emission of interstitials from microstructures has a low probability (because of the large interstitial formation energy), a balance equation for vacancies, a long time after the irradiation is turned off, can be described as:

[Total rate of thermal vacancy emission = total rate of vacancy removal]

Since thermal concentration of intersititals is very low under these circumstances, vacancy removal by mutual recombination is negligible, and the previous balance equation can be written as:

$$P^e = P_{sv} = \lambda_v \bar{c}_v \ . \qquad (9.18)$$

Therefore, $$\bar{c}_v = \frac{P^e}{\lambda_v} \ , \quad \text{or} \qquad (9.19)$$

$$\bar{c}_v = c_v^e \left\{ \frac{4\pi R_c N_c \exp\{(\frac{2\gamma}{R_c} - P_g)\frac{\Omega}{kT}\} + Z_v^a \rho_d^{ea} \exp(\sigma\Omega/kT) + Z_v^n \rho_d^{en} + }{4\pi R_c N_c + Z_v^a \rho_d^{ea} + Z_v^n \rho_d^{en} + } \right.$$

$$\frac{Z_v^a \rho_d^{i\ell a} \exp(\sigma\Omega/kT) \exp(-\frac{\{\gamma_{sf} + F_{e\ell}(r_{i\ell}^a)\}b^2}{kT}) + Z_v^n \rho_d^{i\ell n} \exp(-\frac{\{\gamma_{sf} + F_{e\ell}(r_{i\ell}^n)\}b^2}{kT}) +}{Z_v^a \rho_d^{i\ell a} + Z_v^n \rho_c^{i\ell n} +}$$

$$\left. \frac{Z_v^a \rho_d^{v\ell a} \exp(\sigma\Omega/kT) \exp(\frac{\{\gamma_{sf} + F_{e\ell}(r_{v\ell}^a)\}b^2}{kT}) + Z_v^n \rho_d^{v\ell n} \exp(\frac{\{\gamma_{sf} + F_{e\ell}(r_{v\ell}^n)\}b^2}{kT})}{Z_v^a \rho_d^{v\ell a} + Z_v^n \rho_d^{v\ell n}} \right\}$$

(9.20)

Equation (9.20) shows that the average thermal vacancy concentration is a function of the microstructure and stress. The annealing of voids depends on the vacancy concentration gradient between the surface of the void and the average thermal vacancy concentration in the matrix. This gradient is proportional to the difference in concentrations as shown in Figure (9.16). According to this schematic representation we have one of 5 different situations:

Case	Average Thermal Vacancy Concentration Near Defects
1. Edge dislocations or specimen surfaces only	C_v^e
2. Small interstitial loops only	$C_v^e \exp\{-(F_{e\ell}+\gamma_{sf})\frac{b^2}{kT}\}$
3. Small voids only	$C_v^e \exp(\frac{2\gamma}{R_c} - p)$
4. Small vacancy loops only	$C_v^e \exp\{+(F_{e\ell}+\gamma_{sf})\frac{b^2}{kT}\}$
5. A mixed microstructure	$\bar{C}_v$

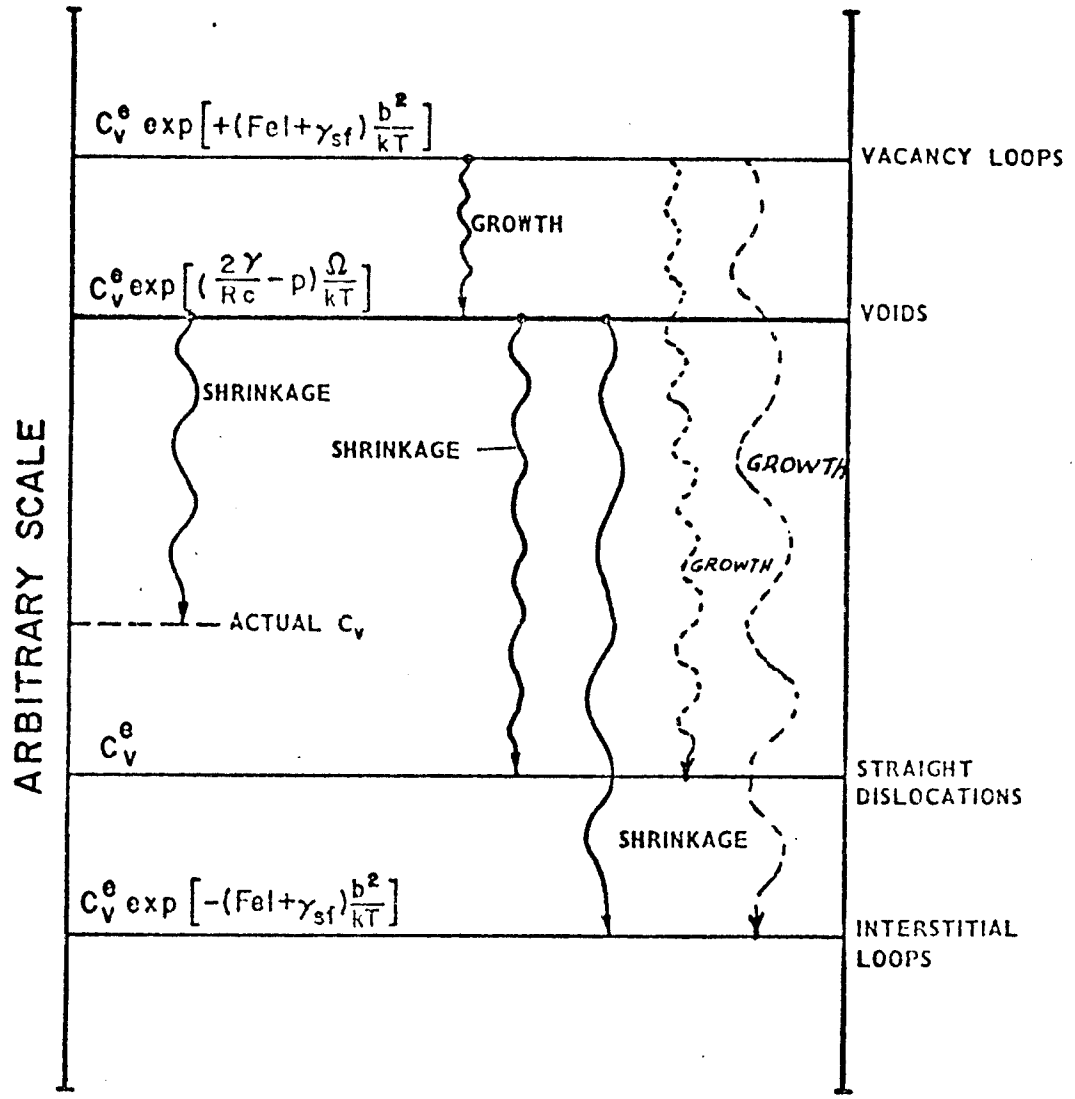

Fig. (9.16). Schematic illustration of main thermal annealing kinetics and their relation to microstructure.

One can see from Figure (9.16) that vacancy loops emit vacancies helping voids to grow has well as causing interstitial loops and dislocations to shrink) while smaller interstitial loops absorb more vacancies than edge dislocations, and therefore, make voids shrink faster.

To study the effect of changing the microstructure on the annealing of voids, the number of voids was fixed to 10^6 voids/cm^3 and their radius to 152 Å. An equivalent number of interstitials to that of vacancies in the voids was distributed on interstitial loops. The only variable in the calculations was the ratio of interstitial loops to voids ranging from 10^{-6} to 10^4 with a negligible concentration of straight edge dislocations. It is evident from Figure (9.17) that voids anneal out much faster for larger ratios while the rate of annealing is slower when voids are the dominant thermal vacancy source/sink.

IX.C.4.b. Conclusions

Annealing of voids was shown to be a sensitive function of many variables, some variables enhance the annealing of voids, while others retard it. To enhance annealing of voids, one or more of the following conditions should exist:

(1) High temperature.

(2) Small void radius.

(3) Large void surface energy.

(4) High density of deformation produced dislocations.

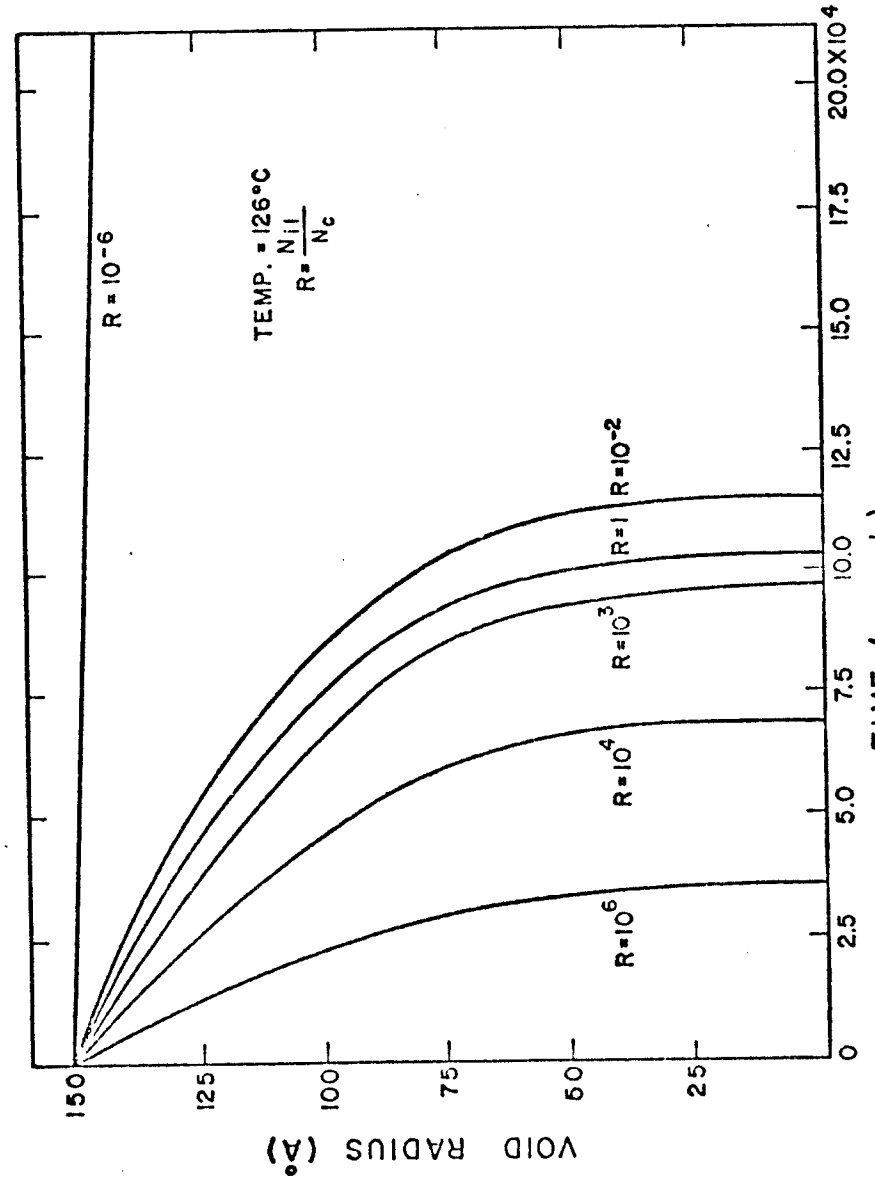

EFFECT OF RATIO OF INTERSTITIAL LOOPS TO VOIDS ON ANNEALING OF VOIDS IN ALUMINUM.

Fig. (9.17)

(5) High concentration of small interstitial loops.

On the other hand, annealing of voids is retarded by one or a combination of the following:

(1) Low temperature.

(2) Large void radius.

(3) Small void surface energy.

(4) The presence of gas atoms inside the voids.

(5) Low density of deformation produced dislocations.

(6) Low density of interstitial loops of large sizes.

(7) High density of vacancy loops.

IX.D. Results of Pulsed Irradiation Analysis in ICTR's

It was previously mentioned that the void growth under steady-state irradiation affected by many irradiation and material variables. Besides all of these variables, the pulsed nature of irradiation has its unique effects on the growth of voids. In this section, we will concentrate on studying the unique features in the void growth phenomenon encountered in the case of pulsed irradiation. We will first discuss the effect of changing the pulse width while keeping the same accumulated dose in the pulse. The influence of the irradiation temperature on the growth kinetics is then discussed. Thereafter, the general features of a train of neutron pulses and the final results such a train produces are studied.

The combined influence of the repetition rate and temperature on determining the final swelling behavior of a 50 Å radius void is analyzed. This is followed by exploring the

effects of different sizes of voids (10 Å radius and 100 Å radius) on the final swelling. Finally the consequences of changing the bias factor on pulsed irradiation are studied.

IX.D.1. Pulse Width

The pulse width and the dose rate time dependence inside the pulse can be predicted by time dependent neutronics calculations[124]. We will examine here two widely differing cases of neutron pulses; one of a nanosecond pulse width and the other of a microsecond pulse width. A total accumulated dose of 10^{-5} dpa was assumed to be the same for the two pulses, thus dose rates of 10^4 dps/sec and 10 dpa/sec are achieved for the nanosecond and the microsecond pulses, respectively. The rate of growth of a 20 Å radius void, in 316 SS at a temperature of 600°C, is shown in Figure (9.18). The decrease in the void volume due to the irradiation pulse reflects the efficiency of point defect mutual recombination. If the point defect mutual recombination rate is high during the pulse, the number of point defects free to migrate to sinks is reduced. For example, the displacement rate of 10^4 dpa/sec in the nanosecond pulse is accompanied by more recombination than in the case of the 10 dpa/sec displacement rate of the microsecond pulse. This causes a smaller net decrease in the void radius for the nanosecond pulse as shown in Figure (9.18). It is found that no matter how many interstitials are dumped into the void, enough vacancies will eventually arrive to the void surface offsetting the decrease in size

EFFECT OF PULSE WIDTH ON VOID KINETICS AT HIGH TEMPERATURE

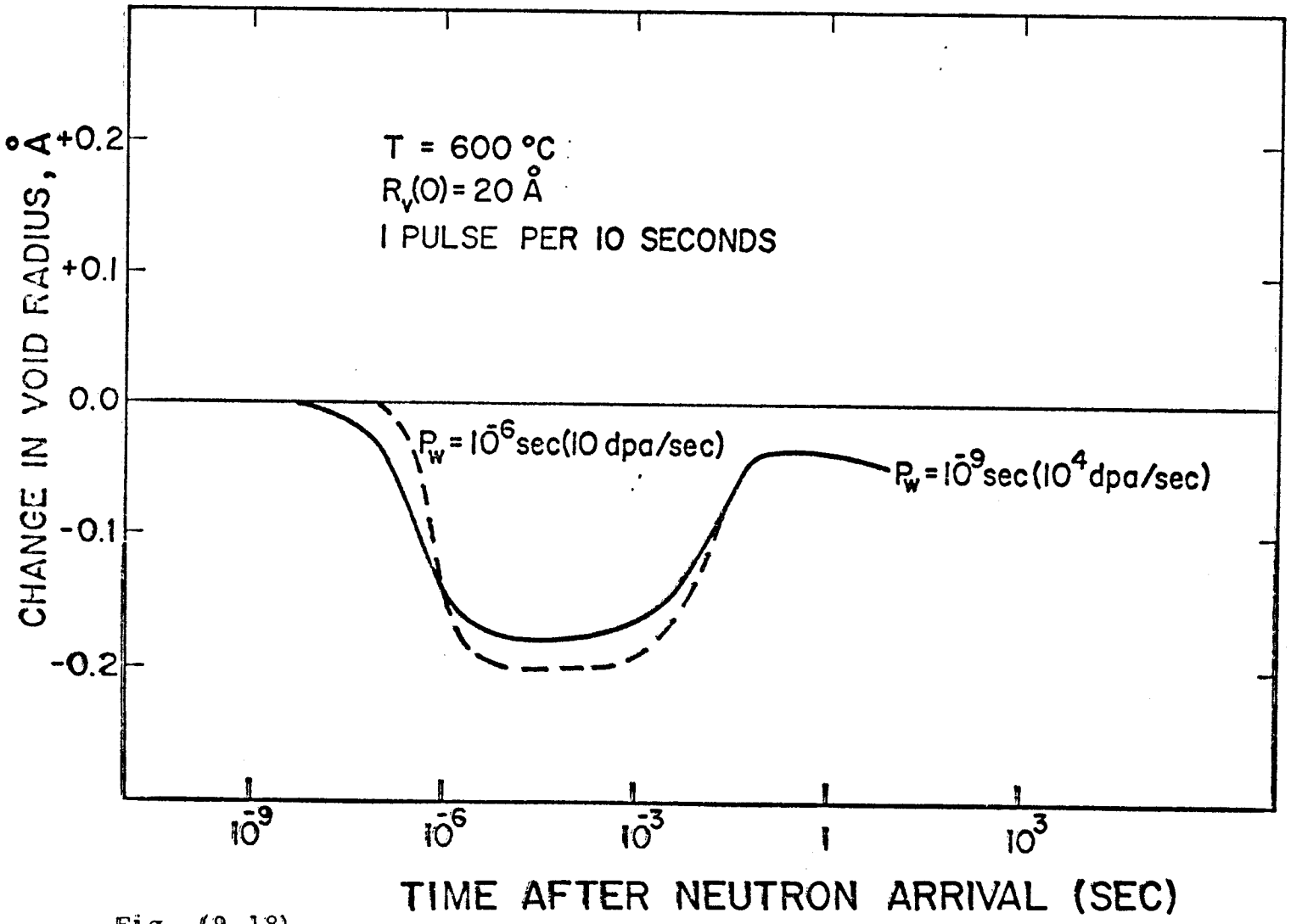

Fig. (9.18)

caused by interstitials. After about a mean vacancy lifetime the void kinetics are entirely dominated by the annealing. One can conclude that in the presently considered ICTR's (with $P_w = 10^{-9}$ to 10^{-6} sec), the pulse width and time structure of the displacement rate inside the pulse are not of significant importance to the overall swelling. Therefore, the accumulated dose in one pulse is the only parameter needed, as far as the damage process is considered.

IX.D.2. Temperature

Irradiation temperature mainly affects the sink densities, point defect mobilities and the annealing kinetics of voids. The effect of temperature on a 20 Å radius void in 316 SS is studied in Figures (9.19) and (9.20). The void is subject to one irradiation pulse of a nanosecond width and a dose rate of 10^4 dpa/sec inside the pulse. At 400°C the interstitial and void densities are high, thus reducing the number of point defects going to the 20 Å radius void. The maximum drop in the void radius due to the interstitial flux is only $\sim$-.012 Å, as shown in Figure (9.19). When the vacancies reach the void around a vacancy mean lifetime, they cause a net increase in the void radius. Since annealing is not strong at 400°C, this net increase in the void radius (growth) is maintained at the end of the period which is 10 seconds. As the irradiation temperature increases, the initial drop in the void radius also increases due to the larger interstitial flux. The reason for this larger drop in the void radius is

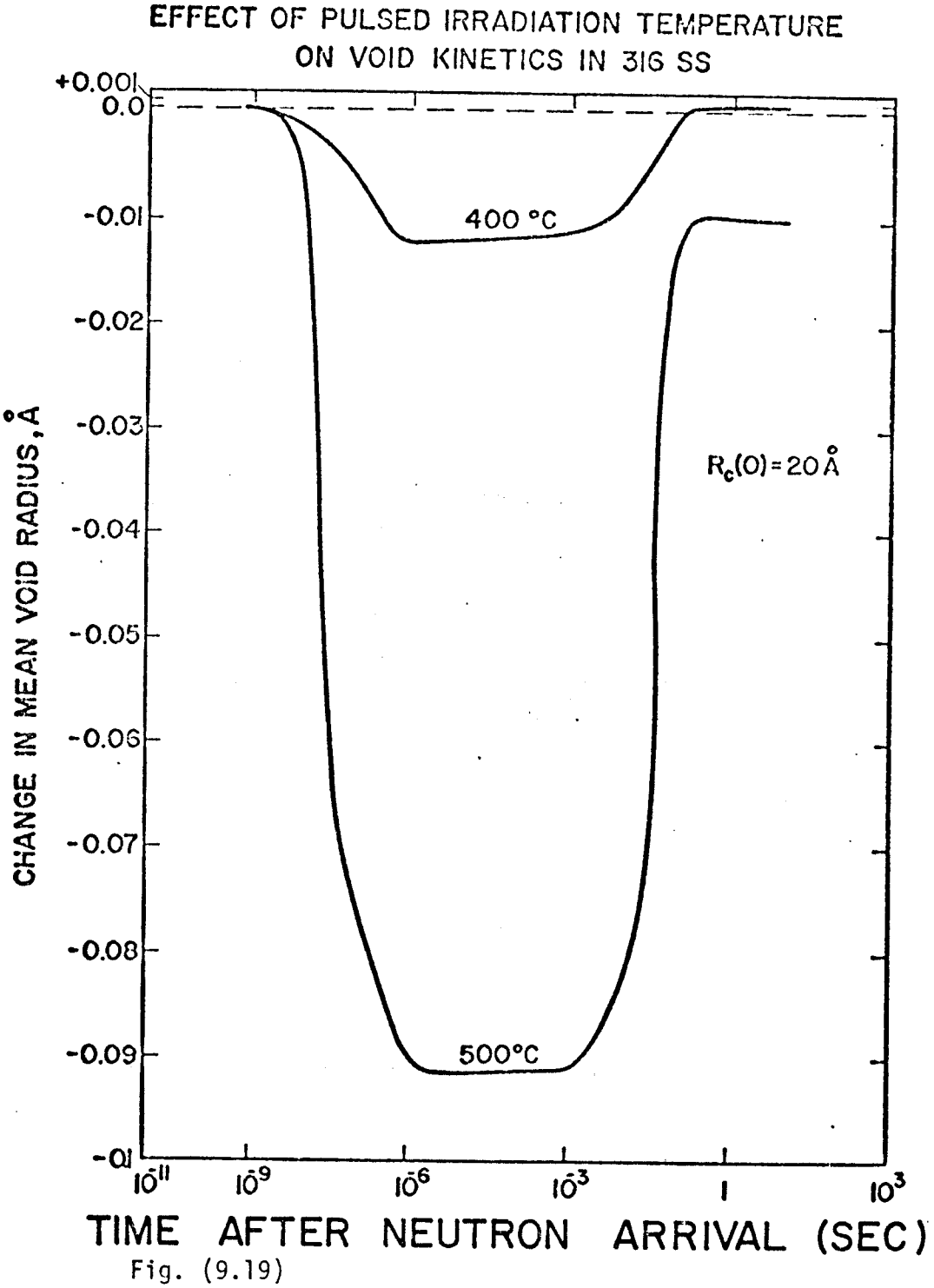
EFFECT OF PULSED IRRADIATION TEMPERATURE
ON VOID KINETICS IN 316 SS
+0.001
0.0
-0.01
-0.02
-0.03
-0.04
-0.05
-0.06
-0.07
-0.08
-0.09
-0.1
400 °C
500°C
$R_c(0) = 20$ Å
CHANGE IN MEAN VOID RADIUS, Å
10^{-11}
10^{-9}
10^{-6}
10^{-3}
1
10^{3}
TIME AFTER NEUTRON ARRIVAL (SEC)

Fig. (9.19)

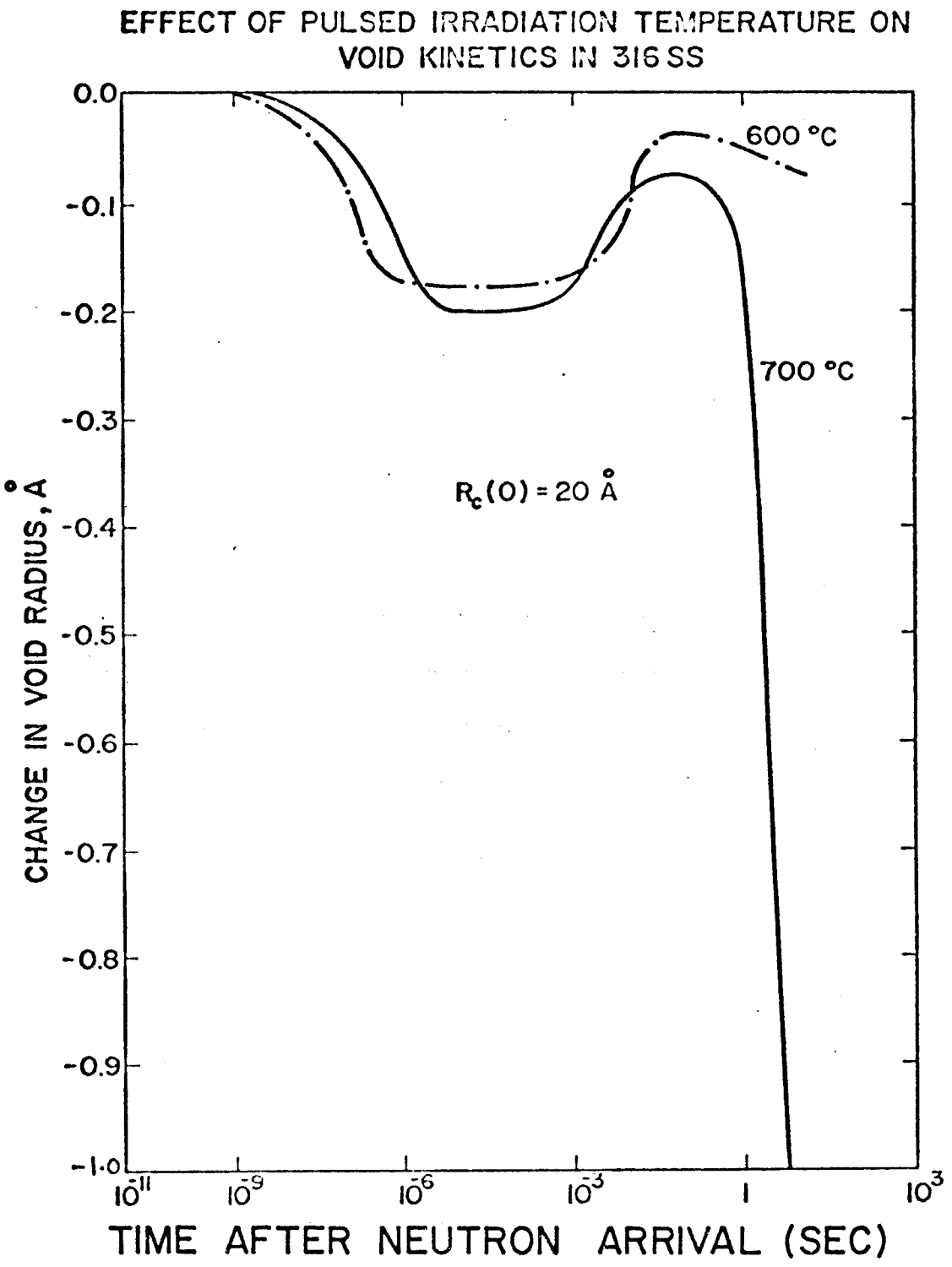
EFFECT OF PULSED IRRADIATION TEMPERATURE ON
VOID KINETICS IN 316 SS
0.0
-0.1
-0.2
-0.3
-0.4
-0.5
-0.6
-0.7
-0.8
-0.9
-1.0
600 °C
700 °C
$R_c(0) = 20$ Å
CHANGE IN VOID RADIUS, Å
10^{-11}
10^{-9}
10^{-6}
10^{-3}
1
10^{3}
TIME AFTER NEUTRON ARRIVAL (SEC)

Fig. (9.20)

the lower sink density. The driving force for the annealing of the void is very sensitive to the temperature, as can be seen from Figure (9.20). Void annealing is very rapid at 700°C and the initial radius of 20 Å become 19 Å in about 6 seconds after the start of the burn (or end of pulse).

IX.D.3. A Train of Neutron Pulses

Certain results can not be completely revealed by the study of metals response under one pulse of irradiation; the ultimate behavior of voids under a train of pulses must be considered. The effect of a train of neutron pulses (10^{-7} dpa each) on the kinetics of a mean void of 20 Å radius at 400°C in 316 SS is shown in Figure (9.21). The corresponding point defect concentration as a function of time, are displayed in Figure (9.22), (notice the linear time scales). As can be seen from Figure (9.22), the interstitial concentration goes to its thermal equilibrium value, almost instantaneously after the pulse. This causes a rapid drop in the void radius, about -1.5×10^{-4} Å in this case. On the other hand, the vacancy concentration slowly declines trying to reach its thermal equilibrium value ($\sim 10^{-12}$ at/at at 400°C). The relatively short pulse period in this case keeps the vacancy concentration within certain bounds (between 6×10^{-9} at/at and 9×10^{-8} at/at). It can be seen that there is a slight increase in the overall concentration, due to accumulation from previous pulses. Although any given void shrinks in the first

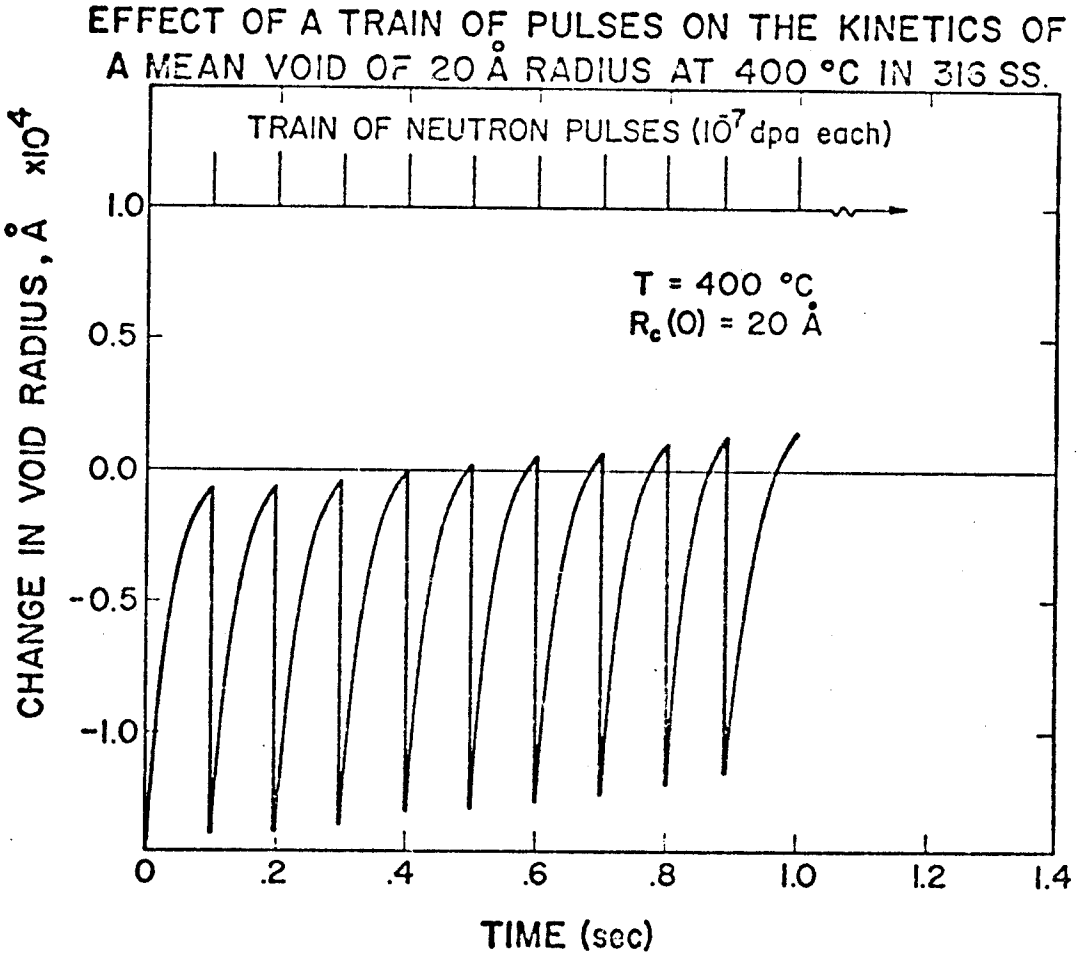
EFFECT OF A TRAIN OF PULSES ON THE KINETICS OF A MEAN VOID OF 20 Å RADIUS AT 400 °C IN 316 SS.
TRAIN OF NEUTRON PULSES (10^{-7} dpa each)
T = 400 °C
$R_c(0)$ = 20 Å
CHANGE IN VOID RADIUS, Å x10^4
1.0
0.5
0.0
-0.5
-1.0
0
.2
.4
.6
.8
1.0
1.2
1.4
TIME (sec)

Fig. (9.21)

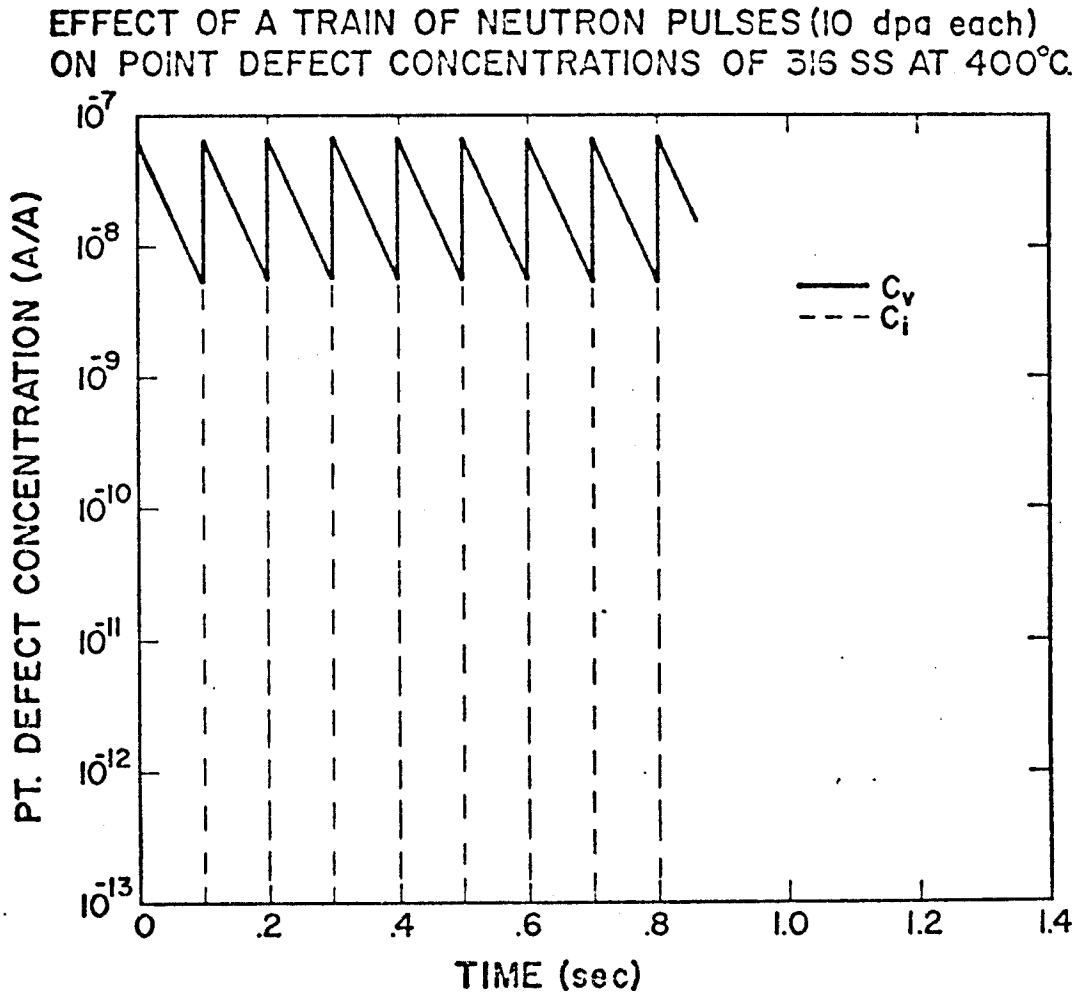
EFFECT OF A TRAIN OF NEUTRON PULSES (10 dpa each)
ON POINT DEFECT CONCENTRATIONS OF 316 SS AT 400°C
PT. DEFECT CONCENTRATION (A/A)
10^{-7}
10^{-8}
10^{-9}
10^{-10}
10^{-11}
10^{-12}
10^{-13}
0
.2
.4
.6
.8
1.0
1.2
1.4
TIME (sec)
C_v
C_i

Fig. (9.22)

few pulses as shown in Figure (9.21), it will eventually regain its initial radius and ultimately grow due to the increasing vacancy concentration. It is then concluded that to compare the results of void growth rates under different pulsing conditions, the calculations should be carried out over several cycles at least until the transient point defect behavior is replaced by more 'steady-state' values.

IX.D.4. The Combined Effect of Temperature and Pulse Repetition Rate

In designing ICTR's, one of the most desired design aspects, is low swelling structural materials. The combination of certain design parameters, namely irradiation temperature and pulse repetition rate, on the final swelling behavior of 316 stainless steel, is studied in detail in this section. First, we will study the behavior of a void under different equivalent pulsed damage conditions. This will be followed by void growth, at different temperatures, as a function of the pulse repetition rate.

The behavior of a 20 Å radius void at 400°C is shown in Figure (9.23), under different pulsed irradiation conditions. The effective plant power output is assumed to be invarient at 1000 MW_t. To achieve this constant power output, pulsing a 10,000 MJ pellet every 10 seconds is equivalent to a 1000 MJ pellet imploded every second or a 100 MJ pellet every 0.1 second. The total damage is also taken into account and of course varies proportional to the size of the pellet yield. In

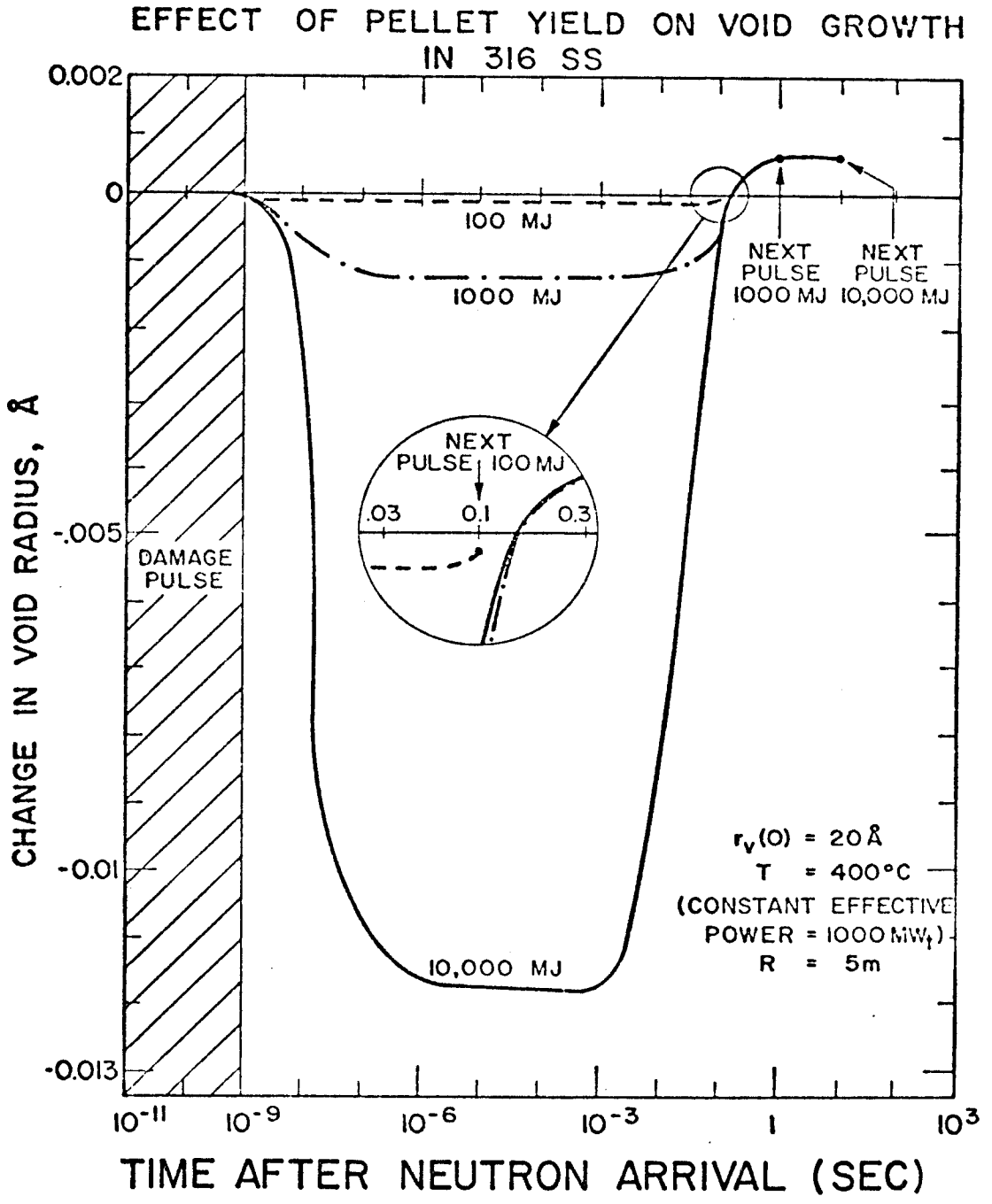
EFFECT OF PELLET YIELD ON VOID GROWTH IN 316 SS
0.002
0
-.005
-0.01
-0.013
CHANGE IN VOID RADIUS, Å
100 MJ
1000 MJ
10,000 MJ
NEXT PULSE 1000 MJ
NEXT PULSE 10,000 MJ
NEXT PULSE 100 MJ
.03
0.1
0.3
DAMAGE PULSE
$r_v(0)$ = 20 Å
T = 400°C
(CONSTANT EFFECTIVE POWER = 1000 MW_t)
R = 5m
10^{-11}
10^{-9}
10^{-6}
10^{-3}
1
10^3
TIME AFTER NEUTRON ARRIVAL (SEC)

Fig. (9.23)

the 10000 MJ case, the damage created by the pulse is very large causing the void radius to decrease by $\sim$-0.012 Å, while the radius decrease caused by the 1000 MJ pellet is only $\sim$-0.0012 Å, and that resulting from the 100 MJ pellet is $\sim$-0.00012 Å, as shown if Figure (9.23). However, the final swelling caused by the 10000 MJ pulse is positive at 400°C. Since the irradiation time at the end of the 10000 MJ pulse is $\sim$5000 τ_v, then the void will continue to grow over the next successive pulses, due to the fact that vacancies will not accumulate from previous pulses. Now, to find out the final equivalent effect of the 1000 MJ pellet system, one has to study at least 10 pulses, and for the 100 MJ pellet system — a 100 pulses.

In the following, a study of the change in a 50 Å radius void in 316 SS after an accumulated dose of 10^{-5} dpa will be described. The change in the radius at different irradiation temperatures and pulse rates, is shown in Figures (9.24) and (9.25). It is assumed that $Z_i = 1.08$, $\varepsilon = 0$, and $P_w = 10^{-6}$ sec and no gas generation. The results of the calculations, with the previously described assumptions, are shown in Table (9.4). Calculations for 1, 10, 100 and 1000 pulses were carried out, and also steady-state results for an equivalent system (10^{-6} dpa/sec dose rate) were performed for comparison. It can be observed from Table (9.4) and Figures (9.24) and (9.25) that at low temperatures (400°C-450°C) void growth in all pulsed systems behaves the same as the corresponding

TABLE (9.4)

Pulsed Irradiation Void Radius Changes (Å)
After 10 Seconds of Irradiation in 316 S.S.

# of Pulses Studied	1	10	100	1000	10^7 (steady-state)
Dose Rate in Pulse, dpa/s	10	1	0.1	0.01	10^{-6}
Period, s	10	1	0.1	0.01	10^{-6}
Pulse Rate, s^{-1}	0.1	1	10	100	10^6
	Å Growth After 10 Seconds				
T = 400°C	$+2.2\times10^{-5}$	$+2.2\times10^{-5}$	$+2.2\times10^{-5}$	$+2.2\times10^{-5}$**	$+2.2\times10^{-5}$
T = 450°C	$+1.8\times10^{-4}$	$+1.9\times10^{-4}$	$+1.9\times10^{-4}$	$+1.9\times10^{-4}$**	$+1.9\times10^{-4}$
T = 500°C	$+7.5\times10^{-4}$	$+1.04\times10^{-3}$	$+1.1\times10^{-3}$	$+1.1\times10^{-3}$	$+1.1\times10^{-3}$
T = 550°C	$+6.0\times10^{-4}$	$+2.7\times10^{-3}$	$+3.7\times10^{-3}$	$+3.8\times10^{-3}$**	$+3.8\times10^{-3}$
T = 600°C	-7.0×10^{-3}	-2.2×10^{-3}	$+3.5\times10^{-3}$	$+4.8\times10^{-3}$	$+4.8\times10^{-3}$
T = 650°C	- .053	- .046	- .032	- .029**	- .025
T = 700°C	- .27	- .26	- .23	- .23**	- .22

*$R_c(0)$ = 50 Å, $P_w = 10^{-6}$ sec, Z_i = 1.08, ε = 0, Av. dose rate = 10^{-6} dpa/s

** Values extrapolated from the results of 100 pulses.

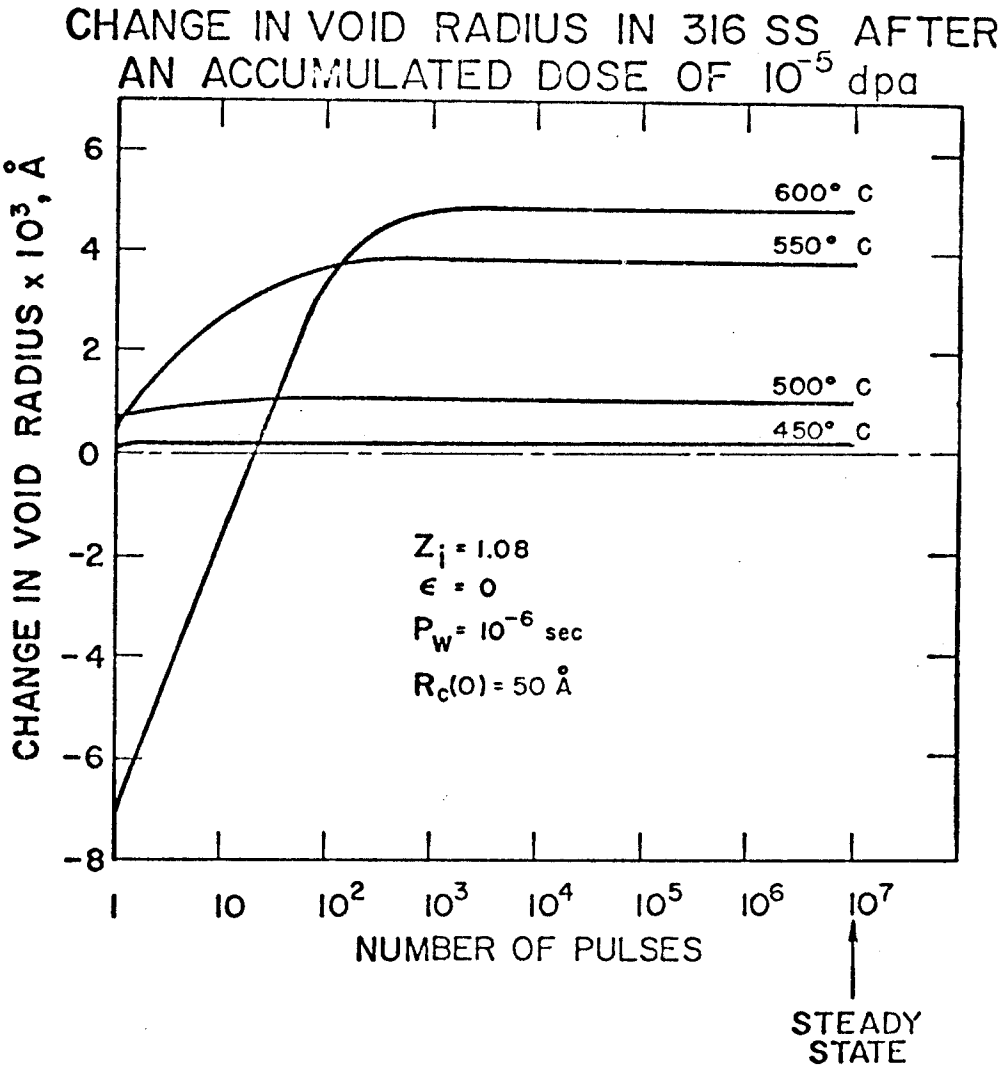
CHANGE IN VOID RADIUS IN 316 SS AFTER AN ACCUMULATED DOSE OF 10^{-5} dpa
CHANGE IN VOID RADIUS x 10^3, Å
6
4
2
0
-2
-4
-6
-8
600° C
550° C
500° C
450° C
Z_i = 1.08
ϵ = 0
P_w = 10^{-6} sec
$R_c(0)$ = 50 Å
1
10
10^2
10^3
10^4
10^5
10^6
10^7
NUMBER OF PULSES
STEADY STATE

Fig. (9.24)

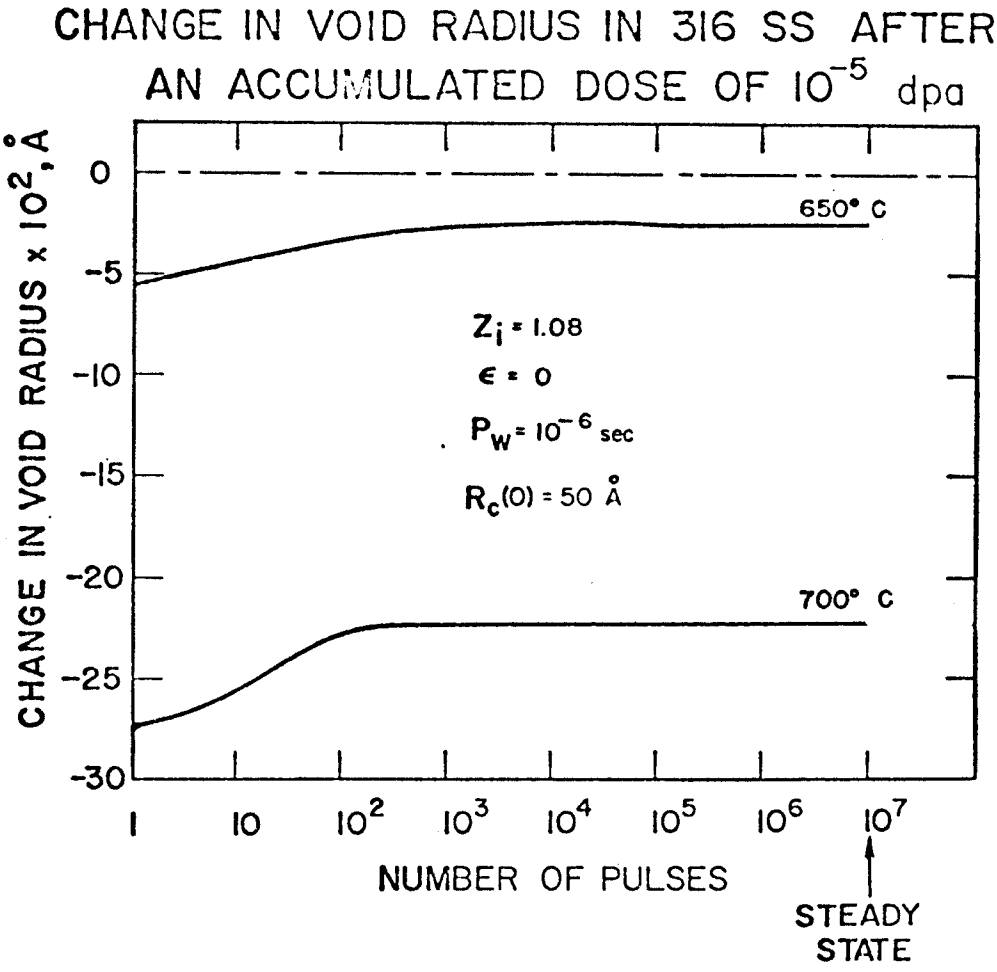
CHANGE IN VOID RADIUS IN 316 SS AFTER AN ACCUMULATED DOSE OF 10^{-5} dpa
CHANGE IN VOID RADIUS x 10^2, Å
0
-5
-10
-15
-20
-25
-30
650° C
700° C
Z_i = 1.08
ϵ = 0
$P_w = 10^{-6}$ sec
$R_c(0)$ = 50 Å
1
10
10^2
10^3
10^4
10^5
10^6
10^7
NUMBER OF PULSES
STEADY STATE

Fig. (9.25)

steady-state case. This behavior occurs because void growth is controlled by the total bias of the system with little effects of annealing on voids in between successive pulses. On the other hand, at higher temperatures the phenomenon of interpulse annealing is more prominant. For example, at 600°C, the 50 Å radius void has a net <u>decrease</u> in radius of -7×10^{-3} Å at the end of one pulse of 10 seconds period. However, the void experiences a net <u>increase</u> in radius of $+3.5 \times 10^{-3}$ after 100 pulses of 0.1 second period each. Steady-state-like void growth conditions are achieved if the repetition rate is 100 pulses per second or greater (for temperatures above about 500°C), as can be seen from Figures (9.24) and (9.25). These important conclusions are summarized in Figure (9.26), where the boundary between void growth and no growth is given as a function of pulsing variables. In steady-state irradiation, this temperature is about 625°C for stainless steel at a dose rate of 10^{-6} dpa/s. The other extreme case of a 10 second pulse period has a cutt off high temperature of only 575°C.

<u>IX.D.5. The Effect of the Initial Void Radius</u>

Void annealing and growth kinetics are strong functions of the initial void radius. With the irradiation conditions of the previous section, the same series of calculations were performed for two different void radii; a small initial void radius of 10 Å, and a large initial void radius of 100 Å. Figures (9.27) and (9.28) demonstrate the void growth behavior

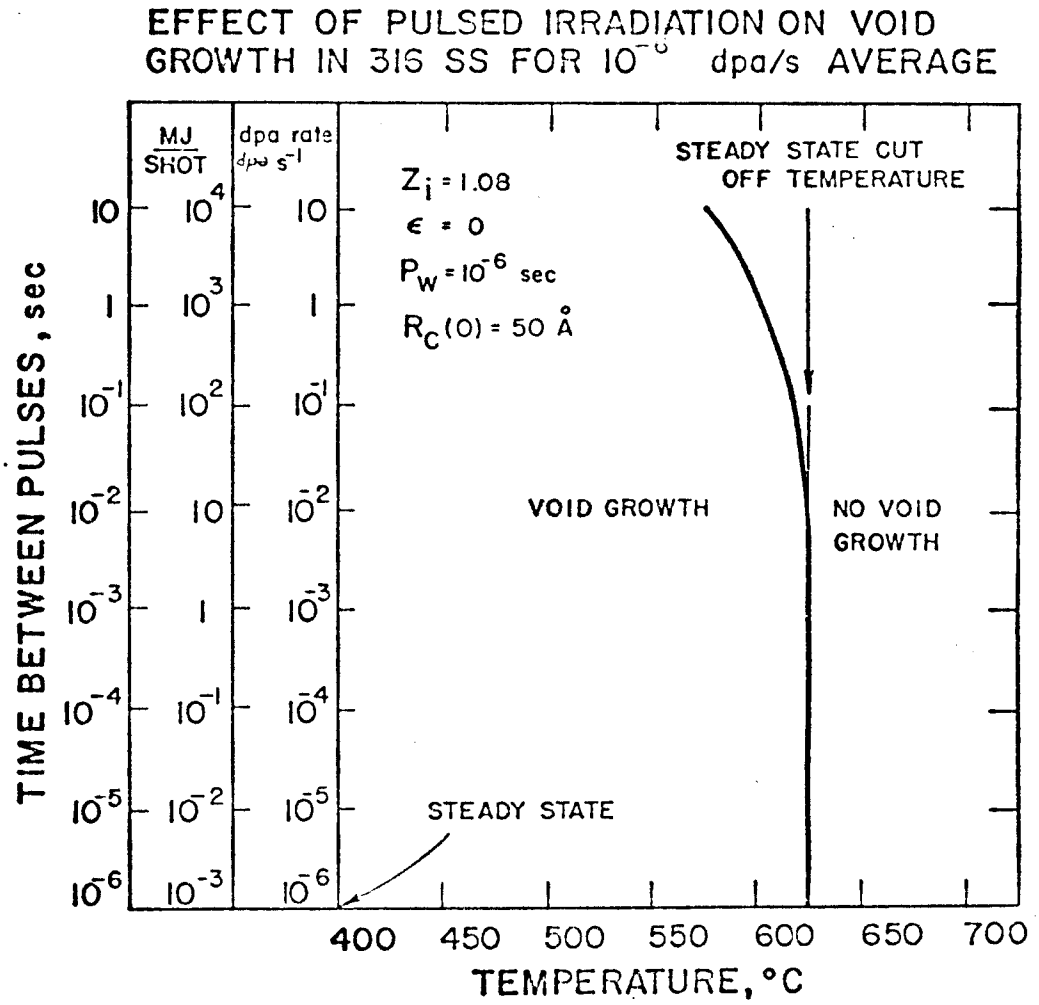
EFFECT OF PULSED IRRADIATION ON VOID GROWTH IN 316 SS FOR 10^{-6} dpa/s AVERAGE
MJ/SHOT
dpa rate dpa s^{-1}
Z_i = 1.08
ϵ = 0
$P_w = 10^{-6}$ sec
$R_c(0)$ = 50 Å
STEADY STATE CUT OFF TEMPERATURE
VOID GROWTH
NO VOID GROWTH
STEADY STATE
TIME BETWEEN PULSES, sec
TEMPERATURE, °C
400 450 500 550 600 650 700

Fig. (9.26)

for the 10 Å radius, as a function of pulse rate, while Table (9.5) shows the changes in the void radius after 10 seconds of irradiation in different equivalent pulsed systems. For this small void radius, it is observed that annealing effects are very pronounced. For a 10 second time between pulses at 550°C, the void radius decreases by -0.082 Å, while for 0.1 second between pulses at the same temperature the radius increases by +0.022 Å. However, at high temperatures (>650°C), void annealing becomes very dominant for all pulse rates and the 10 Å radius void quickly shrinks down to a radius of 5 Å, which is the radius for the equilibrium bubble.

Increasing the void radius affects both the annealing and growth phases of the void kinetic behavior. The 100 Å radius void does not experience shrinkage (negative change in raidus) at 550°C (See Table (9.6) and Figures (9.31) and (9.30)), as the 10 Å radius void showed at the same temperature, (Figure (9.27)). The relative effect of the initial void radius on the growth cut off high temperature is shown in Figure (9.31). The figure also reflects the result that at high temperatures the initial void radius has to be large, if void growth is expected at such temperatures. This is just equivalent to the "free growth void radius" definition previously given in Chapter VII.

IX.D.6. The Effect of the Bias Factor (Z_i)

From the previous studies on the growth behavior of voids, it can be seen that the void growth cut off high temperature is determined by a balance between the void growth aspect.

TABLE (9.5)

Pulsed Irradiation Void Radius Changes (Å), After 10 Seconds of Irradiation in 316 S.S.*

# of Pulses Studied	1	10	100	10^{-7} (steady-state)
Dose Rate in Pulse, dpa/s	10	1	0.1	10^{-6}
Period, s	10	1	0.1	10^{-6}
Pulse Rate, s^{-1}	0.1	1	10	10^{6}
	Å Growth After 10 Seconds			
T = 400°C	$+4.1 \times 10^{-4}$	$+4.2 \times 10^{-4}$	$+4.2 \times 10^{-4}$	$+4.2 \times 10^{-4}$
T = 450°C	+ .0050	+ .0082	+ .0085	+ .0086
T = 500°C	+ .0016	+ .022	+ .036	+ .035
T = 550°C	- .082	- .040	+ .022	+ .029
T = 600°C	- .740	- .680	- .540	- .50
T = 650°C	-5.00**	-5.00**	-5.00**	-5.00**
T = 700°C	-5.00**	-5.00**	-5.00**	-5.00**

*$R_c(0)$ = 10 Å, $P_w = 10^{-6}$ sec, Z_i = 1.08, ϵ = 0, Av. dose rate = 10^{-6} dpa/s

** This value corresponds to the bubble equilibrium radius, assumed to be 5 Å.

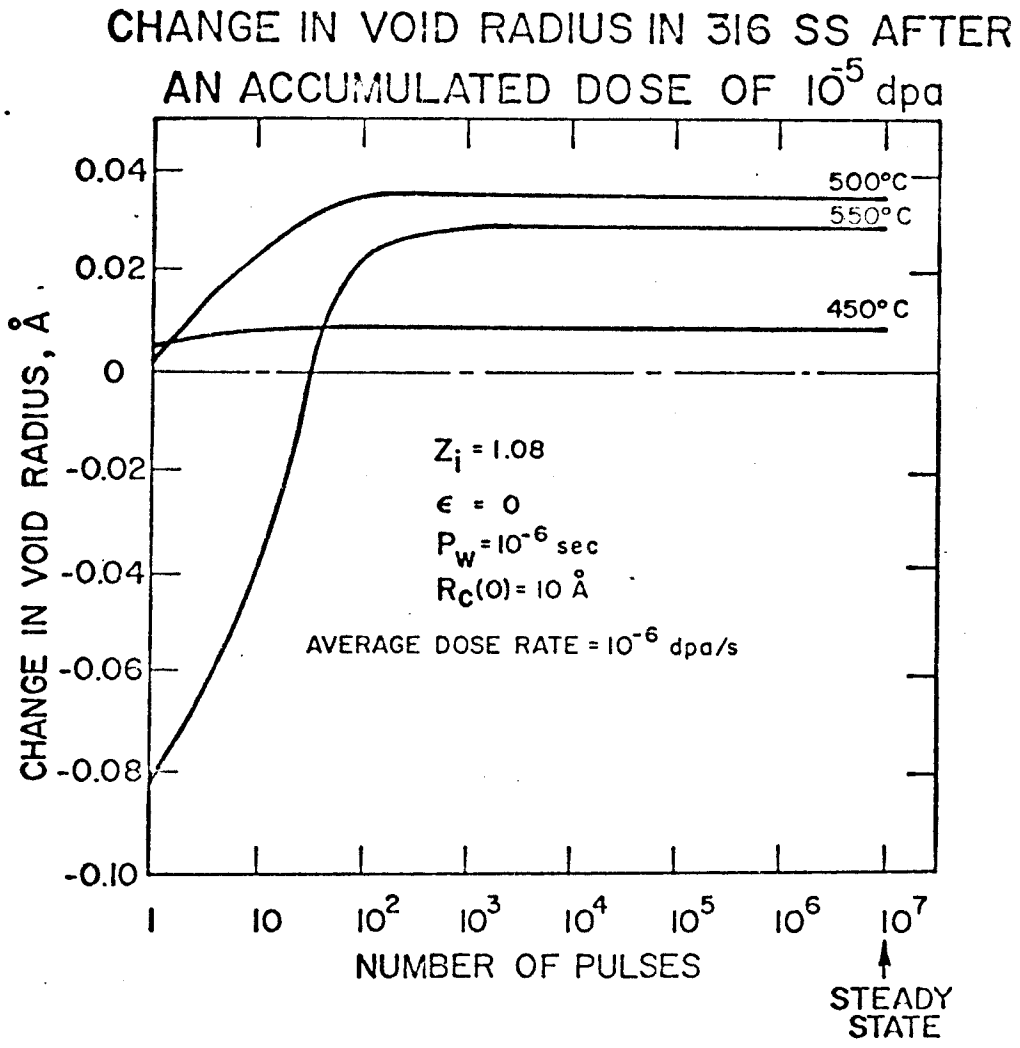
CHANGE IN VOID RADIUS IN 316 SS AFTER AN ACCUMULATED DOSE OF 10^{-5} dpa
CHANGE IN VOID RADIUS, Å
0.04
0.02
0
-0.02
-0.04
-0.06
-0.08
-0.10
500°C
550°C
450°C
$Z_i = 1.08$
$\epsilon = 0$
$P_w = 10^{-6}$ sec
$R_c(0) = 10$ Å
AVERAGE DOSE RATE = 10^{-6} dpa/s
1
10
10^2
10^3
10^4
10^5
10^6
10^7
NUMBER OF PULSES
STEADY STATE

Fig. (9.27)

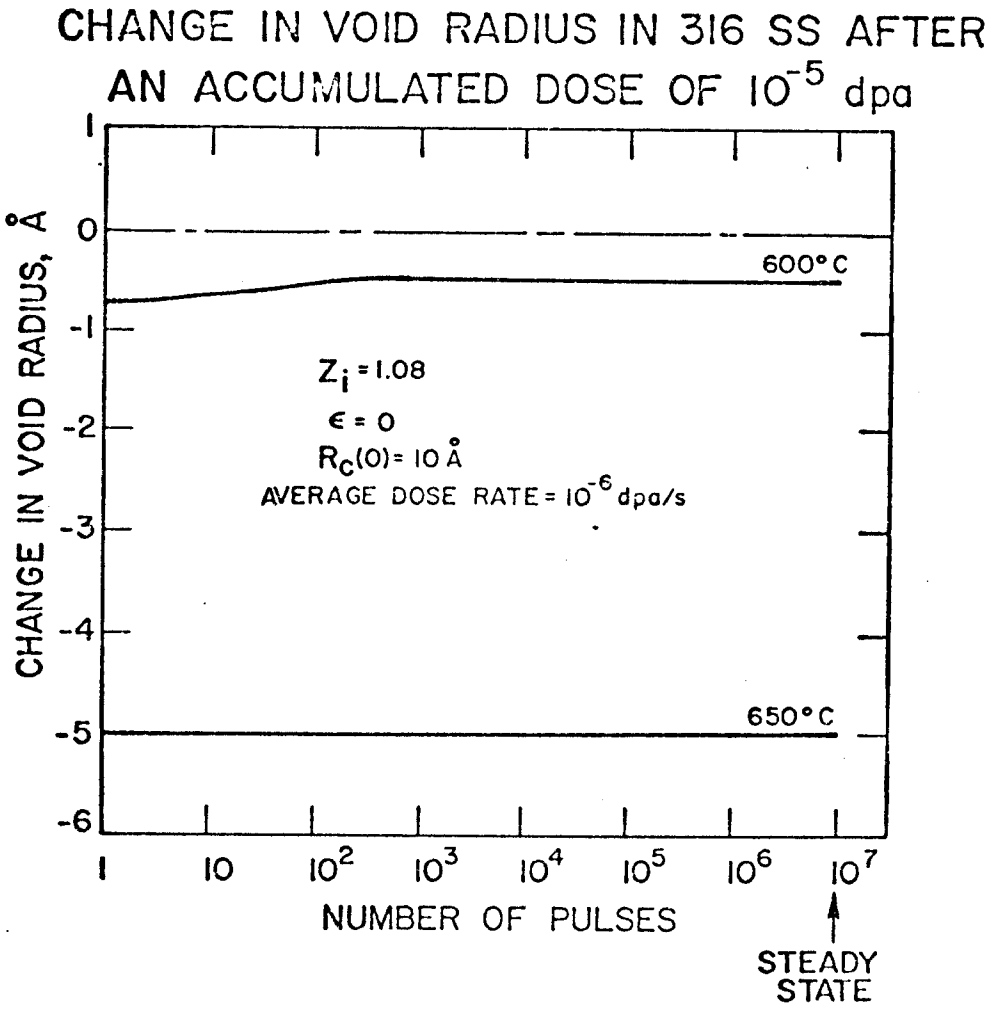
CHANGE IN VOID RADIUS IN 316 SS AFTER AN ACCUMULATED DOSE OF 10^{-5} dpa
CHANGE IN VOID RADIUS, Å
1
0
-1
-2
-3
-4
-5
-6
600° C
650° C
Z_i = 1.08
ϵ = 0
$R_c(0)$ = 10 Å
AVERAGE DOSE RATE = 10^{-6} dpa/s
1
10
10^2
10^3
10^4
10^5
10^6
10^7
NUMBER OF PULSES
STEADY STATE

Fig. (9.28)

TABLE (9.6)

Pulsed Irradiation Void Radius Changes (Å), After 10 Seconds of Irradiation in 316 S.S.*

# of Pulses Studied	1	10	100	10^7 (steady-state)
Dose Rate in Pulse, dpa/s	10	1	0.1	10^{-6}
Period, s	10	1	0.1	10^{-6}
Pulse Rate, s^{-1}	0.1	1	10	10^6
	Å Growth After 10 Seconds			
T = 400°C	$+3.9\times10^{-6}$	$+3.9\times10^{-6}$	$+3.9\times10^{-6}$	$+3.9\times10^{-6}$
T = 450°C	$+3.4\times10^{-5}$	$+3.5\times10^{-5}$	$+3.5\times10^{-5}$	$+3.5\times10^{-5}$
T = 500°C	$+1.7\times10^{-4}$	$+2.0\times10^{-4}$	$+2.0\times10^{-4}$	$+2.0\times10^{-4}$
T = 550°C	$\pm2.9\times10^{-4}$	$\pm6.4\times10^{-4}$	$+7.3\times10^{-4}$	$+7.3\times10^{-4}$
T = 600°C	-1.5×10^{-3}	-1.8×10^{-4}	$+6.8\times10^{-3}$	$+8.2\times10^{-4}$
T = 650°C	-1.4×10^{-2}	-1.1×10^{-2}	-8.1×10^{-3}	-7.0×10^{-3}
T = 700°C	-6.8×10^{-2}	-6.5×10^{-2}	-5.9×10^{-2}	-5.6×10^{-2}

*$R_c(0) = 100$°A, $P_w = 10^{-6}$ sec, $Z_i = 1.08$, $\varepsilon = 0$, Av. dose rate = 10^{-6} dpa/s

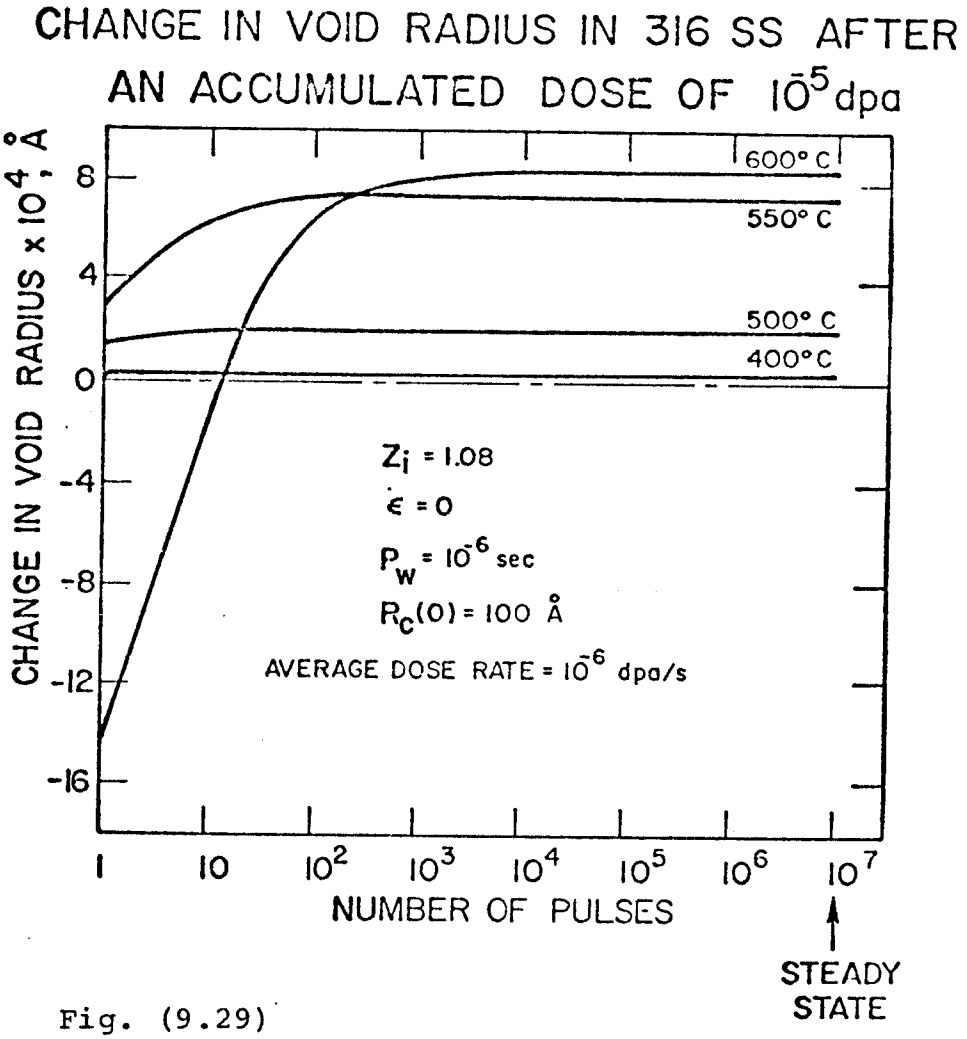
CHANGE IN VOID RADIUS IN 316 SS AFTER AN ACCUMULATED DOSE OF 10^5 dpa
CHANGE IN VOID RADIUS x 10^4; Å
8
4
0
-4
-8
-12
-16
600° C
550° C
500° C
400° C
Z_i = 1.08
$\dot{\epsilon}$ = 0
$P_w = 10^{-6}$ sec
$R_c(0)$ = 100 Å
AVERAGE DOSE RATE = 10^{-6} dpa/s
1
10
10^2
10^3
10^4
10^5
10^6
10^7
NUMBER OF PULSES
STEADY STATE

Fig. (9.29)

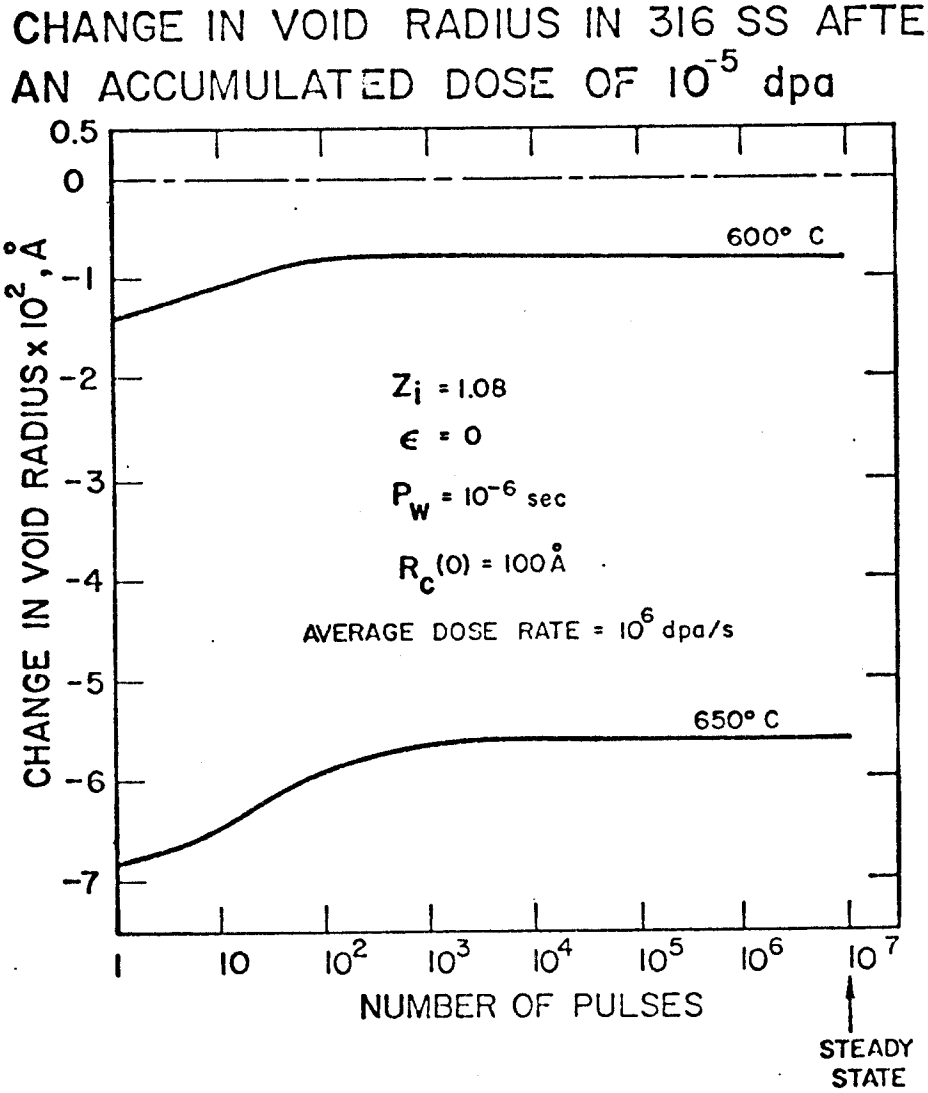
CHANGE IN VOID RADIUS IN 316 SS AFTER AN ACCUMULATED DOSE OF 10^{-5} dpa
0.5
0
-1
-2
-3
-4
-5
-6
-7
CHANGE IN VOID RADIUS x 10^2, Å
600° C
Z_i = 1.08
ϵ = 0
$P_w = 10^{-6}$ sec
$R_c(0) = 100$ Å
AVERAGE DOSE RATE = 10^6 dpa/s
650° C
1
10
10^2
10^3
10^4
10^5
10^6
10^7
NUMBER OF PULSES
STEADY STATE

Fig. (9.30)

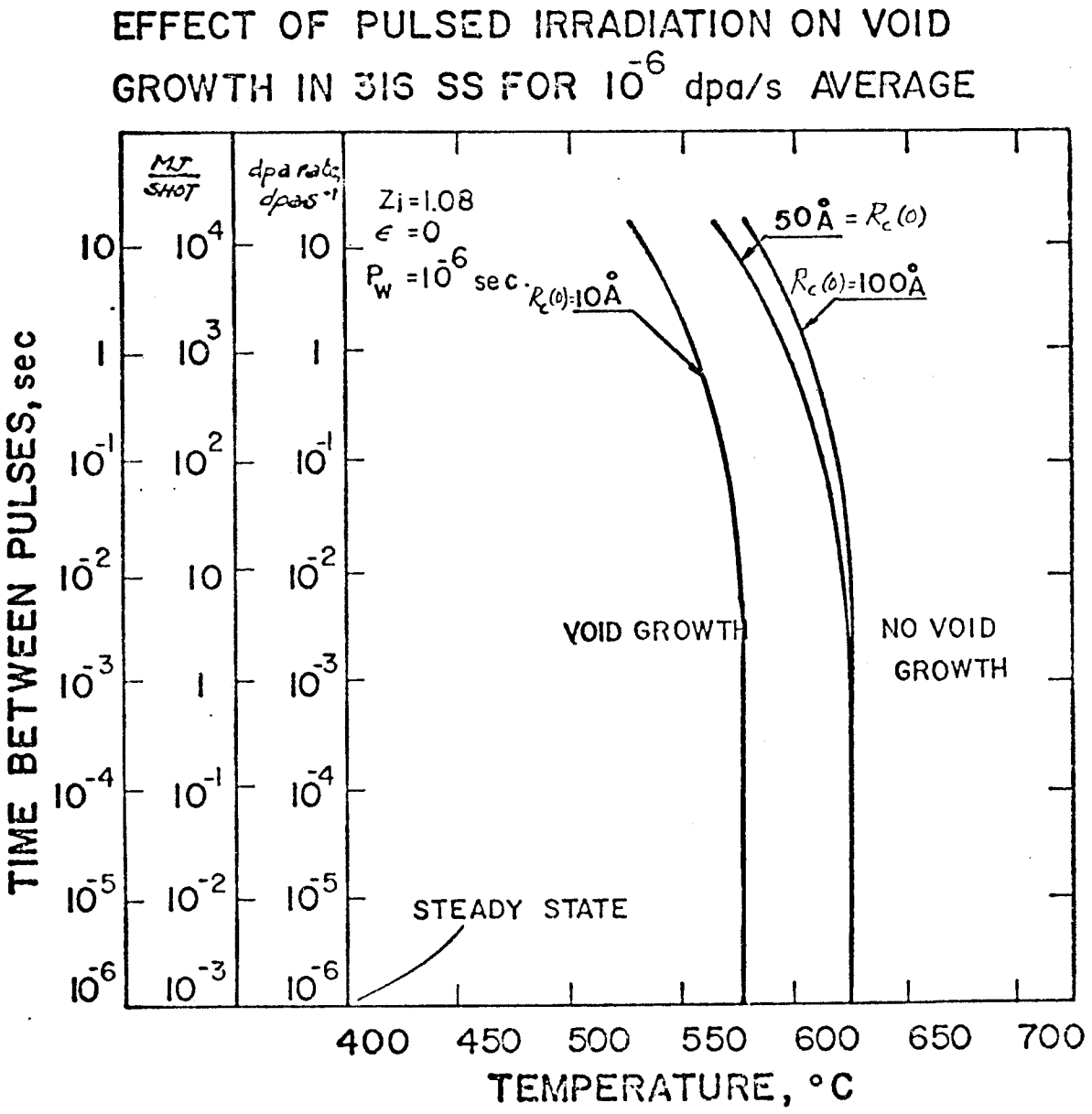

Fig. (9.31). Initial void radius effects on the void growth-no growth temperature.

caused by the net bias of the system, and its tendency to shrink, due to the annealing effects. In the following, we study the effect of changing the dislocation-interstitial bias factor on the growth kinetics.

The same example of the 50 Å radius void is studied here, with all the previous conditions, except for using a different bias factor $Z_i = 1.025$. The results of the calculations for pulsed irradiation void radius changes in different pulsed systems are shown in Table (9.7) and Figure (9.32). A comparison between the growth behavior of a 50 Å radius void with $Z_i = 1.08$ and that of the same void with $Z_i = 1.025$ reveals that in the $Z_i = 1.025$ case, the change in the radius as a function of the pulse rate alters sign from negative to positive at 550°C, while the similar behavior in the $Z_i = 1.08$ case changes sign at 600°C. This indicates that the smaller the bias factor, the lower the void growth cut off high temperature, because of the greater influence of interpulse void annealing. The steady-state cut off temperature is ∿575°C.

IX.E. Concluding Remarks

In this chapter the growth of voids has been studied under a wide variety of pulsed irradiation conditions. It has been shown that pulsed irradiation produces a different void growth behavior, which cannot be described by an inherently steady-state theory. The following points have been made;

TABLE (9.7)

Pulsed Irradiation Void Radius Changes (Å), After 10 Seconds of Irradiation in 316 S.S.*

# of Pulses Studied	1	10	100	10^7 (steady-state)
Dose Rate in Pulse, dpa/s	10	1	0.1	10^{-6}
Period, s	10	1	0.1	10^{-6}
Pulse Rate, s^{-1}	0.1	1	10	10^6
	Å Growth After 10 Seconds			
T = 400°C	$+6.96\times10^{-6}$	$+7.02\times10^{-6}$	$+7.03\times10^{-6}$	$+6.97\times10^{-6}$
T = 450°C	$+5.37\times10^{-5}$	$+5.75\times10^{-5}$	$+5.80\times10^{-5}$	$+5.7\times10^{-5}$
T = 500°C	$+1.59\times10^{-4}$	$+2.58\times10^{-4}$	$+2.79\times10^{-4}$	$+2.71\times10^{-4}$
T = 550°C	-6.94×10^{-4}	-2.02×10^{-4}	$+3.19\times10^{-4}$	$+3.1\times10^{-4}$
T = 600°C	-8.9×10^{-3}	-7.37×10^{-3}	-5.52×10^{-3}	-5.27×10^{-3}
T = 650°C	-5.44×10^{-2}	-5.21×10^{-2}	-4.77×10^{-2}	-4.6×10^{-2}
T = 700°C	- .267	- .264	- .257	- .253

*$R_c(0)$ = 50 Å, $P_w = 10^{-6}$ sec, Z_i = 1.025, ε = 0, Av. dose rate = 10^{-6} dpa/s

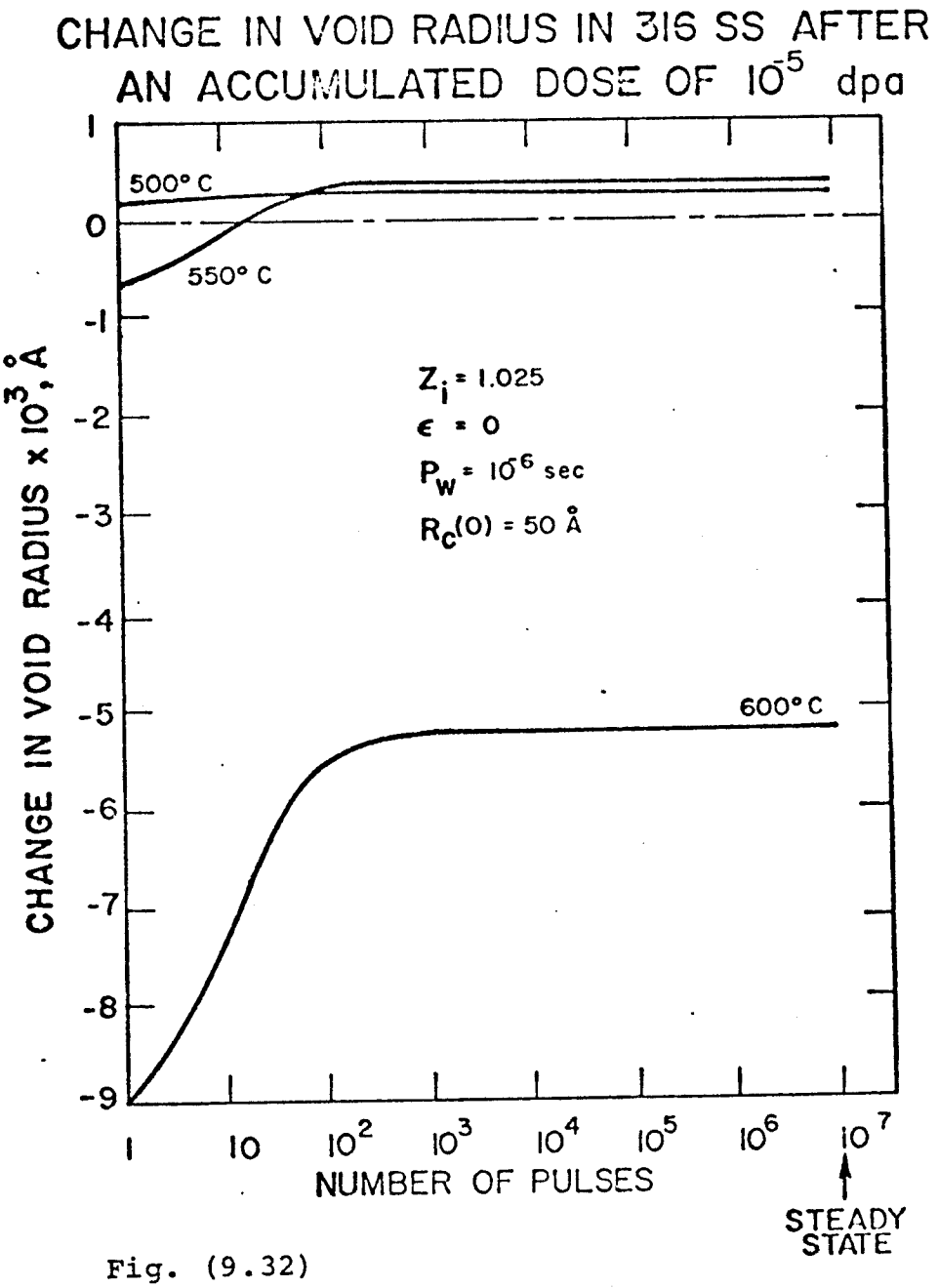
CHANGE IN VOID RADIUS IN 316 SS AFTER AN ACCUMULATED DOSE OF 10^{-5} dpa
500° C
550° C
600° C
Z_i = 1.025
ϵ = 0
$P_w = 10^6$ sec
$R_c(0)$ = 50 Å
CHANGE IN VOID RADIUS x 10^3, Å
1
0
-1
-2
-3
-4
-5
-6
-7
-8
-9
1
10
10^2
10^3
10^4
10^5
10^6
10^7
NUMBER OF PULSES
STEADY STATE

Fig. (9.32)

1. Steady-state response of metals is not achieved for pulsed systems. Even for systems with long burn cycles, (i.e., Tokamaks) point defect concentrations, at the start and end of the cycle, are different from their steady-state values.

2. A qualitative agreement with the rastered Ni ion beam experiment of NRL has been achieved. The study indicated that under rastered ion beam conditions (50 pulses of 2.5×10^{-5} sec width and 0.32 dpa/sec, then a period of no irradiation for 2.5×10^{-3} sec) voids grow much less than the corresponding steady-state irradiation.

3. Annealing of voids in metals is not only a function of the annealing temperature, but also a function of the microstructure present. It has been shown that for a small ratio of interstitial loops to voids ($\sim 10^{-6}$), voids show very little annealing in aluminum at 126°C, provided that there is no other vacancy sources or sinks.

4. For ICTR pulsing conditions and pulse widths ranging from a nanosecond to a microsecond, the time structure of the dose rate inside the pulse is not significant in the determination of the final swelling of first-wall materials. The integrated dose within the irradiation pulse is the important damage parameter.

5. The void growth behavior for the first few pulses in ICTR's is not necessarily an indication of the final metal swelling behavior. The void growth behavior has to be studied

over a time span of about 1000 τ_v-5000 τ_v, to determine the ultimate void growth characteristics.

6. Under pulsed irradiation, void growth behavior is a strong function of both the pulse repetition rate and the irradiation temperature. Voids in stainless steel were shown to exhibit slower growth characteristics at high temperatures and when there are long times between successive pulses. The dividing temperature between growth and no growth of voids can be reduced by as much as 50°C from the corresponding steady-state value, if the time between the pulses is as long as 10 seconds.

7. Pulsed irradiation has been shown to be equivalent to steady-state irradiation, for an average dose rate of 10^{-6} dpa/sec in stainless steel, if the pulse repetition rate is greater than 500 pulses per second.

8. It has been found that smaller void radii and lower interstitial dislocation bias factors tend to accelerate interpulse annealing. This causes a lower net growth and further reduces the temperature between growth and no growth.

9. For a fixed operating temperature, geometry and ICTR plant power output, the amount of swelling in the first-wall can be reduced by using higher yield pellets. This results from higher mutual point defect recombination rates and also because the annealing time between microexplosions of large yield pellets is longer.

10. For a fixed geometry, ICTR power plant output and

pellet yield, the amount of swelling in the first-wall can be reduced by operating at the highest temperatures allowed by other design factors (e.g., embrittlement).

CHAPTER X

CONCLUSIONS OF THE STUDY AND GENERAL RECOMMENDATIONS

This study has been devoted to the development and application of a Fully Dynamic Rate Theory that is equally useful in the analysis of both steady-state and pulsed irradiation. It has been shown that the development of such a theory is essential in the study of situations where the damage rate is time dependent. The study has been concerned with four distinct areas: (a) The development and numerical solution of the Fully Dynamic Rate Theory (FDRT), (b) Calibration of FDRT against experimental results, (c) Application of the theory to steady-state irradiation, (d) Application of the theory to pulsed irradiation. The following points will serve as a summary of the results and conclusions of this study. This will be followed by general recommendations for future research.

X.A. Summary and Conclusions

X.A.1. The Development and Numerical Solution of the Fully Dynamic Rate Theory (FDRT)

In this area, we draw the following main conclusions:

1. State variable approach to the formulation of a Fully Dynamic Rate Theory has been used to describe the behavior of point defects, interstitial loops, vacancy loops and voids under different irradiation conditions. As a result of this dynamic formulation of the Rate Theory, swelling and creep of

metals under steady-state and pulsed irradiation can be analyzed and studied.

2. There is a wide variation in the magnitudes of the eigenvalues (and hence the time constants) in the resulting set of non-linear first order ordinary differential equations. This aspect necessitates the use of special numerical techniques for the solution of the resulting set of stiff ordinary differential equations. The time increment is restricted to small values, by the requirement of accuracy, only where the solution is relatively active. The accuracy is achieved at a minimum cost by allowing both the time increment and the order of the method to vary with time.

3. Based on the theory formulation, and the mentioned numerical methods, a computer code, TRANSWELL, has been developed to solve for the behavior of point defects and microstructure under a wide range of material and irradiation conditions.

4. A computer code, PL3D, has been constructed to efficiently handle and process the data generated by TRANSWELL, and display it in the form of 3-dimensional plots as well as contour plots.

X.A.2. Calibration of FDRT

A calibration of the rate theory has been conducted, with the following conclusions:

1. The results of the present comparisons between the theory and experimental data have shown that the FDRT can predict the high temperature void swelling behavior of both pure metals and alloys. The temperature dependence of swelling over a wide range of displacement rates (10^{-6} to 10^{-1} dpa/sec) and with different bombarding species (neutrons, heavy ions and electrons) has been shown to be simulated by the Fully Dynamic Rate Theory.

2. The use of different spike collapse efficiencies (1.2-4.4% for steel, 0.1% for Al and 1% for Ni) to achieve agreement between theory and experiment reveals that the displacement cascade in Al is rather diffuse and inefficient at retaining vacancies.

3. Different values of the interstitial-dislocation bias factors (1.025-1.08 for 316 SS, 1.015 for Al and 1.022 for Ni) have been used for the calibration of experiments on these materials.

4. The annealing behavior of voids in aluminum has been successfully predicted by the FDRT, which indicates that the bulk limited diffusion model for void annealing and growth is a good approximation.

X.A.3. Application of the Theory to Steady-State Irradiations

Void growth in metals is known to be a strong function of both the intrinsic properties of the material and the irradiation environment. A study of the effects of the

collision cascade efficiency and the dose rate on the swelling phenomenon, under steady-state irradiations, has lead to the following conclusions:

1. The vacancy concentration exhibits a peak value at intermediate temperatures due to the competition between a drop in sink density and a vacancy mobility increase with temperature. This behavior could have an appreciable effect on void nucleation rates calculated at intermediate temperatures since they are sensitive to vacancy supersaturation ratios.

2. The fraction of vacancies retained in vacancy loops has a great influence on void growth kinetics. However, this fraction is very sensitive to temperature and decreases sharply as the temperature increases,becoming of negligible importance in 316 SS about about 550°C.

3. Recombination of point defects can take place either on microstructural defects or by free collisions of vacancies and interstitials in the bulk. The latter mechanism is referred to as bulk recombination. For temperature independent and dose dependent microstructures, with no vacancy loops, bulk recombination is dominant at low temperatures (0.3-0.4 T_m) and sink removal is the major annealing mechanism at high temperatures ($\sim$0.4-0.5 T_m). On the other hand, if the microstructure is both temperature and dose dependent and contains vacancy loops, annealing at sinks dominates over the entire void production range.

4. Vacancy thermal emission from existing microstructure can be neglected compared to point defect production rates for high dose rates (10^{-3} dpa/sec), but it is very important for low dose rates (10^{-6} dpa/s).

5. For ion or neutron irradiation, at temperatures below the swelling peak the vacancy loop line density is around 2 orders of magnitude higher than interstitial loop line density. Therefore, it is a dominant sink of point defects that should be taken into consideration.

6. The Fully Dynamic model for void growth comes close to experimental observations of the peak swelling temperature shift. However, a temperature and dose independent microstructure model does not predict the correct temperature shift.

7. There is a delicate balance in a metal's matrix between the vacancy flux (D_vC_v) and the interstitial flux (D_iC_i). For void growth under irradiation, D_vC_v is greater than D_iC_i. The formation of vacancy loops influences this balance by reducing the free vacancy flux and for high collapse efficiencies the vacancy flux can be less than the interstitial flux. Under these circumstances if more interstitials than vacancies go to voids, growth is inhibited and voids shrink instead of grow. For a value of $Z_i = 1.08$, collision cascade efficiencies greater than 5% to 7.5% will inhibit void growth over a wide range of dose rates.

X.A.4. Application of the Theory to Pulsed Irradiation

It has been shown that pulsed irradiation produces a different void growth behavior, which cannot be described by an inherently steady-state theory. The following points summarize the conclusions in this area:

1. Steady-state response of metals is not achieved for pulsed systems. Even for systems with long burn cycles (i.e., Tokamaks) point defect concentrations, at the start and end of the cycle, are different from their steady-state values.

2. A qualitative agreement with the rastered Ni ion beam experiment of NRL has been achieved. Voids showed size decrease in the rastered beam case, at high temperatures, while they increased in size in the corresponding steady-state case.

3. Annealing of voids in metals is not only a function of the annealing temperature, but also a function of the microstructure present. It has been shown that for a small ratio of intersitial loops to voids ($\sim 10^{-6}$), voids show very little annealing in aluminum at 126°C.

4. For ICTR pulsing conditions and pulse widths ranging from a nanosecond to a microsecond, the time structure of the dose rate inside the pulse is not significant in the determination of the final swelling of first-wall materials. The integrated dose within the irradiation pulse is the important damage parameter.

5. The void growth behavior for the first few pulses in ICTR's is not necessarily an indication of the final metal swelling behavior. The void growth behavior has to be studied over a time span of about 1000 τ_v-5000 τ_v, to determine the ultimate void growth characteristics.

6. Under pulsed irradiation, void growth behavior is a strong function of both the pulse repetition rate and the irradiation temperature. Voids in stainless steel were shown to exhibit slower growth characteristics at high temperatures and when there are long times between successive pulses. The dividing temperature between growth and no growth of voids can be reduced by as much as 50°C from the corresponding steady-state value, if the time between the pulses is as long as 10 seconds.

7. Pulsed irradiation has been shown to be equivalent to steady-state irradiation, for an average dose rate of 10^{-6} dpa/sec in stainless steel, if the pulse repetition rate is greater than 500 pulses per second.

8. It has been found that smaller void radii and lower interstitial-dislocation bias factors tend to accelerate interpulse annealing. This causes a lower void growth and further reduces the temperature between growth and no growth.

9. For a fixed operating temperature, geometry and ICTR plant power output, the amount of swelling in the first-wall can be reduced by using higher yield pellets. This behavior results from higher mutual point defect

recombination rates and also because the annealing time between microexplosions of large yield pellets is longer.

10. For a fixed geometry, ICTR power plant output and pellet yield, the amount of swelling in the first-wall can be reduced by operating at the highest temperatures allowed by other design factors (e.g., embrittlement).

X.B. Recommendations for Future Research

Throughout this study, certain areas of research have proved to be of key importance in understanding the metal swelling phenomenon under irradition. In the following, we list the areas where future research can be important to reveal the relationships between point defects and microstructural behavior and that of the final metal's response under irradiation.

1. In ion or neutron irradiated materials, the efficiency of collision cascades to collapse into vacancy loops is an important aspect of research. The cascade collapse mechanism seriously affects the point defect balance in metals and hence the swelling and creep of metals under irradiation. Experimental and theoretical information on the percentage of vacancies that are produced directly into vacancy loops as a function of irradiation and material's variables is needed. This information may cast light on the behavior of metals that do not swell under irradiation and also can guide the design of swelling resistant alloys.

2. It is obviously necessary to plan a consistent and

interactive irradiation damage experimental program, to augment existing experimental data and to help develop the theory. It is suggested that all experimental information on microstructural data must be reported and categorized as functions of irradiation and materials variables.

3. Single or small aggregates of impurities could greatly influence point defect kinetics. It is suggested that more research efforts be directed towards impurity effects on irradiation induced phenomena. Experiments and theoretical analysis in this area will help to ultimately understand the behavior of alloys under different irradiation environments.

4. A simple linear interpolation has been used to determine the "free growth initial void radius" necessary for the initial conditions of the theory. However, nucleation calculations, when tied to the theory, can provide the magnitude and temperature dependence of the initial void radius.

5. The interaction between the different microstructural components (i.e., dislocation loops, network and void coalescence) when included in the theory, can help to extend the domains of application of the theory to higher irradiation doses.

6. In the present formulation of the rate theory, collision cascade effects are homogenized over space. On the contrary, cascades have localized high damage rates,

which might influence the homogenization assumptions of the rate theory. In low damage rate experiments, isolated spikes could be better simulated by a pulsed source of irradiation, rather than homogenizing their effects.

7. In this study, a time independent temperature and stress have been assumed. However, in pulsed irradiation situations, the temperature and stress accompanying the damage pulse are functions of time. To assess the importance of these time variations, their impact on point defect transport, and on the growth of the microstructural components, research efforts should be directed towards the precise determination of time dependent temperature and stress behavior.

APPENDIX A

THE EFFECT OF DISLOCATION BIAS ON THE TEMPERATURE DEPENDENCE OF SWELLING IN ELECTRON IRRADIATED ST 316 SS

During electron irradiation, the PKA (Primary Knock on Atom) energy is not great enough to cause collision cascades, thus eliminating the direct formation of vacancy loops in cascades. On the other hand, the diffusion of point defects to dislocations, is mainly affected by the interstitial-dislocation bias factor. In this appendix, we show the effect of this bias factor on the magnitude of the temperature dependent void swelling in 316 SS under electron irradiation.

The void swelling temperature dependence of electron irradiated 316 SS is shown in Figure (A.1). Calculations have been made with bias factors varying between $Z_i = 1.01$ and $Z_i = 1.08$. It is noticed that the same general temperature behavior is conserved, with the peak swelling temperature about 625-675°C, irrespective of the bias factor. However, the magnitude of swelling is reduced for lower values of the bias factor. In Figure (A.2), the effect of the excess bias ($\Delta Z_i = Z_i - 1$), on the peak swelling of electron irradiated ST 316 SS, is shown. The peak swelling is almost linear as a function of ΔZ_i except for small values (less than ~ 0.02). As an example, when $Z_i = 1.08$, the peak swelling is $\sim 32\%$ while if $Z_i = 1.02$, the peak swelling is only 6%.

THE EFFECT OF DISLOCATION BIAS ON THE TEMPERATURE DEPENDENCE OF SWELLING IN ELECTRON IRRADIATED ST316S.S.

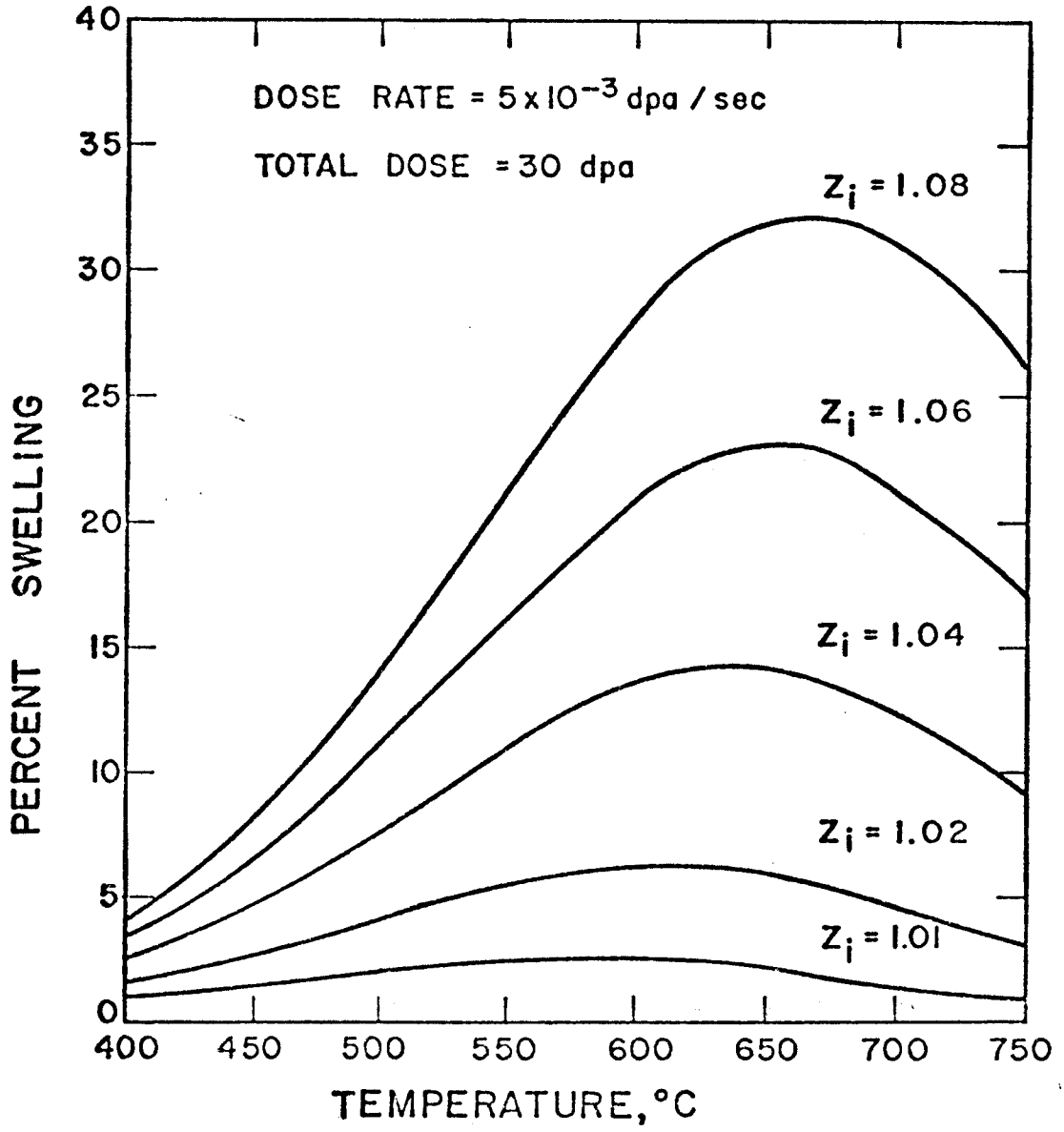

Fig. (A.1)

EFFECT OF DISLOCATION BIAS ON THE PEAK SWELLING OF ELECTRON IRRADIATED ST 316S.S.

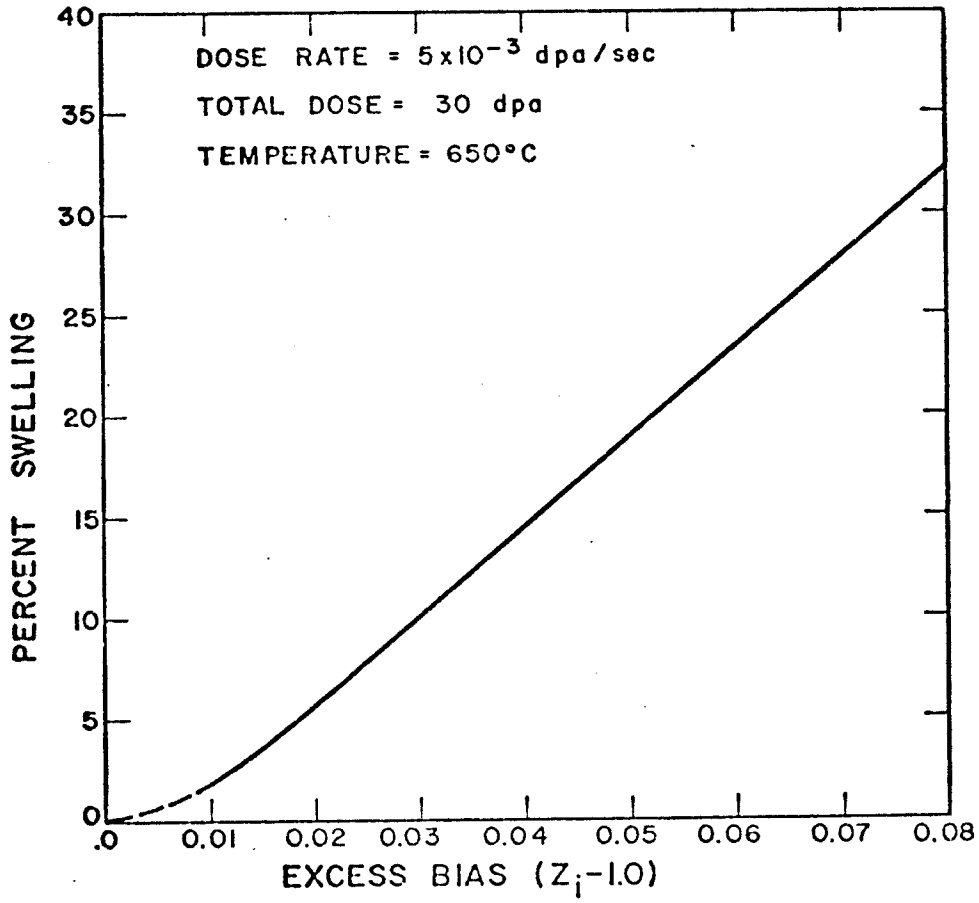

Fig. (A.2)

APPENDIX B

COMBINED EFFECT OF CASCADE COLLAPSE EFFICIENCY AND BIAS FACTOR ON VOID SWELLING IN ION IRRADIATED 316 SS

Because of the importance of the collision cascade collapse in ion or neutron irradiated metals, this appendix will discuss the combined effect of changing the collapse efficiency (ε) and the bias factor (Z_i), on swelling of 316 SS.

The calibration of the experimental results of ion irradiated 316 SS in Chapter VII, considered values of Z_i = 1.08 and ε = 4.4%. This combination of Z_i and ε allowed the theory to correlate with the experimental results. Similar calculations have been carried out, with the following conditions:

$$\text{Dose rate} = 10^{-3}\,\text{dpa/s},$$

$$\varepsilon = 1.2\%,$$

$$Z_i = 1.025,$$

$$R_c(0) = 300\ \text{Å at } 700°C,$$

$$R_c(0) = 30\ \text{Å at } 450°C,$$

and the parameters of 316 SS from Table (6.1).

The temperature dependence of the swelling is shown in Figure (B.1). It can be seen that the theory comes close to the experimental values, even with a different combination of ε and Z_i. This indicates that the individual choice of Z_i and ε is not unique to produce agreement with experimental

THE TEMPERATURE DEPENDENCE OF VOID SWELLING IN M316 S.S. IRRADIATED WITH 22 MeV C^{++} IONS.

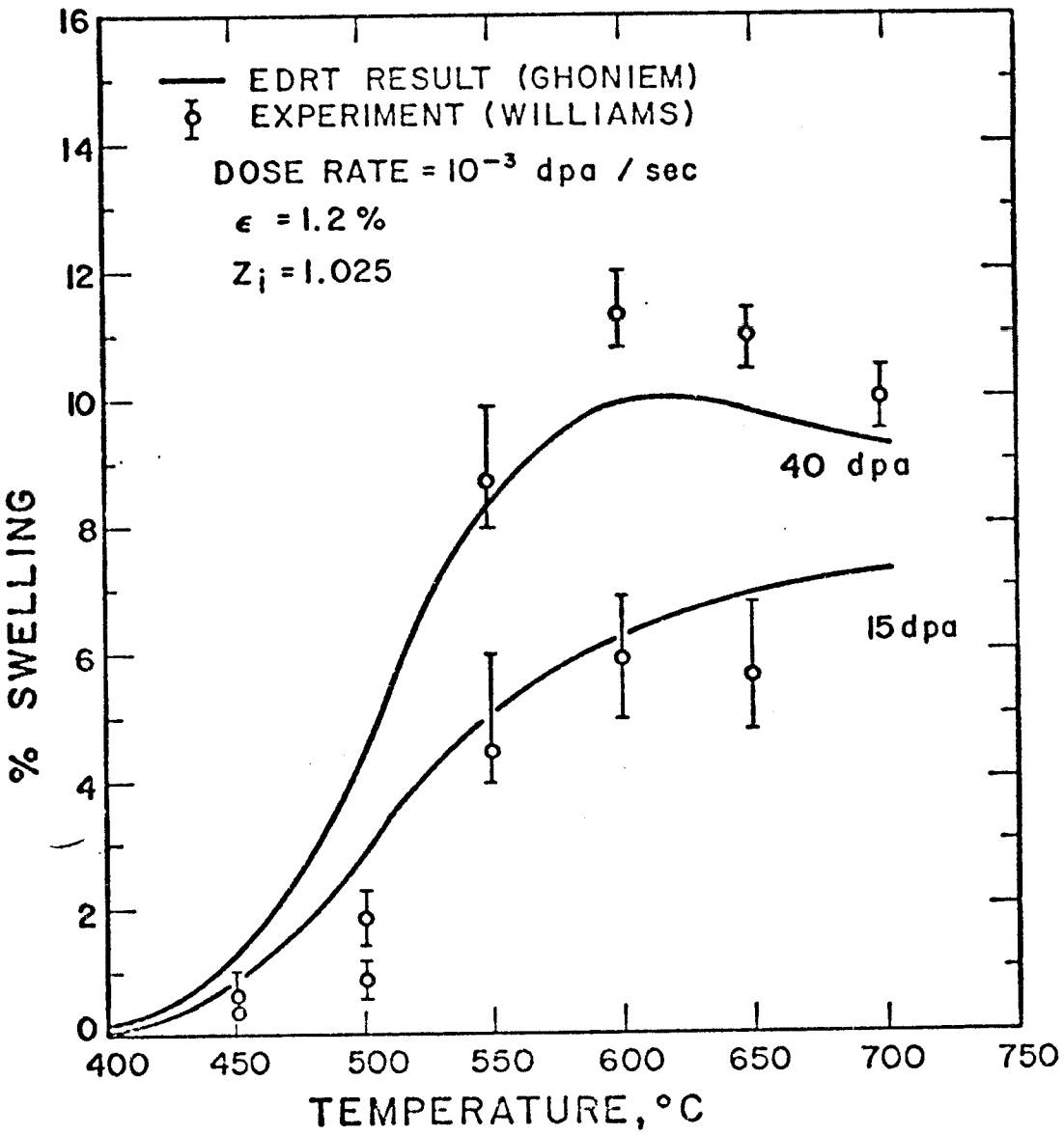

Fig. (B.1)

results, only the combination of both.

The effect of collision cascade and dose rate on the growth of voids, has been discussed in Chapter VIII, with values of Z_i = 1.08 and ε = 4.4%. Calculations have been made with the previous set of conditions to determine the growth — no growth boundary as a function of dose rate and cascade collapse efficiency. As shown in Figure (B.2), a smaller value of Z_i (namely Z_i = 1.025), shifts the boundary towards smaller values of ε, when compared with Figure (8.38). It can be seen that for Z_i = 1.025, values of ε greater than about 1.6% will completely inhibit void growth in 316 SS under ion irradition.

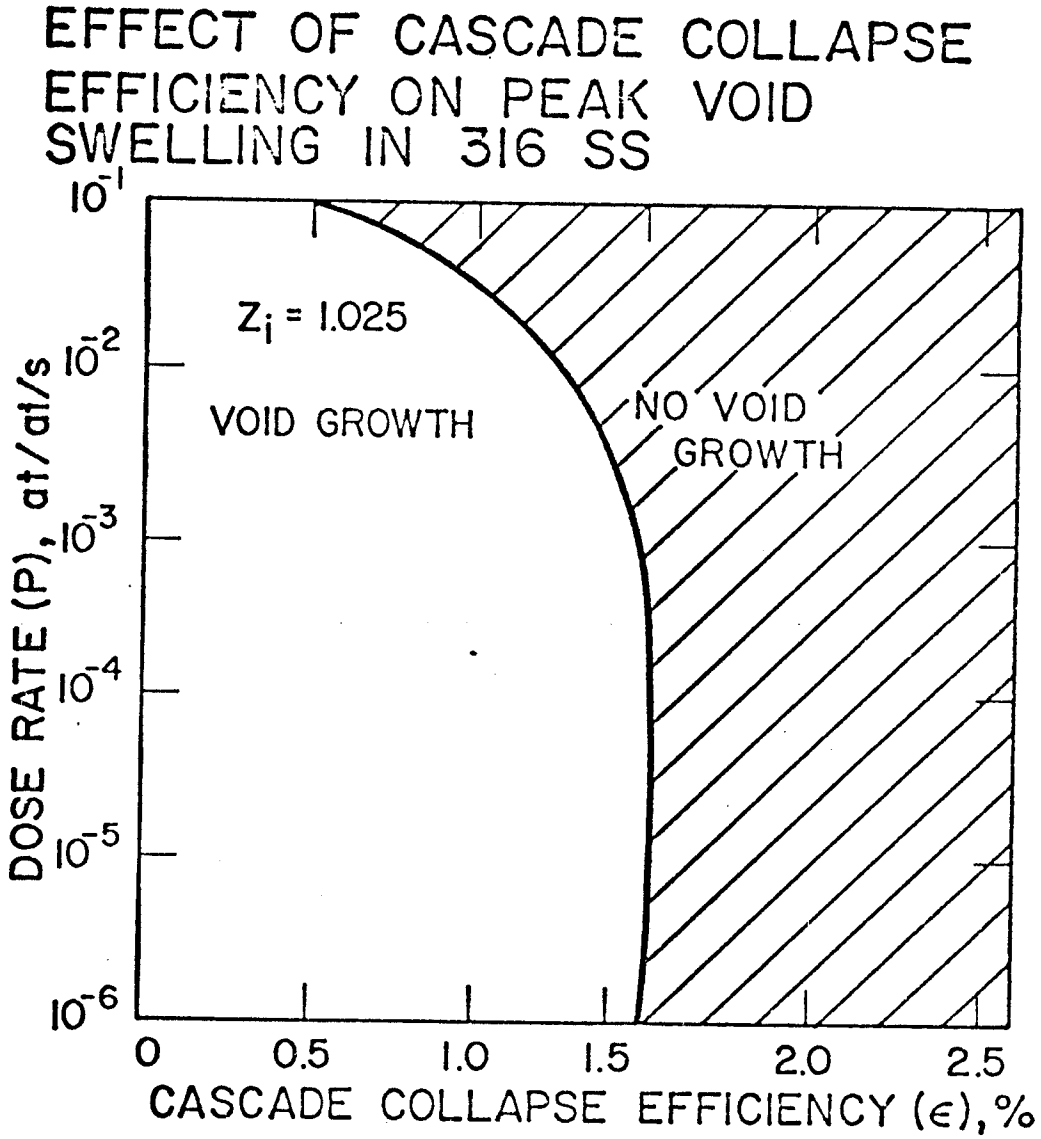
EFFECT OF CASCADE COLLAPSE EFFICIENCY ON PEAK VOID SWELLING IN 316 SS
Z_i = 1.025
VOID GROWTH
NO VOID GROWTH
DOSE RATE (P), at/at/s
10^{-1}
10^{-2}
10^{-3}
10^{-4}
10^{-5}
10^{-6}
0
0.5
1.0
1.5
2.0
2.5
CASCADE COLLAPSE EFFICIENCY (ϵ), %

Fig. (B.2)

REFERENCES

[1] Proc. of B.N.E.S. European Conf. on "Voids Formed by Irradiation of Reactor Materials", Reading Univ., Ed. S.F. Pugh, M.H. Loretto and D.I. Norris, (1971).

[2] Proc. of International Conf. on Voids, Albany, Ed., L.W. Corbett, (1971).

[3] Proc. of Conf. on "Defects and Defect Clusters in B.C.C. Metals and Their Alloys", Gaitherburg, Nucl. Met., Vol. 18, (1973).

[4] Proc. of Conf. on "Physics of Voids", Harwell, Ed. R.S. Nelson, Harwell Research Report AERE-R 7934, (1974).

[5] Proc. of International Conf. on "Fundamental Aspects of Radiation Damage in Metals", Gatlinburg, (USA), Ed. M.T. Robinson and F.W. Young, (1975).

[6] A. Taylor et al., Argonne (USA) Report, ANL/CTR/TM-39, (1975).

[7] J.E. Westmoreland, J.A. Sprague, F.A. Smidt, Jr., and P.R. Malmberg, Application of Ion Beams to Metals, Ed. S.T. Picraux, E.P. Eernisse and F.L. Vook, (Plenum Press, New York, 1974), p. 663.

[8] J.E. Westmoreland et al., Reference (4) above, p. 268.

[9] F.A. Smidt, Jr., and S.A. Metz, Reference (2) above, p. 613.

[10] S.A. Metz and F.A. Smidt, Appl. Physics Lett., Vol. 19 (1971), 207.

[11] J.A. Sprague and F.A. Smidt, Jr., NRL Memorandum Report 2629, (1973).

[12] J.O. Schiffgens and N.J. Graves, Hanford (USA) Report, HEDL-TME 75-76, UC20 (1975).

[13] J.O. Schiffgens and D.G. Doran, Reference (5) above, p. I-532.

[14] J.O. Schiffgens and R.L. Simons, Hanford (USA) Report, HEDL-TME 75-24, UC20 (1974).

[15] Y.H. Choi, A.L. Bement and K.C. Russell, Reference (5) above, p. II-1.

[16] Y.H. Choi, "Computer Simulation of Effect of Fusion Burn Cycle on First Wall Swelling," M.S. Thesis, MIT, (1975).

[17] G.R. Odette and R. Myers, J. Nucl. Mater, to be published.

[18] J.A. Sprague, K.C. Russell, and Y. H. Choi, Reference (5) above, Vol. 2, p. 1181.

[19] A.J. Toepfer, T.H. Martin, M.J. Clauser, D.W. Swain and E.H. Beckner, Sandia Report, SAND 75-5445.

[20] L.P. Bradley and G.W. Kuswa, Phys. Rev. Lett 29, (1972), 1441.

[21] J.R. Kerns and D.J. Johnson, J. Appl. Phys., 45(1974), 5225.

[22] J.C. Davis, J.E. Osher, R. Booth and C.M. Logan, Proc. of the 2nd Topical Meeting on "the Technology of Controlled Nuclear Fusion", Vol. 4, CONF-760935-P4, P.1447.

[23] W.J. McMasters, et al., California Univ. Livermore, Lawrence Radiation Lab., Report UCRL-50174, (1970).

[24] F. Biggs, R. Lighthill, Sandia Labs., Albuquerque, New Mexico, Report SC-PR-710507, (1971).

[25] J.W. Robinson (Ed.), Handbood of Spectroscopy, Vol. 1, (CRC Press, Cleveland, Ohio, (1976).

[26] J.F. Janni, Air Force Systems Command, Kirtland Air Force Base, New Mexico, Report (1966).

[27] F. Bloch, "Bremsvermögen von Atomen mit Mehrern Elektronen", Zeitshiift Für Physik, 81, (1933), 353.

[28] J. Lindhard et al., Mat. Fys-Medd., Dan. Vid. Selsk, 33, No. 14 (1963).

[29] T. Hunter and G. L. Kulcinski, Univ. of Wis. Fusion Design Memo, UWFDM-196, (1977).

[30] J.L. Katz and H. Wiedersich, J. Chem Phys., 55, (1971), 753.

[31] K.C. Russell, Acta Met., 19,(1971), 753.

[32] J.J. Burton, Scripta Met., 5, (1971), 449.

[33] K.C. Russell and R.W. Powell, Acta. Met., 21, (1973), 187.

[34] J.M. Bunch et al., Fifth Symposium on Eng. Problems of Fusion Research, Princeton Univ., (1973).

[35] W.V. Green, J.W. Weertman, Nature, 243, (1973), 159.

[36] S.G. Varnado, et al., Sandia Laboratories Energy Report, SAND 74-0160.

[37] J.L. Emmett, J. Nuckolls and L. Wood, Scientific American, Vol. 230, No. 6, (1974), p. 24.

[38] A.P. Fraas, Oak Ridge National Lab., Report TM-3231, (1971).

[39] L.A. Booth (Compiler) Los Alamos Scientific Lab., LA-4858-MS, Vol. 1, (1972).

[40] J. Williams et al., Fifth Symposium on Eng. Problems of Fusion Research, Princeton Univ., (1973).

[41] J. Hovingth et al., First Topical Meeting on the Technology of Controlled Nuclear Fusion (ANS), (1974).

[42] J.A. Maniscalo, Proc. of 2nd Topical Meeting on Technology of Controlled Nuclear Fusion, Richland, Washington, (1976).

[43] J.A. Maniscalo and W.R. Meier, ANS Transactions, Vol. 26, (1977).

[44] R. Conn et al., Wisconsin Fusion Design Group, Univ. of Wis., Fusion Design Memo, UWFDM-190, (1976).

[45] R.S. Pease, ERATOM-UKAEA Association on Fusion Research --Pulsed Fusion Reactors, International School of Fusion Technology, Erice-Trapani, Sicily, (1974).

[46] J. Williams, et al., Nuclear Technology, Vol. 22, No. 3, (1974).

[47] T.O. Hunter and G.L. Kulcinski, Univ. of Wis. Fusion Design Memo, to be published, (1977).

[48] K.C. Russell, Scripta Met., Vol. 7, (1973), 755.

[49] H. Wiedersich, J.J. Burton and J.L. Katz, J. Nucl. Mater., 51, (1974), 287.

[50] H. Wiedersich, Reference (4) above, p. 147.

[51] H. Wiedersich, Rad. Effects, 12, (1972), 111.

[52] M.R. Hayns, J. Nucl. Mater., 56 (1975), 267.

[53] N. Ghoniem and G.L. Kulcinski, Univ. of Wis. Fusion Design Memo, UWFDM-180 (1976).

[54] R. Bullough and R.C. Perrin, Radiation Damage in Reactor Materials, Symposium Proceedings, Vienna, Vol. 2, (1969), p. 233.

[55] R. Bullough,B.L. Eyre and R.C. Perrin, Harwell Report, AERE-R 6284, (1969).

[56] R. Bullough and R.C. Perrin, Reference (2) above, p. 769.

[57] A.J.E. Foreman, Harwell Report AERE-R7135, (1971).

[58] M.T. Robinson, Proc. of International Conf. on "Fundamental Aspects of Radiation Damage in Metals", Gatlinberg, Ed. M.T. Robinson and F.W. Young, (1975), p. 1.

[59] A.D. Brailsford and R. Bullough, Proc. of the Argonne Conf. on "Properties of Atomic Defects in Metals," (1976).

[60] J.B. Roberto, J. Narayan, and M.J. Saltmarsh, Proc. Intern. Conf. of Radiation Effects and Tritium Technology for Fusion Reactors, Gatlinburg, Tenn., 1-3 October 1976, p. II-159.

[61] B.L. Eyre, M.H. Loretto and R.E. Smallman, Proc. of "Vacancy '76", Univ. of Bristol, (1976).

[62] B.L. Eyre, J. Physics F: Metal Physics 3, (1973), 422.

[63] B.L. Eyre and C.A. English, Reference (4) above, p.239.

[64] M.W. Finnis, to be published (1977).

[65] R. Bullough, E.L. Eyre and R. Krishan, Proc. R. Soc., London, A. 346 (1975), p. 81.

[66] F.R.N. Nabarro, Rep. Conf. on "Strength of Solids," London: Phys. Soc., 47, (1947).

[67] C. Herring, J. Appl. Phys. 21, 437 (1950).

[68] D. J. Mazey, R. Bullough and A.D. Brailsford, J. Nucl. Mat. 62, (1976), 73.

[69] R. Bullough, Private Communications.

[70] R. Lott, G.L. Kulcinski and N. Ghoniem, work in progress.

[71] A.D. Brailsford and R. Bullough, J. Nucl. Mater., 44 (1972), p. 121.

[72] A.D. Brailsford, and R. Bullough, Proc. of Conf. on "Physical Metallurgy of Reactor Fuel Elements", Berkeley, (England), (1973), p. 148.

[73] A.D. Brailsford, R. Bullough and M.R. Hayns, J. Nucl. Mater.,Vol. 60 (1976), 246.

[74] J.C. Maxwell, A Treatise on Electricity and Magnetism,, 3rd Ed. Vol. 1, (Clarendon Press, Oxford, 1892), p.440.

[75] A.H. Cottrell and B.A. Bilby, Proc. of Phys. Soc., Vol. 62, (1949) 49.

[76] R. Bullough and R.C. Newman, Rep. Prog. Phys. 33, (1970) 101.

[77] W.G. Wolfer, M. Ashkin, J. of Applied Physics, Vol. 47, No. 3 (1976).

[78] P.T. Heald, Phil. Mag. 31, 551 (1975).

[79] A.D. Brailsford and R. Bullough, Proc. of "Vacancy '76", Univ. of Bristol, (1976), also Harwell Res. Rep., AERE-TP 679 (1976).

[80] Katsuhiko Ogata, Modern Control Eng., (Prentice-Hall, 1970).

[81] N. Ghoniem and G.L. Kulcinski, Univ. of Wis. Fusion Design Memo, UWFDM-181 (1976).

[82] N. Ghoniem and G.L. Kulcinski, Univ. of Wis. Fusion Design Memo, UWFDM-200 (1977).

[83] T.E. Volin and R.W. Balluffi, Phys. Stat. Vol. 25, 163, (1968).

[84] K.H. Westmacott, R.E. Smallman, and P.S. Dobson, Metals Science Journal, Vol. 2, (1968), p. 177.

[85] L.B. Loeb, The Kinetic Theory of Gases, (Dover Publications, 1961), p. 140.

[86] Kiritani, J. Phys. Soc. Japan, Vol. 4 (1965) 148.

[87] A. Kelly and R.B. Nicholson, Prog. Materials Sci., 10 (1963) 149.

[88] R. Bullough and M.R. Hayns, J. Nucl. Mater. 57, (1975) 348.

[89] P.T. Heald and M.V. Speight, Phil.Mag. 29 (1974) 1075.

[90] W.G. Wolfer, M. Ashkin and A. Boltax, ASTM STP 570 (1976) p. 233.

[91] W.G. Wolfer and J.L. Straalsund, Scripta Met. 7 (1973) 161.

[92] W.G. Wolfer, Scripta Met., 9 (1975) 801.

[93] R. Bullough and J.R. Willis, Phil. Mag., 31 (1975) 855.

[94] S.D. Harkness and Che-Yu Li, Reference (2) above, p.798.

[95] S.D. Harkness and C.Y. Li, Radiation Damage in Reactor Materials, Vol. 2 (1969) p. 189, IAEA, Vienna.

[96] H. Wiedersich, Rad. Effects., Vol. 12, (1972), p. 111.

[97] A.C. Hindmarch, LLL Report UC10-30001, Rev. 3 (1974).

[98] C.W. Gear, Numerical Initial Value Problems in Ordinary Differential Equations (Prentice-Hall, Englewood Cliffs, N.J., 1971).

[99] N. Ghoniem and G.L. Kulcinski, Univ. of Wis., Fusion Design Memo UWFDM-138 (1975).

[100] N. Ghoniem and E. Anderson, Univ. of Wis. Fusion Design Memo, UWFDM-211 (1977).

[101] M.J. Makin and G.P. Walters, Reference (4) above, p. p. 299.

[102] T.W. Williams, Reference (1) above, p. 205.

[103] N.H. Packan, J. Nucl. Mat., 40,(1971),1.

[104] D.G. Doran and N.J. Graves, Hanford Eng. and Development Lab. Report, HEDL-TME 76-70, VC-79 b,d, (1976).

[105] D.G. Doran, Nucl. Sci. Eng., 52, (1973) 398. See also Nucl. Sci. Eng. 49, (1972) 130.

[106] G.L. Kulcinski, D.G. Doran and M.A. Abdou, Univ. of Wis. Fusion Design Memo, UWFDM-15 (1973).

[107] J.O. Stiegler, Reference (2) above, p. 326.

[108] Y. Adda, Reference (2) above, p. 36.

[109] D.J. Mazey, R. Bullough and A.D. Brailsford, Harwell Report, AERE-R 8344 (1976).

[110] J.A. Sprague, J.E. Westmoreland, F.A. Smidt, Jr., and P.R. Malmberg, J. of Nucl. Mater., 54 (1974) 286.

[111] D.I.R. Norris, Phil. Mag., Vol. 23, 181, (1971) 135.

[112] D.I.R. Norris, Phys. Stat.Sol. (a) 4 (1971) k5.

[113] T.S. Lundy and J.F. Murdock, J. Appl. Phys. 33 (1962) 1671.

[114] A. Seeger, J. Phys. F. Metal Physics, 3(2), (1973) 248.

[115] R.E. Smallman and K.H. Westmacott, Reference (1) above, p.159.

[116] N. Ghoniem and G.L. Kulcinski, Univ. of Wis. Fusion Design Memo, UWFDM-199 (1977).

[117] W.G. Johnston, J.H. Rosolowski, A.M. Turkalo and T. Lauriteen, General Electric Technical Information Series, Report No. 73CRD217, (1973).

[118] J.L. Straalsund, J. Nucl. Mater., 51 (1974), p. 302.

[119] J.F. Bates and J.L. Straalsund, Hanford Eng. Dev. Lab., Richland, Wash., HEDL-TME-71-139 (1971).

[120] R. Bullough, R.L. Eyre and G.L. Kulcinski, Univ. of Wis. Fusion Design Memo, UWFDM-184 (1976).

[121] B. Badger, et al., Univ. of Wis. Fusion Design Memo, UWFDM-112, (1975).

[122] B. Badger, et al., Univ. of Wis. Fusion Design Memo, UWFDM-150, (1976).

[123] R.W. Conn, Private Communications.

[124] F. Beranek, Univ. of Wis. Fusion Design Memo, UWFDM-210, (1977).

[125] G. Shuy, Private Communications.

[126] N. Ghoniem and G. Kulcinski, Univ. of Wis. Fusion Design Memo, UWFDM-203, (1977).

[127] N. Ghoniem and G. Kulcinski, to be published in the ANS Transactions for the Winter Meeting, San Francisco, (1977).